Politecnico di Milano

Dept. of Aerospace Science and Technology
Master of Science in Space Engineering

Small bodies gravity field on-board learning and navigation

MSc Thesis of:
Andrea Pasquale
Student ID: **883330**

Supervisor:
Prof. Michéle Lavagna

Advisors:
Capannolo Andrea
Silvestrini Stefano

Academic year 2018/19

Alla mia famiglia.

ABSTRACT

Proximity operations about asteroids are challenging because of the non-uniform gravity field that they generate, which is usually largely uncertain during design phases. Asteroids, in fact, are usually mostly characterized *in-situ*, especially from the gravitational point of view. Hovering and imaging the body are, in fact, fundamental science phases, in the characterization of the object composition and nature. The gravity field reconstruction plays, then, a fundamental role in the data fusion and in particular in the enhancement of the scientific knowledge of the specific object.

In case the orbiter is a micro-satellite, a CubeSat or, in general, a platform with reduced communication capabilities to ground, or a distributed system of platforms with high autonomy requirements, those operations become extremely challenging.

In this framework, this work proposes a new approach to reconstruct the gravity field of an objects using an Artificial Neural Network (ANN): the Hopfield Neural Network (HNN). More specifically, the gravitational field of the object is represented through a Spherical Harmonics Expansion (SHE) the coefficients of which must be estimated. In particular, the identification problem is written as an optimization $\min \mathcal{J}(\mathbf{x})$ and the performances of the identification are presented through several critical case studies in different dynamical environments. Finally, those results are integrated in an Extended Kalman Filter (EKF) navigation filter to assess its performance enhancement due to the higher order model.

Keywords: Perturbed Two-Body Problem (P2BP), Spherical Harmonics Expansion (SHE), Gravity Field, Parametric Identification, Small Bodies, Asteroids, Model Identification, ANN, HNN, Modified Hopfield Neural Network (MHNN), EKF, Navigation Filter.

SOMMARIO

Il design delle fasi operative di prossimitá di missioni aventi asteroidi come soggetti risulta estremamente complesso a causa del campo gravitazionale che essi generano. Infatti, questo risulta spesso differente rispetto al caso di corpo a simmetria sferica, richiedendo una modellazione piú complessa del semplice Problema a Due Corpi. Questo é dovuto alla loro forma irregolare e alla distribuzione di massa, che spesso risulta tutt'altro che omogenea. La ricostruzione del campo gravitazionale gioca un ruolo fondamentale nella *data fusion*, che porta a una crescita sostanziale della conoscenza scientifica dell'oggetto specifico.

Nel caso in cui l'orbiter é un micro-satellite, un CubeSat o, in generale, una piattaforma con ridotte capacitá di comunicazione a terra, o un sistema distribuito di piattaforme con elevate esigenze di autonomia, tali operazioni diventano estremamente impegnative a il loro design risulta un problema incredibilmente sfidante.

In questo contesto, questo lavoro propone un nuovo approccio per ricostruire il campo gravitazionale di un oggetto. In poarticolare, l'estensione della rete neurale ricorrente di Hopfield al problema specifico viene modellata. Il campo gravitazionale dell'oggetto é rappresentato attraverso un'espansione in armoniche sferiche i cui coefficienti vengono stimati dalla rete. In particolare, il problema di identificazione é rappresentato da un'ottimizzazione $\min \mathcal{J}(\mathbf{x})$, risolta dalla rete neurale in analisi. Le prestazioni dell'identificazione sono presentate attraverso diversi casi studio in diversi ambienti dinamici. Il metodo viene quindi esteso a casi di asteroidi binari. Infine, tali risultati sono integrati in un filtro di navigazione (filtro di Kalman esteso) con l'obiettivo di valutare il miglioramento delle sue prestazioni con il modello di ordine superiore.

Keywords: Problema dei Due Corpi Perturbato, Identificazione Parametrica, Asterodi, Identificazione Modello Dinamico, Reti Neurali, Filtro di Navigazione, filtro di Kalman.

ACKNOWLEDGEMENTS

HERE it comes probably the hardest part of writing this thesis, since the are so many people to acknowledge and just a few of them to be selected and cited here.

First of all, I would like to thank my parents, Angelo and Fiorangela, for the endless trust and support they gave me during those five years. Thank you for being my reference, to push me beyond my limits and for hundreds of advices. Thank you for your question and your interest on my research, for the hours of conversation about my work. You've been always able to find the best in me, and I will always be grateful to you for making me the person I am now.

I would like to thank my little (but not too little) sister Giada for sharing many special moments together in those years even though I moved from home.

I want to thank Alessia, for being always by my side. I really thank you for your support, especially during those last months.

I want also to thank all my friends: from the *Camplus-guys* Aldo and Massimo who were here since the beginning, to the new ones, Antonio, Leonardo, Simone, Andrea G., Cristiano and all the other members of the ASSYST group as well as the other classmates that make me really enjoy the time spent at the university during those last years.

I'm extremely grateful to my advisor, Professor Michéle Lavagna, which has always been a great source of motivation and inspiration for me. I also would like to thank her for the invaluable advices, which guided me during this last year in the development of this work. Special thanks to my advisors, Stefano and Andrea, for the countless advices and for providing me, together with Professor Lavagna, the best environment for the development of my research.

Many others deserve my gratitude: special thank you to all of them too.

Andrea

TABLE OF CONTENTS

LIST OF FIGURES

LIST OF TABLES

Part I

Introduction & Background

INTRODUCTION

> Because there is a law such as gravity,
> the universe can and will create itself
> from nothing.
>
> Stephen Hawking

In recent years, the interest in minor celestial bodies such as *asteroids* and *comets* has grown in the scientific community. They are extremely numerous in the Solar System and even though they represent only a tiny fraction of the mass orbiting around the Sun, their study is fundamental to understand the formation and the evolution of the Solar System as well as the birth of life on Earth.

In parallel, advances in CubeSats technology allow the use of these platforms in complex scientific missions: the small volumes and masses, the versatile purpose, as well as the fast development time associated with a potential high return-to-cost ratio are really attractive features and result the origin of the increasing number of new mission proposals. The joint ESA/NASA Asteroid Impact and Deflection Assessment (AIDA) mission is a clear example to how CubeSats supporting capabilities can enhance the scientific as well as the technological return [1]. However, operation of a CubeSat in the deep-space microgravity environment brings additional challenging factors in their development, including the increased radiation environment, the significant contribution of non-gravitational forces to the satellite orbit, the limited communication opportunities as well as the limited computational capabilities. These factors need to be taken into account in the form of modifications to the classic CubeSat architecture. In particular, semi-autonomous satellite operation, navigation, and the active orbit correction are usually required in those cases [2].

From the scientific point of view, one upon the major interests in the characterization of small bodies is the gravitational mapping of the body. In fact, if one think to an autonomous robotic mission to a minor body, the first problem is the model of the body's dynamical environment: it is usually *not* available, at least in the early phases of the mission. Then, the gravitational mapping task appears to be crucial and results even more crucial if the mission includes landings or, in general, proximity operations. The most clear example is the case of ESA mission *Rosetta*, where the complex dynamical environment of the comet 67P/Churyumov-Gerasimenko have been

analysed. Moreover, a fine gravitational mapping is required not only for the proximity operations them self but also to reconstruct *a posteriori* the internal structure of the body and so its origin. In fact, gravity science, in combination with improved knowledge of the shapes of the body from observations obtained from on-board cameras provide insights of the interior of the body, from the core to the crust [3].

Finally, the gravitational mapping of small bodies results even more challenging if a CubeSat or, in general, a platform with reduced communication capabilities to ground is used to do it. In this framework, this work want to provide a new approach to reconstruct the gravity field of either unknown or partially known objects.

0.1 A Brief Literature Review

The simplest technique for measuring *in-situ* a body's gravity from orbit is to measure the orbital period (or semi-major axis) of an object orbiting about it: by tracking the spacecraft's motion, one can estimate properties of the object's gravitational field. Kepler's third law, in fact, allows the body's mass to be determined [4]: this provides complete knowledge of the body's gravity field, if the body's mass distribution is *spherically symmetric*. From this information, the Restricted Two-Body Problem (R2BP) model is built: it is really simple, analytically solvable as well as one of the most used nowadays for mission design purposes [5].

However, the R2BP is not an accurate model even in case the body appears nearly spherical: as an example, consider the case of the Earth. To the Earth, in fact, is associated a flattening of about 0.0033 and as a first approximation, the oblateness coefficient J_2 is crucial in terms of satellite motion determination [6]. In this case, high fidelity models are available tanks to the Gravity field and steady-state Ocean Circulation Explorer (GOCE) ESA mission and Gravity Recovery And Climate Experiment (GRACE) NASA mission [7]. These are unique cases since those missions have the possibility to relay on the GPS for the orbit determination: it gives extremely accurate measurements so that the gravitational mapping results to be extremely accurate too. The results of the model coming from GOCE mission has been then used to reconstruct a fairly accurate geoid model and so a density map of the planet.

In the case of a small body, such as an asteroid or a comet, however, the mass distribution is usually much more *irregular* than the case of the Earth, so that the gravity field results to be *largely unknown* even during the proximity operation phases. However, the gravitational field of those bodies is much weaker that in a planetary case so that in some cases (as in the case of JAXA's Hayabusa2 mission [8]), those bodies are considered as perturbation to the spacecraft heliocentric orbit from the mission analysis point of view.

If, indeed, the body is flown, the R2BP results to be really inaccurate for mission analysis & design purpose, due to the irregularities of the body but also due to the presence of Solar Radiation Pressure (SRP), that is usually comparable to the body's gravity field in magnitude. For these reasons designing a natural periodic orbit about those kind of bodies is a complicated task since exist only with limited geometry and with a complex of orbital shape [9], [10], [11].

For what regards the main gravity field, there have been a certain number of missions that uses radio-science to estimate higher-order terms of the gravitational potential field: Miller et al. [12] presents a 10^{th} order model for 433 Eros tracking NEAR-Shoemaker while Konopliv et al. [3] produced a 20^{th} order gravity field model for 4 Vesta via tracking Dawn. This technique works well for large bodies but its accuracy decreases drastically for smaller bodies due to uncertainties arising from the SRP. Radio-science can be used, in general, in different ways to reconstruct the gravitational field. On one hand, the radio-science data can be processed directly to give a certain expansion of the gravity field of the body: an ellipsoidal harmonics expansion of 433 Eros has been developed in [13], while a spherical harmonics one in [3]. On the other hand, the data can be used to extract a shape model of the body in order to be used in a shape-based gravitational model (such as the constant density polyhedron one). Other authors in [14] propose, instead, a superposition of both this kind of results: a gravity model fitting superimposing point-mascon and spherical harmonic fields to a high-fidelity polyhedral model, resulting in reasonably fast and globally valid Pareto optimal model.

A technique suitable for smaller bodies was employed by the Hayabusa spacecraft at 25143 Itokawa [15]. This involved first propulsively hovering above the asteroid, then ceasing propulsion, to fall freely, measuring height above the asteroid via LIDAR measurements [16]. However, this technique provide a measure of only the mass of the body, without any other information about the higher order harmonics of the gravity field of the body.

In [17] a new technique that uses the fly-bys of a swarm of simple small probes (micro-sat) is proposed for the estimation of the gravity field and the mass of the body. Fly-bys, however, can be used also with more massive spacecraft for the reconstruction of the gravitational features of a body, as in the case of OSIRIS-REx [18]: in this case the spacecraft is tracked from the DSN and from the doppler-range data the gravitational parameter can be recovered. As always, combining it with the volume and the density of the asteroid, a high-fidelity approximation of the gravity field can be recovered using a constant polyhedron model or more refined models.

A recent technique is presented in [19] and uses formation flying: it has two spacecraft flying in formation about a target body, measuring range-rates between them, from which gravity-field parameters are extracted. This method has been used in the GRACE Earth gravity mission, and the GRAIL Lunar gravity mission. However, this technique require two spacecraft flying in formation, and processing the measurements involves a quite complicated non-linear estimation process.

Another novel technique for measuring the gravity field of a body from orbit uses the Tidal Acceleration Gravity Gradiometry (TAGG) technique and is presented in [20]. This method involves measuring the tidal acceleration field at a point offset from the mass-centre of a spacecraft, which is caused by the gravity-gradient of a nearby body, using an absolute (bias-free) accelerometer. This method has been applied (in the study) to the case of Didymoon, the $\sim$ 150 m diameter secondary body of 65803 Didymos binary system, into which NASA plans to impact its DART spacecraft.

Last but not least, it is no worth to underline that, nowadays, a well-established method capable to identify the gravitational field of a body *on-board* and *online* is not available, at least with traditional methods. There are, however, a number of studies in

which novel techniques, such as *machine learning* and *reinforcement learning* ones are proposed. Being most of those methods associated with a neural network, they result lightweight from the computational point of view but usually have a major problem: they need a *training*. In space applications, in fact, a training is not admissible since during it the network can fail dealing to the failure of the mission.

In general, since the aim to reconstruct the gravity field of a body can be related to non-linear system identification there are a number of methods that uses *neural networks* to identify the system from scratch. As an example, Furfaro et al. in [21] propose the use of Extreme Learning Machine (ELM) theories to design, train and validate Single-Layer Forward Networks (SLFN) capable of learning the relationship between the spacecraft position and the gravitational acceleration. Moreover, the analysis of the performances in constant density models for 433 Eros and 25143 Itokawa show that the SLFN is able learn the desired functional relationship both globally and as well as locally resulting in a robust neural algorithm for on-board, real-time calculation of the gravity field needed for close-proximity operations. This method, however, as said before, needs a training for the SLFN.

There are novel techniques that reconstruct the gravitational field in an un-direct way: as an example, Willis et al. in [22] propose to use neural reinforcement learning algorithm to control a spacecraft around a small celestial body whose gravity field is unknown. The controller optimization is formulated as a Markov Decision Process (MDP) learning problem. A Direct Policy Search (DPS) with a genetic algorithm to obtain controller policies is preformed, with a policy architecture presented as a Feed Forward Neural Networks (FFNN) with one hidden layer. Also in this case, a batch of data are needed to be used in the FFNN's parameters optimization.

So, there are a number of studies that proposes the use of evolutionary methods for forward modelling the gravitational environment about asteroids and other bodies but the main problem, as said, is that they're usually associated with a training. Other examples can be the use of Back Propagation Artificial Neural Network (BPANN) for the Earth gravity field approximation is presented in [23] and the use of ANN in [24] for a body gravity field interpretation. It is of interest from this point of view, the use of Radial Basis Functions (RBF)-based networks that are an alternative to the popular Multi-Layer Perceptors (MLP) (e. g., the SLFN and the ANN discussed before) [25]. Moreover, in [26] and [25] it has been shown that a RBF-based networks can be used for the *online* identification of non-linear system.

More recently, in [27] the use of a neural network based Modified State Observer (MSO) is presented. It is a fairly new technique that uses the MSO for estimating the uncertainties that a satellite may experience while in orbit, with the primary advantage that the neural network is trained *online*, meaning that no offline learning is required. This method appears to be one among the most promising but it reconstruct the gravity field in a indirect way: in fact the MSO reconstruct the accelerations along three axis as (a_x, a_y, a_z), without giving any other informations. Indeed, if a spherical harmonics expansion model wanted to be used to model the gravity field of the body, a forward least-square optimization must be performed with those reconstructed accelerations to extract the expansion.

0.2 Problem Definition & Thesis Outline

The main objective of this work is the *online* and *in-situ* identification of the gravitational field of bodies such as asteroids and comets with platforms with reduced computational capabilities and communication opportunities. In particular, the identification goal is to reconstruct the SHE model of the selected body and not to reconstruct directly the resulting accelerations. Once the SHE model is reconstructed, then, the preliminary design of a navigation filter based on the reconstructed model is assessed, by the use of an EKF. These goals are achieved through 9 chapters organized as follows:

Cpt.1 In this chapter the dynamical models used for the orbital dynamics as well as to represent the dynamical environment of the small bodies are presented. The models allow to represent the dynamics of a spacecraft coupled with the rotation of the body as well as to represent and design orbits in binary systems.

Cpt.2 This chapter, instead, deals with the mathematical models used to represent the gravitational field of the selected bodies, $\mathcal{U}$. In particular, different models are presented: the spherical harmonics expansion model, the shape-based constant density polyhedron model and the tri-axial ellipsoid one.

Cpt.3 The last chapter of the first part has to be considered as a brief analysis on the gravitational field of small bodies, being it much different from the point-mass one. So, some examples are presented and some gravitational models are compared from a qualitative and a quantitative point of view.

Cpt.4 This chapter deals with the mathematical modelling of the neural network that is used to reconstruct the SHE coefficients. In particular, the parametric identification problem is formulated as an optimization problem to be solved by a specific tailored ANN called MHNN as well as the convergence is assured by a Lyapunov stability analysis.

Cpt.5 This chapter is a transition one: since the HNN has never being used in gravitational identification problems, its convergence velocity and accuracy is analysed on simple non-rotating, axis-symmetric bodies. Some useful hints are extracted as well as the network instability phenomena is underlined.

Cpt.6 In the *conceptual mission* chapter, the idea is to think how a scientific mission that approach a partially known object would refine the gravitational model of the body using the MHNN. To do so, some parametric analysis are performed on the body shapes and masses as well as on the spacecraft's orbits used.

Cpt.7 The core of the gravitational model identification is presented in this chapter. The cases of *Bennu*, *Eros*, *Castalia* as well as the binary *KW4* are presented. Parametric analysis are performed on the influence of rotational state, force perturbations (mainly SRP), instruments noise as well as orbital initial conditions to the network convergence.

Cpt.8 The third part of the work is dedicated to the navigation of the body. More specifically this chapter deals with the mathematical modelling of the EKF as well as to some hints of its numerical implementation.

Cpt.9 The last chapter, indeed, present some case studies in which the aim is to

integrate the EKF model with the higher-order SHE models reconstructed by the MHNN. Also in this case parametric analysis are performed to understand how the convergence of the filter behaves with different dynamical models as well as different bodies.

MINOR BODIES: CLASSIFICATION, SHAPE MODELS AND SELECTION

In addition to the eight planets, there are populations of smaller objects orbiting the Sun: comets, asteroids, and trans-neptunian objects. These populations differ significantly from each other by the orbits and physical properties of their members. *Comets* are icy bodies in the outer Solar system with stellar and galactic perturbations delivering some of them periodically close to the Sun. *Trans-neptunian* objects, as well, are icy, but have orbits that constantly keep them in the outer borders of the Solar system.

Asteroids, which are the subjects of this thesis, are rocky bodies remnants left over from the early formation of our solar system about 4.6 billion years ago.Most of them can be found orbiting the sun between Mars and Jupiter within the main asteroid belt, that will be called *main belt* from now one. From Figure 1 and Figure 2 can be seen that the distribution of these objects is really dense.

Asteroids were discovered in 1801, when *Ceres* was first observed by Piazzi. The name asteroid ("star-like") was given by William Herschel in 1802, because these objects are so small compared to their distance from the Earth that they are observed as point sources, just like stars. The next three asteroids *Pallas*, *Juno*, and *Vesta* were discovered within the next seven years, after which it took almost 40 years to discover the next one. Ever since, increasing numbers of new asteroids have been discovered per each year. At the moment, according to [28], there are almost 790000 numbered asteroids and almost 20000 numbered near-Earth asteroids (as of February, 2019). The estimated total number of 1-km-sized objects or larger is 1.1-1.9 million (in the main belt only), according to the results from the ISO (The Infrared Space Observatory) Deep Asteroid Search.

The determination of diameter and shape of asteroids can be done using several different methods [29], such as inverse light-curve technique, occultation methods, radio-location method, and finally direct on-site inspection. In any case, the physical model of the body is a reconstruction from indirect measurements and so it is exact within a certain accuracy. As an example, if a inverse light-curve method is used, the accuracy if function of the sampled the light-curve points [30]. The more densely sampled the light-curve points are, the more detailed information is obtained i. e., the most accurate the model is.

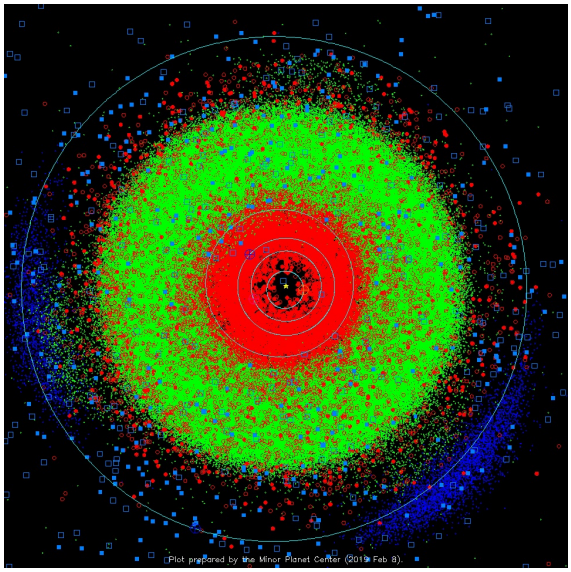

Figure 1: Inner solar system minor bodies. Credits [28].
In green, Main Belt objects; in red, near-Earth objects; in blue, Trojans.

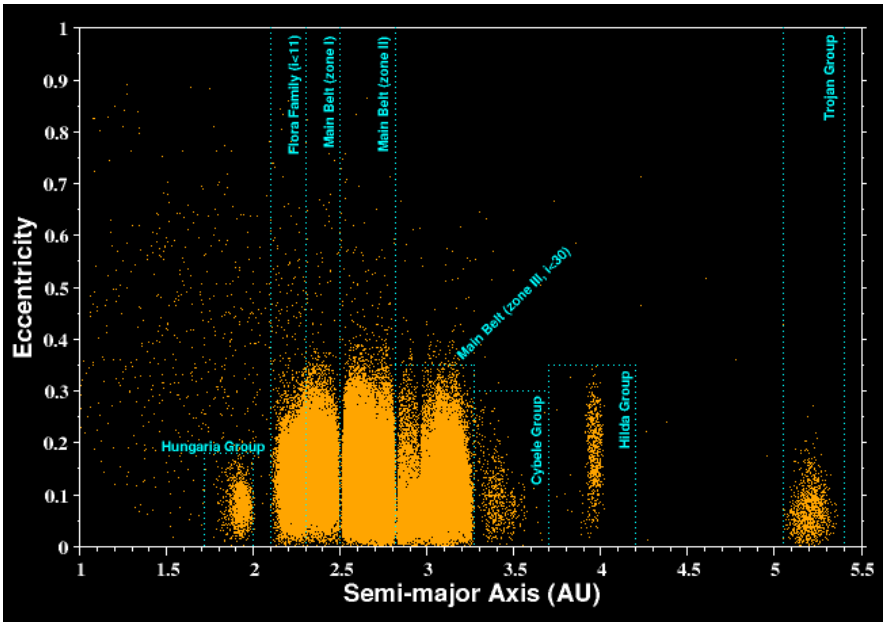

Figure 2: Main belt bodies distribution in function of the semimajor axis and the eccentricity. Credits Alan, Chamberlin (2007, JPL/Caltech).

0.1 Classification

Asteroids lie within three regions of the solar system. Most asteroids lie in the *main belt*, that is estimate to contain more than 200 asteroids larger than 100 km, between 1.1 million and 1.9 million asteroids larger than 1 km in diameter and millions of smaller ones. Many asteroids lie also outside the main belt. Trojan asteroids orbit a larger planet in two special places, known as Lagrange points, where the gravitational pull of the sun and the planet are balanced. Jupiter Trojans are the most numerous, boasting nearly as high a population as the main asteroid belt. Neptune, Mars and Earth also have Trojan asteroids.

NEA circle closer to Earth than the Sun. According to European Space Agency (ESA), roughly 10'000 of known asteroids are in this class. *Amor* asteroids have close orbits that approach but no not cross Earth's path, according to NASA. *Apollo* asteroids have Earth-crossing orbits but spend most of their time outside the planet's path. *Aten* asteroids also cross Earth's orbit but spend most of their time inside Earth's orbit. *Atira* asteroids are near-Earth asteroids whose orbits are contained within Earth's orbit.

In addition to classifications of asteroids based on their orbits, most asteroids fall into three classes based on composition:

- The **C-type or carbonaceous asteroids** are grayish in color and are the most common, including more than 75 percent of known asteroids. They probably consist of clay and stony silicate rocks, and inhabit the main belt's outer regions.
- The **S-type or silicaceous asteroids** are greenish to reddish in color, account for about 17 percent of known asteroids, and dominate the inner asteroid belt. They appear to be made of silicate materials and nickel-iron.
- The **M-type or metallic asteroids** are reddish in color, make up most of the rest of the asteroids, and dwell in the middle region of the main belt. They seem to be made up of nickle-iron.

0.2 Shape Models

In this study, we consider a set of asteroids with different dynamical environments as well as fairly different inertial and physical properties. We assume, to test the learning algorithm, that the shape is known *a-priori* from previous studies, but with the aim to eliminate the "dependence" of the method on the body, thus to generalize also to cases in which the body properties are *not known a-priori*.

In general, the shape model of a celestial body represents its topographical characteristics by means of certain model parameters. Usually the raw data coming from an Astronomical Observatory or from a Deep Space Probe must be elaborated, reduced and transformed in a topographic map, representing the surface of the body, for the successive analyses. This map is then transformed in a *vertex model*, consisting on a finite set of point describing the geometry of the body and in particular, its surface.

In general, the coordinates of these points are expressed in Cartesian or in a Spherical reference system centred in the centre of mass of the body.

Then, in order to convert all these single points in a topological entity, a connectivity list between the numbered vertices must be provided to univocally define the shape of the body. The connectivity list is simply a list of the *vertices* that must be connected together in a certain order to obtain the elemental constituent of the whole shape model. The connectivity list can be computed performing a *Delaunay triangulation* [31] in a 3D Euclidean space, or can be obtained through a longitudinal and latitudinal connection pattern of the vertices.

In the following sections there are presented a series of shape models that consists in a vertex list, expressed in the 3D Cartesian reference with the origin in the centre of mass of the body and the axis aligned with the principal inertia axes of the uniform body. These axis are oriented in such a way that the $\hat{\mathbf{z}}$ axis is the one of the maximum inertia axis, while the $\hat{\mathbf{x}}$ is along the minimum inertia axis and $\hat{\mathbf{y}}$ completes the right-hand reference frame.

0.3 Physical Properties

The characterization of the asteroid starts from its physical properties, such as mass, density, volume. Since the shape models are assumed to be known and of polyhedrical type, the volume (V) of the body is known or can be computed in a simple way. Then, since the mass (M) is assumed to be known or estimated in some way, the average density of the model (ϱ) can be computed by the simple relation $\varrho = M/V$. Note that this is the *average* density, not the true density distribution of the body. Moreover, it is no worth to be said that since the body is composed by polyhedrons, its inertial properties depends on the discretization. Indeed the computation of the inertial properties refers to the method presented in [32].

0.3.1 Shape descriptors

Since the majority of asteroids is non-spherical, and may have irregular, randomly shaped geometries, they can be classified with descriptors comprising the characterization of the global shape compared with a sphere. The descriptors used in this study are:

- *Sphericity descriptor*, ref. Wadell (1932):

$$\Psi_{\mathrm{S}} = \frac{A_{\mathrm{true}}}{A_{\mathrm{cs}}} = \left(\frac{V_{\mathrm{true}}}{V_{\mathrm{cs}}}\right)^{\frac{1}{3}}$$

  where here V_{true} (A_{true}) is the volume (area) of the body while V_{cs} (A_{cs}) is the volume (area) of the smallest circumscribing sphere. Sphericity values range from 0 (non-spherical) to 1 (perfect sphere).

- *Roundness descriptor*, ref. Wadell (1932):

$$\Psi_{\mathrm{R}} = \frac{R_{\mathrm{min}}}{R_{\mathrm{max}}} \tag{1}$$

which is the ration of the radius of curvature of the largest inscribed circle (so in this case, the minimum radius) and the radius of the smallest circumscribing sphere. On the base of Ψ_{R} it is possible to classify the objects according with 1.

Table 1: *Power's scale of roundness.*

Class	Very Angular	Angular	Sub-Angular	Sub-Rounded	Rounder	Well Rounded
Ψ_{R}	0.12 - 0.17	0.17 - 0.25	0.25 - 0.35	0.35 - 0.49	0.49 - 0.70	0.70 - 1.00

The defining S as the smallest dimension, I as the mean dimension and L as the longest dimensions of the body, three other ratios can be defined:

- *Aspect ratio*: $\Psi_{\mathrm{AR}} = S/L$
- *Elongation*: $\Psi_{\mathrm{E}} = I/L$
- *Flatness*: $\Psi_{\mathrm{F}} = I/S$

By the use of those 5 descriptors, in the next section the physical characterization of some shape models, with different level of accuracy, is performed.

0.3.2 Bulk properties

Density is perhaps the most fundamental property for dis- criminating the composition and internal structure of asteroids. It is also extremely difficult to measure, and the number of precisely measured asteroid densities is still very limited. This is because both mass and volume are required to determine the density of an asteroid. However, a density estimate by itself can restrict the list of possible components of an asteroid's composition. The internal structure can be constrained using a comparison of the asteroid bulk density (ϱ) with the grain density of its most likely constituents (ϱ_C) [33].

- If $\varrho \ll \varrho_C$ the asteroid is *underdense*. This is the case of asteroids that have porous internal structure i. e., a fraction of volume is occupied by empty space $p = 1 - \varrho/\varrho_C$.
- If $\varrho \gg \varrho_C$ the asteroid is *overdense*, and some highdensity material must be present in its interior. This could be due to gravitational self-compression or the result of the collision between two bodies of different densities. Most asteroids with a mass above 10^{19} kg are overdense, while the majority of asteroids below that threshold present some level of porosity.
- If $\varrho \sim \varrho_C$ no clear conclusions can be made. However, given the comparable spectral properties observed among members of dynamical families, it may be reasonable to assume that the body is homogeneous.

This last case is the one taken into account in that work, however more complex bulk density distributions can be used to refine the analysis in the underdense and overdense case.

0.3.3 The rubble-pile hypothesis

Originally, scientists predicted small asteroids to be hard and rocky, as any loose surface material (regolith) generated by impacts was expected to escape their weak gravity. Aggregate small bodies were not thought to exist, because the slightest sustained relative motion would cause them to separate. But observations and computer modeling are proving otherwise, in fact most asteroids larger than a kilometer are now believed to be composites of smaller pieces.

The rubble hypothesis, proposed decades ago by scientists, lacked evidence, until the planetologist Shoemaker realized that a huge craters on the asteroid Mathilde and its very low density could only make sense together: a porous body such as a rubble pile can withstand a battering much better than an integral object. It will absorb and dissipate a large fraction of the energy of an impact; the far side might hardly feel a thing. At first, the rubble hypothesis may appear conceptually troublesome. The material strength of an asteroid is nearly zero, and the gravity is so low one is tempted to neglect that too. The truth is neither strength nor gravity can be ignored: gravity binds a rubble pile together.

The size of an asteroid should determine which force dominates. One indication is the observed pattern of asteroidal rotation rates. Some collisions cause an asteroid to spin faster; others slow it down. If asteroids are monolithic rocks undergoing random collisions, a graph of their rotation rates should show a bell-shaped distribution with a statistical 'tail' of very fast rotators. If nearly all asteroids are rubble piles, however, this tail would be missing, because any rubble pile spinning faster than once every two or three hours would fly apart.

0.4 Characterization of Selected Objects

0.4.1 Asteroids

A selection of asteroids is presented here. Data credits [34].

101955 Bennu Discovered by the LINEAR Project 11 Sept. 1999, *101955 Bennu* is a carbonaceous asteroid in the Apollo group. It is the target of the OSIRIS-REx mission which is intended to return samples to Earth in 2023 for further study. The shape mode of the body is presented in 3 on the next page at the maximum resolution.

433 Eros Discovered on Aug. 13, 1898 by Gustav Witt, and independently on the same day by Auguste H.P. Charlois. Eros is famous as the first asteroid to be orbited by a spacecraft, and as the first one on which a spacecraft landed. Eros is an S-type asteroid, the most common type in the inner asteroid belt. It's a typical member of the *Amors* group of NEAs, which cross Mars' orbit but do not quite reach that of Earth. The shape mode of the body is presented in 4 on the facing page at the maximum resolution.

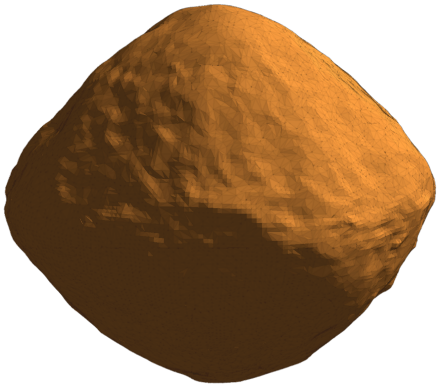

Figure 3: Polyhedron Shape Model for 101955 Bennu. *(2018)*
Credits: *NASA/Goddard/University of Arizona. High-res. model ∼ 50k faces.*
On-line resource: *https://www.asteroidmission.org/*

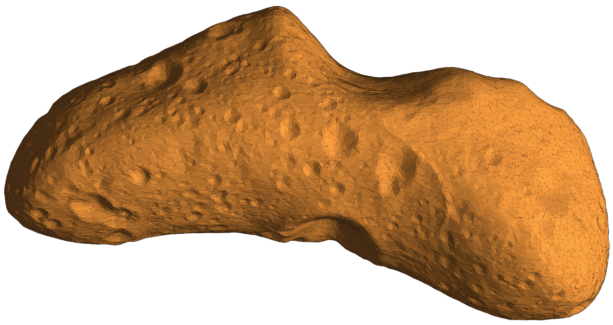

Figure 4: Polyhedron Shape Model for 433 Eros. *(2008)*
Credits: *NASA Planetary Data System. High-res. model ∼ 200k faces.*
On-line resource: *https://space.frieger.com/*

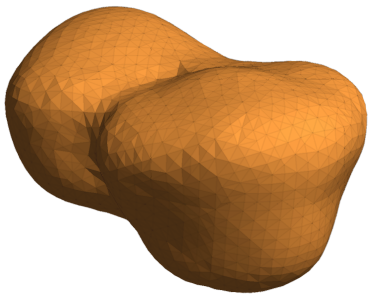

Figure 5: Polyhedron Shape Model for 4769 Castalia.
Credits: *NASA Planetary Data System. Low-res. model ∼ 5k faces.*
On-line resource: *https://sbn.psi.edu/pds/resource/rshape.html*

4769 Castalia Is a near-Earth crossing asteroid that was discovered by Eleanor F. Helin (Caltech) on August 1989. It has a dumbell shape and is about 1.8 kilometers across at its widest. Its two distinct lobes are about 0.75 kilometers across. The two lobes were probably separate objects that came together after a relatively gentle collision. The surface of both lobes have similar composition and roughness. The effective resolution of the reconstruction is about 100 meters. This is the first detailed 3D model of a near Earth asteroid yet produced, and the most conclusive evidence to date of a "contact-binary" object in the solar system. The shape mode of the body is presented in 5.

65803 Didymos Is a sub-kilometer asteroid and synchronous binary system, classified as potentially hazardous asteroid and near-Earth object of both the Apollo and Amor group. It is the target of the proposed *AIDA* asteroid-mission. The asteroid was discovered in 1996, by the Spacewatch survey at Kitt Peak, and its small 170-meter minor-planet moon was discovered in 2003. Due to its binary nature, it was then named "Didymos", the Greek word for twin.

0.4.1.1 Binary system (66391) 1999 KW4

The 1.5-kilometer-diameter primary (Alpha) is an unconsolidated gravitational aggregate with a spin period ∼2.8 hours, bulk density ∼2 grams per cubic centimeter, porosity ∼50%, and an oblate shape dominated by an equatorial ridge at the object's potential-energy minimum. The ∼0.5-kilometer secondary (Beta) is elongated and probably is denser than Alpha. Its average orbit about Alpha is circular with a radius ∼2.5 kilometers and period ∼17.4 hours, and its average rotation is synchronous with the long axis pointed toward Alpha. Exotic physical and dynamical properties may be common among near-Earth binaries [35].

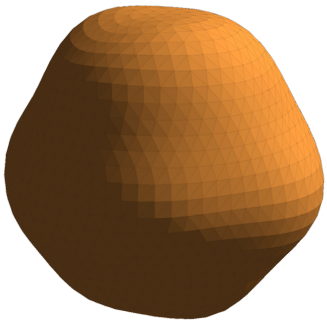

Figure 6: Polyhedron Shape Model for 65803 Didymos A.
Credits: *NASA Planetary Data System. Low-res. model ∼ 5k faces.*
On-line resource: *https://space.frieger.com/*

Table 2: *Asteroids shape model parameters.*

	Rounded		*Irregularly Shaped*	
Asteroid	Bennu	Didymos A	Eros	Castalia
V (m^3)	6.1713e7	1.2488e8	2.5072e12	6.6782e08
ϱ (10^3 kg/m^3)	1.2628	4.1875	2.6672	0.7487
$\bar{g}$ (m/s^2)	8.5521e-5	4.5402e-3	3.6032e-4	1.0123e-4
Ψ_R (-)	0.7577	0.8244	0.1716	0.2963
Ψ_S (-)	0.6254	0.7020	0.1092	0.2331
Ψ_{AR} (-)	0.7577	0.8244	0.1716	0.2963
Ψ_E (-)	0.4263	0.4460	0.2811	0.3258
Ψ_F (-)	0.5625	0.5410	1.6389	1.0995
T_r (h)	4.2880	2.2593	5.2656	4.0950

Table 3: *Binary system KW4 shape model parameters.*

	Alpha	*Beta*
M (10^{12} kg)	2.353	0.135
V (m^3)	1.1953e9	4.8035e7
ϱ (10^3 kg/m^3)	1.9685	2.8105
$\bar{g}$ (m/s^2)	3.6542e-04	1.8409e-04
Ψ_R (-)	0.7144	0.5785
Ψ_S (-)	0.5926	0.4423
Ψ_{AR} (-)	0.7144	0.5785
Ψ_E (-)	0.4182	0.3737
Ψ_F (-)	0.5854	0.6460
R_{max} (km)	0.7838	0.2960
R_{min} (km)	0.5600	0.1712
T_r (h)	2.7645 $\pm$ 0.0003	17.4223

Part II

Modelling Small Bodies Environment

CHAPTER 1

NON-KEPLERIAN DYNAMICAL MODELS FOR SMALL SOLAR SYSTEM BODIES

THIS chapter deals with the fundamental background knowledge needed to model the dynamical environment in the vicinity of small solar system bodies. So the mathematical formulation is presented as well as the properties of each dynamical model are discussed when relevant in the spacecraft trajectory design.

In general, the dynamics of a particle about such kind of bodies is extremely different from the R2BP, where the attractor is reduced to a point mass and an analytical solution exists [5]. In fact, in the case of small solar system bodies, this reduction cannot be performed and the exact shape of the body must be taken into account to recover the orbital path of the particle. Moreover, in order to fully describe the environment in the vicinity of the body is necessary to take into account also the rotational dynamics of the body and therefore the orbital dynamics of the particle will be *non-linearly coupled* with the motion of the body. This characteristic, in fact, leads to trajectories that depends on the body spin rate. Finally, the non-gravitational perturbations such as the SRP and third-body perturbation usually are comparable to the gravitational ones making the design of the trajectory even more difficult. If a binary system of bodies is then considered, the difficulties increase because of the strong coupling between the rotational dynamics of the two bodies and their mutual gravity field.

The description of the dynamical models needed to describe the particle motion starts form the definition of the reference frames in which those models are expressed. In particular, this section is divided in two parts: the first is relative to the reference frame, the notation and the equation of motion needed in the case the trajectory design is associated to a single body, or P2BP, while the second describes the one needed in the case of a the design of a trajectory in the case of a binary system or Modified Circular Restricted Three-Body Problem (MCR3BP). Finally, some hints about the

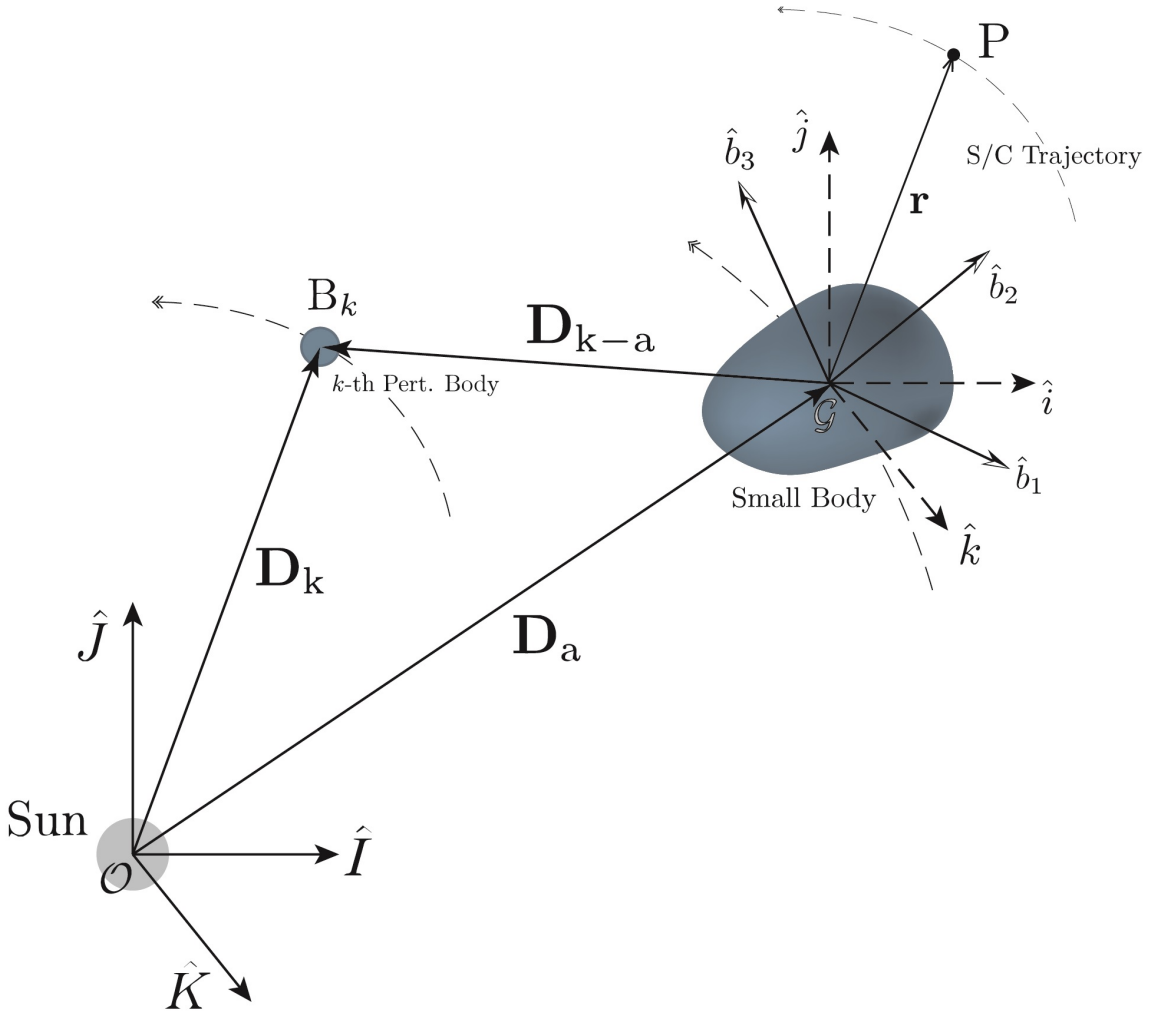

Figure 1.1: Fundamental geometry and reference frames used for the P2BP.

implementation for the numerical integration of the problem are presented, in order to highlight methods used and difficulties encountered.

1.1 The Perturbed Two-Body Problem

The fundamental geometry for this problem is presented in Figure 1.1. Three reference frames are represented there: an inertial frame $\mathcal{T}_o = \mathrm{span}\{\hat{I}, \hat{J}, \hat{K}\}$ centred in $\mathcal{O}$. This frame, in particular, is coincident with the J2000 reference frame. Then two frames centred in $\mathcal{G}$, the centre of mass of the body, are defined. An inertial frame $\mathcal{T}_n = \mathrm{span}\{\hat{i}, \hat{j}, \hat{k}\}$ and a body-fixed one $\mathcal{T}_b = \mathrm{span}\{\hat{b}_1, \hat{b}_2, \hat{b}_3\}$. This last frame is of interest since usually small solar system bodies rotates.

Now, let us call $\mathbf{R}(t)$ the position of the attracted massless particle P in the $\mathcal{T}_n$ frame. It can be expressed in the body-fixed frame $\mathcal{T}_b$ as $\mathbf{r}(t) = \mathbb{R}_n^b(t) \cdot \mathbf{R}(t)$, where $\mathbb{R}_n^b(t)$ indicates the direct cosine matrix from the $_n$ to the ^{b} reference. For this specific problem other quantities of interest are:

- $\mathbf{D}_a(t)$: position of the small body in the $\mathcal{T}_o$ reference;
- $\mathbf{S}(t) = -\mathbf{D}_a(t)$: position of the Sun in the $\mathcal{T}_n$ reference;
- $\mathbf{s}(t) = \mathbb{R}_n^b(t) \cdot \mathbf{S}(t)$: position of the Sun in the $\mathcal{T}_b$ reference;
- $\mathbf{D}_{\mathrm{k}}(t)$: position of the k-th perturbing body in the $\mathcal{T}_o$ reference;
- $\mathbf{D}_{\mathrm{k-a}}(t)$: position of the k-th perturbing body in the $\mathcal{T}_n$ reference.
- $\mathbf{d}_{\mathrm{k-a}}(t) = \mathbb{R}_n^b(t) \cdot \mathbf{D}_{\mathrm{k-a}}(t)$: position of the k-th perturbing body in the $\mathcal{T}_b$ reference.

Where those quantities are useful to compute the non-gravitational perturbations that will be defined in the following part.

Now, the equation of motion for the problem can be written in either the $\mathcal{T}_o$, the $\mathcal{T}_n$ or the $\mathcal{T}_b$ reference frame. In this work the integration of the equation of motion is performed in the $\mathcal{T}_b$ being, in this frame, the gravitational field not-dependant on time but only on the position of the particle. This will be a big advantage, as shown later. Since the position vector in the rotating coordinates can be computed as $\mathbf{r}(t) = \mathbb{R}_n^b(t) \cdot \mathbf{R}(t)$ then, being $\mathbb{R}_b^n(t) = \left(\mathbb{R}_n^b(t)\right)^{-1} = \left(\mathbb{R}_n^b(t)\right)^{\mathrm{T}}$:

$$\mathbf{R}(t) = \mathbb{R}_b^n(t) \cdot \mathbf{r}(t) \tag{1.1}$$

Then the velocity and the acceleration vectors reads:

$$\dot{\mathbf{R}} = \dot{\mathbb{R}}_b^n \cdot \mathbf{r} + \mathbb{R}_b^n \cdot \dot{\mathbf{r}} \tag{1.2}$$

$$\ddot{\mathbf{R}} = \ddot{\mathbb{R}}_b^n \cdot \mathbf{r} + 2\dot{\mathbb{R}}_b^n \cdot \dot{\mathbf{r}} + \mathbb{R}_b^n \cdot \ddot{\mathbf{r}} \tag{1.3}$$

Here the time dependence is omitted for clarity. Calling $\mathbf{a}_{\mathrm{T}}(t)$ the sum of the accelerations acting on the particle in the $\mathcal{T}_b$ reference then $\mathbf{A}_{\mathrm{T}}(t) = \mathbb{R}_b^n(t) \cdot \mathbf{a}_{\mathrm{T}}(t)$, so:

$$\ddot{\mathbb{R}}_b^n \cdot \mathbf{r} + 2\dot{\mathbb{R}}_b^n \cdot \dot{\mathbf{r}} + \mathbb{R}_b^n \cdot \ddot{\mathbf{r}} = \mathbb{R}_b^n \cdot \mathbf{a}_{\mathrm{T}} \tag{1.4}$$

At this point, right-multiplying each term Eq. (1.4) for $\mathbb{R}_n^b$ and recalling that $\mathbb{R}_n^b \cdot \mathbb{R}_b^n = \mathbb{I}_{3\mathrm{x}3}$, the following expression is obtained:

$$\ddot{\mathbf{r}} + \mathbb{R}_n^b \ddot{\mathbb{R}}_b^n \cdot \mathbf{r} + 2\mathbb{R}_n^b \dot{\mathbb{R}}_b^n \cdot \dot{\mathbf{r}} = \mathbf{a}_{\mathrm{T}} \tag{1.5}$$

1.1.1 Rotational kinematics

Eq. (1.5) can be written with explicit dependence with respect to a general angular velocity vector $\boldsymbol{\omega}$ of the $\mathcal{T}_b$ with respect to $\mathcal{T}_n$. In particular, the time dependence of the rotation matrix can be related to the angular velocity. According to [36], [37]:

$$\dot{\mathbb{R}}_n^b = -[\boldsymbol{\omega}] \cdot \mathbb{R}_n^b \tag{1.6}$$

Where here $[\boldsymbol{\omega}]$ is the skew symmetric cross product matrix, defined as:

$$[\boldsymbol{\omega}] = \begin{bmatrix} 0 & -\omega_z & \omega_y \\ \omega_z & 0 & -\omega_x \\ -\omega_y & \omega_x & 0 \end{bmatrix} \tag{1.7}$$

Then once $\boldsymbol{\omega}(t)$ is known then Eq. (1.6) can be integrated in order to compute $\dot{\mathbb{R}}_n^b(t)$ at the next time instant. But, taking into account the numerical errors, $\dot{\mathbb{R}}_n^b(t)$ is not guaranteed to stay orthogonal, then, it is necessary to implement a numerical orthogonalization procedure that, at each time step, enforces the orthogonality.

1.1.2 Translational dynamics

The equation of motion for the particle can be derived from Newton's second law of motion. So can be written as in Eq. (1.5). Then by using the rotational kinematics equation, the equation of motion can be written:

$$\ddot{\mathbf{r}} + \underbrace{2\boldsymbol{\omega} \times \dot{\mathbf{r}}}_{Coriolis} + \underbrace{\boldsymbol{\omega} \times (\boldsymbol{\omega} \times \mathbf{r})}_{Centrifugal} + \dot{\boldsymbol{\omega}} \times \mathbf{r} = \mathbf{a}_{\mathrm{T}} \tag{1.8}$$

Where here the right hand side of the equation can be expressed as:

$$\mathbf{a}_{\mathrm{T}}(\mathbf{r}, \mathbf{s}, \mathbf{d}_{\mathrm{k-a}}) = \mathbf{a}_{\mathrm{G}}(\mathbf{r}) + \mathbf{a}_{\mathrm{SRP}}(\mathbf{r}, \mathbf{s}) + \sum_{k=1}^{N} \mathbf{a}_{3\mathrm{rd_k}}(\mathbf{r}, \mathbf{d}_{\mathrm{k-a}}) \tag{1.9}$$

here $\mathbf{a}_{\mathrm{G}}$ is the gravitational acceleration due to the gravity field of the body, $\mathbf{a}_{\mathrm{SRP}}$ the acceleration contribution due to the SRP and $\mathbf{a}_{3\mathrm{rd_k}}$ the acceleration contribution due to the k-th third-body. Note that here the dependence of each contribution is shown.

1.1.3 Rotational dynamics

The quantities in Eq. (1.8) are connected with the rotational dynamics of the main body and are related together by the rigid body motion equation. It is possible to express the Euler's second law in the body fixed frame as:

$$\dot{\mathbf{h}} + \boldsymbol{\omega} \times \mathbf{h} = \mathbf{m} \tag{1.10}$$

where here the angular momentum is expressed as $\mathbf{h} = \mathbb{I} \cdot \boldsymbol{\omega}$, with $\mathbb{I}$ is the inertia tensor of the body. Since the body frame is assumed to be the principal inertia reference, then:

$$\mathbb{I} = \begin{bmatrix} I_x & 0 & 0 \\ 0 & I_y & 0 \\ 0 & 0 & I_z \end{bmatrix} \tag{1.11}$$

Then Eq. (1.10) becomes:

$$\mathbb{I}\dot{\boldsymbol{\omega}} + \boldsymbol{\omega} \times \mathbb{I}\boldsymbol{\omega} = \mathbf{m} \tag{1.12}$$

So, recognizing that $\boldsymbol{\omega} = [\omega_x, \omega_y, \omega_z]$ and $\mathbf{m} = [m_x, m_y, m_z]$ it is possible to obtain the Cartesian scalar form of Eq. (1.12).

1.1.4 Complete fully-coupled model

The complete dynamical and kinematic model for the P2BP is now defined. It is important to note that the equation of motion presented in the previous sections are coupled and so they must be solved together to correctly propagate the dynamics. Hence, the full model is composed by a (3×3) first order matrix differential equation defined in Eq. (1.6), a (3×1) second order differential equation defined in Eq. (1.8) and a (3×1) first order differential equation defined in Eq. (1.12). Moreover, for the numerical integration, Eq. (1.8) must be transformed in a first order equation leading to a (6×1)

differential equation. Then the complete coupled model is composed by 18 different first order scalar differential equations, expressed in the Cartesian body-fixed reference frame. So the state vector of the whole system may be represented as:

$$\mathbf{q} = \{R_{11}, R_{12}, \ldots, R_{33}, \omega_x, \omega_y, \omega_z, x, y, z, \dot{x}, \dot{y}, \dot{z}\}^{\mathrm{T}} \tag{1.13}$$

where $R_{11}, R_{12}, \ldots, R_{33}$ are the 9 components of the direct cosine matrix $\dot{\mathbb{R}}_n^b$. The entire system model can be written as:

$$\dot{\mathbf{q}} = \boldsymbol{f}(\mathbf{q}) \tag{1.14}$$

with known initial conditions $\mathbf{q}_0$, evaluated at $t = 0$.

1.2 The Reduced-Order Perturbed Two-Body Problem

A reduced order model for the P2BP can be recovered in the case the body is considered to rotate at a constant speed about its major inertia axis, that is assumed to be $\mathbf{b}_3$. Then, in this case $\boldsymbol{\omega} = \boldsymbol{\Omega} = \Omega\mathbf{b}_3$ and so $\mathbf{m} = \mathbf{0}$. So there is no need to integrate for the angular velocities as well as for the kinematic since a direct time-dependence can be extracted for $\mathbb{R}_n^b$. Assuming that, at $t = 0$ the two references $\mathcal{T}_n$ and $\mathcal{T}_b$ are coincident, then $\mathbb{R}_n^b(t) = \mathbb{T}_\Omega(t)$ such that:

$$\mathbb{T}_\Omega(t) = \begin{bmatrix} \cos(\Omega t) & \sin(\Omega t) & 0 \\ -\sin(\Omega t) & \cos(\Omega t) & 0 \\ 0 & 0 & 1 \end{bmatrix} \tag{1.15}$$

so the equation of motion presented in Eq. (1.8) can be written as:

$$\ddot{\mathbf{r}} = \Omega^2 \mathbb{I}_{3\times 3}\mathbf{r} - 2\Omega \begin{bmatrix} 0 & -1 & 0 \\ 1 & 0 & 0 \\ 0 & 0 & 0 \end{bmatrix} \dot{\mathbf{r}} + \mathbf{a}_{\mathrm{T}} \tag{1.16}$$

That is, in scalar Cartesian form:

$$\begin{cases} \ddot{x} - 2\Omega\dot{y} = \Omega^2 x + a_{\mathrm{T_x}} \\ \ddot{y} + 2\Omega\dot{x} = \Omega^2 y + a_{\mathrm{T_y}} \\ \ddot{z} = a_{\mathrm{T_z}} \end{cases} \tag{1.17}$$

Note that Eq. (1.17) is the *only* one that has to be integrated in the case in which the ROP2BP model is considered. This is an important simplification that lower the variables of the problem from 18 to 6.

1.3 The Modified Circular Restricted Three-Body Problem

The fundamental geometry for the problem is defined on the basis of the one presented in the P2BP. The major change is in the vicinity of the body, where another synodic reference is defined as $\mathcal{T}_s = \mathrm{span}\{\hat{x}_s, \hat{y}_s, \hat{z}_s\}$, centred in the COM of the binary system

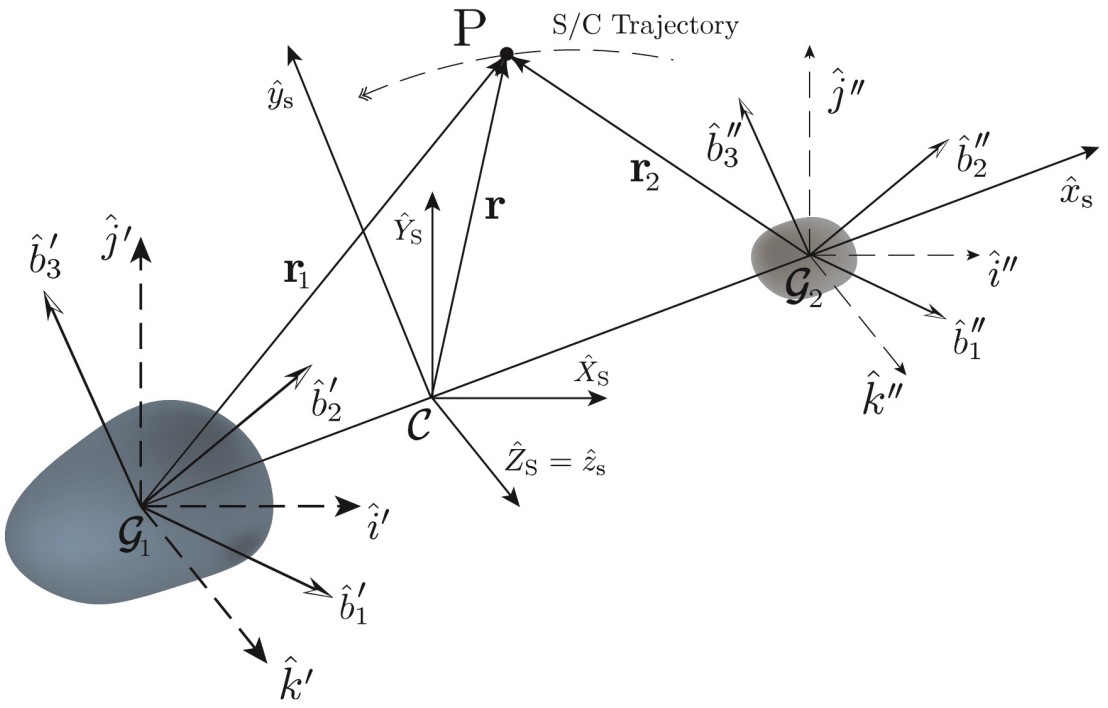

Figure 1.2: Fundamental geometry and reference frames used for the MCR3BP.

and rotating with a constant angular velocity Ω_S as well an inertial reference centred in the COM $\mathcal{C}$ is defined as $\mathcal{T}_S = \text{span}\{\hat{X}_S, \hat{Y}_S, \hat{Z}_S\}$. Here the angular velocity is associated to the two-body motion of the primaries and can be computed as:

$$\Omega_S = \sqrt{\frac{G(m_1 + m_2)}{d_{12}^3}} \tag{1.18}$$

where m_1 and m_2 are the primary and the secondary mass, with centre of mass $\mathcal{G}_1$ and $\mathcal{G}_2$ respectively. Recall that here, being a restricted problem, the mass of the flying spacecraft is neglected. Moreover, the distance d_{12} is intended to be the distance between the centre of mass of the two bodies.

In this study, the synodic angular velocity Ω_S is considered to be constant. In particular $\mathbf{\Omega}_S = \Omega_S \hat{Z}_S$ so that the orbit of the two bodies are circular about $\mathcal{C}$. This is a strong assumptions since, in the most general case, those orbits are not circular and are also time-dependant, due to the mutual attraction of the two bodies. In fact, the MCR3BP can be seen as a simplification of the Full Two-Body Problem (F2BP) and of the Full Restricted Three-Body Problem (FR3BP), as shown in [38] since those kind of models goes beyond the purpose of this thesis. So, in this sense, the mutual interaction is considered only in terms of the rotational dynamics of the bodies about their principal axis.

Now let us briefly describe the other frames used in this part. First of all each of the two bodies have its own $\mathcal{T}_n$ and $\mathcal{T}_b$. In particular the principal has quantities denotes with $'$ while the secondary quantities denotes with $''$. In order to clarify at the most the notation, let us briefly discuss some transformations: first of all, call $\mathbf{R}_1$ the position of the particle with respect to the primary in the $\mathcal{T}_S$ frame. Defining the transformation

matrix form the $\mathcal{T}_S$ to the $\mathcal{T}_s$ frame $\mathbb{T}_{\Omega_S}(t)$ then, under the previous assumptions:

$$\mathbb{T}_{\Omega_S}(t) = \begin{bmatrix} \cos(\Omega_S t) & \sin(\Omega_S t) & 0 \\ -\sin(\Omega_S t) & \cos(\Omega_S t) & 0 \\ 0 & 0 & 1 \end{bmatrix} \tag{1.19}$$

Then assume that the $\mathcal{T}_S$ and the $\mathcal{T}_n$ references of the two bodies are parallel so that no rotation is needed to pass from a reference to another. Now consider the position vector $\mathbf{r}_1'$ as the vector $\mathbf{r}_1$ expressed in the $\mathbf{T}_b'$ reference. If Ω_1 is the uniform angular velocity of the primary about its $\mathbf{b}_3'$ axis, then:

$$\mathbf{R}_1 = \mathbb{T}_{\Omega_1}^T(t)\mathbf{r}_1' \tag{1.20}$$

The same procedure can be applied to any vector referred to the primary or, equivalently, to the secondary. It is of particular interest to express the position $\mathbf{r}_1'$ in the $\mathcal{T}_b'$ (or $\mathbf{r}_2''$ in the $\mathcal{T}_b''$) as a function of the position $\mathbf{r}$ in the $\mathcal{T}_s$ frame since the gravitational field in the $\mathcal{T}_b'$ frame is time-independent. To do so, calling $\mathbf{L}_1$ the distance of the primary to the centre of mass of the system in the $\mathcal{T}_S$:

$$\begin{aligned} \mathbf{R}_1 + \mathbf{L}_1 &= \mathbf{R} \\ \mathbb{T}_{\Omega_S}\left(\mathbf{R}_1 + \mathbf{L}_1\right) &= \mathbf{r} \\ \mathbb{T}_{\Omega_S}\left(\mathbb{T}_{\Omega_1}^T\mathbf{r}_1' + \mathbf{L}_1\right) &= \mathbf{r} \end{aligned}$$

So that:

$$\mathbf{r}_1' = \mathbb{T}_{\Omega_1}\left(\mathbb{T}_{\Omega_S}^T\mathbf{r} - \mathbf{L}_1\right) = \mathbb{T}_{\Omega_1}\mathbb{T}_{\Omega_S}^T\left(\mathbf{r} - \mathbf{l}_1\right) = \mathbb{T}_{\Omega_1}\mathbb{T}_{\Omega_S}^T\mathbf{r}_1 \tag{1.21}$$

Then the equation of motion can be written in the inertial, $\mathcal{T}_S$ frame as:

$$\ddot{\mathbf{R}} = \ddot{\mathbb{T}}_{\Omega_S}^T\mathbf{r} + 2\dot{\mathbb{T}}_{\Omega_S}^T\dot{\mathbf{r}} + \mathbb{T}_{\Omega_S}^T\ddot{\mathbf{r}} \tag{1.22}$$

At this point, right-multiplying each term of the previous equation by $\mathbb{T}_{\Omega_S}$, and recalling that $\mathbb{T}_{\Omega_S}\mathbb{T}_{\Omega_S}^T = \mathbb{I}_{3\times3}$ the following expression is obtained:

$$\ddot{\mathbf{r}} = \Omega_S^2\mathbb{I}_{3\times3}\mathbf{r} - 2[\Omega_S]\dot{\mathbf{r}} + \mathbb{T}_{\Omega_S}\ddot{\mathbf{R}} \qquad \text{with} \quad [\Omega_S] = \Omega_S \begin{bmatrix} 0 & -1 & 0 \\ 1 & 0 & 0 \\ 0 & 0 & 0 \end{bmatrix} \tag{1.23}$$

Where here:

$$\ddot{\mathbf{R}} = \nabla\mathcal{U}_1(\mathbf{R}_1) + \nabla\mathcal{U}_2(\mathbf{R}_2) \tag{1.24}$$

1.3.1 Equation of motion for the Classical CR3BP

The classical CR3BP formulation considers point-mass gravitational potential, so that the potential functions in Eq. (1.24) may be written as:

$$\begin{aligned} \mathcal{U}_1(\mathbf{R}_1) &= \frac{Gm_1}{R_1} = \frac{Gm_1}{||\mathbf{R} - \mathbf{L}_1||} \\ \mathcal{U}_2(\mathbf{R}_2) &= \frac{Gm_2}{R_2} = \frac{\mu}{1-\mu}\frac{Gm_1}{||\mathbf{R} - \mathbf{L}_2||} \end{aligned}$$

Note that since rotation matrix preserves the length of the rotated vector, then $||\mathbf{R}|| = ||\mathbf{r}||$. Then Eq. (1.24), being $\nabla\mathcal{U}_k(\mathbf{R}_k)) = \mathbb{T}^T_{\Omega_S}\nabla\mathcal{U}_k(\mathbf{r}_k))$, becomes:

$$\ddot{\mathbf{r}} = \Omega_S^2\mathbb{I}_{3\times3}\mathbf{r} - 2[\Omega_S]\dot{\mathbf{r}} + \nabla\mathcal{U}_1(\mathbf{r}_1) + \nabla\mathcal{U}_2(\mathbf{r}_2) \tag{1.25}$$

When the components of position vectors of the three bodies are written as:

$$\mathbf{l}_1 = \begin{Bmatrix} -x_{P1} \\ 0 \\ 0 \end{Bmatrix} \qquad \mathbf{l}_2 = \begin{Bmatrix} x_{P2} \\ 0 \\ 0 \end{Bmatrix} \qquad \mathbf{r} = \begin{Bmatrix} x \\ y \\ z \end{Bmatrix} \tag{1.26}$$

If the mass ratio between the primaries is defined as:

$$\mu = \frac{m_2}{m_1 + m_2} \tag{1.27}$$

Then:

$$\mathbf{r}_1 = \mathbf{r} - \mathbf{l}_1 = \begin{Bmatrix} x + \mu d_{12} \\ y \\ z \end{Bmatrix} \qquad \mathbf{r}_2 = \mathbf{r} - \mathbf{l}_2 = \begin{Bmatrix} x - (1-\mu) d_{12} \\ y \\ z \end{Bmatrix}$$

So that the equations of motion for the CR3BP model results:

$$\begin{cases} \ddot{x} &= \Omega_S^2 x + 2\Omega_S\dot{y} - Gm_1\left\{\dfrac{1}{r_1^3}(x+\mu d_{12}) + \dfrac{\mu}{1-\mu}\dfrac{1}{r_2^3}[x-(1-\mu)d_{12}]\right\} \\ \ddot{y} &= \Omega_S^2 y - 2\Omega_S\dot{x} - Gm_1\left(\dfrac{1}{r_1^3} + \dfrac{\mu}{1-\mu}\dfrac{1}{r_2^3}\right)y \\ \ddot{z} &= -Gm_1\left(\dfrac{1}{r_1^3} + \dfrac{\mu}{1-\mu}\dfrac{1}{r_2^3}\right)z \end{cases} \tag{1.28}$$

1.3.1.1 Pseudopotential function and Jacobi integral

From the CR3BP associated theory, it is possible to extract the concept of *pseudopotential* function $\mathcal{V}$ that is defined as [39]:

$$\mathcal{V}(x,y,z) = \frac{1}{2}\boldsymbol{\Omega}_S \times (\boldsymbol{\Omega}_S \times \mathbf{r}) + \mathcal{U}(x,y,z) \tag{1.29}$$

According to [39], moreover, it can be shown that the CR3BP has a useful integral of motion. In particular, the following relation holds:

$$\frac{d}{dt}\left[\frac{1}{2}\dot{\mathbf{r}}\cdot\dot{\mathbf{r}}\right] = \frac{d\mathcal{V}}{dt} \tag{1.30}$$

Then, integrating, the integral of motion is found:

$$\frac{1}{2}\dot{\mathbf{r}}\cdot\dot{\mathbf{r}} = \mathcal{V}(x,y,z) - \frac{\mathcal{C}}{2} \tag{1.31}$$

where here $\mathcal{C}$ is the integration constant. This quantity is associated to the energy of the particle through the relation $\mathcal{C} = -2\mathcal{E}$ and is called *Jacobi constant*. Note that, due to the opposite sign, if the energy increases, Jacobi constant decreases and viceversa.

1.3.1.2 Equilibrium points location and stability

One of the known properties of the CR3BP is the fact that it posses equilibrium points. It is, in fact, well known that there are five equilibrium solutions: three on the x axis, called *collinear points* and two forming equilateral triangles with the two primaries, called *triangular or equilateral points*. Their location can be easily found [39] by equating $\nabla\mathcal{V} = 0$.

From a stability analysis, moreover it results that (see [39]) collinear points are saddle points (unstable), while triangular points are stable if $\mu < 0.03852$.

1.3.2 Equation of motion for the MCR3BP

In this case, since each of the two bodies is considered to have a certain shape, different from the spherical one, it would be beneficial (for numerical reasons but not only) to evaluate the accelerations in Eq. (1.24) in the body frame of the bodies and the to transform them in the synodic reference. To do so, consider the case in which the primary rotates uniformly about it's $\mathbf{b}'_3$ axis. Then Eq. (1.20) holds. Thus:

$$\nabla\mathcal{U}_1(\mathbf{R}_1) = \nabla\mathcal{U}_1(\mathbb{T}^T_{\Omega_1}\mathbf{r}'_1) = \mathbb{T}^T_{\Omega_1}\nabla\mathcal{U}_1(\mathbf{r}'_1) \tag{1.32}$$

So, Eq. (1.22) becomes:

$$\ddot{\mathbf{r}} = \Omega_S^2\mathbb{I}_{3\times3}\mathbf{r} - 2[\Omega_S]\dot{\mathbf{r}} + \mathbb{T}_{\Omega_S}\mathbb{T}^T_{\Omega_1}\nabla\mathcal{U}_1(\mathbf{r}'_1) + \mathbb{T}_{\Omega_S}\mathbb{T}^T_{\Omega_2}\nabla\mathcal{U}_2(\mathbf{r}''_2) \tag{1.33}$$

Where here:

$$\mathbf{r}'_1 = \mathbb{T}_{\Omega_1}\mathbb{T}^T_{\Omega_S}(\mathbf{r} - \mathbf{l}_1) = \mathbb{T}_{\Omega_1}\mathbb{T}^T_{\Omega_S}\mathbf{r}_1 \tag{1.34}$$

$$\mathbf{r}''_2 = \mathbb{T}_{\Omega_2}\mathbb{T}^T_{\Omega_S}(\mathbf{r} - \mathbf{l}_2) = \mathbb{T}_{\Omega_2}\mathbb{T}^T_{\Omega_S}\mathbf{r}_2 \tag{1.35}$$

Note, finally, that having defined $\Delta\Omega_k = \Omega_S - \Omega_k$:

$$\begin{aligned}\mathbb{T}_{\Omega_S}\mathbb{T}^T_{\Omega_k} &= \begin{bmatrix}\cos(\Omega_S t) & \sin(\Omega_S t) & 0\\ -\sin(\Omega_S t) & \cos(\Omega_S t) & 0\\ 0 & 0 & 1\end{bmatrix}\begin{bmatrix}\cos(\Omega_k t) & -\sin(\Omega_k t) & 0\\ \sin(\Omega_k t) & \cos(\Omega_k t) & 0\\ 0 & 0 & 1\end{bmatrix}\\ &= \dots\\ &= \begin{bmatrix}\cos(\Delta\Omega_k t) & \sin(\Delta\Omega_k t) & 0\\ -\sin(\Delta\Omega_k t) & \cos(\Delta\Omega_k t) & 0\\ 0 & 0 & 1\end{bmatrix}\end{aligned}$$

If $\Omega_S = \Omega_k$ so that both the synodic frame $\mathcal{T}_s$ and the k-th body rotates at the same angular velocity, then $\mathbb{T}_{\Omega_S}\mathbb{T}^T_{\Omega_k} = \mathbb{I}_{3\times3}$.

1.4 Periodic Orbits in the Restricted Three-Body Problem

The numerical methods employed to generate a periodic or quasi-periodic orbit are based on the capability to predict motions nearby a reference solution. Such understanding is essential to estimate a series of incremental adjustments to the reference, that may converge on the desired translational history [40].

1.4.1 Linear variational equations

Consider a generic system of nonlinear ordinary differential equations, written in vector form:

$$\dot{\mathbf{X}} = \mathbf{f}(\mathbf{X},t) \tag{1.36}$$

and a reference solution $\mathbf{X}^*(t)$. The first order, time-free variation to this reference at time $t + \delta t$ is given by [41],[42]:

$$\delta\mathbf{X}(t+\delta t) = \delta\tilde{\mathbf{X}}(t) + \dot{\mathbf{X}}^*(t)\delta t \tag{1.37}$$

Here, the fixed-time variation is obtained by mapping the initial perturbation forward using the State Transition Matrix (STM) $\mathbf{\Phi}(t, t_0)$:

$$\delta\tilde{\mathbf{X}}(t) = \mathbf{\Phi}(t, t_0)\delta\tilde{\mathbf{X}}(t_0) \tag{1.38}$$

This result can be obtained substituting $\mathbf{X} = \mathbf{X}^* + \delta\tilde{\mathbf{X}}$ into Eq. (1.36) and expanding the right-hand side in a Taylor series, centred in $\mathbf{X}^*$:

$$\mathbf{f}(\mathbf{X}^* + \delta\mathbf{X}) = \mathbf{f}(\mathbf{X}^*) + \left.\frac{\partial\mathbf{f}}{\partial\mathbf{X}}\right|^* \delta\tilde{\mathbf{X}} \tag{1.39}$$

So it results that:

$$\delta\dot{\tilde{\mathbf{X}}} = \left.\frac{\partial\mathbf{f}}{\partial\mathbf{X}}\right|^* \delta\tilde{\mathbf{X}} \tag{1.40}$$

This equation has Eq. (1.38) as solution, then for the STM it results:

$$\begin{aligned}\dot{\mathbf{\Phi}}(t, t_0) &= \mathcal{J}\mathbf{f}^* \cdot \mathbf{\Phi}(t, t_0)\\ \mathbf{\Phi}(t_0, t_0) &= \mathbb{I}_{6\times6}\end{aligned}$$

where here $\mathcal{J}\mathbf{f}^*$ is the Jacobian matrix, defined as:

$$\mathcal{J}\mathbf{f}^* = \left.\frac{\partial\mathbf{f}}{\partial\mathbf{X}}\right|^* \tag{1.41}$$

So Eq. (1.37) may be written as:

$$\delta\mathbf{X}(t+\delta t) = \mathbf{\Phi}(t, t_0)\delta\tilde{\mathbf{X}}(t_0) + \dot{\mathbf{X}}^*(t)\delta t \tag{1.42}$$

In the case of the CR3BP, in the non-dimensional form (look at [42] for the details), the Jacobian results in:

$$\mathcal{J}\mathbf{f}(t) = \begin{bmatrix}\mathbb{O}_{3\times3} & \mathbb{I}_{3\times3}\\ \mathcal{V}_{\mathbf{xx}} & 2[\mathbf{\Omega}]\end{bmatrix} \tag{1.43}$$

where here:

$$\begin{aligned}\mathbb{O}_{3\times3} &= \text{zero matrix}\\ \mathbb{I}_{3\times3} &= \text{identity matrix}\\ \mathcal{V}_{\mathbf{xx}} &= \text{matrix of second order derivatives of } \mathcal{V}\\ -[\mathbf{\Omega}] &= \text{skew-symmetric angular velocity matrix}\end{aligned}$$

1.4.2 Trajectory design strategies

There are several different ways of generating periodic or quasi-periodic orbits in the CR3BP. In this section a brief hint on the method used in this study is presented. For a more detailed analysis, look at [43], [41]. Note that everything will be discussed in that part could be extended to the case of the MCR3BP.

In general, to built up a family of periodic orbits, three main elements are needed:

1. an initial condition should be available as initial guess;
2. a corrector;
3. a continuation method.

Assuming that the initial condition is computed in some way (depending on the orbital family), the corrector method can be either a single shooting or a multiple shooting method. Assume, in general, a vector of n design variables $\bar{\mathbf{X}}$. To ensure that the trajectory is quasi periodic, the free variables are subjected to m constraint, represented by the constraints vector $\mathbf{F}(\bar{\mathbf{X}})$. The objective of the method is a solution vector that satisfy the constraints vector within some acceptable accuracy. Note that an initial guess in needed. So, considering an initial free variable vector $\bar{\mathbf{X}}^0$, $\mathbf{F}(\bar{\mathbf{X}})$ can be expanded, using Taylor series, as:

$$\mathbf{F}(\bar{\mathbf{X}}) \approx \mathbf{F}(\bar{\mathbf{X}}^0) + \mathcal{D}\mathbf{F}(\bar{\mathbf{X}}^0)(\bar{\mathbf{X}} - \bar{\mathbf{X}}^0) \tag{1.44}$$

Therefore, according to [41], a *single shooting method* may be written as:

$$\bar{\mathbf{X}}^{j+1} = \bar{\mathbf{X}}^j - \mathcal{D}\mathbf{F}(\bar{\mathbf{X}}^j)\left[\mathcal{D}\mathbf{F}(\bar{\mathbf{X}}^j)\mathcal{D}\mathbf{F}(\bar{\mathbf{X}}^j)^{-1}\right]\mathbf{F}(\bar{\mathbf{X}}^j) \tag{1.45}$$

1.4.2.1 Design of DROs

In this part the design of DROs is addressed. To do so, for symmetry considerations, in the CR3BP, the initial state of a DRO can be written as:

$$\mathbf{X}_0 = \begin{Bmatrix} x_0 & 0 & 0 & 0 & \dot{y}_0 & 0 \end{Bmatrix}^T \tag{1.46}$$

and so does the state after half period of the orbit. It T is the orbital period then $T_h = T/2$. In this particular case, then:

$$\delta\mathbf{X}_h = \mathbf{\Phi}(T_h, t_0)\delta\mathbf{X}_0 + \dot{\mathbf{X}}_h\delta T_h \tag{1.47}$$

Therefore, a choice for the design variables vector, as well as the constraints vector and its derivative can be:

$$\bar{\mathbf{X}} = \begin{Bmatrix} \dot{y}_0 \\ T_h \end{Bmatrix} \quad , \quad \mathbf{F}(\bar{\mathbf{X}}) = \begin{Bmatrix} y_h \\ \dot{x}_h \end{Bmatrix} \quad , \quad \mathcal{D}\mathbf{F}(\bar{\mathbf{X}}) = \begin{bmatrix} \Phi_{25} & \dot{y}_h \\ \Phi_{45} & \ddot{x}_h \end{bmatrix} \tag{1.48}$$

1.5 Force Models

In this section the acceleration model needed for the integration of the equation of motion presented before is built. In fact when dealing with the orbital motion of a particle in the small body environment the dominant force is usually from the small body gravitational field but significant perturbations arise from other gravitational and non-gravitational sources. The prime source of these perturbations are the Sun, both gravitational and non-gravitational. Additional sources of perturbation include planetary gravitational perturbations, which could become significant when the small body has a close passage by a planet.

1.5.1 Third-Body Gravitational Perturbations

Solar and planetary gravitational perturbations are simple to specify if one assumes the small body lies in a two-body orbit relative to the Sun or to the planet. The *absolute* gravitational attraction that a particle would experience is simply given by [44]:

$$\mathbf{A}_{3\mathrm{rd},k}^{\mathrm{abs}} = -\frac{GM_k}{||\mathbf{R} - \mathbf{D}_{\mathrm{k-a}}||}(\mathbf{R} - \mathbf{D}_{\mathrm{k-a}}) \tag{1.49}$$

Where M_k is the mass of the k-th perturbing body, while $\mathbf{R}$ and $\mathbf{D}_{\mathrm{k-a}}$ are defined in the previous sections but here it is recalled that $\mathbf{R}$ is the vector from the small body centre of mass to the particle while $\mathbf{D}_{\mathrm{k-a}}$ is the position vector from the small body centre of mass to the perturbing body in the $\mathcal{T}_n$ frame. The absolute acceleration, however, is not the relevant one to be considered. In fact, in this case the *relative* acceleration is needed, that is:

$$\mathbf{A}_{3\mathrm{rd},k} = -GM_k \left[\frac{\mathbf{R} - \mathbf{D}_{\mathrm{k-a}}}{||\mathbf{R} - \mathbf{D}_{\mathrm{k-a}}||^3} + \frac{\mathbf{D}_{\mathrm{k-a}}}{||\mathbf{D}_{\mathrm{k-a}}||^3}\right] \tag{1.50}$$

Then in the $\mathcal{T}_b$ reference:

$$\mathbf{a}_{3\mathrm{rd},k} = -GM_k \left[\frac{\mathbf{r} - \mathbf{d}_{\mathrm{k-a}}}{||\mathbf{r} - \mathbf{d}_{\mathrm{k-a}}||^3} + \frac{\mathbf{d}_{\mathrm{k-a}}}{d_{\mathrm{k-a}}^3}\right] \tag{1.51}$$

for the k-th perturbing body. For the Sun case, instead:

$$\mathbf{a}_{\odot} = -GM_{\odot} \left[\frac{\mathbf{r} - \mathbf{s}}{||\mathbf{r} - \mathbf{s}||} + \frac{\mathbf{s}}{s}\right] \tag{1.52}$$

For the use in perturbation analysis, however it is convenient to reason in terms of perturbing acceleration potential. In the case of third-body perturbation, the potential may be expressed as:

$$\mathcal{R}_{3\mathrm{rd}} = \sum_k GM_k \left[\frac{1}{||\mathbf{r} - \mathbf{d}_{\mathrm{k-a}}||} - \frac{\mathbf{r} \cdot \mathbf{d}_{\mathrm{k-a}}}{d_{\mathrm{k-a}}^3}\right] \tag{1.53}$$

where

$$\mathbf{a}_{3\mathrm{rd},k} = \frac{\partial \mathcal{R}_{3\mathrm{rd}}}{\partial \mathbf{r}} \tag{1.54}$$

Of particular note is the fact that $d_{k-a} \gg r$. If we define as θ_k the angle between $\mathbf{r}$ and $\mathbf{d}_{\mathrm{k-a}}$, then:

$$\frac{\mathbf{r}\cdot\mathbf{d}_{\mathrm{k-a}}}{d_{\mathrm{k-a}}^3} = \frac{1}{d_{\mathrm{k-a}}}\left(\frac{r}{d_{\mathrm{k-a}}}\right)\cos\theta_k \tag{1.55}$$

Moreover it is possible to expand in terms of Legendre polynomials of argument θ_k the first term of Eq. (1.53) as:

$$\frac{1}{||\mathbf{r}-\mathbf{d}_{\mathrm{k-a}}||} = \frac{1}{d_{\mathrm{k-a}}}\frac{1}{\sqrt{1+\left(\frac{r}{d_{\mathrm{k-a}}}\right)^2 - 2\left(\frac{r}{d_{\mathrm{k-a}}}\right)\cos\theta_k}} = \frac{1}{d_{\mathrm{k-a}}}\sum_{n=0}^{\infty}\left(\frac{r}{d_{\mathrm{k-a}}}\right)^n \mathcal{P}_n(\cos\theta_k) \tag{1.56}$$

Then note that:

- If $n = 0$ then the expansion gives $\frac{1}{d_{\mathrm{k-a}}}$ that is negligible being $d_{\mathrm{k-a}} \gg r$ and being not dependant on r;
- If $n = 1$ then the term of the expansion and Eq. (1.55) cancels;
- Only the terms $n \geq 2$ remains.

Then the perturbing acceleration results to be:

$$\mathcal{R}_{3\mathrm{rd}} = \sum_k \frac{GM_k}{d_{\mathrm{k-a}}}\sum_{n=2}^{\infty}\left(\frac{r}{d_{\mathrm{k-a}}}\right)^n \mathcal{P}_n\left(\frac{\mathbf{r}\cdot\mathbf{d}_{\mathrm{k-a}}}{r d_{\mathrm{k-a}}}\right) \tag{1.57}$$

Now recalling that $\mathcal{P}_2(x) = \frac{3}{2}x^2 - \frac{1}{2}$ and that $\mathcal{P}_3(x) = \frac{5}{2}x^3 - \frac{3}{2}x$ then it results that the first terms of the expansion are:

$$\mathcal{R}^{(2)}_{3\mathrm{rd},k} = \frac{1}{2}\frac{GM_k}{d_{\mathrm{k-a}}^3}\left[3\left(\mathbf{r}\cdot\hat{d}_{\mathrm{k-a}}\right)^2 - r^2\right] \tag{1.58}$$

$$\mathcal{R}^{(3)}_{3\mathrm{rd},k} = \frac{1}{2}\frac{GM_k}{d_{\mathrm{k-a}}^4}\left[5\left(\mathbf{r}\cdot\hat{d}_{\mathrm{k-a}}\right)^3 - 3r^2\left(\mathbf{r}\cdot\hat{d}_{\mathrm{k-a}}\right)\right] \tag{1.59}$$

Then the the perturbation acceleration results [5], [44]:

$$\mathbf{a}_{3\mathrm{rd},k} = -\frac{GM_k}{d_{\mathrm{k-a}}^3}\left[\underbrace{\mathbf{r} - 3\frac{\mathbf{r}\cdot\mathbf{d}_{\mathrm{k-a}}}{d_{\mathrm{k-a}}^2}\mathbf{d}_{\mathrm{k-a}}}_{Second\ order\ term} - \underbrace{\frac{15}{2}\left(\frac{\mathbf{r}\cdot\mathbf{d}_{\mathrm{k-a}}}{d_{\mathrm{k-a}}^2}\right)^2\mathbf{d}_{\mathrm{k-a}}}_{Third\ order\ term} + \ldots\right] \tag{1.60}$$

The case in which the expansion in Eq. (1.60) is stopped at the second order term is of particular interest since it coincides with the so called Hill problem.

1.5.2 Solar Radiation Pressure Perturbation

Associated also with the Sun are non-gravitational perturbations due to momentum transfer from solar photons striking and recoiling off the orbiting body. The simplest model for computing solar radiation accelerations is to assume that the spacecraft presents a constant area perpendicular to the sun-line, and that the total momentum

transfer is modelled as *insolation* plus *reflection*. Then the net acceleration have the general form [44]:

$$\mathbf{a}_{\mathrm{SRP}} = -\frac{(1+\rho)P_0 A_{\mathrm{sc}}}{m_{\mathrm{sc}}} \frac{\mathbf{s}-\mathbf{r}}{||\mathbf{s}-\mathbf{r}||^3} \tag{1.61}$$

here ρ is the total reflectance or albedo of the body in question. An important parameter is the mass to area ratio, denoted as $B_{\mathrm{sc}} = m_{\mathrm{sc}}/A_{\mathrm{sc}}$, since it controls the relative strength of this perturbation. Typically the range of values for this parameter is between 20 and 40 kg/m^2. This simple form of the SRP can be written as a potential in the form:

$$\mathcal{R}_{\mathrm{SRP}} = -\frac{(1+\rho)P_0}{B_{\mathrm{sc}}} \frac{1}{||\mathbf{s}-\mathbf{r}||} \tag{1.62}$$

If the spacecraft is close to the body, than this potential can be expanded. If the first term of this expansion is kept then:

$$\mathcal{R}_{\mathrm{SRP}} = -\frac{(1+\rho)P_0}{B_{\mathrm{sc}}} \frac{\mathbf{r}\cdot\mathbf{s}}{s^3} \tag{1.63}$$

So the resulting acceleration can be found to be:

$$\mathbf{a}_{\mathrm{SRP}} = \frac{\partial \mathcal{R}_{\mathrm{SRP}}}{\partial \mathbf{r}} = -\frac{(1+\rho)P_0}{B_{\mathrm{sc}} s^3}\mathbf{s} \tag{1.64}$$

1.5.3 Force Model Implemented

In this section, for clarity, the complete acceleration model used for the dynamics presented in the previous sections is presented. So for Eq. (1.9) the acceleration model is, in the $\mathcal{T}_b$ frame:

$$\begin{aligned}\mathbf{a}_{\mathrm{T}}(\mathbf{r},\mathbf{s},\mathbf{d}_{\mathrm{k-a}}) = {} & \overbrace{\mathbf{a}_G(\mathbf{r})}^{Main\ gravity} - \overbrace{\frac{(1+\rho)P_0}{B_{\mathrm{sc}}s^3}\mathbf{s}}^{SRP} - \overbrace{\frac{GM_\odot}{s^3}\left[\mathbf{r} - 3\frac{\mathbf{r}\cdot\mathbf{s}}{s^2}\mathbf{s}\right]}^{Sun} + \dots \\ & \cdots - \underbrace{\sum_k \frac{GM_k}{d_{\mathrm{k-a}}^3}\left[\mathbf{r} - 3\frac{\mathbf{r}\cdot\mathbf{d}_{\mathrm{k-a}}}{d_{\mathrm{k-a}}^2}\mathbf{d}_{\mathrm{k-a}} - \frac{15}{2}\left(\frac{\mathbf{r}\cdot\mathbf{d}_{\mathrm{k-a}}}{d_{\mathrm{k-a}}^2}\right)^2 \mathbf{d}_{\mathrm{k-a}}\right]}_{Other\ bodies}\end{aligned} \tag{1.65}$$

where here the accelerations associated with the main gravity of the body can be computed according to the gravitational models presented in the next chapter.

1.5.4 Ephemeris Models and Perturbations Analysis

For the computation of third-body and SRP perturbations an ephemeris model is needed for the asteroid, for the Sun as well as for the other bodies whose contribution is intended to be included. For this purpose, in this work a simple orbital propagator based on the R2BP is implemented. The initial conditions are taken for all the bodies from the NASA's HORIZONS System [45] at 2019/07/25 at the noon.

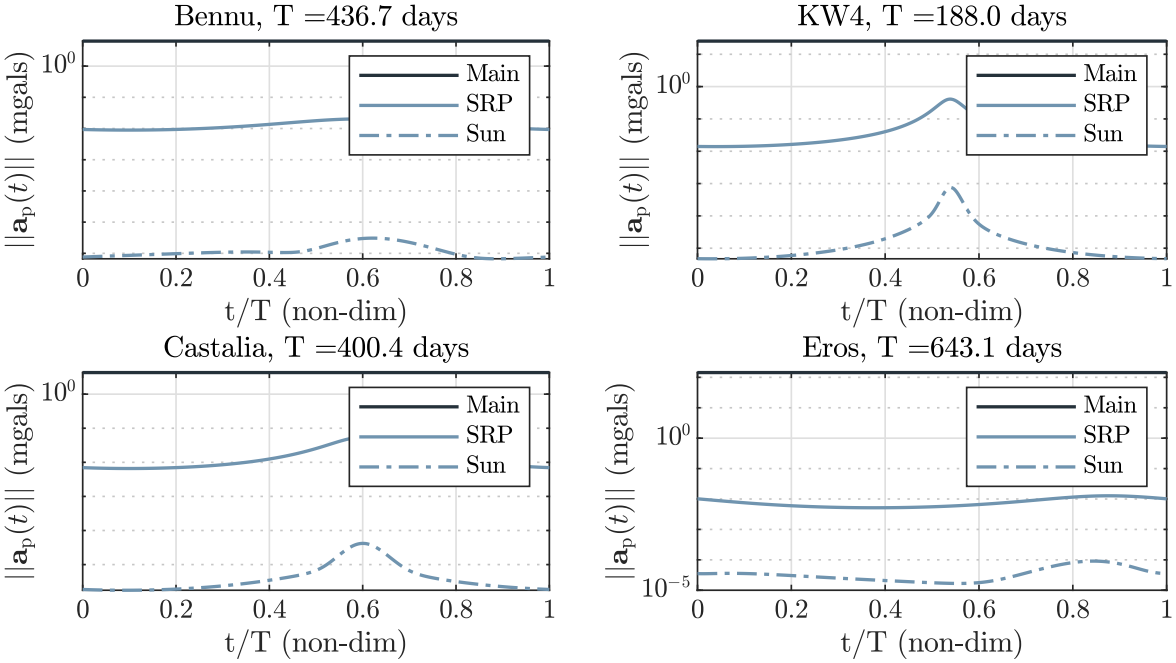

Figure 1.3: SRP and 3rd-body Sun perturbations magnitudes for some selected bodies. Here the quantities are computed at a reference distance of $R_{\max}$ to the body, and assuming $\rho = 0.1$ and $B_{sc} = 30$ kg/m^2 for the SRP model.

In Figure 1.3 are shown the results for the computation of the SRP and Sun 3rd-body perturbations for some selected bodies, over a period of revolution of the selected body about the Sun. The results are shown in Figure 1.3 while in Figure 1.4 and Figure 1.5 a parametric analysis of the SRP perturbation is performed in function of B_{sc} and ρ. As expected, the lower the mass-to-area ratio is the higher is the perturbation magnitude as well as the higher the reflectance ρ is the higher the perturbation magnitude results. Finally, can be computed that other perturbations such as the one of planets is negligible since of the order of 10^{-15} mgals.

1.5.4.1 Binary Asteroid 66391 (1999 KW4)

The case of the binary system 66391 has some particular features that must be analysed separately, for what regards the perturbations to the main gravity field of KW4-α. In fact this case can be treated with either the P2BP or the MCR3BP. The aim of this section is to analyse the KW4-β 3rd-body perturbation to the motion of a particle in the vicinity of the binary system as well as to understand when each dynamical model is the more appropriate. According to the model presented in Eq. (1.60), the

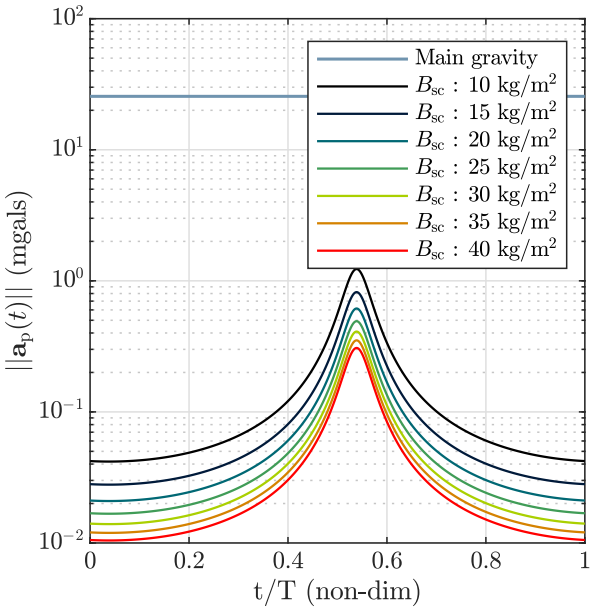

Figure 1.4: SRP perturbation magnitude for KW4 with $\rho = 0.1$ and varying B_{sc}.

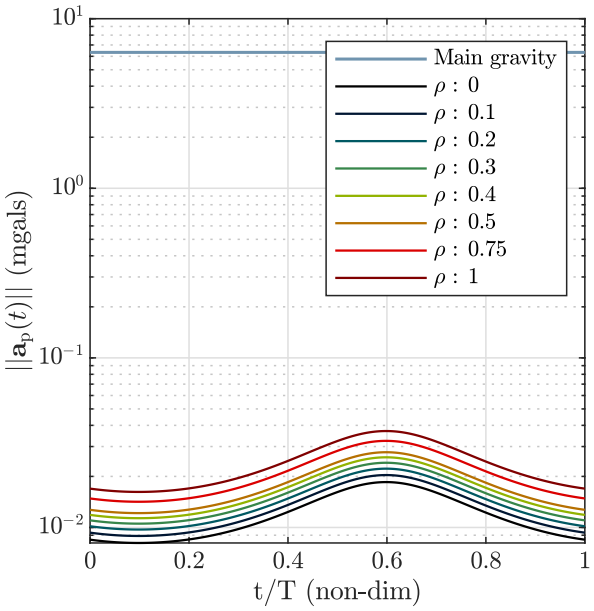

Figure 1.5: SRP perturbation magnitude for Bennu varying ρ.

gravitational perturbation of β can be expanded as:

$$\mathbf{a}_\beta = \mu_\beta \left[\frac{\mathbf{R} - \mathbf{r}}{||\mathbf{R} - \mathbf{r}||^3} - \frac{\mathbf{R}}{R^3} \right] \tag{1.66}$$

where here $\mathbf{R}$ is the relative position of β which respect to α, obtained considering the system $\alpha - \beta$ as a R2BP while $\mathbf{r}$ is the particle position which respect to α. Note that in this case those vectors are expressed in the $\mathcal{T}_n$ reference frame since the magnitude of the acceleration is of interest as well as the two bodies are *point masses* for this analysis. Here ephemeris of β are obtained with the numerical integration of the associated R2BP, using as initial conditions the one presented in Table 1.1.

Table 1.1: *Keplerian parameters of KW4-β in the $\mathcal{T}_n$ reference. Credits [46].*

a (m)	e (-)	i (deg)	Ω (deg)	ω (deg)
2548 ± 15	0.0004 ± 0.0019	156.1 ± 2	105.4 ± 3	319.7 ± 182

In order to understand which dynamical model is the more appropriate between the the P2BP and the MCR3BP it is needed to define a *boundary* in which the P2BP is a good model. In order to do so, as extensively discussed in [43], the concept of Sphere of Influence (SOI) is not significant. Instead the concept of Surface of Equivalence (SOE) is of interest. In this case, the SOE is defined as the surface where the 3rd-body gravitational perturbation of β becomes of the same order of magnitude of the main gravity of α. This surface can be found as the solution of $\mathcal{F}(\mathbf{r}, \mathbf{R}) = 0$, where here, having defined the two-body acceleration as:

$$\mathbf{a}_{2BP} = -\frac{\mu_\alpha}{r^3}\mathbf{r} \tag{1.67}$$

Then:

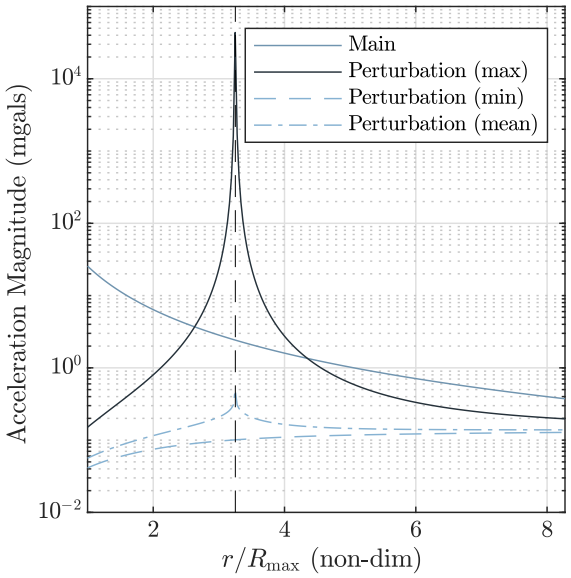

Figure 1.6: Perturbation and main gravity magnitude.

Note that in Figure 1.6 there are three curves associated to the perturbation: the dash light one is the one related to $\min_{\lambda,\theta}\{||\mathbf{a}_\beta(r,\lambda,\theta)||\}$ while the dash dot one is related to $\text{mean}_{\lambda,\theta}\{||\mathbf{a}_\beta(r,\lambda,\theta)||\}$. The min and the mean curves indicates that it is possible to select certain points in the configuration space in which the perturbation would remain a perturbation $\forall r$.

$$\mathcal{F}(\mathbf{r},\mathbf{R}) = ||\mathbf{a}_{2\text{BP}}|| - ||\mathbf{a}_\beta|| = \left|\left|-\frac{\mu_\alpha}{r^3}\mathbf{r}\right|\right| - \left|\left|\mu_\beta\left[\frac{\mathbf{r}_{\text{rel}}}{||\mathbf{r}_{\text{rel}}||^3} - \frac{\mathbf{R}}{R^3}\right]\right|\right| \tag{1.68}$$

Having defined $\mathbf{r}_{\text{rel}} = \mathbf{R} - \mathbf{r}$. Now, defining the non-dimensional parameter γ as:

$$\gamma = \frac{m_\beta}{m_\alpha} = \frac{\mu_\beta}{\mu_\alpha} \tag{1.69}$$

Eq. (1.68) may be expressed in non-dimensional form using the fact that $\bar{r} = r/R$ and $\bar{r}_{\text{rel}} = r_{\text{rel}}/R$:

$$\mathcal{F}^*(\bar{\mathbf{r}},\hat{R}) = \mathcal{F}(\mathbf{r},\mathbf{R})\frac{R^2}{\mu_\alpha} = \underbrace{\left|\left|-\frac{\bar{\mathbf{r}}}{\bar{r}^3}\right|\right|}_{\mathbf{a}^*_{2\text{BP}}} - \gamma\underbrace{\left|\left|\left[\frac{\bar{\mathbf{r}}_{\text{rel}}}{\bar{r}^3_{\text{rel}}} - \hat{R}\right]\right|\right|}_{\mathbf{a}^*_\beta} \tag{1.70}$$

where here $\hat{R} = \mathbf{R}/R$. Then a more convenient form of the $\mathcal{F}(\mathbf{r},\mathbf{R})$ is:

$$\bar{\mathcal{F}}(\bar{\mathbf{r}},\hat{R}) = \frac{\mathcal{F}^*(\bar{\mathbf{r}},\hat{R})}{||\mathbf{a}^*_{2\text{BP}}||} = 1 - \gamma\frac{||\mathbf{a}^*_\beta||}{||\mathbf{a}^*_{2\text{BP}}||} \tag{1.71}$$

For this particular case, however, the definition of the SOE can be simplified having that the orbit of β has $e \approx 0$. So if a circular orbit is considered as the reference for the computation then the problem of finding the SOE is reduced to $\mathcal{F}(\mathbf{r}) = 0$. A further simplification can be applied if the problem is reformulated as follows: in the general case, $\mathbf{a}_\beta(r,\lambda,\theta)$ while $\mathbf{a}_{2\text{BP}}(\mathbf{r})$. Then the curve $\mathcal{F}_r(r) = \max_{\lambda,\theta}\{||\mathbf{a}_\beta(r,\lambda,\theta)||\}$ is compared to the one associated with the R2BP, that is $||\mathbf{a}_{2\text{BP}}(r)||$. Defining $\mathcal{F}^*_{\bar{r}}(r)$:

$$\mathcal{F}^*_{\bar{r}}(\lambda,\theta) = 1 - \frac{||\mathbf{a}_\beta(\bar{r},\lambda,\theta)||}{||\mathbf{a}_{2\text{BP}}(\bar{\mathbf{r}})||} = 1 - \frac{f_\beta(\lambda,\theta)}{f(r)} \tag{1.72}$$

with $\bar{r} = 2.631R_{\max}$ (that is the first intersection between $f(r)$ and $\mathcal{F}_r(r)$. Results in Figure 1.6. Moreover the concept of SOE can take into account for the error in

orientation of the acceleration vectors. In fact we can define the angular measure of the deviation of the P2BP acceleration with respect to the R2BP one:

$$\psi_{\text{rel}}(\lambda,\theta) = \arccos\left(\frac{\mathbf{a}_{\text{2BP}}(\bar{\mathbf{r}})\cdot(\mathbf{a}_{\text{2BP}}(\bar{\mathbf{r}})+\mathbf{a}_{\beta}(\bar{r},\lambda,\theta))}{||\mathbf{a}_{\text{2BP}}(\bar{\mathbf{r}})||\,||\mathbf{a}_{\text{2BP}}(\bar{\mathbf{r}})+\mathbf{a}_{\beta}(\bar{r},\lambda,\theta)||}\right) \tag{1.73}$$

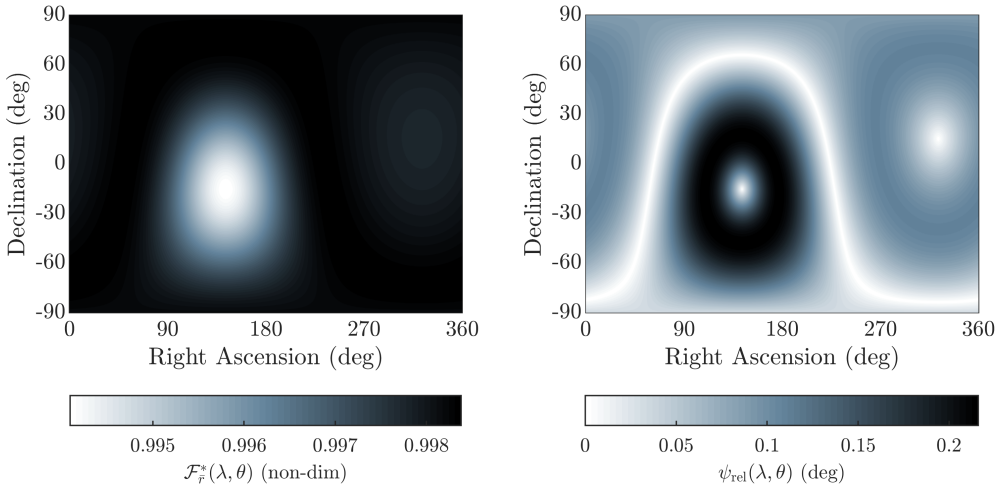

Figure 1.7: Relative magnitude and direction of accelerations in case $\bar{r} = R_{\max}$.

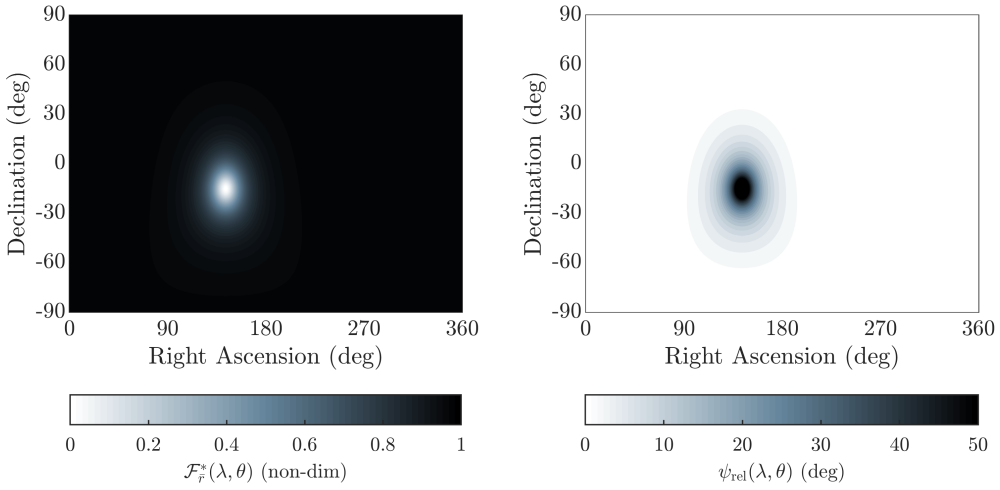

Figure 1.8: Relative magnitude and direction in case $\bar{r} = 2.631R_{\max}$.

Figure 1.7 and Figure 1.8 are the results for $\mathcal{F}^*_{\bar{r}}(\lambda,\theta)$ and $\psi_{\text{rel}}(\lambda,\theta)$ in two different cases. In the first case we are close to the surface of α so that the effect of β is only a perturbation while instead in the second case there is a perfect match between the perturbation and the main gravity at a $RA = 143.1986°$ and $\delta = -15.2925°$ so that the β effect cannot be consider a perturbation anymore. Note also that, also in the second case if a polar orbit with a RA distant from 143.2° is selected, say 300°, then the effect of β can be *still* be considered a perturbation if and only if the orbit is *highly-stable*.

CHAPTER 2

GRAVITY FIELD MODELS

This chapter dealt with the mathematical modelling of the gravity field of solar generical system bodies via different techniques, with different level of accuracy and fidelity. Since the aim of this work is to find a *high-fidelity* analytical or semi-analytical approximation for the gravity field of a irregularly-shaped small body, the theory of spherical harmonics and spherical Bessel functions is recalled.

The importance of this is that high-fidelity models, such as polyhedron or mascons models, are really heavy from the computational point of view, so cannot be used as models on-board of a satellite. On the other hand, a good analytical model is much less expensive from this point of view and can be easily used for real-time, on-board applications despite the fact that, in some cases, the approximation that they give of the gravitational environment can be quite significant.

2.1 The Newtonian Potential Function

The Newtonian potential function of a rigid irregular body is described in this section. In particular, the reference frame $\mathcal{T}_b$ is important from this point of view since the gravity field can be seen as *steady* in this reference. Then, the Newtonian potential function $\mathcal{U}$ is defined as:

$$\mathcal{U}(x,y,z) \triangleq G\int_{\mathcal{V}} \frac{\varrho(\mathbf{r}')}{||\boldsymbol{r}-\boldsymbol{r}'||}dv = G\int_{\mathcal{B}} \frac{1}{\rho}\,dm \tag{2.1}$$

here dm is the mass element defined as $dm = \varrho dv = \varrho\, d\xi\, d\eta\, d\zeta$. Note that the function $\mathcal{U}$ is a function of the coordinates only x, y, z i. e., $\mathcal{U}$ is function of the position of the attracted point P as expressed in the $\mathcal{T}_b$ frame, $r = (x, y, z)$.

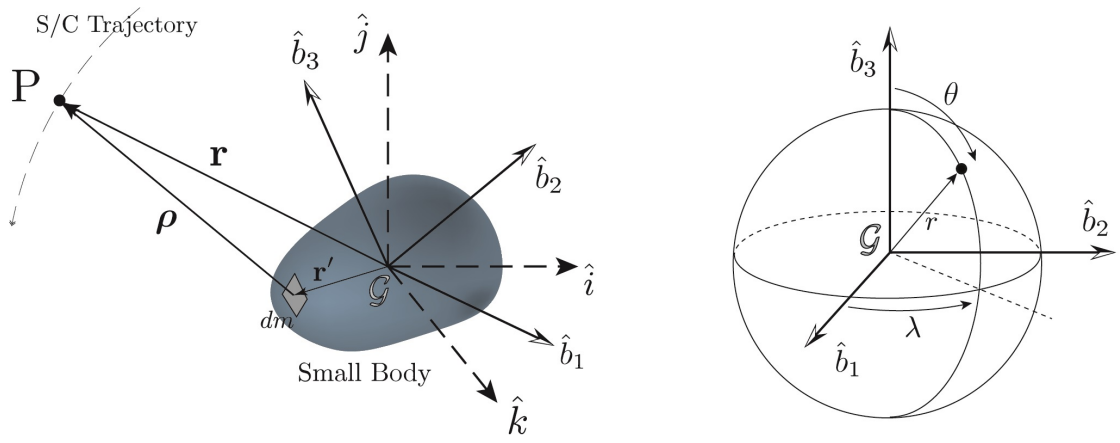

Figure 2.1: Problem geometry.

2.1.1 Laplace's equation

The potential expression Eq. (2.1) satisfies Laplace's equation outside the body, in fact, as reported in **cite**, from Eq. (2.1), we have:

$$\frac{\partial \mathcal{U}}{d\mathbf{r}} = -G \int_{\mathcal{B}} \frac{\boldsymbol{\rho}}{\rho^3}\, dm \tag{2.2}$$

which yields to

$$\frac{\partial^2 \mathcal{U}}{\partial \boldsymbol{r}^2} = -G \int_{\mathcal{B}} \frac{1}{\rho^3} \left[\mathbb{I}_{3\times 3} - 3\frac{\boldsymbol{\rho}\boldsymbol{\rho}}{\rho^2} \right] dm \tag{2.3}$$

where $\mathbb{I}_{3\times 3}$ is a 3×3 identity matrix. Thus, Laplace's equation is given by computing the trace of the second-order partial of potential.

$$\nabla^2 \mathcal{U} = 0 \tag{2.4}$$

which is valid anywhere outside the body.

2.1.2 Poisson's Equation

Theorem 1. *(Gauss's Theorem)* Let $\mathcal{S}_{\mathcal{B}}$ be a closed surface surrounding a region D containing attracting matter with total mass M; if F_n is the normal component of the force at any point of $\mathcal{S}_{\mathcal{B}}$ due to the attraction of the mass within $\mathcal{S}_{\mathcal{B}}$ and also any matter external to $\mathcal{S}_{\mathcal{B}}$. Then we have:

$$\int_{\mathcal{S}} F_n d\mathcal{S}_{\mathcal{B}} = -4\pi G M \tag{2.5}$$

Here:

$$\begin{aligned} F_n = \boldsymbol{F} \cdot \hat{n} = \frac{\partial \mathcal{U}}{\partial \boldsymbol{r}} \cdot \hat{n} &= \left(\frac{\partial \mathcal{U}}{\partial x}\hat{i} + \frac{\partial \mathcal{U}}{\partial y}\hat{j} + \frac{\partial \mathcal{U}}{\partial z}\hat{k} \right) \cdot \left(\frac{\partial x}{\partial n_1}\hat{i} + \frac{\partial y}{\partial n_2}\hat{j} + \frac{\partial z}{\partial n_3}\hat{k} \right) \\ &= \sum_{i=1}^{3} \frac{\partial \mathcal{U}}{\partial n_i} = \frac{\partial \mathcal{U}}{\partial n} \end{aligned}$$

Then:

$$\int_{\mathcal{S}} \frac{\partial \mathcal{U}}{\partial n} d\mathcal{S}_{\mathcal{B}} = -4\pi M = -4\pi G \int_{\mathcal{B}} \varrho d\mathcal{B} \tag{2.6}$$

Where here we re-wrote the total mass in terms of the density distribution ϱ over the volume $\mathcal{B}$.

Theorem 2. *(Green's Theorem)* Let $\mathcal{U}$ be continuous, with first and second derivatives uniform and continuous at all points of a space $\mathcal{B}$ bounded by a surface $\mathcal{S}_{\mathcal{B}}$. Then if ∇^2 is the Laplacian:

$$\int_V = \frac{\partial \mathcal{U}}{\partial n} d\mathcal{S}_{\mathcal{B}} = \int_{\mathcal{B}} \nabla^2 \mathcal{U} d\mathcal{B} = -\int_B 4\pi G \varrho d\mathcal{B} \tag{2.7}$$

Then since it holds at any point within $\mathcal{B}$, Poisson's equation is recovered i. e.,

$$\nabla^2 \mathcal{U} = -4\pi G \varrho \tag{2.8}$$

2.2 Exterior Gravity Field: Spherical Harmonics Expansion

For simple boundaries, Laplace's equation is relatively easy to solve provided there is an appropriate coordinate system. For near-spherical objects, for example, the solutions can be easily found approximating the boundary by a sphere. So, assuming a small body as a nearly-spherical body a natural choice of coordinates are the spherical coordinates, that are illustrated in Figure 2.1:

$$\begin{aligned} x &= r \sin\theta \cos\lambda \\ y &= r \sin\theta \sin\lambda \\ z &= r \cos\theta \end{aligned}$$

With the aim of approximating the *exterior* gravity field of a small body in the exterior space of the Brillouin sphere, Laplace's equation, in spherical coordinates, takes the form, according to [47], of:

$$\nabla^2 \mathcal{U} = \frac{1}{r^2}\frac{\partial}{\partial r}\left(r^2 \frac{\partial \mathcal{U}}{\partial r}\right) + \frac{1}{r^2 \sin\theta}\frac{\partial}{\partial \theta}\left(\sin\theta \frac{\partial \mathcal{U}}{\partial \theta}\right) + \frac{1}{r^2 \sin^2\theta}\frac{\partial^2 \mathcal{U}}{\partial \lambda^2} = 0 \tag{2.9}$$

Where here r is the *radius*, θ the *colatitude* and λ the *longitude* respectively. A solution to $\nabla^2 \mathcal{U} = 0$ can be found, by the method of separation of variables. Then the gravitational potential at an exterior point of the Brillouin sphere can be written as:

$$\mathcal{U} = \frac{GM}{r} \sum_{n=0}^{\infty} \left(\frac{R_0}{r}\right)^n \sum_{m=0}^{n} \Big(C_{nm} R_{n,m}(\theta,\lambda) + S_{nm} S_{n,m}(\theta,\lambda)\Big) \tag{2.10}$$

where R_0 is the radius of the Brillouin sphere, the coefficients $R_{n,m}$ and $S_{n,m}$ are defined as follows:

$$\begin{aligned} R_{n,m}(\theta,\lambda) &= \mathcal{P}_{n,m}(\cos\theta)\cos m\lambda \\ S_{n,m}(\theta,\lambda) &= \mathcal{P}_{n,m}(\cos\theta)\sin m\lambda \end{aligned}$$

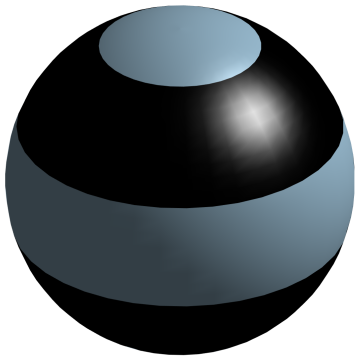

Figure 2.2: An example of *zonal harmonic* (4,0) • Zonal harmonics model the gravitational departure from a perfect sphere from the latitudinal point of view: oblateness of the body is well represented by them.

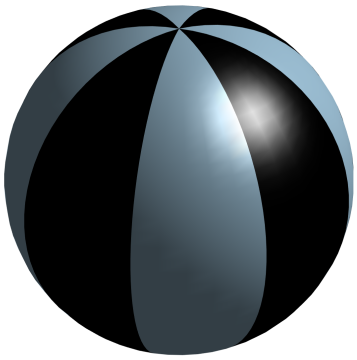

Figure 2.3: An example of *sectorial harmonic* (4,4) • Sectorial harmonic take into account the extra mass distribution in the longitudinal region of the body.

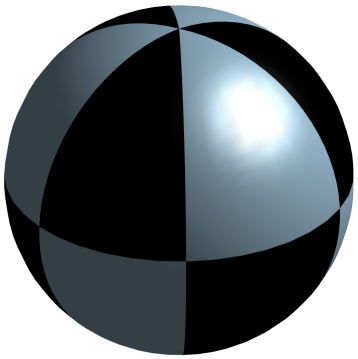

Figure 2.4: An example of *tesseral harmonic* (4,3) • Tesseral harmonics attempt to model specific region of the body which depart from a perfect sphere.

Here, the $\mathcal{P}_{n,m}$ are *associated Legendre polynomial* that can be expressed as, defining $\mu = \cos\theta$:

$$\mathcal{P}_{n,m}(\mu) = \frac{(1-\mu^2)^{m/2}}{2^n\, n!}\frac{d^{n+m}(\mu-1)^n}{d(\mu)^{n+m}} \tag{2.11}$$

Where here $\mu = \cos\theta$. Finally, C_{nm}, S_{nm} can be determined using the *orthogonality* properties of the harmonic functions. In order to prevent numerical problems, the coefficients are normalized according to [48]. So that model results:

$$\mathcal{U} = \frac{GM}{r}\sum_{n=0}^{\infty}\left(\frac{R_0}{r}\right)^n \sum_{m=0}^{n}\left(\bar{C}_{nm}R_n^m(\theta,\lambda) + \bar{S}_{nm}S_n^m(\theta,\lambda)\right) \tag{2.12}$$

with:

$$\begin{aligned} R_n^m &= \mathcal{P}_n^m(\cos\theta)\cos m\lambda \\ S_n^m &= \mathcal{P}_n^m(\cos\theta)\sin m\lambda \\ \mathcal{P}_n^m &= \frac{\mathcal{P}_{n,m}}{\Pi_{nm}}, \quad \bar{C}_{nm} = C_{nm}\cdot\Pi_{nm},\ \bar{S}_{nm} = S_{nm}\cdot\Pi_{nm} \end{aligned}$$

where here the Kaula [48] normalization is being used.

$$\Pi_{nm} = \left(\frac{(n+m)!}{(n-m)!(2-\delta_{m0})(2n+1)}\right)^{1/2}$$

δ_{m0} is the Kronecker delta, i. e., $\delta_{m0} = 1$ for $m = 0$. Then the final form of the gravitational potential is recovered as:

$$\begin{aligned} \mathcal{U} = \frac{GM}{r}\Bigg\{1 + \overbrace{\sum_{n=2}^{N}\left(\frac{R_0}{r}\right)^n \bar{C}_n\,\mathcal{P}_n^0(\cos\theta)}^{\text{zonal}} + \dots \\ \dots + \underbrace{\sum_{n=2}^{N}\sum_{m=1}^{n}\left(\frac{R_0}{r}\right)^n \left(\bar{C}_{nm}\cos(m\lambda) + \bar{S}_{nm}\sin(m\lambda)\right)\mathcal{P}_n^m(\cos\theta)}_{\text{sectorial \& tesseral}}\Bigg\} \end{aligned} \tag{2.13}$$

2.2.1 Stokes coefficients

The expression for the Stokes coefficients in the general case are taken from [44]:

$$(C,S)_{nm} = \frac{2-\delta_{m0}}{M}\frac{(n-m)!}{(n+m)!}\int_{\mathcal{B}}\left(\frac{r}{R_0}\right)^n \mathcal{P}_{n,m}(\theta)\, cs(m\lambda)\varrho dV \tag{2.14}$$

where $\varrho dV = \varrho(r,\theta,\lambda)r^2\sin\theta\, dr\, d\theta\, d\lambda$ and where cs stays for $\cos(m\lambda)$ and $\sin(m\lambda)$.

Axial-symmetric case. Suppose then that $R = R(\theta)$ so there is no dependence on the longitude λ which means that the solid body is axial-symmetric, then:

$$\varrho\int_{\mathcal{B}}(\cdot)\, dV = \frac{\varrho}{R_0^n}\cdot\frac{1}{3+n}\int_0^{2\pi} cs(m\lambda)d\lambda\cdot\int_0^{\pi} R(\theta)^{3+n}\,\mathcal{P}_{n,m}(\theta)\sin\theta\, d\theta$$

Note that the integrals $\int_0^{2\pi} cs(m\lambda)\, d\lambda \neq 0$ if and only if $m = 0$. So in the case the asteroid is built as a solid of revolution about the z axis, the only $(C, S)_{nm}$ components that are non-zero are the ones associated to *zonal harmonics*. This result is physically sensible since in this case, since ϱ is considered to be constant, there cannot be variations in the gravity field that depends on λ i. e., it must be constant with respect to it. Moreover, note that in this particular case, being $\int_0^{2\pi} \sin(m\lambda) = 0$, $S_{n0} = 0$ as expected from the theory and $\int_0^{2\pi} \cos(m\lambda) = 2\pi$. Having that that in mind, equation Eq. (2.14) becomes:

$$C_n = \frac{2\pi\varrho}{M} \frac{1}{(3+n)} \int_0^{\pi} \left(\frac{R(\theta)}{R_0}\right)^n R(\theta)^3\, \mathcal{P}_{nm}(\theta) \sin\theta\, d\theta \tag{2.15}$$

So that the gravity potential can be reduced to:

$$\mathcal{U} = \frac{GM}{r}\left[1 + \sum_{n=2}^{\infty} \left(\frac{R_0}{r}\right)^n C_n \mathcal{P}_n(\cos\theta)\right]$$

Note that the *direct* computation of the Stokes coefficients is possible using Eq. (2.15) if and only if the function $R(\theta)$ is analytical.

Constant-density polyhedron case. The computation of the Stokes coefficients from a constant-density polyhedron starts from Eq. (2.14) then it can be developed is two main ways in according with [49],[32] or [50]. The method used in this work is the one of Werner, presented in [49] and recalled here. Within this method, the author defines a new parameter that corresponds mathematically to the integrand of Eq. (2.14) and physically to the contribution of each polygonal face to the final value of spherical harmonics coefficients:

$$\begin{Bmatrix} c_{nm} \\ s_{nm} \end{Bmatrix} = \frac{2 - \delta_{0,m}}{M} \frac{(n-m)!}{(n+m)!} \left(\frac{r}{R_0}\right)^n P_{n,m}(\cos\theta)) \begin{Bmatrix} \cos m\lambda \\ \sin m\lambda \end{Bmatrix} \tag{2.16}$$

Then using the recurrence relations of ALFs, we have have recurrences in the coefficients c_{nm}, s_{nm}. With increasing n, m the ALFs becomes huge and the Stokes coefficients become small. So, for numerical reasons, fully normalized ALFs are used in this study. This leads to normalized integrands $\bar{c}_{nm}, \bar{s}_{nm}$ with analogous expressions with respect to the one presented before. Now specified the integration over a polyhedrical body surface with constant density and triangular faces. In this case, each face of the polyhedron can be divided from the rest in terms of a tetrahedron whose vertices are at (x_1, y_1, z_1), (x_2, y_2, z_2), (x_3, y_3, z_3) and (0,0,0). The order $1, 2, 3$ is taken in counter clockwise direction. Now we can operate a transformation of coordinates to reach the so called *standard simplex*, that have each vertex located at a unit distance over each axis except the 4^{th} vertex that is at the origin. The change of variables is then:

$$\begin{aligned} x(X, Y, Z) &= x_1 X + y_1 Y + z_1 Z \\ y(X, Y, Z) &= x_2 X + y_2 Y + z_2 Z \\ z(X, Y, Z) &= x_3 X + y_3 Y + z_3 Z \end{aligned}$$

Then, can be shown that, after the change of variables the normalized integrands $\bar{c}_{nm}, \bar{s}_{nm}$ are homogeneous polynomials of degree n in the variables X, Y, Z i. e.,

$$\begin{Bmatrix} \bar{c}_{nm} \\ \bar{s}_{nm} \end{Bmatrix} = \sum_{i+j+k=n} \begin{Bmatrix} \bar{\alpha}_{ijk} \\ \bar{\beta}_{ijk} \end{Bmatrix} X^i Y^j Z^k \tag{2.17}$$

where the summation is taken over all the combinations of non-negative exponents i, j, k which sum to n. The symbols $\bar{\alpha}_{ijk}$ and $\bar{\beta}_{ijk}$ represent the X, Y, Z trinomial coefficients. With the change of variables, the integrands must be multiplied by the determinant of the Jacobian matrix J of the transformation. J is constant with respect to the new integration variables X, Y, Z and can be computed as:

$$J = \frac{\partial(x, y, z)}{\partial(X, Y, Z)} = \begin{bmatrix} x_1 & x_2 & x_3 \\ y_1 & y_2 & y_3 \\ z_1 & z_2 & z_3 \end{bmatrix} \tag{2.18}$$

So the final expressions for the integrated normalized harmonic coefficients are derived as follows:

$$\begin{aligned} \begin{Bmatrix} \bar{C}_{nm} \\ \bar{S}_{nm} \end{Bmatrix} &= \iiint_{\text{extended body}} \begin{Bmatrix} \bar{c}_{nm} \\ \bar{s}_{nm} \end{Bmatrix} dm = \varrho \sum_f \iiint_{\text{tetrahedron}} \begin{Bmatrix} \bar{c}_{nm}(x, y, z) \\ \bar{s}_{nm}(x, y, z) \end{Bmatrix} dx\, dy\, dz \\ &= \varrho \sum_f \iiint_{\text{simplex}} \begin{Bmatrix} \bar{c}_{nm}(X, Y, Z) \\ \bar{s}_{nm}(X, Y, Z) \end{Bmatrix} \det(J)\, dX\, dY\, dZ \\ &= \varrho \sum_f \det(J)_f \iiint_{\text{simplex}} \left(\sum_{i+j+k=n} \begin{Bmatrix} \bar{\alpha}_{ijk} \\ \bar{\beta}_{ijk} \end{Bmatrix} X^i Y^j Z^k \right) dX\, dY\, dZ \\ &= \varrho \sum_f \det(J)_f \sum_{i+j+k=n} \begin{Bmatrix} \bar{\alpha}_{ijk} \\ \bar{\beta}_{ijk} \end{Bmatrix} \iiint_{\text{simplex}} X^i Y^j Z^k\, dX\, dY\, dZ \end{aligned}$$

here the first summation is performed over the faces. Note that the evaluation of the coefficients is reduced to the one of the integral of the trinomial function over the simplex volume. This integral has an elegant solution has it can be found in [32] and reported here.

$$\iiint_{\text{simplex}} X^i Y^j Z^k\, dX\, dY\, dZ = \frac{i!j!k!}{(n+3)!}$$

So the final solution can be expressed as:

$$\begin{Bmatrix} \bar{C}_{nm} \\ \bar{S}_{nm} \end{Bmatrix} = \varrho \sum_f \left(\frac{\det(J)_f}{(n+3)!} \sum_{i+j+k=n} i!j!k! \begin{Bmatrix} \bar{\alpha}_{ijk} \\ \bar{\beta}_{ijk} \end{Bmatrix} \right) \tag{2.19}$$

2.3 The Gravitational Field of a Constant Density Polyhedron

Among the different available techniques, one of the most effective for the computation of the gravitational field of a body is the constant density polyhedron one. In that case, following the procedure presented in [37], [51], the potential of a constant density attractor can be derived as:

$$\mathcal{U} = G\varrho \int_V \frac{1}{r}\, dV \tag{2.20}$$

where V is the overall volume and r the modulus of the vector $\mathbf{r}$ between the field point and the infinitesimal mass element $dm = \varrho dV$. Defining the unit vector

$$\hat{r} = \frac{\mathbf{r}}{r} \tag{2.21}$$

Then, exploiting the Gauss divergence theorem

$$\mathcal{U} = \frac{1}{2} G\varrho \int_V (\nabla \cdot \hat{r})\, dV = \frac{1}{2} G\varrho \int_S (\hat{n} \cdot \hat{r})\, dS \tag{2.22}$$

where $\hat{n}$ is the unit normal to the infinitesimal surface. This can be transformed, for a polyhedron model with a certain number of faces n_f to

$$\mathcal{U} = \frac{1}{2} G\varrho \sum_{\text{faces}} \hat{n}_f \cdot \mathbf{r}_f \int_S \frac{1}{r} dS \tag{2.23}$$

with $\mathbf{r}_f$ the vector from the field point to any point of the plane in which lies the tetrahedron's face. Exploiting properties of the polygons and defining $\hat{n}_e^f$ the unit normal to tetrahedron's edge e lying on the face's f plane and $\mathbf{r}_e^f$ the vector from the field point to a generic point on the edge e extension, then

$$\mathcal{U} = \frac{1}{2} G\varrho \sum_{\text{faces}} \sum_{\text{edges}} \left(\mathbf{r}_f \cdot \hat{n}_f \hat{n}_e^f \cdot \mathbf{r}_e^f L_e^f \right) - \frac{1}{2} G\varrho \sum_{\text{faces}} \left(\mathbf{r}_f \cdot \hat{n}_f \hat{n}_f \cdot \mathbf{r}_f \omega_f \right) \tag{2.24}$$

where here

$$L_e^f = \ln \frac{l_1 + l_2 + e}{l_1 + l_2 - e} \tag{2.25}$$

with l_1 the distance from the field point to the first end of the edge, l_2 the distance from the field point to the second end of the edge and e the length of the edge. Here, also ω_f is intended to the be solid angle subtended by the face S, when viewed from the field point and defined as

$$\omega_f = \int_S \frac{\Delta z}{r^3}\, dS \tag{2.26}$$

Finally defining the following dyads:

$$\mathbb{E} = \hat{n}_{f_1} \hat{n}_e^{f_1} + \hat{n}_{f_2} \hat{n}_e^{f_2} \qquad \text{and} \qquad \mathbb{F}_f = \hat{n}_f \hat{n}_f$$

where f_1 and f_2 referred to two faces having the edge e in common, leads to the final expression of the potential:

$$\mathcal{U} = \frac{1}{2} G\varrho \sum_{\text{edges}} \mathbf{r}_e \cdot \mathbb{E}_e \cdot \mathbf{r}_e L_e - \frac{1}{2} G\varrho \sum_{\text{faces}} \mathbf{r}_f \cdot \mathbb{F}_f \cdot \mathbf{r}_f \omega_f \tag{2.27}$$

From that, the computation of the the field derivatives is straightforward. In fact, for the first derivative:

$$\nabla \mathcal{U} = G\varrho \sum_{\text{faces}} \mathbb{F}_f \cdot \mathbf{r}_f \omega_f - G\varrho \sum_{\text{edges}} \mathbb{E}_e \cdot \mathbf{r}_e L_e \tag{2.28}$$

While for the Laplacian:

$$\nabla^2 \mathcal{U} = -G\varrho \sum_{\text{faces}} \omega_f \tag{2.29}$$

2.4 The Gravitational Field of a Triaxial Ellipsoid

In studying the orbiter dynamics about small bodies it is sometimes convenient to leave the gravitational harmonics formulation aside and concentrate on specific mass distribution which have closed form solution for their gravitational field. For this purpose, the gravitational field associated to a triaxial ellipsoid fits perfectly [52]. In this paragraph the formulation is briefly recalled. If the total size of a body is $a \times b \times c$ where $a \geq b \geq c$, than the associated ellipsoid has major semiaxes $\alpha = a/2, \beta = b/2$ and $\gamma = c/2$. Given a constant density ϱ for the body, its gravitational parameters results in:

$$\mu = \frac{4\pi}{3} G\varrho\alpha\beta\gamma \tag{2.30}$$

Defining x, y, z the body fixed coordinates of the ellipsoid, with x lying along α, y along β and z along γ respectively, then the potential of a point, external to the ellipsoid surface can be expressed [52],[53]:

$$\mathcal{U}_g = \frac{3\mu}{4} \int_{\kappa}^{\infty} \phi(x, y, z; u) \frac{du}{\Delta(u)} \tag{2.31}$$

where here:

$$\phi(x, y, z; u) = \left[\frac{x^2}{\alpha^2 + u} + \frac{y^2}{\beta^2 + u} + \frac{z^2}{\gamma^2 + u} - 1 \right] \tag{2.32}$$

$$\Delta(u) = \sqrt{(\alpha^2 + u)(\beta^2 + u)(\gamma^2 + u)} \tag{2.33}$$

Where here κ is obtained as the solution of:

$$\phi(x, y, z; \kappa(x, y, z)) = 0 \tag{2.34}$$

It is of particular interest for this study the perturbation effect generated from a triaxial ellipsoid related to the oblate spheroid model. This effects is included in the harmonic coefficients C_{20} and C_{40} that for a constant density triaxial ellipsoid may be computed as [52], [44]:

$$C_{20} = -\frac{1}{10\alpha^2}(\alpha^2 + \beta^2 - 2\gamma^2) \tag{2.35}$$

$$C_{22} = \frac{1}{20\alpha^2}(\alpha^2 - \beta^2) \tag{2.36}$$

$$C_{40} = \frac{15}{7}(C_{20}^2 + 2C_{22}^2) \tag{2.37}$$

$$C_{42} = \frac{5}{7} C_{20} C_{22} \tag{2.38}$$

$$C_{44} = \frac{5}{28} C_{22}^2 \tag{2.39}$$

CHAPTER 3

THE GRAVITATIONAL FIELD OF ASTEROIDS

The computation of the gravity field for this kind of small solar system object is usually a quite complicated task due to the unknown or partially-known shape of the body and to the completely unknown internal structure of it. Usually, high fidelity models can be recovered by the use of the constant density polyhedron model. This works also for the case of highly irregular bodies [54] but it is limited by the fact that the density is usually not constant. In fact, specially highly irregular bodies have a quite heterogeneous density distribution, due to their formation and this make extremely challenging the modelling of the gravitational field.

However, since the aim of the work is not to built an high-fidelity model for the gravity field of those kind of bodies then the problem of the computation of the gravitational field associated to the bodies presented in Chapter 0.2 on page 9 reduces to the adoption of one of the models presented in Chapter 2 on page 39.

According to Chapter 2 on page 39, then the gravitational model of a selected object can be obtained with either the use of shape-based methods, such as the constant density polyhedron one or by the use of a spherical harmonics expansion matched with a spherical Bessel functions expansion. The constant density polyhedron model is considered to be the high-fidelity representation of the gravitational field of the selected object in this work but it has to be recalled that it can't be used for on-board applications since it is computationally heavy. So a discussion on the analytically expanded field is needed since it will be the model used on board as well as the model that the learning will refine.

3.1 The Gravity Field of Some Selected Object

The case of *rounded objects* is of particular interest for this study since a large number of minor bodies are rounded as well as some simplifications can be adopted in that case. In terms of shape descriptors, this is the case in which $\Psi_{\mathrm{R}}, \Psi_{\mathrm{S}} \to 1$. In particular, for this study, an object with $\Psi_{\mathrm{R}} > 0.7$ is considered rounded, according to Power's scale of roundness. However, most of asteroid are irregularly shaped so that the analysis of irregular bodies is needed to despite the fact that it is much more difficult due to the complicated shape. Now, in this part some selected object are characterized in terms of their gravity field as well as to the approximations adopted.

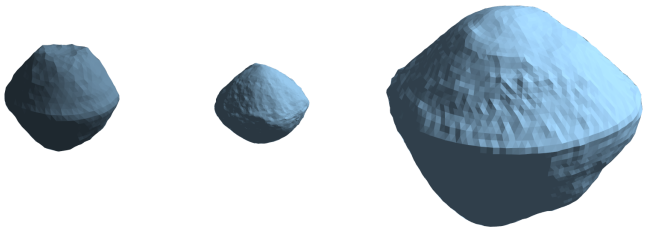

Figure 3.1: Selected rounded asteroids: shape models in real scale.
From left to right: Didymos A, Bennu, KW4 Alpha

3.1.1 Axisymmetric approximation of rounded objects

Since rounded asteroids have usually a quasi-axisymmetric shape, one can think to do an approximation of their shape. In particular an approximation can be a simplified model in which the shape of the asteroid is approximated by a solid of revolution obtained with, as its basis, an interpolated function $R^*(\theta)$ such that for $\theta \in (0, \pi)$, $R^*(\theta) = E_\lambda \left[R(\theta, \lambda)\right]$, where:

$$E_\lambda \left[R(\theta, \lambda)\right] \triangleq \frac{1}{2\pi} \int_0^{2\pi} R(\theta, \kappa)\, d\kappa = R^*(\theta)$$

The function $R^*(\theta)$ extracted applying the *mean* operator will be, practically, discrete and can be interpolated to recover an analytical expression. Several methods can be exploited for the interpolation, including Fourier based one and splines. For simplicity (but also effectiveness), a polynomial interpolation is performed in this work, resulting in the following approximate form for $R^*(\theta)$:

$$R^\circ(\theta) \triangleq \sum_{k=0}^{n} a_k\, \theta^k \simeq R^*(\theta)$$

The coefficient a_k are computed using a Least-Square Method (LSM). In this study they can be easily recovered using the `polyfit` algorithm implemented in MATLAB. To validate this axisymmetric approximation, a comparison with the real shape model is performed. In particular, a map of the difference in altitude between the real and the

axisymmetric approximated shape models is built. To do so, consider a generic point $R(\theta, \lambda) \in \mathcal{S}_{real}$, where $\mathcal{S}_{real}$ is the surface of the object with the real shape and the equivalent point $R_{apprx}(\theta, \lambda) \in \mathcal{S}_{apprx}$ where $\mathcal{S}_{apprx}$ is made by the solid revolution of $R^{\circ}(\theta)$ from 0 to 2π. Here $\theta \in (0, \pi)$ being the *colatitude*. Then the altitude difference map is built such as, for a fixed longitude $\bar{\lambda}$:

$$\mathcal{D}map(\theta, \bar{\lambda}) \triangleq \frac{|R^{\circ}(\theta) - R(\theta, \bar{\lambda})|}{R(\theta, \bar{\lambda})} \cdot 100 \; : (\theta, \lambda) \mapsto \mathcal{D}map(\theta, \lambda) \tag{3.1}$$

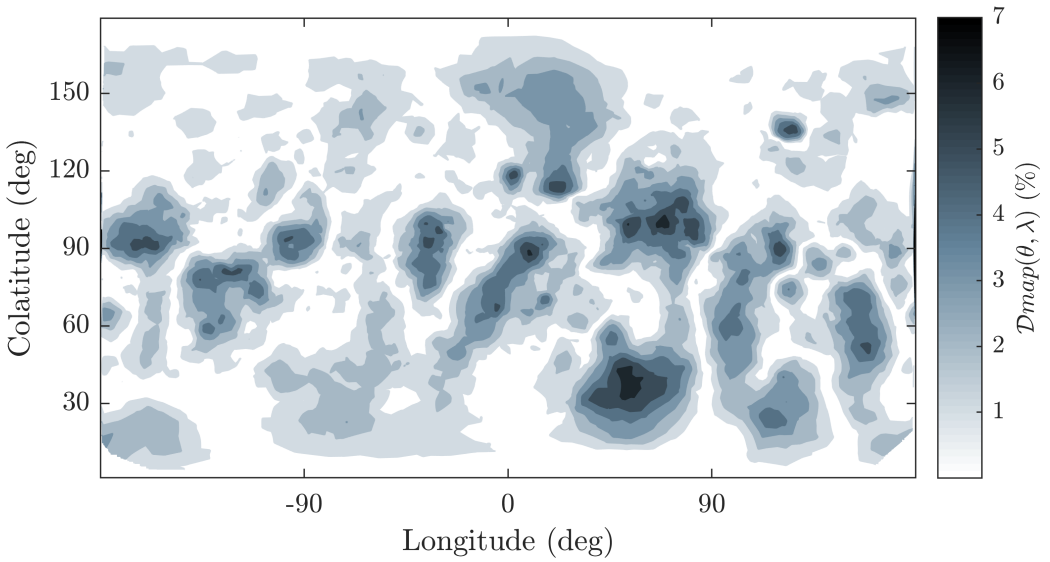

Figure 3.2: $\mathcal{D}map(\theta, \lambda)$ contour plot for the asteroid *Bennu*

The results are shown for the case of the asteroid Bennu in Figure 3.2: the axisymmetric approximation give an approximation of the shape up to a <10% error on it. It can be shown that the error, instead, is much lower in the case of bigger objects, such as quasi-spherical moons. In any case, the aim of this approximation is to introduce a simplification in the gravitational field of the body. In fact, being axisymmetric, the only terms of a spherical harmonics expansion that are non-zero are the zonal one making an expansion with only zonal terms the exact one e. g.,

$$\mathcal{U} = \frac{GM}{r}\left[1 + \sum_{n=2}^{\infty}\left(\frac{R_0}{r}\right)^n \mathcal{P}_n(\cos\theta)\right] \tag{3.2}$$

Then, defining $a_{p_n}(x, y, z)$ the acceleration due to the n-th term of the expansion,

$$a_{p_n}(x, y, z) = \left|\nabla\left\{\frac{GM}{r}\left(\frac{R_0}{r}\right)^n \mathcal{P}_n(\cos\theta)\right\}\right| \tag{3.3}$$

then for axisymmetric bodies $a_{p_n} = a_{p_n}(r, \theta)$. Finally, an integral measure of the acceleration associated with the n-th term of the expansion can be expressed as:

$$A_{p_n}(n, r) = E_{\theta}[a_{p_n}(r, \theta)] = \frac{1}{\pi}\int_0^{\pi} a_{p_n}(r, \vartheta)\, d\vartheta \tag{3.4}$$

Moreover, it can be of interest, since the acceleration in this case is function of the colatitude θ, to have a measure of the sensitivity of it with respect to the θ instead of $r \in [R_{\max}, R_{\text{SOI}}]$ (which sensitivity is analysed with A_{p_n}). Then, another integral measure can be introduced as:

$$\Theta_{p_n}(\theta, n) = \int_0^{\infty} a_{p_n}(\xi, \theta)\, d\xi \approx \int_0^{R_{\text{SOI}}} a_{p_n}(\xi, \theta)\, d\xi \tag{3.5}$$

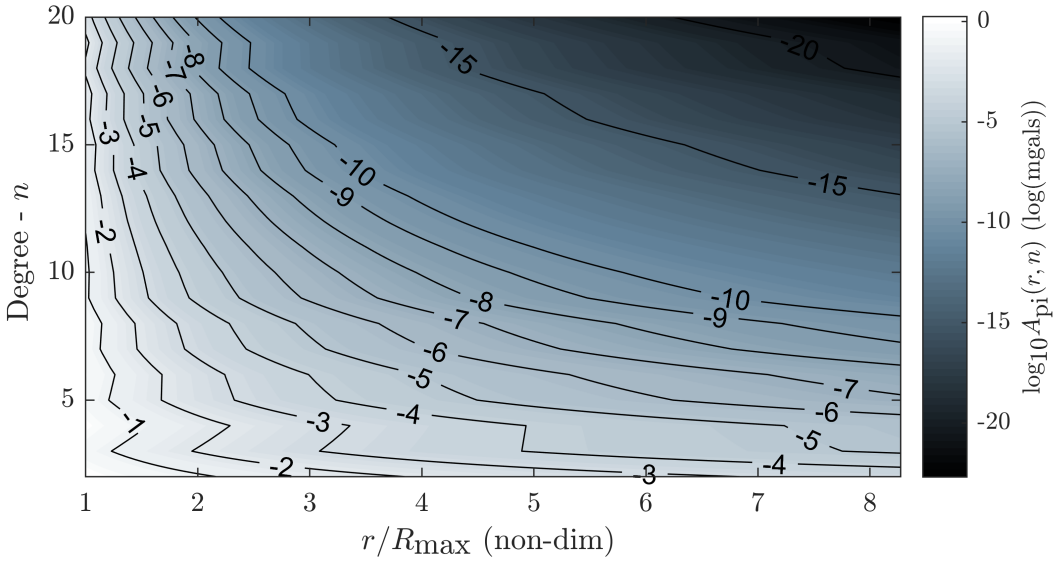

Figure 3.3: $\log_{10} A_{p_i}(n, r)$ contour plot for the axisymmetric approximation of *KW4-α*.

The results for $A_{p_n}(n, r)$ in the case of the asteroid KW4-Alpha are shown in Figure 3.3. In general, these maps gives a way to determine, from an integral point of view, the order of magnitude of the contribution of the n-th term of the expansion at a distance r from the body. For example, as it can be seen, as $R_{\text{SOI}}/R_{\max} = \mathcal{O}(1)$ then, the order of magnitude of the n-th term is approximately 10^{-n} (mgals). Thus the higher the distance from the body, the more difficult will be to identify high order terms.

The results for $\Theta_{p_n}(\theta, r)$ are shown instead in Figure 3.4 for the case of KW4-Alpha too. Note that the inclination of the orbit $i = 90° - \theta$. Now, being the order of magnitude of the n-th contribution to the acceleration a function of the colatitude and so of the inclination of the orbit, if a Keplerian orbit about the body is considered, then it would be preferred to have high-inclined orbits instead of equatorial ones to have an higher perturbative effect. This result could be expected since $a_{\text{p}}(r, \theta)$ and so to have an high-inclined orbit would be beneficial since the "range" of latitudes covered is much higher, resulting in the complete exploitation of the spherical harmonics expansion. If instead a nearly-equatorial orbit is chosen then only some of the low-degree harmonics would be seen.

Despite the fact that the axisymmetric model is an approximate model those, these results can be generalized also to the case in which the true gravity field of the body is under exam. In particular, the considerations that have been done can be generalized too. In fact, while in the identification of the zonal harmonics a polar orbit would

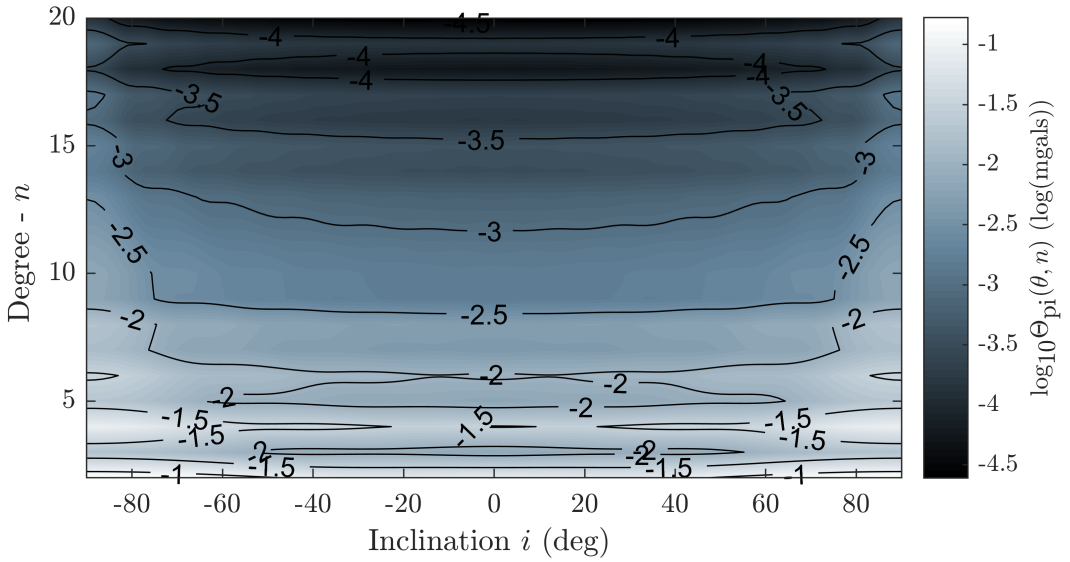

Figure 3.4: $\log_{10} \Theta_{p_n}(\theta, r)$ contour plot for the axisymmetric approximation of *KW4-α*.

be beneficial, in the case the aim is to reconstruct the effect of sectorial harmonics an equatorial orbit would be the best choice for the same considerations done in the zonal case. For what regards the tesseral harmonics, unfortunately, it is not possible to extract any kind of behaviour from this analysis.

On the model order choice. The previous analysis shown that the influence to the model of the single expansion term obviously decreases as increasing the order of the model itself. So a spontaneous question arise: how should one choose the model order to stop the expansion? Basically, for the own SHE model structure, the higher the model the better the approximation would be. But from an operative point of view, if a model is intended to be used on-board, a compromise between model order and expected accuracy must be considered. In particular, in the case of asteroid's missions the accuracy (and so the model order) basically depends on the application. For example, *formation flying* requires an accurate model to "work" properly so a model of model $N_f \gg 1$ should be used. If the mission objective is instead the *gravimetric characterization* of the body then the model order $N_g \gg N_f$. If, instead, the intention is only to have a fairly good prediction of the orbital dynamics about the body than the accuracy requirements can be relaxed, since usually the orbits are not so close so that only the lower degree harmonics influence the orbital path.

3.1.2 Polyhedron model gravity field

In the case of rounded objects, only the external spherical harmonics expansion is used as the *physics* of the reconstructed model, if the aim is to orbit the body at a reasonable distance. But, in any case, the expansion is an approximation of the real gravity field. Also, in the case of irregular bodies, the analytical expansion of the gravity field can be obtained matching the internal and the external expansions.

However, in the hypothesis of constant density model, the *true* gravity field associated to the body is assumed to be the one computed with the polyhedron model. So, the aim of this section is to provide an insight of the resulting gravity fields for some selected bodies in such a way, once the field will be then approximated with an expansion, one can compute how much it differs from the true one.

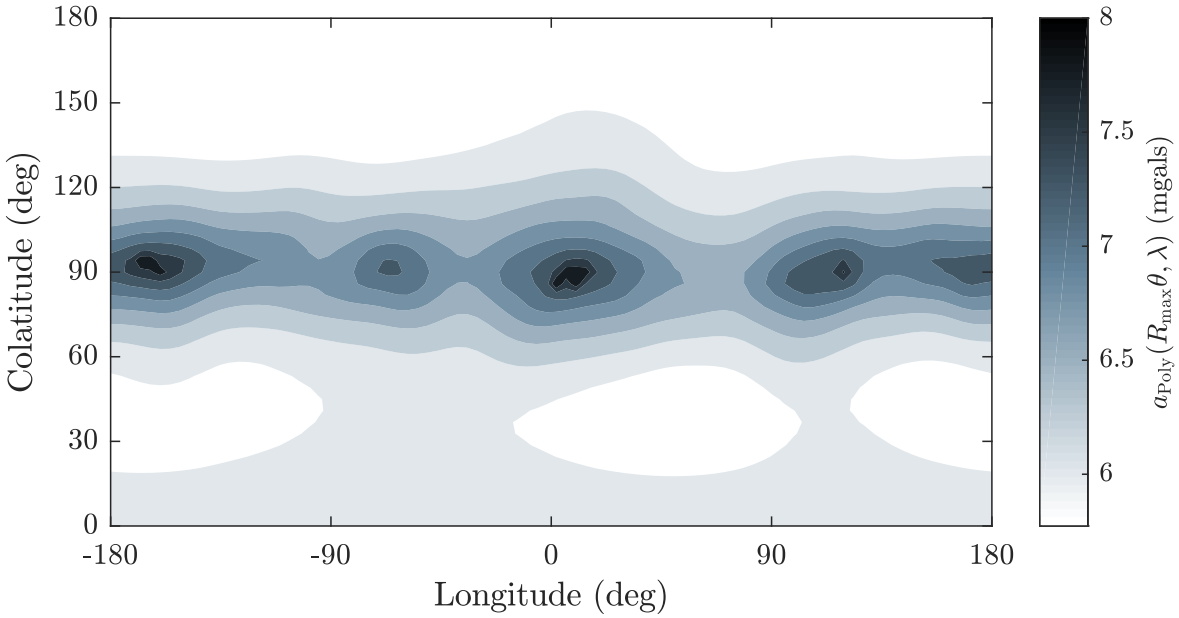

Figure 3.5: Polyhedron accelerations at a distance $r = R_{\max}$ for Bennu.

In particular in Figure 3.5 are shown the accelerations for the asteroids Bennu. In can be noticed that, due to the bulged shape of the bodied, these get higher in proximity of the equatorial plane and lower at the poles of the bodies. It is not worth to say that as far as r increases as far as the magnitude of the gravitational acceleration decreases. Moreover increasing the distance to the body would give a more uniform acceleration

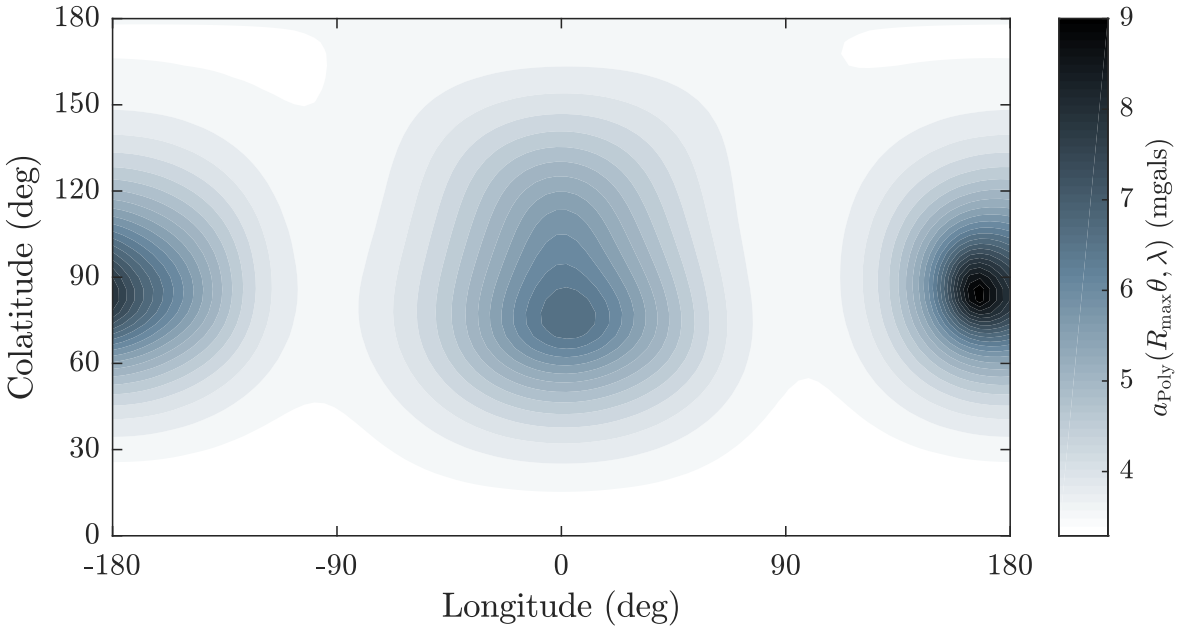

Figure 3.6: Polyhedron accelerations at a distance $r = R_{\max}$ for Castalia.

field. The limit case is when $r \to \infty$ where the acceleration of the body would be the point-mass one.

In Figure 3.6, instead, the results for the shape-based gravity field are presented. This case is much different with respect to the case of Bennu since the filed have maxima in correspondence of the bulged regions while the other regions have much smaller attraction. This results in large differences in the gravity field magnitude as a function of longitude and latitude which respect to the Bennu case. This characteristic is pe-

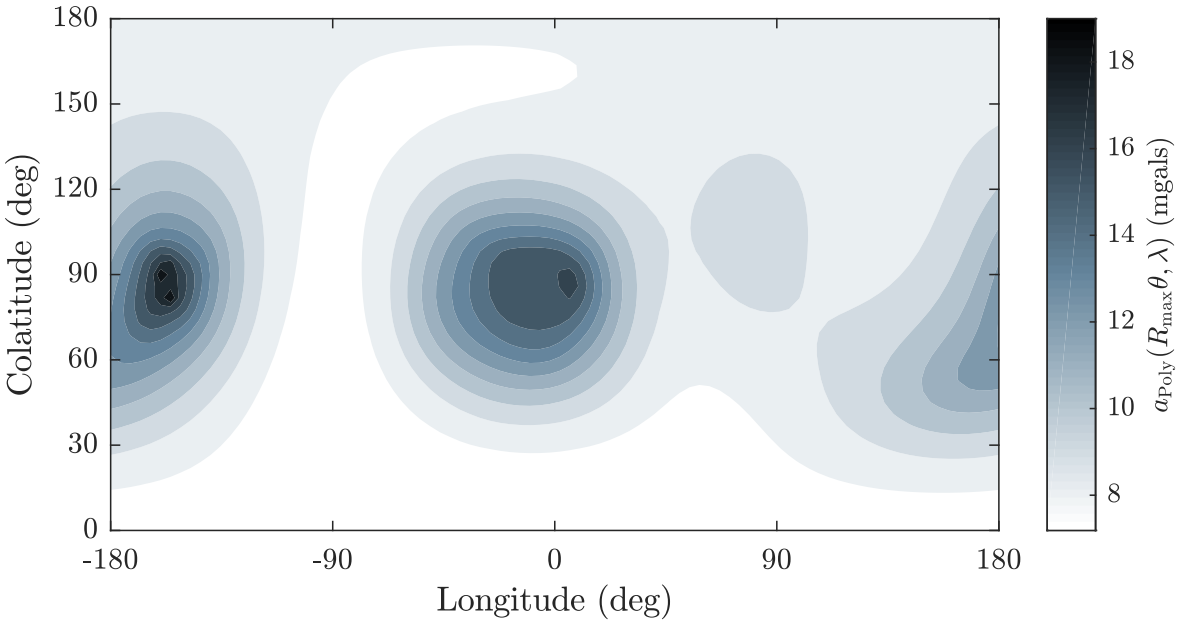

Figure 3.7: Polyhedron accelerations at a distance $r = R_{\max}$ for the comet 67P.

culiar of irregularly shaped bodies, as it can be seen for the case of the comet 67P in Figure 3.7 and makes extremely difficult flight around them.

3.1.3 Spherical harmonics expansion gravity field

In the case of rounded objects the spherical harmonics expansion of the gravity field converges to the true gravity field retaining only a limited number of terms. This is a big advantage since it would reduce the dimension of the estimation problem presented in Chapter 4 on page 59 as well as would reduce the space required to store the reconstructed gravitation model. However, if the intention is to model the field of highly irregular bodies then the number of harmonics needed to reconstruct correctly the field are much higher, increasing the complexity of the estimation problem. In Figure 3.8 and Figure 3.9 the results for the case of Bennu, respectively with a 4th order zonal expansion and a 4th order (complete) expansion at a distance $2R_{\max}$ are shown. The error is here defined as an acceleration error:

$$\mathcal{D}\mathbf{a} = \frac{a_{\text{Poly}} - a_{\text{SHE}}}{a_{\text{Poly}}} \cdot 100 \tag{3.6}$$

It can be noticed that even the zonal representation gives a good approximation even with a low-degree harmonics expansion. This is not the case for highly irregular bodies.

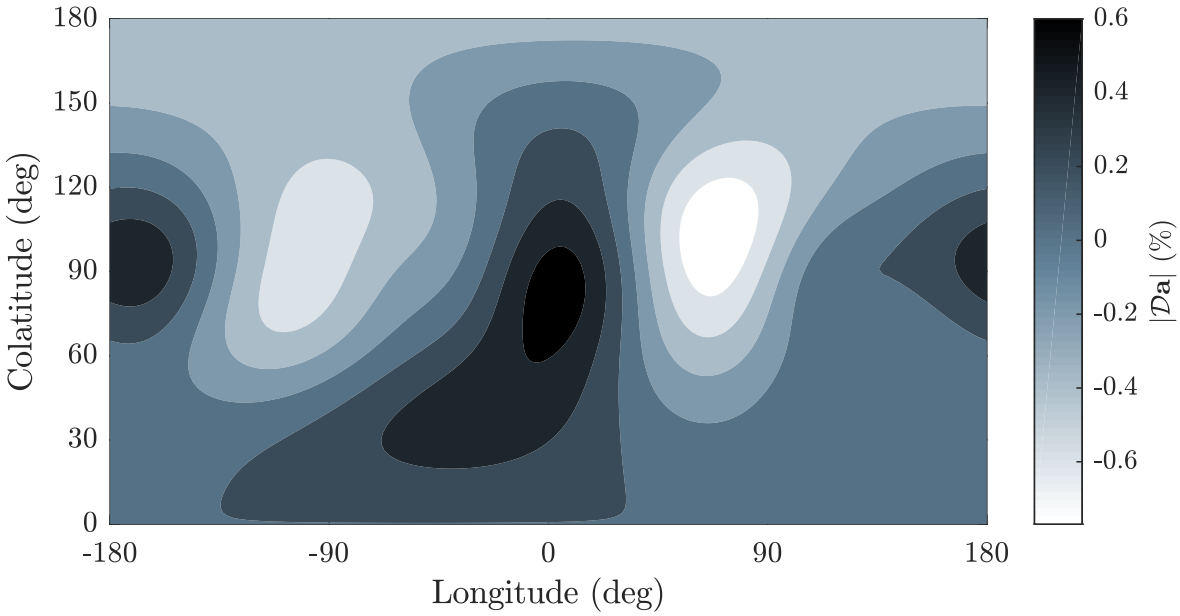

Figure 3.8: $\mathcal{D}\mathbf{a}$ for the case of Bennu with max degree $n = 4$ and considering only the zonal terms of the expansion.

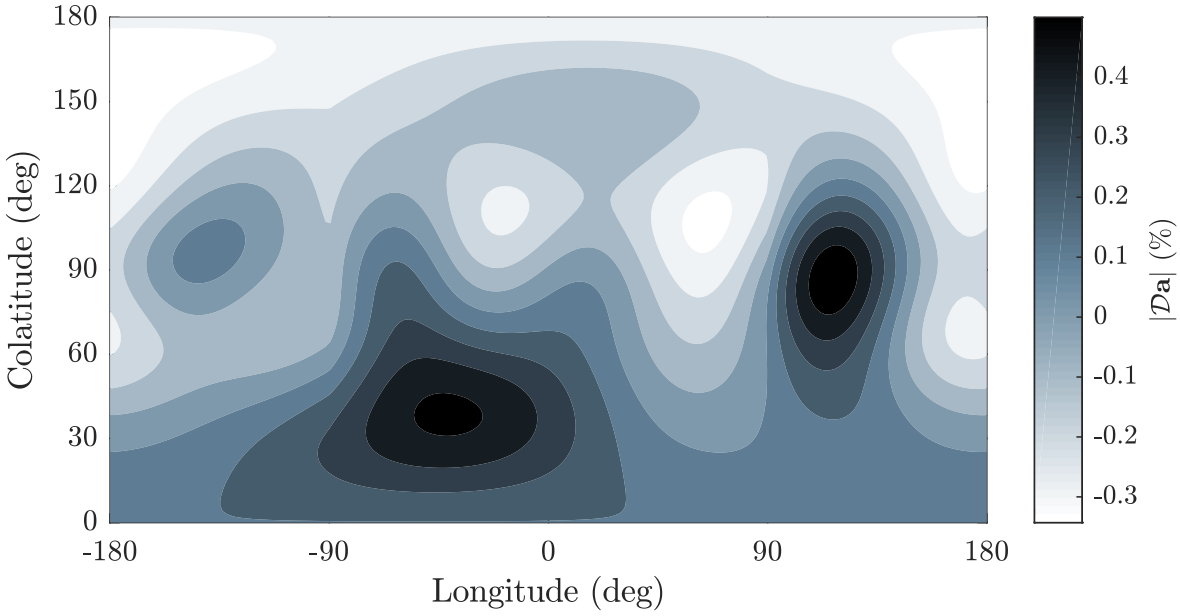

Figure 3.9: $\mathcal{D}\mathbf{a}$ for the case of Bennu with max degree $n = 4$.

Part III

Gravity Field Identification: Methods, Performance & Applications

CHAPTER 4

PARAMETRIC IDENTIFICATION OF GRAVITY FIELD MODELS COEFFICIENTS

THE field of parametric identification or parameters estimation of non-linear systems is one of the most crucial within the framework of system engineering. It consists in modelling the internal model of a dynamical system from observations of its external behaviour. In general, identification techniques can be classified according to whether a model of the system under exam has been formulated, either by the application of physical laws or the intuition of expert. When these models are not available then linear models are usually adopted due to their simplicity and the fact that existing methods for the identification of linear systems are well established. On the other hand when a physical model of the phenomena is recovered methods that incorporates them are not only appealing from the methodological point of view but also attain a more accurate identification. In fact when the overall structure of a model is known, identification reduces to determining the numerical values of some of the parameters of the system model. Hence in that case identification is usually referred to as *parametric identification* or, simply, parameter estimation.

From the mathematical view point, this study deals with the application of parametric identification on ODEs. In general, these kind of differential equations can be represented as $\dot{\mathbf{x}} = \mathbf{f}(\mathbf{x}, \mathbf{u}, \mathbf{p}, t)$, where $\mathbf{x}$ is the state of the system under consideration, $\mathbf{u}$ the inputs, $\mathbf{p}$ the vector of parameters and t the time. In the case of the identification of gravitational field coefficients, however, there is another way to write the mathematical model of the system, due to the form of the gravitational potential itself. For simplicity and clarity, let us consider the case in which the spherical harmonics expansion of the gravity field of a body is developed in such a way the zonal terms only are retained. In this case we can express the gravitational potential as $\mathcal{U} = \mathcal{U}_{2\mathrm{B}} + \mathcal{U}_{\mathrm{Pert}}$,

where $\mathcal{U}_{2\mathrm{B}} = \mu/r$ and:

$$\mathcal{U}_{\mathrm{Pert}} = \sum_{n=2}^{N} \left\{ \frac{\mu}{r} \left(\frac{R_0}{r} \right)^n \mathcal{P}_n(\cos(\theta)) \right\} C_n = \mathbf{P}^T(\mathbf{x}(t)) \cdot \mathbf{p}$$

Where here the vector of parameters $\mathbf{p}$ contains the spherical harmonics expansion coefficients. Then, the equation of motion of the system can be written as, defining the state vector $\mathbf{x}$ as $\mathbf{x} = \{\mathbf{r}, \mathbf{v}\}^{\mathrm{T}}$, as follows:

$$\dot{\mathbf{x}} = \begin{Bmatrix} \dot{\mathbf{r}} \\ \dot{\mathbf{v}} \end{Bmatrix} = \begin{Bmatrix} \mathbf{v} \\ -\frac{\mu}{r^3}\mathbf{r} + \nabla\mathcal{U}_{\mathrm{Pert}} \end{Bmatrix} \tag{4.1}$$

Note, in particular that here the parameters appears only in $\nabla\mathcal{U}_{\mathrm{Pert}} = \nabla\mathcal{U}_{\mathrm{Pert}}(\mathbf{r}(t), \mathbf{p})$. Then defining $\mathbb{A} = \nabla\mathbf{P}^{\mathrm{T}}$, it is possible to write the equation in the so called linear in the parameters (LIP) form, that is:

$$\mathbf{y} = \mathbb{A}(\mathbf{x}) \cdot \mathbf{p}$$

In order to match the LIP form with the equation of motion on the left-hand side there must be all the terms that does not depends on the parameters, thus:

$$\mathbf{y} = \dot{\mathbf{v}} + \frac{\mu}{r^3}\mathbf{r}$$

Finally note that, being the gravitational force a positional force, in this case the matrix $\mathbb{A}$ depends only on the position, thus $\mathbb{A}(\mathbf{r})$ Note also that $\mathbb{A}$ is, in general, *non*-square. Then the LIP form of the equation of motion is:

$$\mathbf{y}(\mathbf{r}, \dot{\mathbf{v}}) = \mathbb{A}(\mathbf{r}) \cdot \mathbf{p} \tag{4.2}$$

Note that the equation is linear with the respect to the parameters despite the fact that it is *non-linear* with respect to the state. Now, suppose to have a-priori guess $\mathbf{p}_0$ of the parameters and define $\delta\mathbf{p}$ this deviation, then the LIP equation of motion becomes:

$$\mathbf{y}(\mathbf{r}, \dot{\mathbf{v}}) = \mathbb{A}(\mathbf{r}) \cdot (\mathbf{p}_0 + \delta\mathbf{p})$$

Suppose to use an estimation algorithm to estimate $\delta\mathbf{p}$ and the estimation provided is $\delta\mathbf{p}^*$. The goal of the estimation is to minimize the so called *estimation error* defined as $\Delta\mathbf{p} = \delta\mathbf{p} - \delta\mathbf{p}^*$. In practice, the estimation error cannot be used since $\delta\mathbf{p}$ is not available. Instead the *prediction error*, $\mathbf{e} = \mathbf{y} - \mathbb{A} \cdot \delta\mathbf{p}^*$, is used.

4.1 Problem Formulation

Assuming that the mathematical model can be written in the LIP form $\mathbf{y}(t) = \mathbb{A}(t) \cdot \mathbf{p}$, for some $\mathbf{y} : [t_0, +\infty[\to \mathbb{R}^m$, $\mathbb{A} : [t_0, +\infty[\to \mathbb{R}^{m \times n}$, $\mathbf{p} \in \mathbb{R}^n$ is the vector of parameters to be estimated on-line. Furthermore, a series of assumptions are needed [55]:

(H1) $\mathbf{y}, \mathbb{A} \in \mathcal{C}^1$;

(H2) $\mathbf{y}, \mathbb{A}$ are bounded;

(H3) $\mathbf{y}(t), \mathbb{A}(t)$ are known or can be measured or reconstructed at each time;

(H4) $\mathbf{p} \in]-c, c[^n$ for some known $c > 0$

To solve the on-line estimation problem, an algorithm $\mathcal{A}$ should generate at time t an estimation $\mathbf{p}^*$ of $\mathbf{p}$ based on the available informations: c and the values of $\mathbf{y}$ and $\mathbb{A}$. Some desirable properties for the algorithm are:

(P1) $\forall t > t_0\, \mathbf{p}^*(t) \in]-c, c[^n$;

(P2) $\lim_{t \to +\infty} \mathbf{p}^*(t) = \mathbf{p}(t)$.

The property (P1) defines the search region for the algorithm while the property (P2) defines the ultimate goal of the on-line estimator. The difference between different estimators will be, of course, in the trajectory $\mathbf{p}^*(t)$. Having defined the prediction error as $\mathbf{e}(t, \mathbf{p}^*(t))$ then the on-line estimation should solve an optimization problem, defined as:

$$\min_{\mathbf{p} \in]-c,c[^n} \left\{ \sup_{t \in [t_0, +\infty[} \left\{ \frac{1}{2} \mathbf{e}^{\mathrm{T}}(t, \mathbf{p}^*(t)) \cdot \mathbf{e}(t, \mathbf{p}^*(t)) \right\} \right\} \tag{4.3}$$

There are, in general, two families of methods that can be used to solve this kind of problem: least-square estimators and gradient-based estimators.

4.1.1 Least-square estimators

It works on the minimization of the square of the prediction error, summed along the whole temporal evolution of the system and defined as:

$$E(\mathbf{e}) = \frac{1}{2} \left(\mathbf{e}^T \mathbf{e} \right)$$

Thus, it is natural to think of least square as a *batch* algorithm. In fact, as an example, a cost function for the minimization can be defined as:

$$\mathcal{J} = \int_0^t ||E(\mathbf{e}(\tau))||_2 \, d\tau = \sum_{t_k} ||E(\mathbf{e}(t_k))||_2 \tag{4.4}$$

Which means that the temporal evolution of the prediction error must be known a-priori. In contrast, *on-line* estimation if often required. Then there are some variants of least square algorithms that allows for on-line estimation but the computational complexity of them is much higher. Last but not least, when the parameters are time-varying, additional corrections must be added, increasing again complexity.

As an example, the results of a LSM are shown in Figure 4.1 and Figure 4.2. As it can be seen, the optimization is capable to compute almost *exactly* the two coefficients C_2 and C_3 of the spherical harmonic expansion.

4.1.2 Gradient-based estimators

According to [56], a common technique for on-line estimation is the gradient method that, due to its simplicity, presents some advantages over least mean squares algorithms

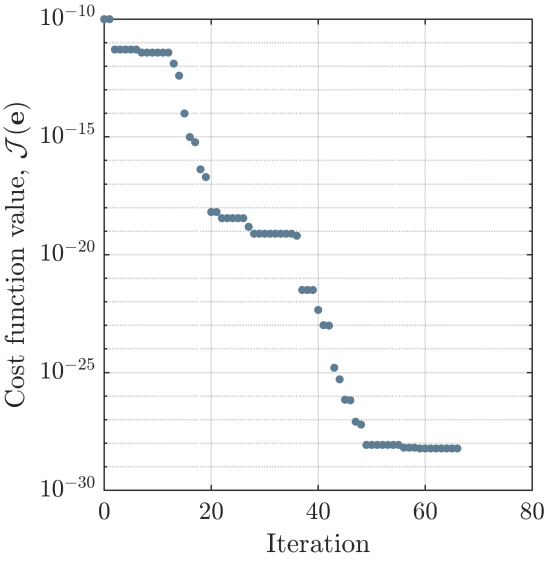

Figure 4.1: Cost function value vs iteration for the `particleswarm` optimization.

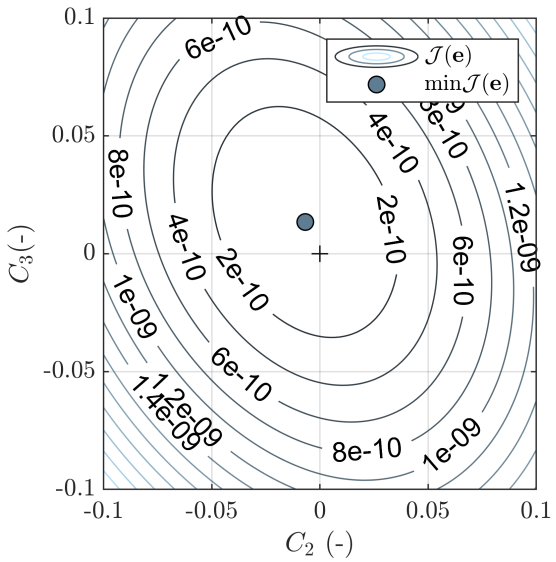

Figure 4.2: Location of the minima of $\mathcal{J}(\mathbf{e})$ in function of the parameters value, for the *test* model.

in estimation of time-varying parameters. In the gradient method, the estimation is continuously modified in the direction that best minimizes the prediction error i. e., the direction of the gradient of the square of the prediction error as a function of the estimation vector $\mathbf{p}^*$ i. e.,

$$\dot{\mathbf{p}}^* = -k\nabla\left(\mathbf{e}^T\mathbf{e}\right) \tag{4.5}$$

here k is a design parameter, which must be critically chosen as a trade-off between small values - slow convergence and large values - oscillations. The asymptotical convergence to zero of the prediction error can be proved if $\mathbb{A}$ and $\mathbf{y}$ are constant, but the result is also valid as long as $\mathbb{A}$ and $\mathbf{y}$ change slowly, which we assume in the sequel.

4.1.3 The modified Hopfield Neural Network

Among the others, it has been shown that there are two main types of ANN that are capable to solve combinatorial optimization problems: the *feed-forward* RBF neural network - where the neurons belonging to the same layer receive inputs from neurons of the previous layer and send their values only to neurons of the next layer, and the *feedback* HNN - where the neurons belonging to the same layer send their output to neurons of the next and previous layers [57]. A training phase is needed in both cases and it involves adjusting the weights on the interconnections in the network until the error which is the difference between the actual output and the target output is small. In this application, in particular, an *online* adjustment of the network is needed, meaning that *no offline training is available for the network*. For this reason, this is an *unsupervised learning* problem. In [57] a deep comparison between RBF and HNN is presented and the HNN appears to be the most promising because:

- It is a *global network* which means that every input vector produce activation while RBF are *local network* meaning that only onput vectors in the close neigh-

borhood of centers produce activation and the other inputs have negligible values;

- Use unsupervised learning while RBF is an hybrid learning algorithm;
- HNN have a simple technical implementation using electronic or optical devices.

In general, HNNs are a kind of ANNs formulated by Hopfield in its paper [58]. The model developed as well as its stability has been extensively studied in the last decades. In the original Hopfield's formulation of the network, the dynamics of the neuron i is governed by the ODE, [55] :

$$\frac{dp_i}{dt} = -p_i + \sum_{j=1}^{N} w_{ij}\phi_j(p_j(t)) - b_i \tag{4.6}$$

where $p_i(t)$ is the total input to the neuron i, ϕ_j is a continuous non-linear, bounded and strictly increasing function called *activation function*, and w_{ij} and b_i are parameters corresponding respectively to the synaptic efficiency associated with the connection from neuron j to neuron i, and the bias of the neuron i.

$$s_i(t) = \alpha \tanh\left(\frac{p_i(t)}{\beta}\right) \tag{4.7}$$

where $\beta > 0$ is a coefficient to eventually regulate the slope of the activation function while α is chosen such that $s_i(t) \in]-\alpha, \alpha[$. Then according to [59], [58], in order to prove that the neural system defined in Eq. (4.6) is stable, the candidate Lyapunov function:

$$V(\mathbf{s}) = -\frac{1}{2}\sum_{i=1}^{n}\sum_{j=1}^{n} w_{ij}s_i s_j + \sum_{i=1}^{n} b_i s_i + \beta \sum_{i=1}^{n}\int_0^{s_i} \tanh^{-1}(g)\, dg \tag{4.8}$$

is defined and is proved that it is indeed a Lyapunov function, as long as the conditions $w_{ii} = 0$ and $w_{ij} = w_{ji}$ hold for the network weights. Therefore, Lyapunov stability theory [60] guarantees that the states of the ODE converge towards a minimum of the Lyapunov function. The key concept associated to the theory of HNN is the fact that:

$$\frac{\partial V}{\partial s_i} = -\frac{dp_i}{dt} \tag{4.9}$$

so that the network defines a *gradient system*. This can read as *the network states evolve in the direction that minimized the Lyapunov function*. So the application of Hopfield networks to the solution of optimization problems is a direct consequence of the dynamical properties of the network and, in particular, of the existence of Lyapunov function. Then, the optimization procedure consist in matching the Lyapunov function 4.8 to the target function of the considered optimization problem. Many optimization problems posses a quadratic target function that matches the first two terms of 4.8 but this formulation has a problem: the integral term. In fact, it makes the network deviate from the minimum of the target function.

Abe formulation [61] of the problem is generally preferred in the case the network is applied to optimization since its Lyapunov function does not contain any integral term i. e., is defined as:

$$V(\mathbf{s}) = -\frac{1}{2}\sum_{i=1}^{n}\sum_{j=1}^{n} w_{ij}s_i s_j + \sum_{i=1}^{n} b_i s_i \tag{4.10}$$

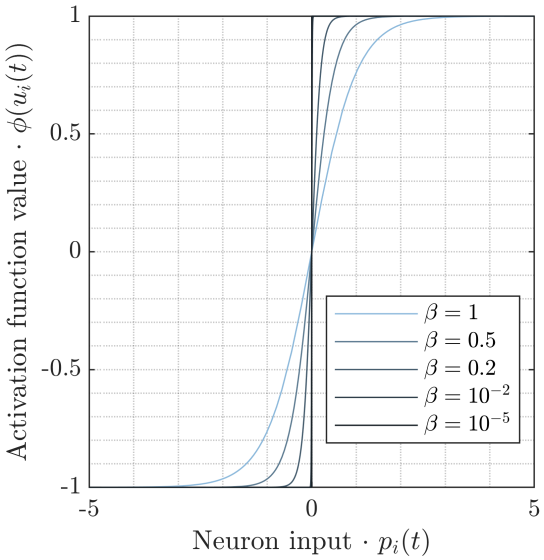

Figure 4.3: Activation function values in function of the parameter β.

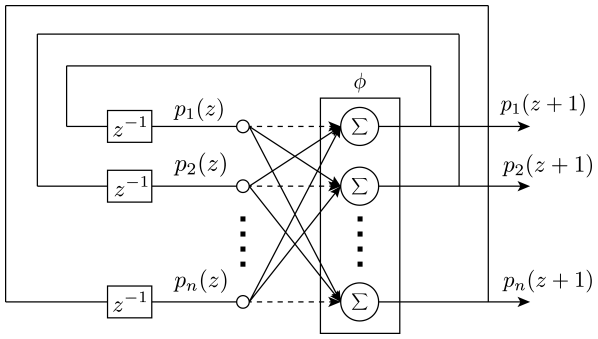

Figure 4.4: Hopfield neural network structure: note that the HNN is a recurrent network. Here, a discrete version of the network is presented.

Then, the network is formulated as a ODE:

$$\frac{dp_i(t)}{dt} = net_i(t) = \sum_{j=1}^{n} w_{ij}s_j - b_i \quad \text{with} \quad s_i(t) = \alpha \tanh\left(\frac{p_i(t)}{\beta}\right) \tag{4.11}$$

Now, applying the chain rule:

$$\frac{ds_i}{dt} = \frac{1}{\alpha\beta}\left(\alpha^2 - s_i^2\right)\left(\sum_{j=1}^{N} w_{ij}s_j - b_i\right) \tag{4.12}$$

A further note has to be done here since the previous procedure to recover a ODE system in the state $s_i(t)$ can be applied only in case the Abe formulation is considered otherwise, if the Hopfield formulation is used as the model, this procedure would bring to a differential algebraic problem. The previous equation may be written in matrix notation as follows:

$$\frac{d\mathbf{s}(t)}{dt} = \frac{1}{\alpha\beta}\,\mathbb{D}\cdot\left(\mathbb{W}\mathbf{s}(t) - \mathbf{b}\right) \tag{4.13}$$

where:

$$\mathbb{D}(\mathbf{s}(t)) = \operatorname{diag}\left((\alpha^2 - s_i^2)_{i\in n}\right)$$

is positive definite and invertible. This is a non-autonomous non linear dynamic system whose architecture is fully determined by the number of neurons, and whose dynamics is fully characterized by $\alpha, \beta, \mathbb{W}, \mathbf{b}$ and $\mathbf{s}(t_0)$. Note also that the two-step dynamics defined in equation Eq. (4.11) is, strictly speaking, a Differential Algebraic Equation (DAE), while, instead Eq. (4.13) is a *simple* ODE which ease the numerical implementation. Note also that the equation may be re-written also as in the so called *linear-gradient form*:

$$\frac{d\mathbf{s}}{dt} = \frac{1}{\alpha\beta}\mathbb{D}\,\nabla V(\mathbf{s})$$

Thus, it is easy to show the stability of the estimator in the case of an autonomous network [62], using Lyapunov stability theory. In fact, since a Lyapunov function exists, the only possible long-term behaviour is for trajectories to asymptotically approaching a point that belongs to the set of fixed points. Those *fixed points* are defined ad the points where $dV/dt = 0$ i. e.,

$$\frac{dV}{dt} = \sum_{i=1}^{n} \frac{\partial V}{\partial s_i} \frac{ds_i}{dt} = -\sum_{i=1}^{n} net_i \left(\alpha^2 - s_i^2\right) net_i = 0$$

Then the fixed points can a be vertex of the hypercube where $|s_i| = \alpha$ or an interior points $net_i = 0$. A remarkable property of the network is then that trajectories always remain within the hypercube $]-\alpha, \alpha[^n$ as long as the initial values belongs to the hypercube too i. e., the hypercube is *invariant*. In any case, the stability of the method is shown in [55], [56] where a non-autonomous HNN is shown to be the solution of the optimization problem defined in Eq. (4.3) if $\forall t \geq t_0$ then $\ker(\mathbb{A}(t)) = \{\mathbf{0}\}$ holds. Then the solution is obtained at any time with:

$$\begin{aligned} \mathbb{W} &= -\mathbb{A}^{\mathrm{T}}\mathbb{A} \\ \mathbf{b} &= -\mathbb{W}\mathbf{p}_0 - \mathbb{A}^{\mathrm{T}}\mathbf{y} \end{aligned}$$

Note that $\mathbb{A}$:

- Is a square, symmetric and positive definite matrix;
- Can be seen as an estimator of the covariance of the state, if normalized by the mean:
$$\sigma_{j_1,j_2} = E[a_{j_1} a_{j_2}] \simeq \frac{1}{m} \sum a_{j_1} a_{j_2}$$
- The w_{ii} are the *variances* associated to the $\mathbb{A}$ matrix i. e., $\mathrm{tr}(\mathbb{W}) > 0$;
- Since $\mathbb{W}$ is symmetric then its eigenvalues are real and positive while the eigenvectors:
$$\mathbb{W} = \Lambda \mathbb{V} \Lambda = \sum_i \lambda_i \mathbf{v}_i \mathbf{v}_i^{\mathrm{T}}$$
then $\det \mathbb{W} = \prod_i \lambda_i > 0$ since $\lambda_i > 0 \, \forall i$.

4.1.4 Discrete modified Hopfield networks

In this section, for the sake of comparison, we describe the conventional discretization that is usually adopted to implement Hopfield networks. According to [63] and [64] the usual discretization of Hopfield networks results from replacing the derivative $\frac{dp_i}{dt}$ by a finite difference Euler method, such as:

$$\frac{dp_i}{dt} = \frac{\Delta p_i}{h} = \frac{(p_i)_{k+1} - (p_i)_k}{h} \tag{4.14}$$

where h is the time step. The discrete dynamics resulting from this approximation is then:

$$(p_i)_{k+1} = (p_i)_k + h \, (net_i)_k \tag{4.15}$$

where

$$(net_i)_k = \sum_{j=1}^{n} (w_{ij})_k (s_j)_k - (b_i)_k \quad \text{then} \quad (s_i)_{k+1} = \alpha \tanh\left(\frac{(p_i)_{k+1}}{\beta}\right) \tag{4.16}$$

Then this two-step dynamics can be rewritten as an one-step map as follows:

$$(s_i)_{k+1} = \alpha \tanh\left(\frac{1}{\beta}\left((p_i)_k + h\,(net_i)_k\right)\right) = \alpha \frac{(s_i)_k + \tanh\left(\frac{h}{\beta}(net_i)_k\right)}{1 + (s_i)_k \tanh\left(\frac{h}{\beta}(net_i)_k\right)} \tag{4.17}$$

Now, according to [63], this equation does not coincide with any reported numerical method and in particular it is no longer the Euler method applied to the single ODE given in Eq. (4.12) which, instead, is given by:

$$(s_i)_{k+1} = (s_i)_k + \frac{h}{\alpha\beta}\left(\alpha^2 - (s_i)_k^2\right)\left(\sum_{j=1}^{N} (w_{ij})_k (s_j)_k - (b_i)_k\right) \tag{4.18}$$

Note that Eq. (4.17) is bounded but it is not continuous when $1+(s_i)_k \tanh\left(\frac{h}{\beta}(net_i)_k\right) = 0$. In principle, this condition cannot be achieved since $|s_i| < \alpha$, but in a computer implementation must decide which value is adopted to avoid this singularity that can appears due to round-off errors. The choice in this study is to set $(s_i)_{k+1} = (s_i)_k$ if the singularity is encountered. In this way the fixed points of the systems are also preserved. Obviously the methods presented are equivalent.

CHAPTER 5

PARAMETRIC IDENTIFICATION OF SIMPLIFIED MODELS

In this part the HNN is extensively tested on the basis of the model Eq. (4.1), with $\nabla\mathcal{U}_{\text{pert}}$ containing only the *zonal* terms of the expansion. To give an applicative meaning to this simplified model, one can think to a rounded body that can be well approximated in an axisymmetric manner. For this case, series of tests have been done in order to understand how the network behaves on the parametric identification of gravity field coefficients and how it can be improved. Note that in this part *only* the gravity of the main body is taken into account. However the Sun third-body perturbation as well as the SRP must be taken into account for orbits about this kind of bodies since they can be of the same order of magnitude of the gravity field of the body. But in this part, since the aim is to test the HNN capability of computing correctly the Stokes coefficients, these effects are not yet considered. Other strong assumptions considered in this part are:

- The minor body is considered to be *steady*;
- A perfect determination is assumed for the state of the orbiting object: the state vector is, in fact, assumed to be known and expressed with respect to the exact centre of mass of the body.

Before starting the tests, recall from Chapter 3 on page 49 that:

(R1) The order of magnitude of the n-th element of a spherical harmonic expansion decrease as far as the distance from the body increases;

(R2) The higher the inclination of the orbit, the higher the order of magnitude of the perturbation will be (from an integral point of view and zonal perturbations).

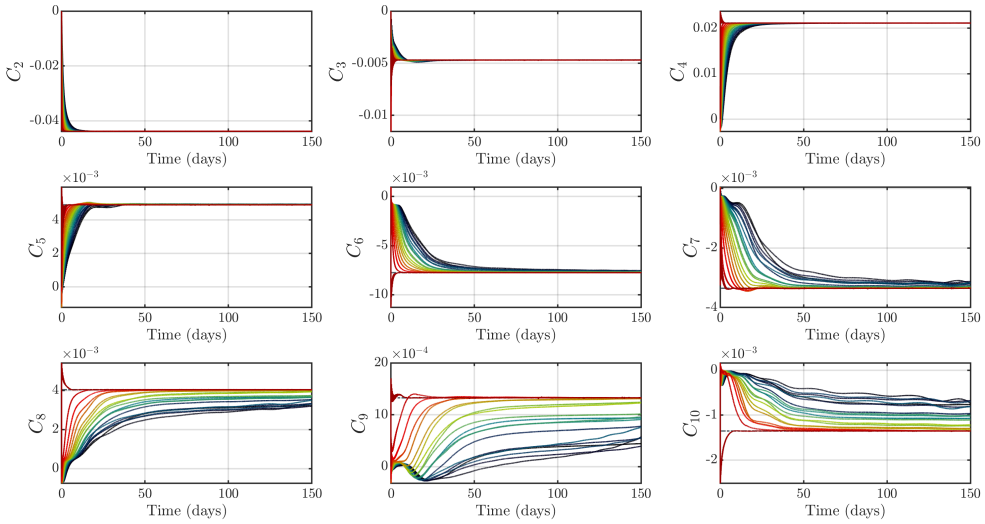

Figure 5.1: *Test 1(a)* · Results with $a_0 = 1.5R_{\max}$.
Color scale goes from black ($\beta = 1\text{e}-3$) to red ($\beta = 1\text{e}-6$).

Recall also that the HNN used here is fully determined once $\alpha, \beta, \mathbb{W}, \mathbf{b}$ and $\mathbf{s}(t_0)$ are given. Thus once the initial conditions on the orbit i. e., $\mathbf{r}(t_0)$ and $\mathbf{v}(t_0)$ are given and the newtork is initialized with a certain $\mathbf{s}(t_0)$, then the performances would depends on the values of the two parameters α, β. The dependence of the performances on the orbit itself is implicit in the definition of $\mathbb{W}$ and $\mathbf{b}$ and meets the points (R1) on the previous page and (R2) on the preceding page. So, in general, the study of the convergence of the network for the j-th parameters p_j is a function of some arguments:

$$p_j = p_j(\alpha, \beta, p_{i_0}; a_0, e_0, i_0, \Omega_0, \omega_0; t) \tag{5.1}$$

Then considering an axisymmetric body would reduce the function to:

$$p_j = p_j(\alpha, \beta, p_{i_0}; a_0, e_0, i_0; t)$$

Moreover, in this case we consider to initialize the network with $\mathbf{s}(t_0) = \mathbf{0}$, and we consider the case in which $e_0 = 0$. This last assumption is for simplicity. A case in which $e_0 \in]0, 1[$ will be analysed later as well a case in which $e_0 > 1$. So then:

$$p_j = p_j(\alpha, \beta; a_0, i_0; t) \tag{5.2}$$

Moreover, a statistical measure can be introduced to eliminate the time dependence: the Maximum Likelihood Estimation (MLE). It would have an estimated value $\hat{p}_j = \hat{p}_j(\alpha, \beta; a_0, i_0)$ as well as variance associated $\sigma_j^2 = \tilde{p}_j(\alpha, \beta; a_0, i_0)$. Then, since all those functions are different for each parameter, in general we can write them in the form $\mathcal{F}(j; \alpha, \beta; a_0, i_0)$. Thus in order to plot the results, one have to fix at least three between the arguments of the function $\mathcal{F}$. Now a series of tests on the asteroid KW4-α are performed to understand how the function $\mathcal{F}$ can be interpreted.

Test 1 (a),(b). This test is performed varying the value of β and keeping fixed the other arguments of the function. In particular, the case in which $a_0 = 1.5R_{\max}$ (a)

and $2R_{\max}$ (b), $i_0 = 90°$ and $T = 150$ days is considered, while $\beta \in [1\text{e}-3, 1\text{e}-6]$. The results are shown in Figure 5.1 and Figure 5.2: small values of β guarantee a faster convergence and the convergence is improved as far as the distance to the body is small.

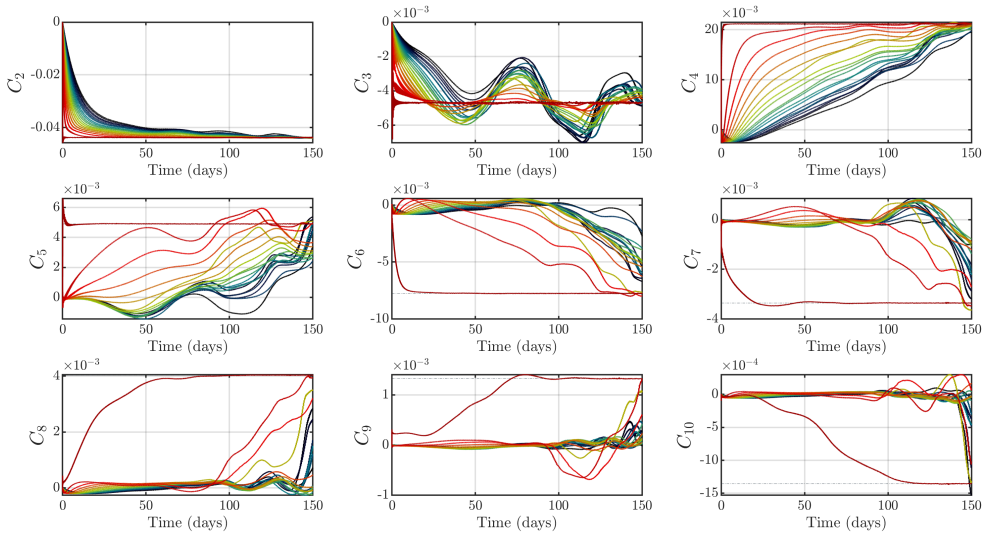

Figure 5.2: *Test 1(b)* · Results with $a_0 = 2R_{\max}$.
Color scale goes from black ($\beta = 1\text{e}-3$) to red ($\beta = 1\text{e}-6$).

Moreover, as the distance to the body increases, as it can be seen from Figure 5.2, as the convergence is less smooth.

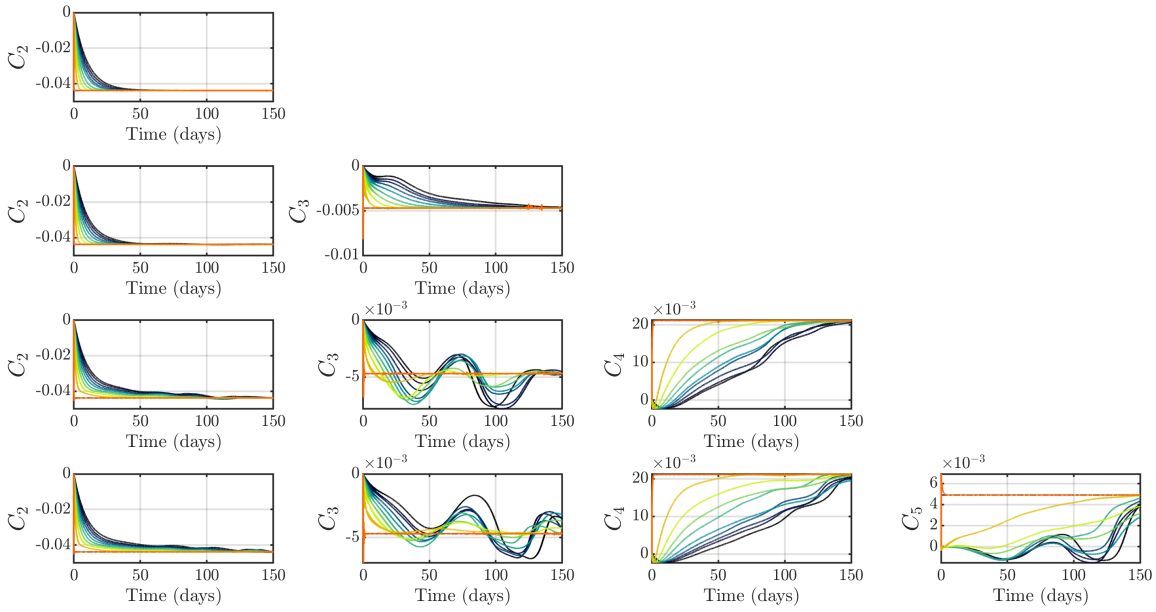

Figure 5.3: *Test 1(b)* · Results with $a_0 = 2R_{\max}$, parametrized for the number of Stokes coefficients. Color scale goes from black ($\beta = 1\text{e}-3$) to red ($\beta = 1\text{e}-6$).

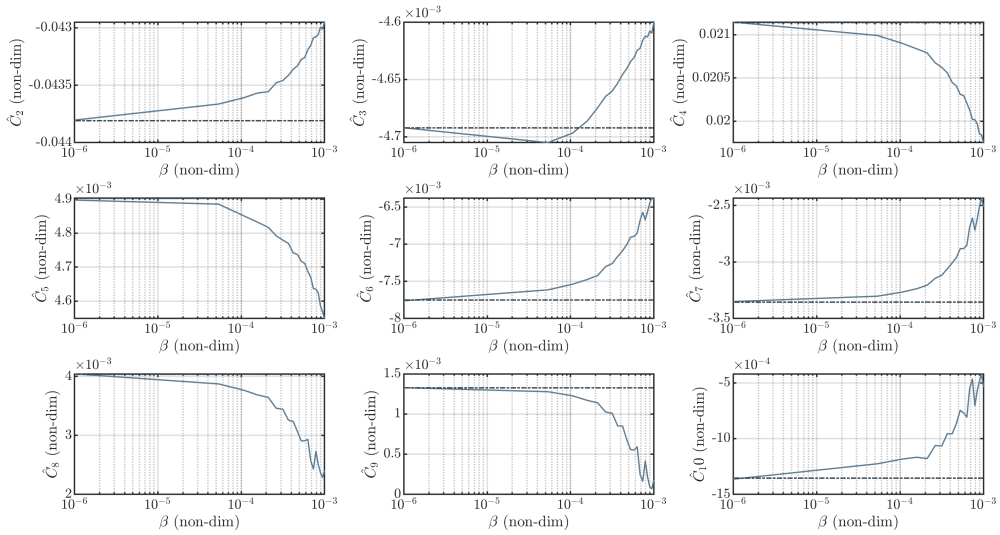

Figure 5.4: *Test 1(a)* · Results with $a_0 = 1.5R_{\max}$: MLE, mean.

Last but not least, the convergence rate and smoothness depends, in this case, also from the number of coefficient to be estimated. In Figure 5.3 a clear example: looking at the coefficient C_3, it can be seen that in the second row it converges smoothly while in the third, when another coefficient is added, the behaviour is different.

The previous considerations, finally, can be reinforced with the MLE analysis, whose results are shown in Figure 5.4: as far as β gets smaller, as far as the estimated mean tends to the true value of the coefficient. It should be said that, however, too small values of β would bring the network to instability: an example, with $\beta = 1\text{e} - 8$ is shown in Figure 5.5.

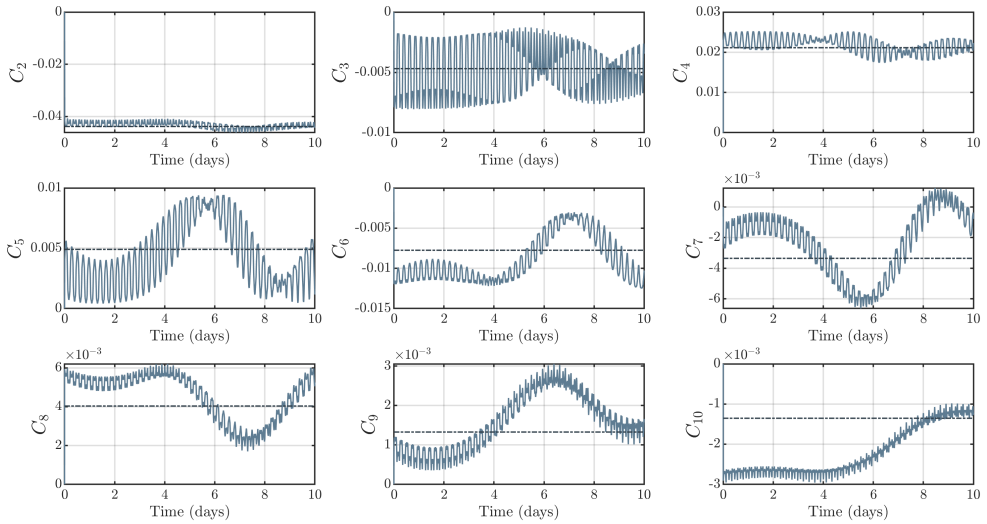

Figure 5.5: *Test 1(a)* · Results with $a_0 = 1.5R_{\max}$: instability phenomenon.

Note that the instability would influence the convergence to the method through oscillations about the true value of the coefficient. This is due to the fact that the activation

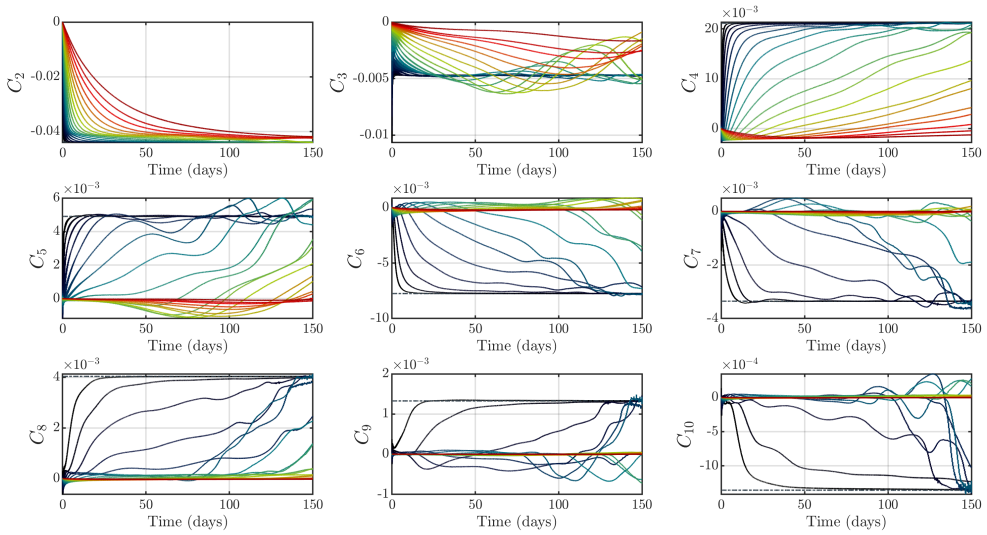

Figure 5.6: *Test 2* · Results.
Color scale goes from black ($a_0 = 1.5R_{\max}$) to red ($a_0 = 3R_{\max}$)

function is too steep and even small variations of the neuron state would give a large output. Note also that, in case the network is unstable, a dense fitting is needed to catch its behaviour: if the fitting is not enough dense then the network would converge to the vertex of the hypercube, for numerical reasons, and gives $\pm\alpha$.

Test 2. This test is performed varying the value of a_0 and keeping fixed the other arguments of the function. In particular, the case in which $a_0 \in [1.5R_{\max}, 3R_{\max}]$, $i_0 = 90°$ and $T = 150$ days is considered, while $\beta = 1\text{e}-4$. The results are shown in Figure 5.6. In this case the higher order terms convergence is largely influenced by the value of a_0: as far as the distance to the body increases as slow as it is the convergence to the real parameter value. Of course, the behaviour has a strong dependence on β and i_0 as it can be seen from Figure 5.7.

The results shown in Figure 5.7 are of interest also because the parameters converges, depending on the distance to a different estimated value and this value is not the actual value of the parameter. This results comes from the fact that the body is axisymmetric and the orbit considered is equatorial so that the estimation error is dominated by a *bias error* due to the lack of informations. Those error gets smaller as far as i_0 increases as shown in Figure 5.8.

As in *test 1* the convergence depends also on the number of parameters to be estimated, due to the cross-correlations present in the model, as can be seen in Figure 5.9.

Test 3. This test is performed varying the value of i_0 and keeping fixed the other arguments of the function. All the previous considerations are valid and as i_0 gets higher as the convergence in fast as well as the network converges in a reasonable time. In particular with $a_0 = 2R_{\max}$ and $\beta = 1\text{e}-4$ fixed it is interesting to look at the results parametrized for the number of coefficients, varying $i_0 \in [0, 90°]$.

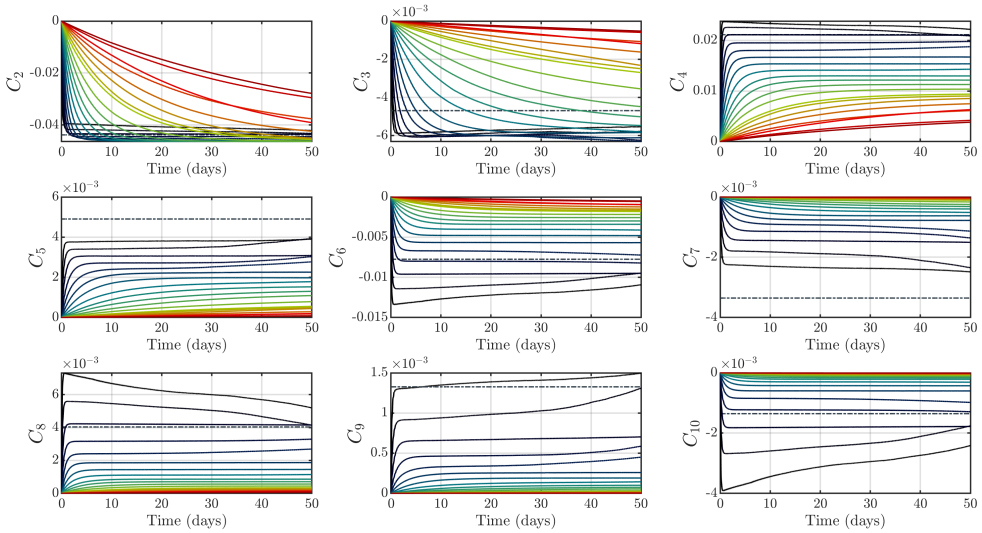

Figure 5.7: *Test 2* · Results with $i_0 = 0°$.
Color scale goes from black ($a_0 = 1.5R_{\max}$) to red ($a_0 = 3R_{\max}$)

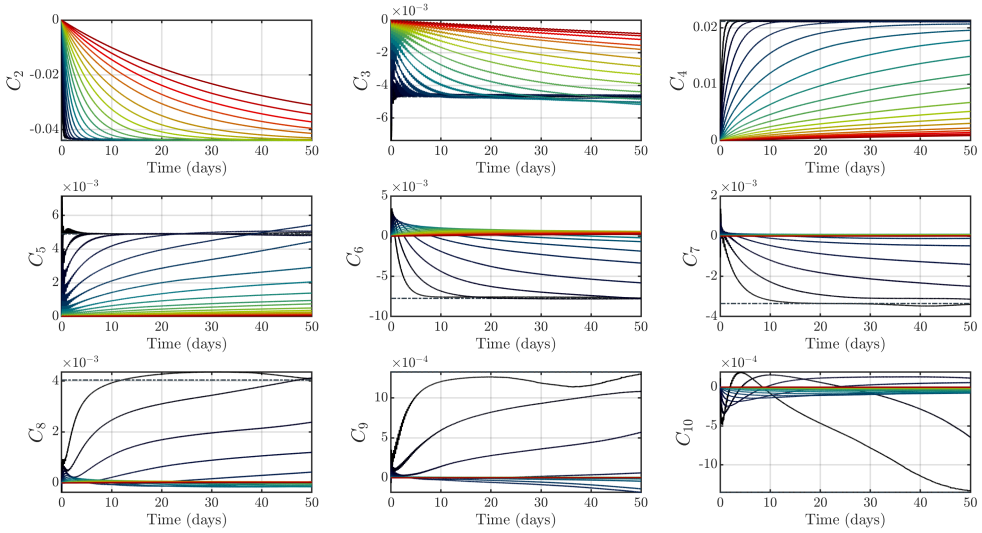

Figure 5.8: *Test 2* · Results with $i_0 = 60°$.
Color scale goes from black ($a_0 = 1.5R_{\max}$) to red ($a_0 = 3R_{\max}$)

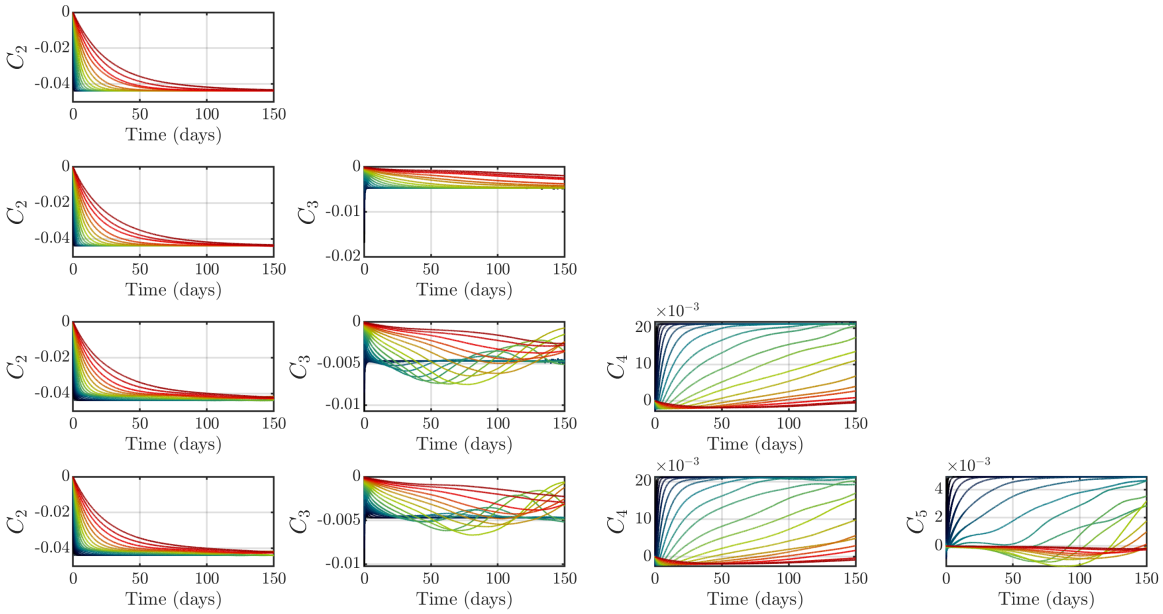

Figure 5.9: *Test 2* · Results parametrized for the number of Stokes coefficients. Color scale goes from black ($a_0 = 1.5R_{\max}$) to red ($a_0 = 3R_{\max}$)

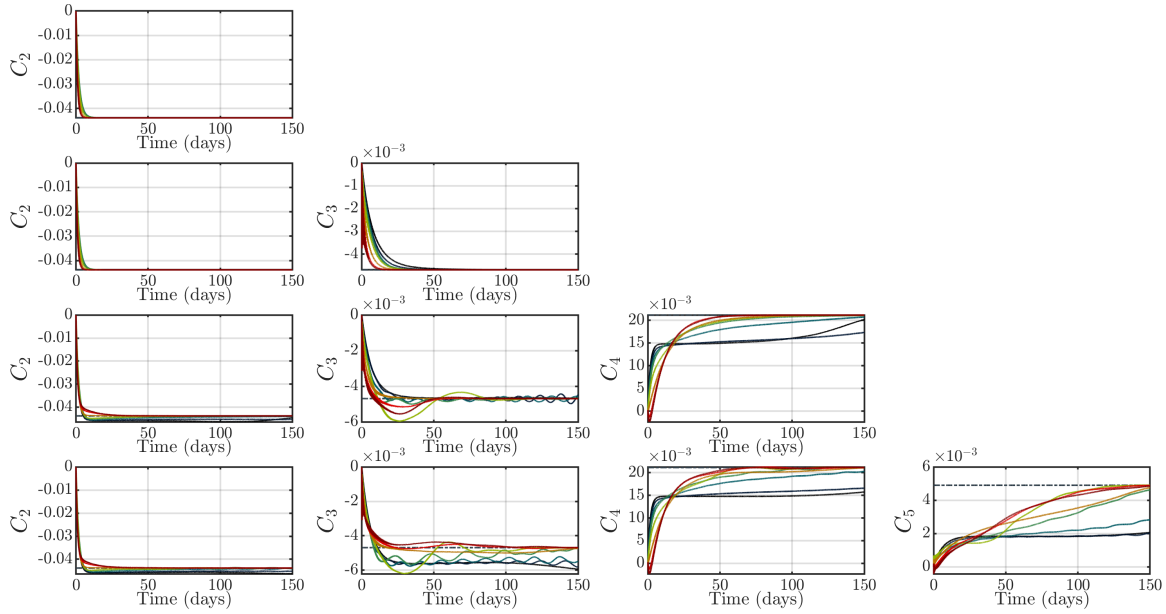

Figure 5.10: *Test 3* · Results parametrized for the number of Stokes coefficients. Color scale goes from black ($i_0 = 0°$) to red ($i_0 = 90°$)

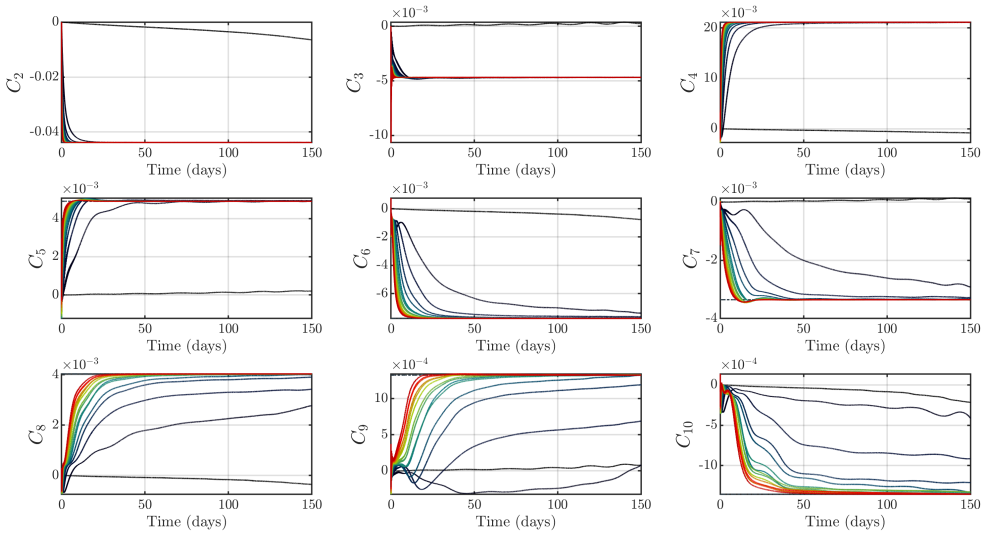

Figure 5.11: *Test 4* · Results.
Color scale goes from black ($\alpha = 1$) to red ($\alpha = 1\mathrm{e}+4$)

Then the results shown in Figure 5.10 can be read in several ways:

(T3.1) The convergence of the low degree coefficients, in particular C_2 and C_3 does not show a strong dependence on the inclination;

(T3.2) In general, the network convergence do depends on i_0 and the number of coefficients to be estimated;

(T3.3) Higher order coefficients associated with small i_0 suffer a bias error. This error decreases as far as i_0 gets larger.

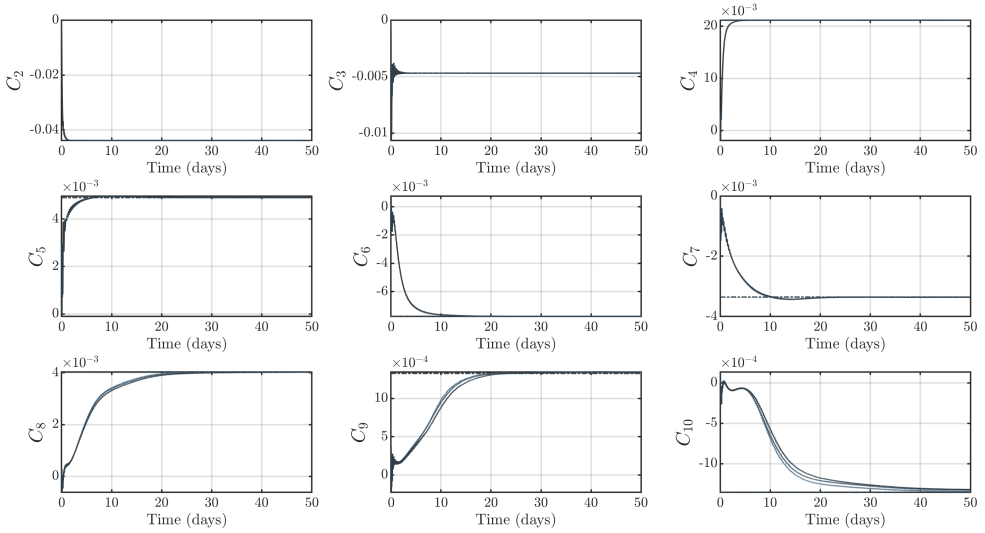

Figure 5.12: *Test 5* · Results.

Test 4. In this case the value of $\beta = 1$, $a_0 = 1.5R_{\max}$ and $i_0 = 90°$ while effect of the variation of $\alpha \in [1, 1e+4]$ are analysed. The results in Figure 5.11 show a increase in the convergence speed as far as α gets larger. Also in that case, as it was for *test 1*, it is possible to make the network unstable, if the value of α is chosen too large.

Test 5. The previous tests underline that the variation of both the parameters α and β strongly influence the convergence rate. So in this test a series of combinations of those parameters is analysed in order to understand how they affect the performances of the network. In particular $\alpha = \{1e4, 1e2, 1\}$ and $\beta = \{1, 1e-2, 1e-4\}$. Results are shown in Figure 5.12: as one can see, the behaviour is quite similar in all the cases, so we can conclude that the effect of the changes in α or β are mostly equivalent with respect to the performances of the network.

Recall that in this chapter all the results are shown in the particular case of KW4-α, so they're not general at all but the global behaviour of the network in case of the analysis of a rounded body can be extracted.

5.1 On the tuning of the MHNN

As underlined in the previous paragraphs, the tuning of β is essential to have a fast and accurate response of the network. In this section is presented a brief discussion on how it has to be tuned in cases different with respect to the axisymmetric one presented in the chapter. In general, assume that:

$$\beta = \beta(\mu, r) \tag{5.3}$$

Note also that:

$$\mu = GM = G\varrho V \tag{5.4}$$

So that:

$$\beta = \beta(M, r) = \beta(\varrho, R_0, r) \tag{5.5}$$

Since there is a strong correlation between the mission scenario and the tuning of the network, assume a simple oblate spheroid. In this case:

$$V = \frac{4}{3}\pi R_x^2 R_z \rightarrow \frac{V}{R_x^3} = \frac{4}{3}\pi p_x^2 p_z \tag{5.6}$$

So that in general one would expect:

$$\beta = \beta(\varrho, R_0, p_x, p_z, a, i) \tag{5.7}$$

The choice of the spheroid is made since in that case there is no dependence on the ascending node position and so on Ω and ω. Moreover, from the analysis of the previous results, the inclination of the orbit is setted to be 90°, since zonal harmonics have to be estimated. So, β results:

$$\beta = \beta\left(\varrho, R_x, a\right) \tag{5.8}$$

since here one can assume $R_z = p_{xz} R_x$. Note that from those considerations it results that β is, for sure, non-linearly coupled with its variables. This can be seen, for

example from the fact that the volume of the body $V \propto \varrho R_x^3$ so that the gravitational parameter varies linearly with ϱ and cubically with the body dimensions, and so does the gravitational attraction, at a fixed distance from the body. So, in general, at a fixed ϱ, in case of a spherical body $p_{xz} = 1$, the point mass gravity exhibit the behaviour presented in Figure 5.13. In general, a dependence of β on the mass of the body is

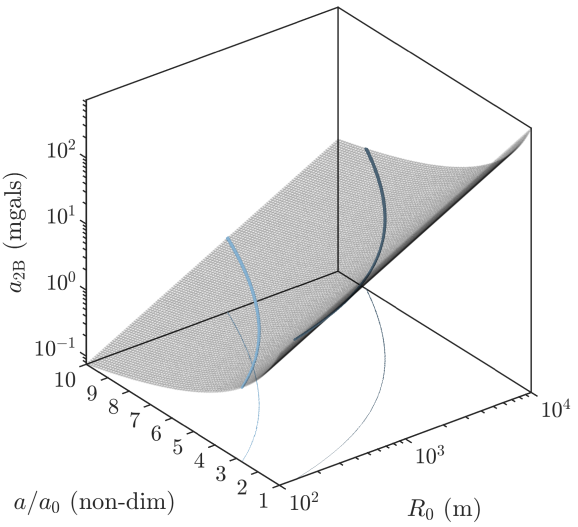

Figure 5.13: g values with $\varrho = 2700$ kg/m^3.

something expected as well as the fact that the higher the gravitational force will be the higher/faster the response of the network. This is something expected since the state of the network $\mathbf{p}$, at each time step, is weighted by $\mathbb{W}$ that being constructed from $\mathbb{A}$ results to be $\propto \mu^2/r^4$.

In fact, even in the case the activation function is not too steep ($\beta \geq 1$), which operatively means that $\mathbf{s} \approx \mathbf{p}$, then assuming that the n-th zonal term potential can be written as $\mathcal{U}_n = \frac{\mu}{r} u_n(x, y, z)$, then the neuron signal results amplified by a factor that $\propto \mu/r^2 = g$ where the proportionality is given by a term $u_{nn}^2 \leq 1$. So the higher the accelerations the more responsive the network should be.

Figure 5.13, however, can be read in several different ways:

1. One can enter with R_0 (so with the mass) and can built a function $g(\bar{a})$
2. One can enter with g and so built a relation between $\bar{a}$ and R_0 (so a correlation orbit-mass with the same g values). This second way seems to be more interesting for this tests since I would expect that the network will behave in the same way for different bodies/orbit couples having the same g values. From the plot in Figure 5.13, in fact we could extract curves $\bar{a} = f(R_0)$. This, by using the simple point mass relation $g = \frac{\mu}{a^2}$ lead to the following result:

$$\bar{a} = \frac{a}{R_0} = \frac{0.2067 \varrho^{1/3}}{\sqrt{g}} \mu^{1/6} = 0.005285 \sqrt{\frac{\varrho R_0}{g}} = C_g \sqrt{\frac{\varrho R_0}{g}} \tag{5.9}$$

where here the constant C_g is computed as:

$$C_g = \sqrt{\frac{4}{3}\pi G \cdot 10^5} \tag{5.10}$$

Since g is considered to be in mgals.

The previous results and considerations can be extended to an oblate spheroid. For this study, consider $p_{xz} \neq 0$. In that case the expression for $\bar{a}$ is equal while the C_g results:

$$C_g = \sqrt{\frac{4}{3}\pi G p_{xz} \cdot 10^5} \tag{5.11}$$

So now we have a simple tool to be used to generate normalized semi-major axis at fixed g, varying the principal physical properties of the body i. e., dimensions and density. This is a fundamental tool to be exploited since

Operative $\beta(\mu, r)$ dependence. From the operative point of view, the dependence of β on the body as well as on the orbit can be easily shown considering the case in which μ or r are fixed. In the case of the simple spheroid, $r \to a$ so that either μ or a have to be fixed, assuming $i = 90°$. If a $1.5R_x$ orbit is selected as well as $\beta = 1e-3$, as

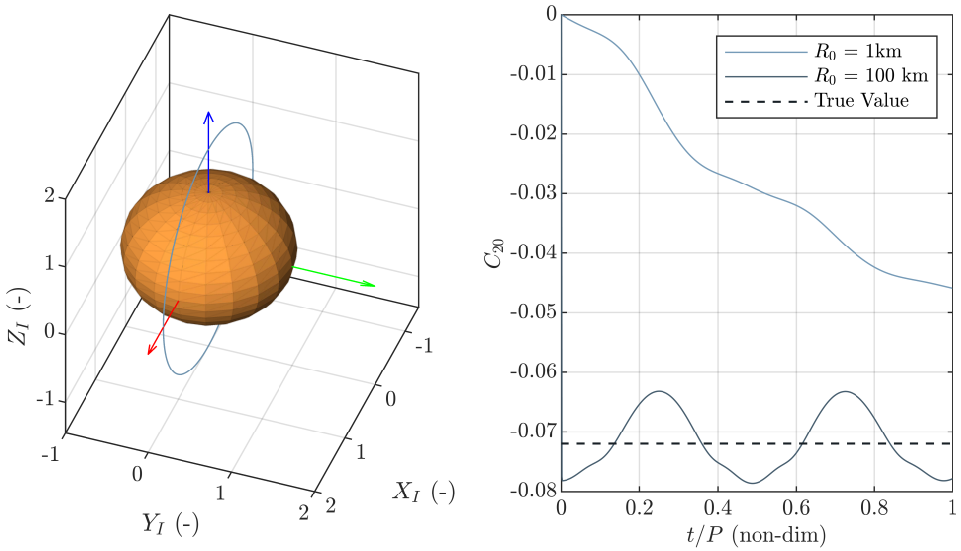

Figure 5.14: $\beta(\mu)$ dependence example in the C_{20} identification.

a guess, then the dependence on μ is clear from Figure 5.14. Similarly, keeping fixed β and increasing a we expect slower response of the network.

Fixed-g analysis. From the network formulation presented in Chapter 4 it is clear that the principal informations that enters the network are accelerations. In this chapter, in fact, it was pointed out that the network barely solve an optimization problem with cost function (and so Lyapunov function):

$$\mathcal{J} = V = -\frac{1}{2}\mathbf{s}^T\mathbb{A}^T\mathbb{A}\mathbf{s} + \mathbf{s}^T\mathbb{A}^T\mathbf{y} + \mathcal{O}(\mathbf{y}^2) \tag{5.12}$$

In particular, a major point was that the linear gradient form of the network simplified the formulation. In this case consider the fact that the parameters to be estimated are always <1. The network parameter α is setted to be 1. It results that the MHNN formulation results:

$$\frac{d\mathbf{s}}{dt} = \frac{1}{\beta}\text{diag}\left\{1 - \mathbf{s}_i^2\right\}\nabla V \tag{5.13}$$

Now consider the case of the identification of a single term, recalling that $\mathbb{A} \propto g$:

$$\nabla V = -\mathbb{A}^T\mathbb{A}s + \mathbb{A}^T y \propto -g^2\mathbf{s} + g\mathbf{y} \propto -g^2 s + g\partial g \tag{5.14}$$

Resulting in:

$$\frac{ds}{dt} \propto \frac{g^2}{\beta}(1 - s^2)\left(s - \frac{\partial g}{g}\right) \tag{5.15}$$

But, more in details:

$$\frac{\partial g}{g} \propto \frac{\nabla U_n}{g} \propto \bar{a}^n \rightarrow \frac{\partial g}{g} = f(\mu, n) \tag{5.16}$$

So that the temporal behaviour of $s(t)$, even in the case of fixed g results to be dependant, in some way, on the inertial properties of the body and so on its mass. Moreover, this dependence seems to be non-linear with respect to the problem parameters.

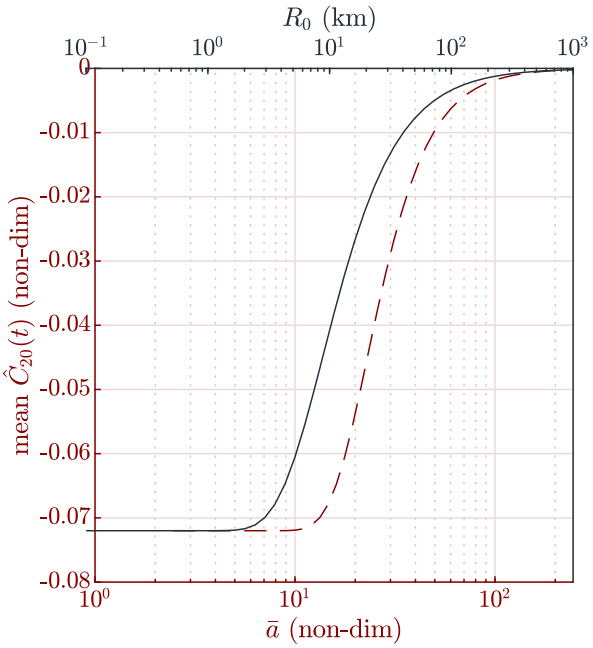

Figure 5.15: MHNN convergence in function of $\bar{a}$ (or R_0), β = 1e-9.

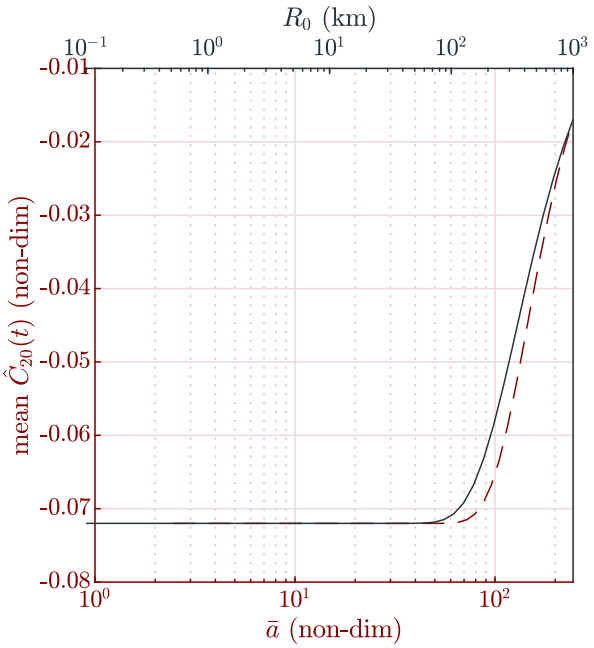

Figure 5.16: MHNN convergence in function of $\bar{a}$ (or R_0), β = 1e-10.

In Figure 5.15 and Figure 5.16 the results of the mean identified coefficient C_{20} in the case $g = 1$ (mgal), $\varrho = 2700$ kg/m^3 and $p_{xz} = 0.8$ are presented for two different value of β. This test is a *model matching* one since the gravity field of the body is assumed to be a SHE of the 2$^{\text{nd}}$ degree and the network estimates only the associated coefficient. The convergence to the real value of C_{20}, at fixed g appears to be independent on $\bar{a}$ (or μ or R_0) for a fraction of them. But it is also evident that the correct tuning of β can lead to basically a μ-independent behaviour at fixed g. In fact, if β is optimally setted to 1e-12 then the network converges for all the values of $\bar{a}$ or R_0 within the selected

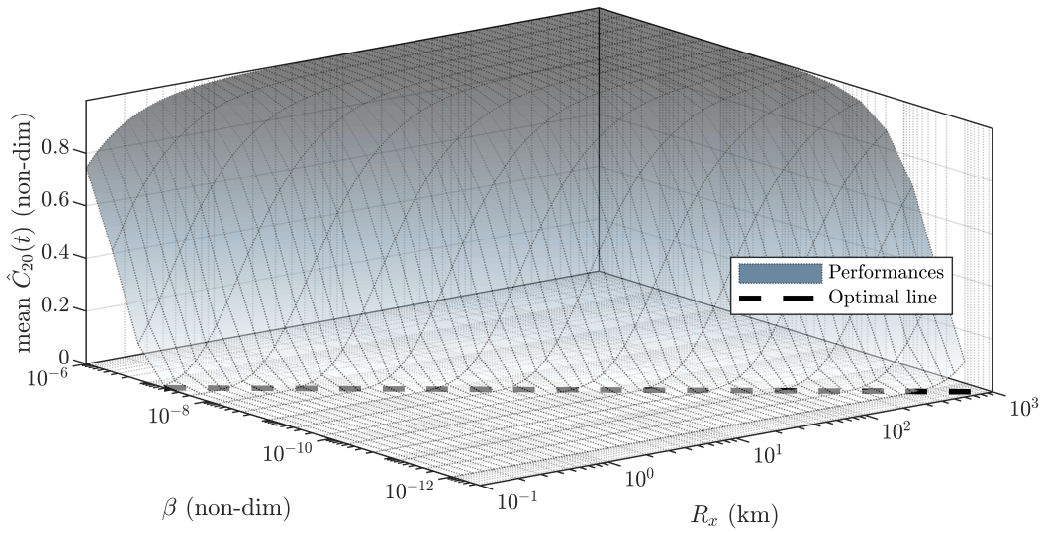

Figure 5.17: Normalized mean value error for the 1 mgals case.

range to the exact solution. This dependence is further analysed in Figure 5.17 where the results for the optimal β tuning is addressed. The minimization process is based on the mean value of the identified coefficient $\hat{C}$:

$$\mathcal{J}(\beta) = \text{mean}\,\hat{C}(t) = \int_T \hat{C}(\beta, \tau)\, d\tau \tag{5.17}$$

where here the integral do depend on the choice of β. The optimal line, so, can be written as a function $\beta = \beta(R_x)$. This can be traduced to a function $\beta(\mu)$ for a network working at fixed g value. So:

1. β do depends on the mass of the body even in the fixed g case.
2. A choice of a small β, say 1e-12, can basically eliminate the dependence on the mass *but* it should be recalled that in this case a single-coefficient model matching example is presented. So in real applications a β that is too small can lead to instability of the network. This can be avoided by putting a "margin" on the choice of β in such a way instability are avoided, but lowering the network convergence velocity.
3. In general, $\beta(R_x) = a_1 R_x^{a_2}$ results to be a good interpolation for this case, where a_1 and a_2 do depends on the g level. For example in the case $g = 1$ mgals, $a_1 = 2.5e-9$ and $a_2 = -1.25$ while for the case $g = 10$ mgals, $a_1 = 4.6e-6$ and $a_2 = -1.527$ and for the case $g = 50$ mgals, $a_1 = 3e-2$ and $a_2 = -1.58$.
4. The dependence $a_1(g)$ and $a_2(g)$ can be also extracted. In particular, interpolating previous results, $a_2 = a_3 g^{a_4} + a_5$ while $a_1 = a_6 g^{a_7}$, so that $a_3 = 0.3595$, $a_4 = -0.6394$, $a_5 = -1.609$, $a_6 = 1.4e-8$ and $a_7 = 3.716$.

From the previous analysis *trends* of the results are more important that the results them-self. In fact:

$$\beta(R_x, g) = a_1(g) R_x^{a_2(g)} = 1.4e-8 \cdot g^{3.716} R_x^{0.36 g^{-0.64} - 1.6} \propto 1.5e-8 \cdot g^4 \cdot R_x^{-n(g)} \tag{5.18}$$

where here $n(g) \sim 1$. So the function $\beta(R_x, g)$ can be used to have an idea of the correct order of magnitude of β in function of the mass/the dimensions of the body (R_x) as well as of the orbit (g). Of course this function is built for a simple slightly-oblate body so that a more detailed analysis is needed in case of more complex shapes.

As an example, the tuning of a model-matching network for oblate spheroids is addressed through a Montecarlo optimization coupled with an optimization. In particular the Montecarlo is performed over the parameters $\alpha = \beta$ of the spheroid always keeping them $> \gamma$ and on the density ϱ. The optimization, instead have the objective function defined before, $\mathcal{J}(\beta)$. The coefficient C_{20} is identified though a polar orbit.

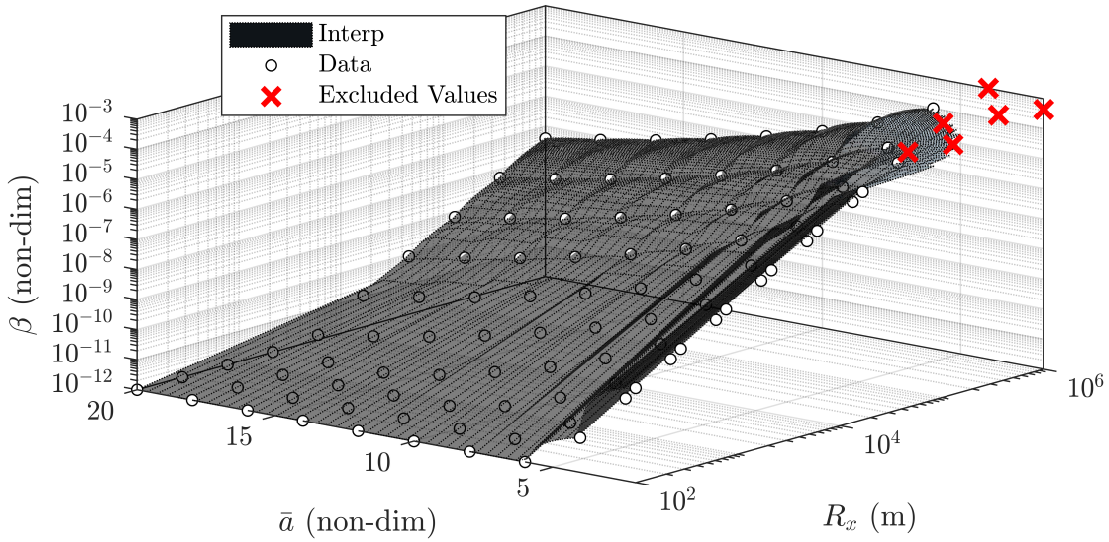

Figure 5.18: Montecarlo β optimum.

The results for this specific analysis are presented in Figure 5.18. Note that there are some *excluded values*: those values are the one which the identification does not converge within one period. Note, also, that these results have to be seen in an *indicative* way: they're not general at all, but can be used to generate a good first guess for β.

5.2 Adaptive learning with gradient descent method

Another approach, based on gradient descent method is presented here. Gradient descent is a first-order iterative optimization algorithm for finding the minimum of a function. To find a local minimum of a function using gradient descent, one takes steps proportional to the negative of the gradient (or approximate gradient) of the function at the current point. So the idea is to find a way to relate the a relative change on β to the convergence of the network. To do so, consider a simple network with only one neuron and the hyper-parameter $\alpha = 1$. According to Eq. (4.13), the neuron dynamics can be written as:

$$\dot{s} = \frac{ds}{dt} = \frac{1}{\beta}(1 - s^2)(Ws - b) \tag{5.19}$$

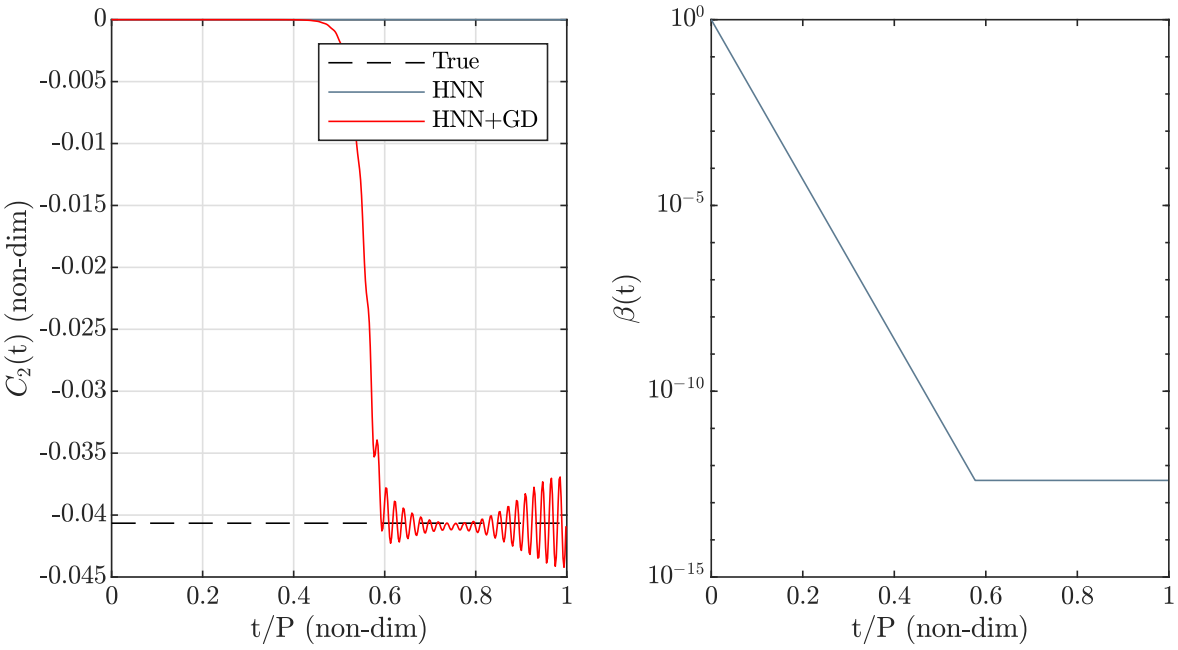

Figure 5.19: Adaptive MHNN vs MHNN.

where W and b are the weight and bias matrices and are associated with the actual orbital state. Let us call $\dot{s}$ the *neuron state velocity*. Now:

$$\frac{\partial \dot{s}}{\partial \beta} = -\frac{1}{\beta^2}(1-s^2)(Ws-b) \tag{5.20}$$

Then β changes as a function of the neuron state velocity as:

$$\frac{\partial \beta}{\partial \dot{s}} = -\frac{\beta^2}{(1-s^2)(Ws-b)} = \frac{\partial \beta}{\partial s}\partial t \approx \frac{\beta_{k+1}-\beta_k}{s_{k+1}-s_k}h \tag{5.21}$$

Now assuming γ small (<1) and positive,

$$\beta_{k+1} = \beta_n + \gamma\frac{s_{k+1}-s_k}{h}\frac{\partial \beta}{\partial \dot{s}} = \beta_k - \gamma\left|\frac{s_{k+1}-s_k}{h}\frac{\beta_k^2}{(1-s_k^2)(Ws_k-b)}\right| \tag{5.22}$$

Note that here the coefficient γ has been introduced to rescale the gradient term i. e., to do not get unstable the method. Note also that this formulation is anti-proportional to the network convergence so that a stop criteria for the update of β is needed. In particular note that as far as s approach the true value of the parameter:

- $s_{k+1} - s_k$ is bounded and small;
- $1 - s_k^2 \simeq 1$, being $s_k \ll 1$ usually;
- $Ws_k - b$ is bounded and small too, being $\nabla\mathcal{V}$. Note that $Ws_k - b$ should be, in theory, negative. But due to the fact that there is not a exact matching between the real model and the reconstructed one, it can oscillate about zero, once the network is converged.

In Figure 5.19 the results for a sample-case identification of C_{20}. The central body is Bennu and a $\Gamma_{45}^{10R_{\max}}$ orbit is selected. β_0 is setted to be 1, assuming no previous knowledge of the body so that none of previous analysis can be used. The Gradient

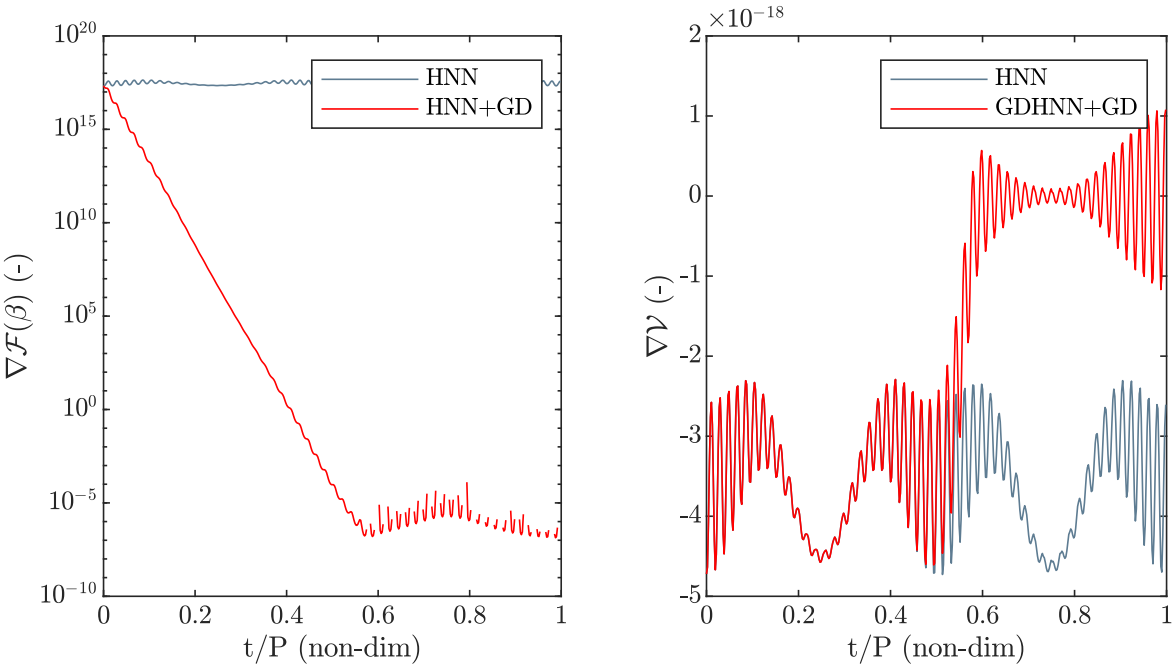

Figure 5.20: Adaptive MHNN vs MHNN: gradients convergence

Algorithm 1 GD-HNN simil-code.

Require: $\beta_0, s(0)$
for $k = 1, \ldots, n_{\text{steps}}$ **do**
  procedure BUILT HNN
    Here W_k, b_k are built: $net_k = W_k s_k - b_k$.
  end procedure
  if $|net_k| > \varepsilon$ **then**
    Update β_{k+1} with gradient-descent method.
  else
    Keep the same β i. e., $\beta_{k+1} = \beta_k$.
  end if
end for

Descent (GD) relaxation term γ is setted to 0.1 for this simulation. Figure 5.20, instead, show the behaviour of two important parameters for the performances evaluation:

1. $\nabla\mathcal{V}$ that in this case is simply $d\mathcal{V}/ds = Ws - b$: it should converge to zero when the network converges to the exact solution. In this case it oscillates since the model reconstructed does not match the real one. If, instead, a 2^{nd}-degree harmonics expansion is used as model for the propagation, instead, the Lyapunov theory result is confirmed, as it can be seen from Figure 5.21 and Figure 5.22.
2. $\nabla\mathcal{F}(\beta)$, that is all the term that multiply γ in the gradient formulation and it is associated to the network dynamics. At the end of the optimization (GD-based), it should converge to a small value, as it does.

Finally, a remark on the implementation of the adaptive algorithm is performed: as said before, since $Ws - b \to 0$, ideally the gradient term would become ∞. To avoid that, the algorithm is implemented as in Algorithm 1. $\varepsilon = 1e - 19$.

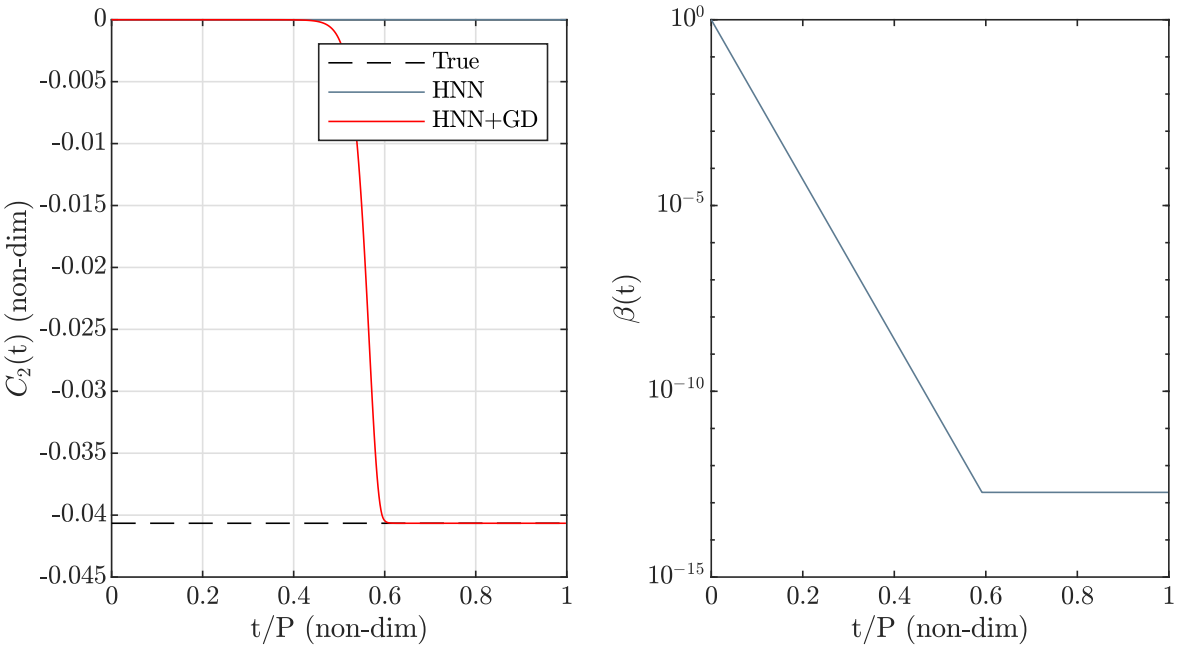

Figure 5.21: Adaptive MHNN vs MHNN: model matching case.

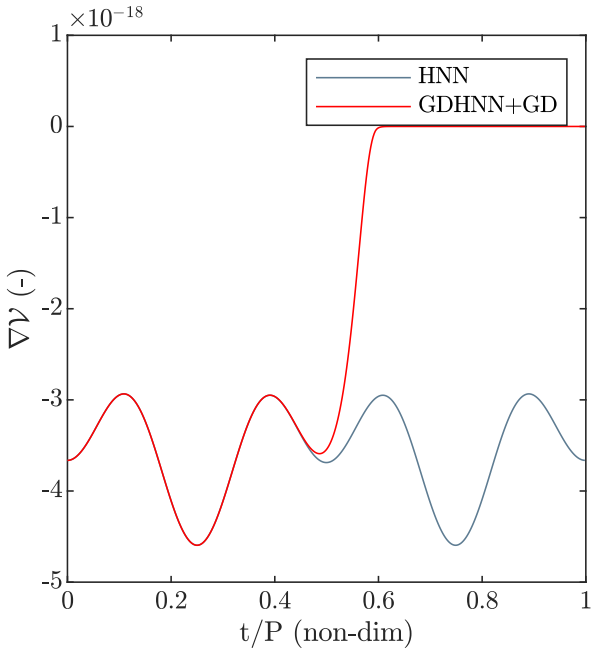

Figure 5.22: Adaptive MHNN vs MHNN: Lyapunov function gradient in the case of model matching.

CHAPTER 6

CONCEPTUAL MISSION DESIGN

In this chapter the conceptual design of a mission to an unknown or a partially know object is considered. One of the first things that scientific missions to small solar system bodies do is the to understand the dynamical environment of the body. This includes, at first, the determination or the refinement of mass, inertia and angular velocity vector of the body. Then a characterization of the gravitational field of the body. In this framework, this work proposes a new way to reconstruct on board an approximation of the gravitational field of the body with the aim to unload at the most the need to communicate to ground for instructions as well as to enhance the autonomy of the spacecraft.

From the conceptual point of view, the reconstruction of the gravitational field of the body through the use of a MHNN can be subdivided in 4 sub-phases:

(P.1) *2B-Identification* : in this phase the point mass model is being reconstructed. The MHNN, in fact, can be used to identified/refine the mass of the body.

(P.2) *Inspection*: in this phase the main objective is to reconstruct a guess of the lower degree coefficients to have an idea of both the shape of the body and to have a good initial guess of them for the next phases;

(P.3) *Identification*: in this phase the initial guesses are refined through the use of specific orbits. Also, higher degree coefficients can be included;

(P.4) *Refinement*: the main task of this phase is to refine some specific coefficients to increase the accuracy of the model.

It is obvious that such phases cannot be completely autonomous, but the use of the MHNN investigated in this work would can guarantee a much higher degree of autonomy.

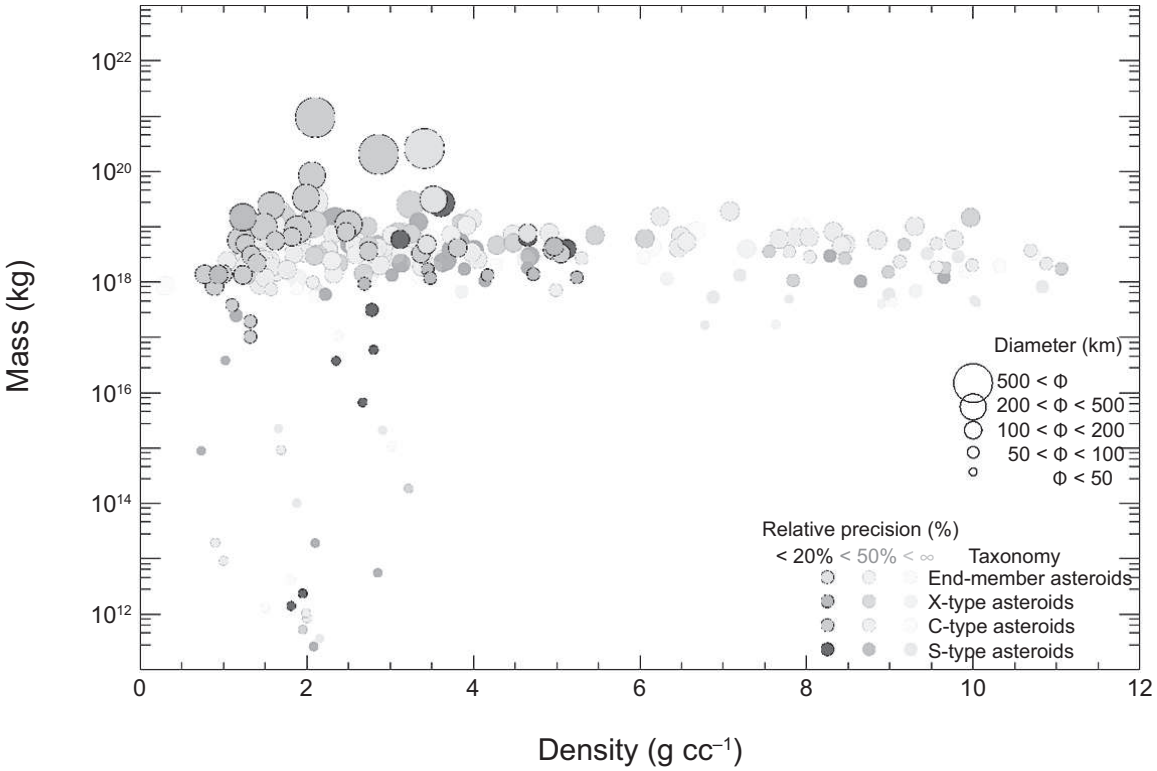

Figure 6.1: Mass and density estimates of asteroids. Symbol size represents asteroid diameter. The colour and contrast of the symbols represent taxonomy and measurement uncertainty, respectively S-type asteroids (red) are on average more dense (average: 2.7 g/cm^3) than C-type (grey, average: 1.3 g/cm^3). Average X-type: 1.85 g/cm^3. Credits [33].

Table 6.1: *Average density taxonomic classes where density determinations more accurate than 20% are available. Credits [33].*

Class	Density (g/cm^3)
S	2.72 ± 0.54
Sq	3.43 ± 0.20
C	1.33 ± 0.58
X	1.85 ± 0.81
Xc	4.86 ± 0.81
K	3.54 ± 0.21

In general, the shapes and the masses of minor bodies are different from body to body but two "major" families can be distinguished: convex and concave objects. Convex objects can be approximated by spheres, ellipsoids and tri-axial ellipsoids while those approximations gives poor results in case of concave ones (e. g., in case of highly irregular bodies). For this reason the spherical harmonic expansion of the body give better results in the case of convex objects (i. e., rounded bodies) with respect to the case of concave ones, as explained before. For this reason, the design of a conceptual mission about a rounded/convex object is considered and parametric analysis are performed on tri-axial ellipsoid shaped bodies. To do so, first a correlation between the mass and the density of the body is extracted from Figure 6.1: in Table 6.1 the resulting class-density correlation.

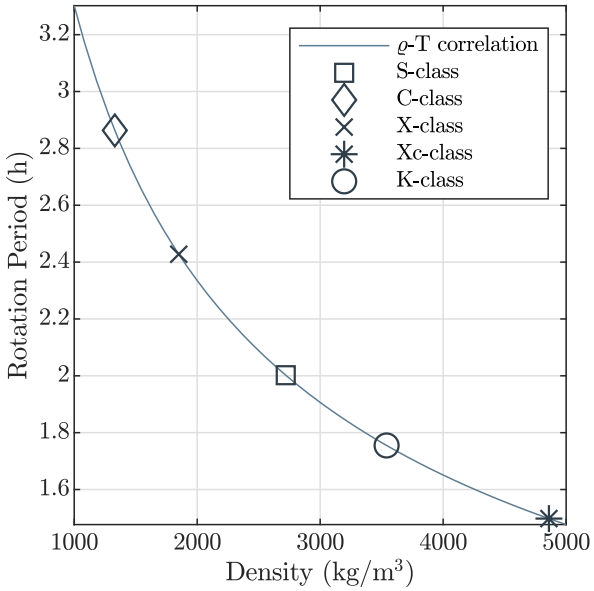

Figure 6.2: ϱ-period correlation for the limit spin rate.

For what regards the asteroid rotation, instead, the limit spin rate ω_s is given by [33]:

$$\omega_s = \sqrt{\frac{4\pi G\varrho}{3}} \tag{6.1}$$

where G is the gravitational constant and ϱ the bulk density of the body. This limit is essentially the spin rate at which internal tensile stresses would be present within a spherical, constant density object (the actual spin rate for a body also depends strongly on its elongation). This spin rate also corresponds to local circular speed at the surface of the body, at which centrifugal forces equal the gravitational attraction of the body. In Figure 6.2 the resulting limit spin rate for the various classes.

6.1 2B-Identification Phase

The first phase of such conceptual mission is associated to the refinement of the point-mass model. To do so, the LIP form of the network results in:

$$\mathbf{y} = \left(-\frac{\mathbf{r}}{r^3}\right) \cdot \mathrm{GM} \tag{6.2}$$

6.1.1 Model-matching of spherical bodies

In this case, to simplify the analysis as well as to obtain significant results the analysis of the 2B-IP are referred to the model matching of the gravitational parameter GM. Here with *model matching* we refer to the reconstruction of the exact dynamical model, not on the identification of an approximation of it. In particular we refer to the capability of the network to match exactly a dynamical model. So, in this case, the central body is modelled as a spherical mass with radius R_0 and density ϱ in such a way the model on the base of the matching is the R2BP. The combination (R_0, ϱ) can be then associate at Figure 6.1 and so to observed objects.

If the MHNN is used to identify a object that is assumed to be unknown e. g., initializing the network from zero, the identification is extremely fast ($\sim$ seconds, at most minutes) if the network is correctly tuned. Recall that since it can be that GM > 1, then the network parameters (α, β) must be carefully chosen. In particular, α must be chosen $>$ 1 otherwise the network will converge to its fixed points (± 1) if GM > 1: the network should be tuned is such a way $\alpha \geq$ GM. Now in order to analyse the convergence, a *time parameter* τ_m is defined:

$$\tau_m = t_{\text{cv}} \sqrt{\frac{GM}{R_0^3}} \tag{6.3}$$

Where here t_{cv} is defined as the time at which the mass error, defined as

$$e_m(t) = \frac{|\hat{M}(t) - M|}{M} \tag{6.4}$$

is less than a certain threshold ε_m e. g., $e_m(t_{\text{cv}}) \leq \varepsilon_m$. Here, with M is denoted the true mass value while with $\hat{M}(t)$ its reconstruction. In the case of optimized model matching, the convergence is monotonic so that $e_m(t) \to 0$ from above. Note also that:

$$\tau_m^* = \frac{T}{t_{\text{cv}}} \tau_m = 2\pi \left(\frac{a_0}{R_0} \right)^{3/2} = 2\pi \bar{a}_0^{3/2} \tag{6.5}$$

This quantity is of interest because correlates the semimajor-axis of the orbit with the expected performances of the network. In the model matching case, it remains constant because the orbit is *not* perturbed while in real cases can be used as a parameter of merit: the more it diverges from its initial value, the more the orbit is perturbed.

By setting the network with $\alpha = 10^{\log(2R_0)}$ and $\beta = 1e-7$, one can obtain the performance presented in Figure 6.3. In this case $\varepsilon_m = 1e-8$. From that results, then, some considerations can be extracted:

1. In *model matching*, the network is extremely fast (as it has been pointed-out also in previous chapters);
2. There is a correlation between the network performances e. g., the time parameter, and the shape/mass of the body;
3. τ_m increases with the sphere radius, R_0;
4. τ_m increases with the density, ϱ;
5. τ_m increases with a_0 for a fixed couple (R_0, ϱ).

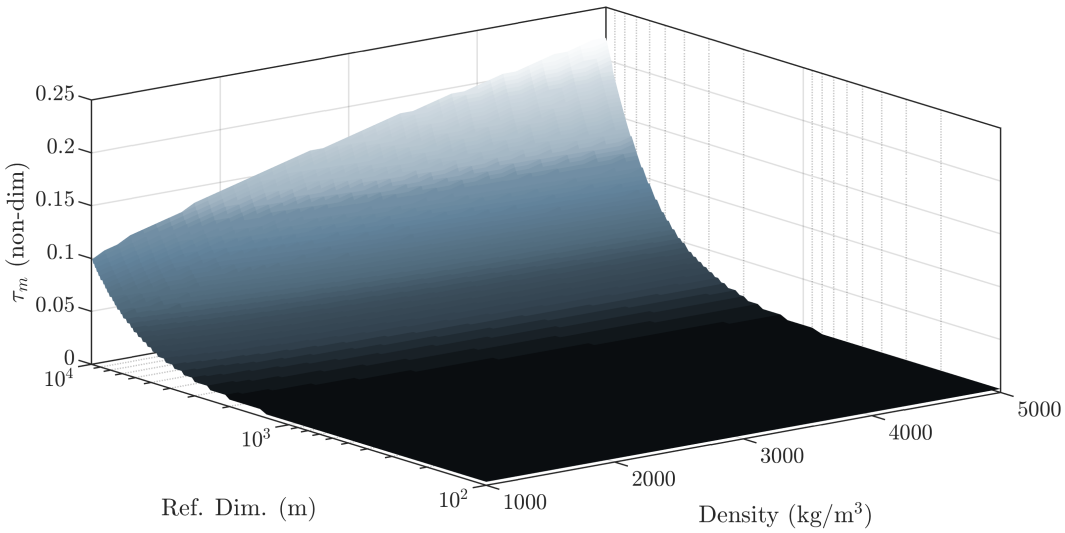

Figure 6.3: $\tau_m(\varrho, R_0)$ correlation for a $\Gamma_0^{3\mathrm{R}_{\max}}$ orbit about a sphere.

6.1.2 Oblate-prolate ellipsoid model identification

The simple case of an oblate-prolate spheroid is useful to understand how the network behaves in the identification of the mass in case the perturbations to the spherical shape becomes relevant. In this case, since t_{cv} cannot be defined in an unique way, the parameter of merit is:

$$\bar{e}_m = \frac{1}{T^*} \int_0^{T^*} e_m(\tau)\, d\tau \tag{6.6}$$

In this case $T^* = 0.8T_{\max}$, where $T_{\max} = T/10$. The oblate spheroid is defined through

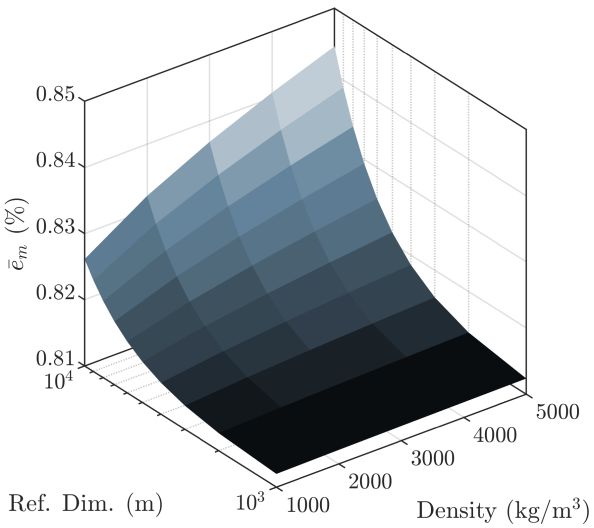

Figure 6.4: $\bar{e}_m(\varrho, R_0)$ correlation for a $\Gamma_0^{3\mathrm{R}_{\max}}$ orbit about an oblate spheroid.

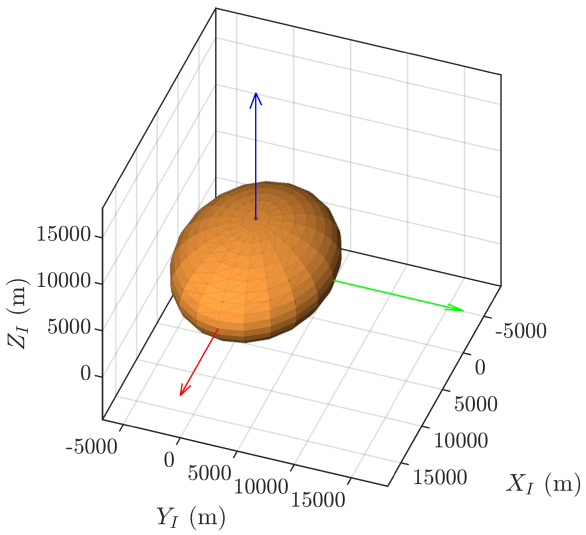

Figure 6.5: Oblate ellipsoid model.

$\chi_\alpha = 1$, $\chi_\beta = 0.75$ and $\chi_\gamma = 0.5$, where $\chi = l/R_0$ and l are the axis of the ellipsoids.

The prolate spheroid is defined, instead, as $\chi_\alpha = 0.5$, $\chi_\beta = 0.75$ and $\chi_\gamma = 1$. Then

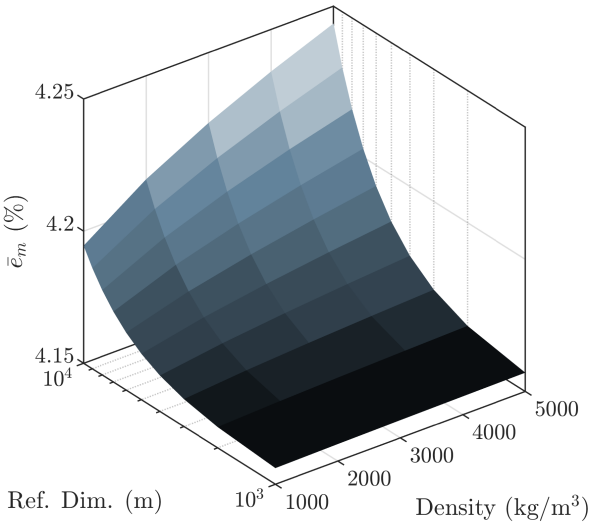

Figure 6.6: $\bar{e}_m(\varrho, R_0)$ correlation for a $\Gamma_0^{3\mathrm{R}_{\max}}$ orbit about a prolate spheroid.

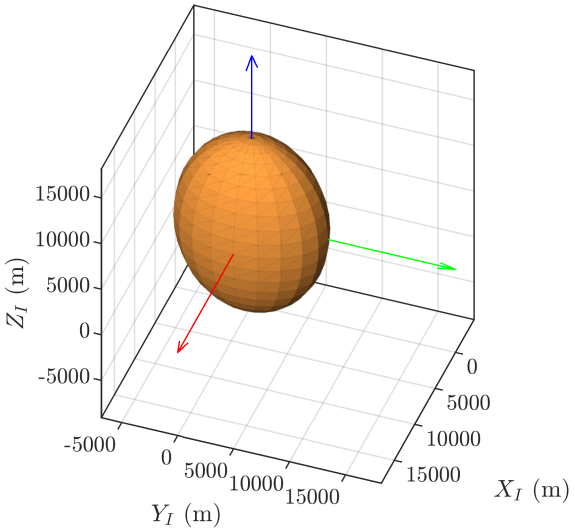

Figure 6.7: Prolate ellipsoid model.

for those cases there are differences in the identification of the mass of the body if it is considered to be oblate or prolate. However, the error express a similar dependence on ρ and R_0, meaning that the behaviour of the network is basically independent on the body shape in absolute terms.

6.2 Inspection/Identification Phase

An inspection phase can be thought to be the first step in the characterization of the gravitational field of the body. In general, scientific missions to asteroid are rich of sensors so that even in the approach to the body an estimation of the shape and rotational dynamics of it is available.

If those informations are not available one should remember that, in this phase, due to the distances to the body its the gravity field is really close to the one of a point mass i. e., the perturbations are small. Then the MHNN can be used to reconstruct at first the 2-body gravity and then, among the others, low degree harmonics, that are the only that can be seen from the dynamical point of view. Note that the a first (rough) information of the shape of the body can be identified using the tri-axial ellipsoid model only later. In this case, in fact, it is possible to relate analytically the semi-axis α, β, γ to the zonal and sectorial harmonics associated. In particular, in Chapter 2.4 on page 47 some non-linear relation $C_{ij} = C_{ij}(\alpha, \beta, \gamma)$ were presented. So having identified 3 among those coefficients it is possible to recover the semi-axis of the ellipsoid. This information, in case the body is an oblate/prolate spheroid (as in the case of Bennu, KW4-α) or have a elliptical shape (as in the case of Itokawa) is a good approximation of the true shape of the body.

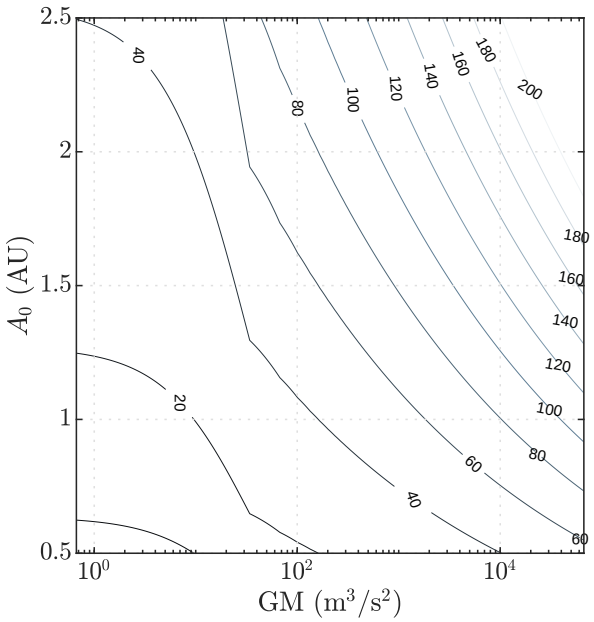

Figure 6.8: SRP order of magnitude analysis with $\varrho = 2200$ kg/m^3 and $C(0.1, 20)$.

6.2.1 Distant body-centred orbits

There are some different ways through which the low degree harmonics can be reconstructed. One among the others is to use distant body-centred orbits. They can be built according to the P2BP but in this case the perturbations coming from the Sun becomes comparable to the main body ones, and is some cases, depending on the mass of the body, prevalent. For this reason the design of a body-centred orbit can be quite difficult and, in particular, the design of a stable orbit can result impossible.

To understand if the non-gravitational perturbations are comparable to the gravitational one a simple order of magnitude analysis is performed. Assuming Eq. (1.64) as the force model for the SRP, then it may be compared to the main body gravitational acceleration as:

$$\frac{\mu_{\text{body}}}{r^2} = \frac{C(\rho, B_{sc})}{A_0^2} \tag{6.7}$$

Where A_0 denotes the semi-major axis of the body orbit about the Sun. Then it is possible to compute the non dimensional radius at which the two accelerations becomes equal as:

$$\bar{r} = \frac{1}{R_{\max}} \sqrt{\frac{\mu_{\text{body}} A_0^2}{C(\rho, B_{sc})}} \tag{6.8}$$

If now, one assume that the body is spherical with radius $R = R_{\max}$ then:

$$R = \left(\frac{m}{\frac{4}{3}\pi \varrho} \right)^{1/3} \rightarrow \bar{r} = \left(\frac{4}{3}\pi \right)^{1/3} \sqrt{G} \cdot \left(\frac{1}{C(\rho, B_{sc})} \right)^{1/2} \cdot \varrho^{1/3} \cdot A_0 \cdot m^{1/6} \tag{6.9}$$

So basically if one among the density of the body ϱ, the distance of the body to the Sun A_0 and the mass of the body m increases then $\bar{r}$ increases, meaning that orbit closer to the body will be mainly driven by the body gravity field.

6.2.1.1 Oblate-spheroid case

An oblate spheroid is defined as a triaxial ellipsoid with $\chi_\alpha = \chi_\beta \neq (>)\chi_\gamma$. In the case of an oblate spheroid, only zonal harmonics are different from zero. In those simulations SRP and Sun 3BP is included.

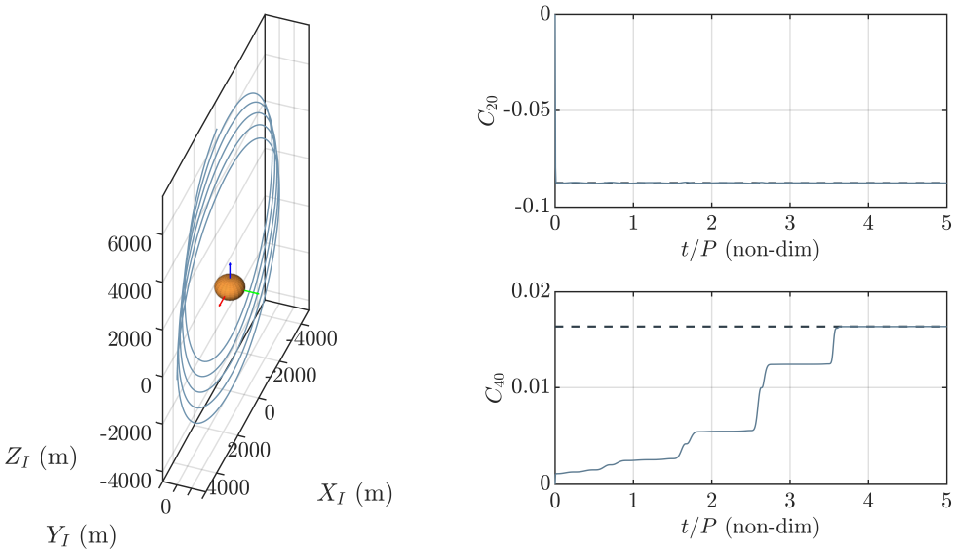

Figure 6.9: 2.5 AU, S-class oblate spheroidal body. $\Gamma_{90}^{10R_0}$ orbit, with R_0= 500 m, χ_γ = 0.75, $\chi_\alpha = \chi_\beta = 1$ and $C(0.1, 20)$. Network $\beta = 1e-12$.

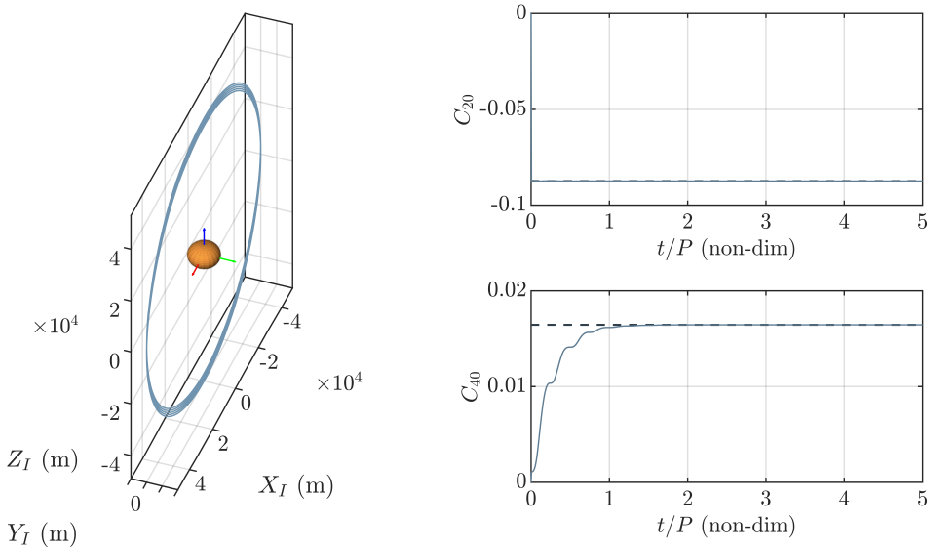

Figure 6.10: 2.5 AU, S-class oblate spheroidal body. $\Gamma_{90}^{10R_0}$ orbit, with R_0= 5 km, χ_γ = 0.75, $\chi_\alpha = \chi_\beta = 1$ and $C(0.1, 20)$. Network $\beta = 1e-12$.

In Figure 6.9 and Figure 6.10 the results for a S-class body (ϱ = 2700 kg/m^3) for two different values of R_0. Note that the convergence gets better in the second case: the network is faster in this case since the orbit is more stable as well as, being the

perturbations dependant on the mass m linearly and being $m \propto \varrho R_0^3$, the perturbation is stronger.

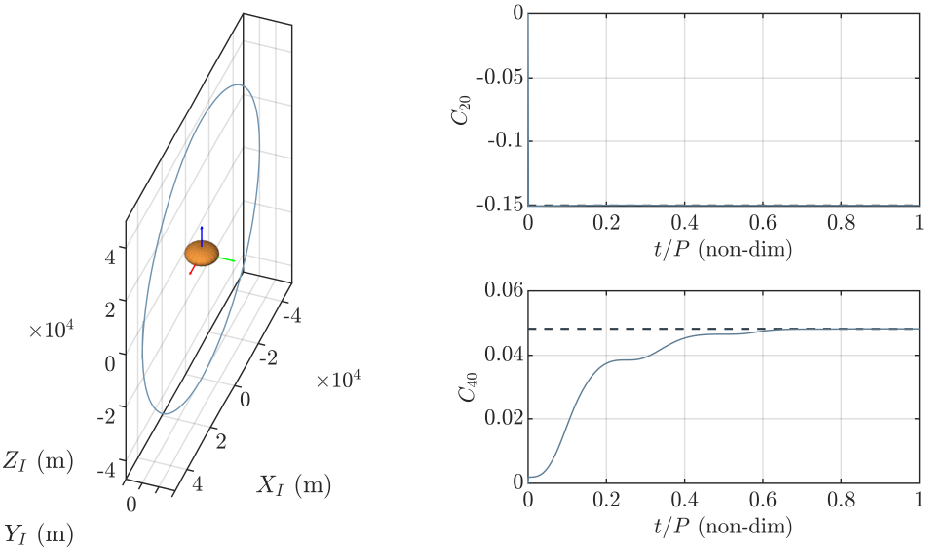

Figure 6.11: NEA (1 AU), Xc-class oblate spheroidal body. $\Gamma_{90}^{10R_0}$ orbit, with R_0= 5 km, $\chi_\gamma = 0.50$, $\chi_\alpha = \chi_\beta = 1$ and $C(0.1, 20)$. Network $\beta = 1e-12$.

6.2.1.2 Prolate-spheroid case

A prolate spheroid is defined as a triaxial ellipsoid with $\chi_\alpha = \chi_\beta \neq (<)\chi_\gamma$. In Fig-

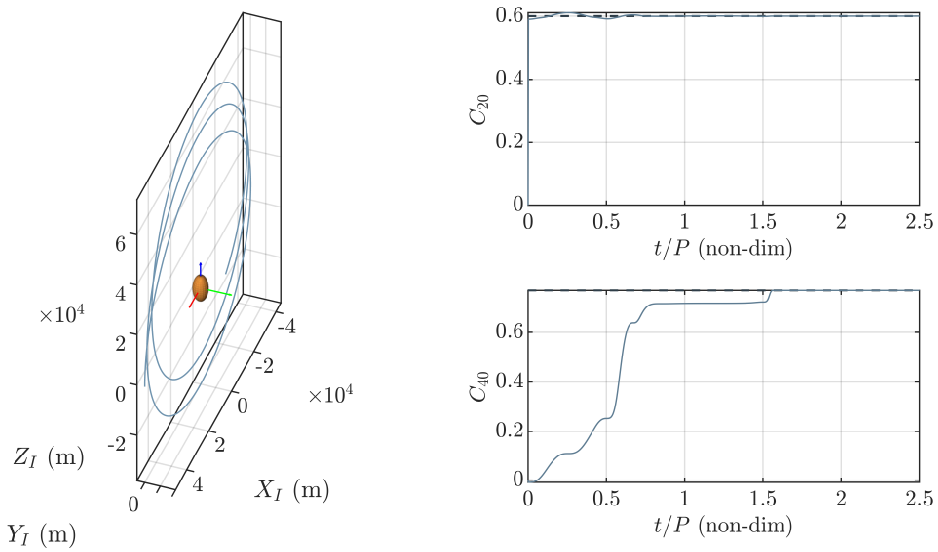

Figure 6.12: NEA (1 AU), S-class prolate spheroidal body. $\Gamma_{90}^{10R_0}$ orbit, with R_0= 5 km, $\chi_\gamma = 1$, $\chi_\alpha = \chi_\beta = 0.5$ and $C(0.1, 20)$. Network $\beta = 1e-12$.

ure 6.12 the results for a S-class body. It can be seen that the network convergence is not so different with respect to the oblate spheroid case.

6.2.1.3 Oblate/prolate-ellipsoid case

In this case oblate/prolate ellipsoids are built and the network convergence is studied.

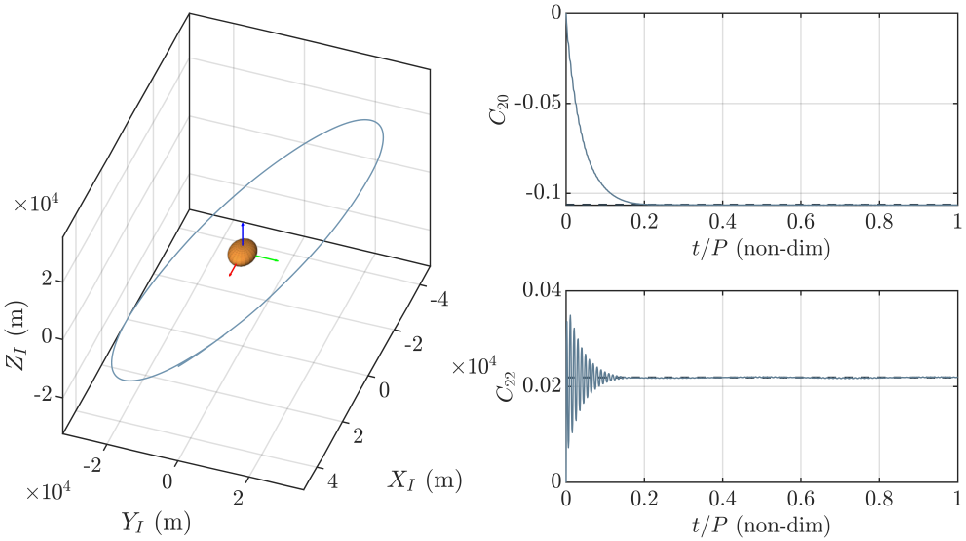

Figure 6.13: NEA (1 AU), Xc-class oblate spheroidal body. $\Gamma_{45}^{10R_0}$ orbit, with R_0= 5 km, $\chi_\alpha = 1$, χ_β =0.75 $\chi_\beta = 0.5$ and $C(0.1, 20)$. Network $\beta = 1e-9$.

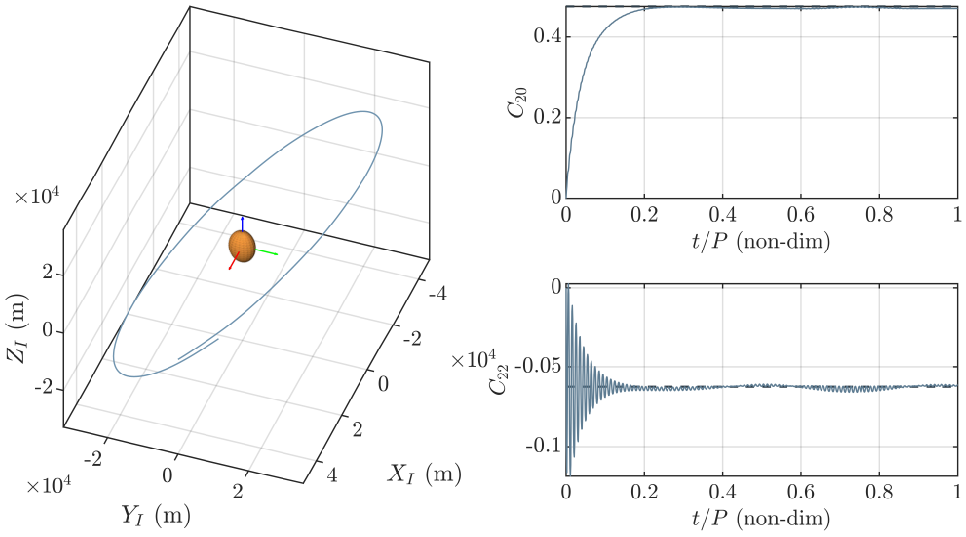

Figure 6.14: NEA (1 AU), Xc-class prolate spheroidal body. $\Gamma_{45}^{10R_0}$ orbit, with R_0= 5 km, $\chi_\alpha = 0.5$, χ_β =0.75 $\chi_\beta = 1$ and $C(0.1, 20)$. Network $\beta = 1e-9$.

In Figure 6.13 and Figure 6.14 the results for, respectively, an oblate and a prolate Xc-class body. The convergence is, also in this case, unchanged for low-degree harmonics. In Figure 6.15 and Figure 6.16 the results of a parametric analysis on χ_γ: the behaviour of the identification changes as far as ξ_β changes from 0.2 to 0.8: in the first case the body is almost always a prolate ellipsoid, being $\chi_\beta \leq \chi_\gamma < \chi_\alpha = 1$ while in the other case the body is almost always an oblate ellipsoid. However the performances of the

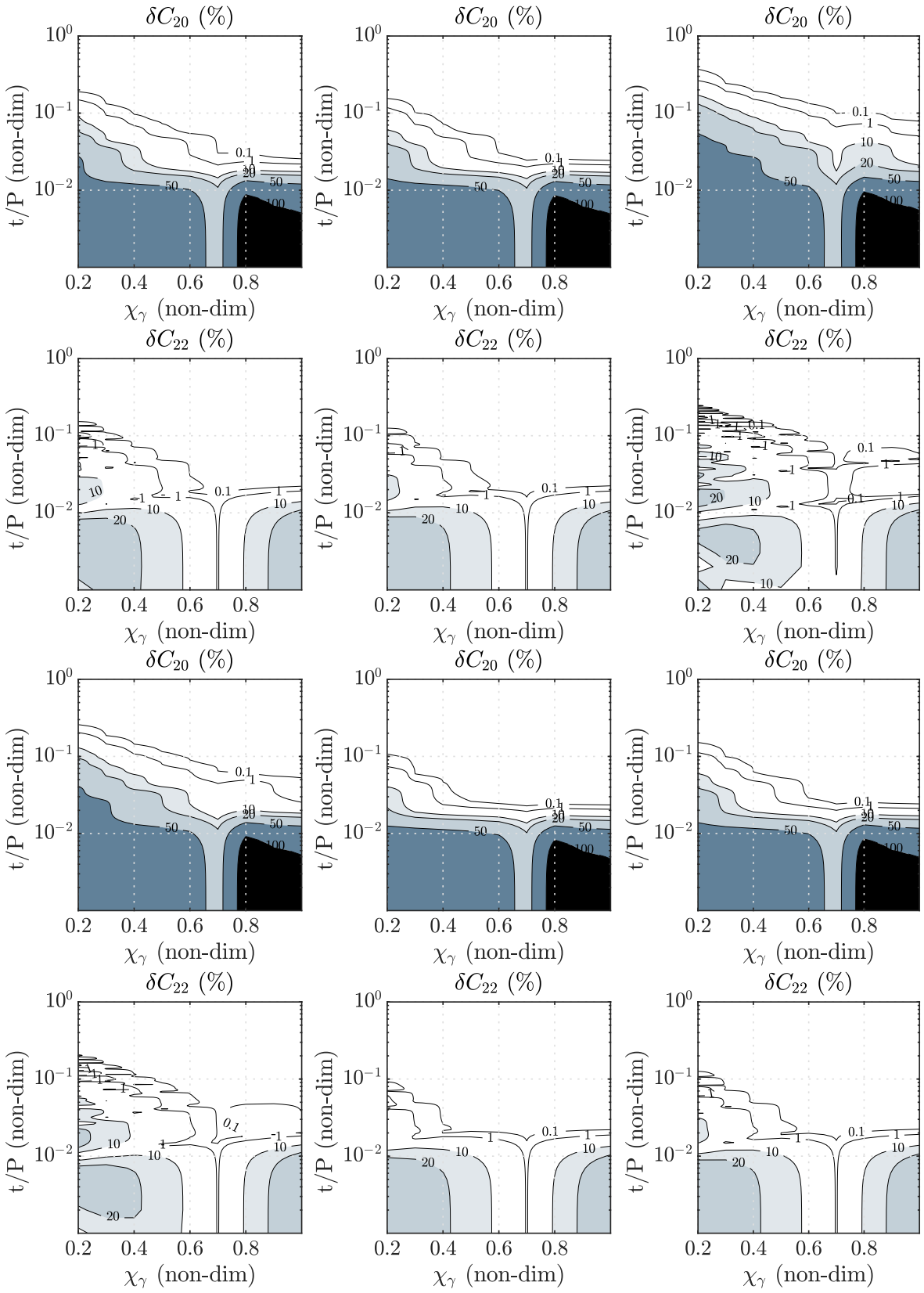

Figure 6.15: $\Gamma_{45}^{3R_0}$ orbit identification in the case of oblate/prolate body with χ_α=1 and $\chi_\beta = 0.2$. Results divided in the classes presented in Table 6.1 from upper left.

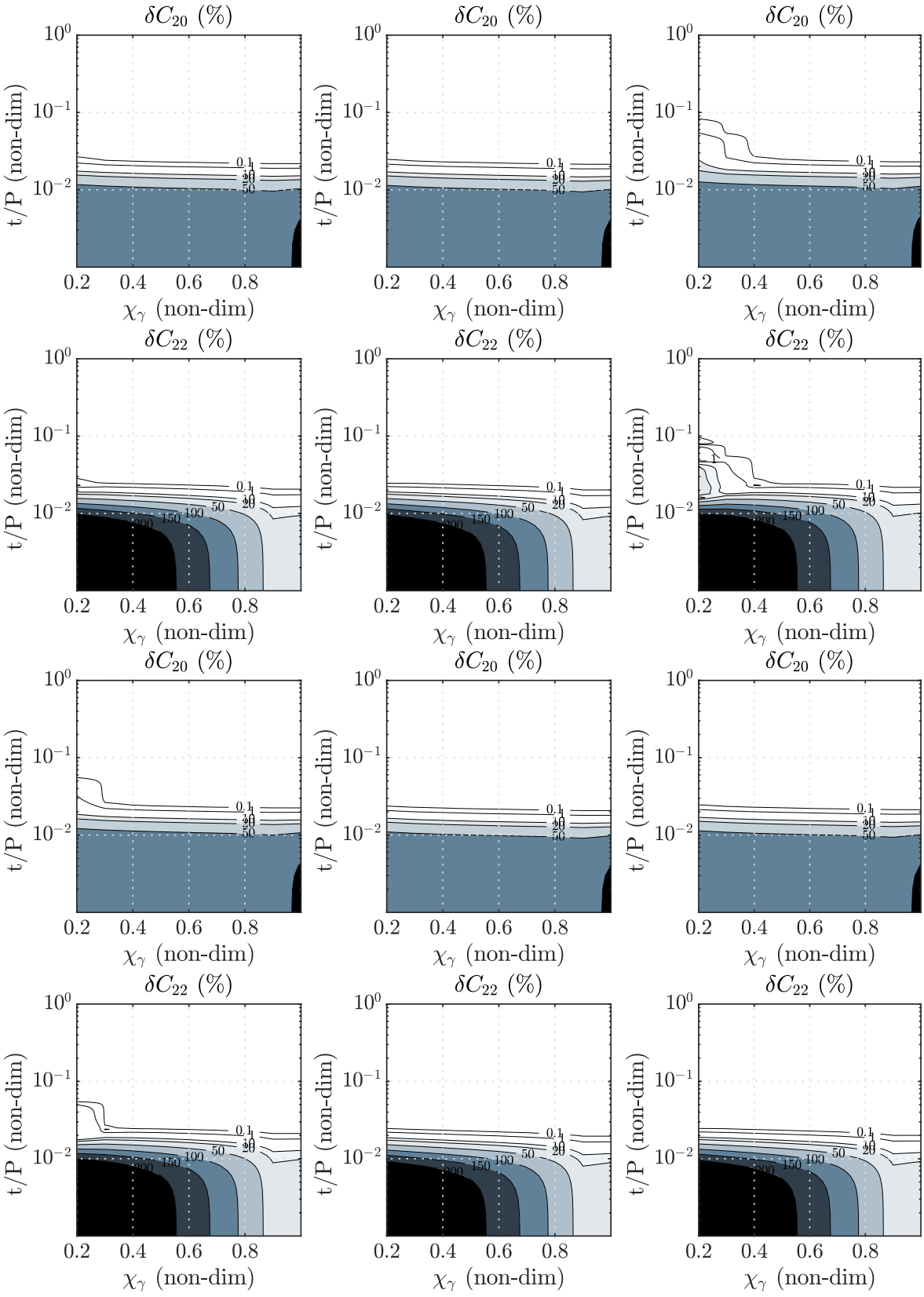

Figure 6.16: $\Gamma_{45}^{3R_0}$ orbit identification in the case of oblate/prolate body with χ_α=1 and $\chi_\beta = 0.8$. Results divided in the classes presented in Table 6.1 from upper left.

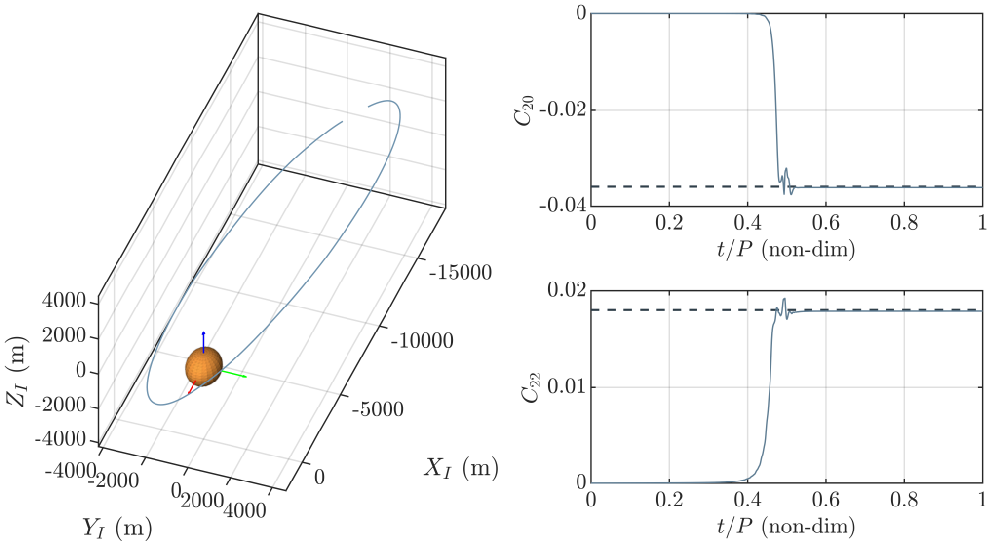

Figure 6.17: $\Gamma_{45}^{10R_0}$ orbit identification in the case of oblate S-class body with $R_0 =$ 1 km, χ_α=1 and $\chi_\beta = \chi_\gamma = 0.8$. Network tuned with $\beta = 1e-7$. $\nu_0 = 180°$.

network in the identification are fair good for both coefficients and both cases, decaying the error δC_{nm} (%) under 0.1% after $\sim 0.1T$. This result underline once more that the network is capable to work in several different dynamical environments without being affected (too much) by them.

6.2.2 High-elliptical orbits

High elliptical orbits or can also be used to reconstruct the lower degree harmonics, but their design can be challenging if the free-dynamics wanted to be exploited and the non-gravitational perturbation included. As an example, the case of a high elliptical orbit with $e_0 = 0.8$, $a_0 = 10R_0$ and and inclination of 45° is presented in the case the non-gravitational perturbations are included in Figure 6.17 and Figure 6.18.

The convergence of the network is fast in proximity of the perigee. However, in this case it can be beneficial for the network to be tuned with a $\beta(m, r)$, in such a way the network convergence would be improved. Note that the dependence is associated not only on the orbit (r) but also on the body (and so on the mass m). Recall that $m \propto \varrho R_0^3$ so that $\beta(\varrho, R_0, r)$ or $\beta(\varrho, \bar{r})$. For a fixed body e. g., a fixed couple (ϱ, R_0), then $\beta(r)$ only. It can be further simplified by using a Taylor expansion:

$$\beta(r) \simeq \beta_0 + \left.\frac{\partial \beta}{\partial r}\right|_0 (r - r_0) \tag{6.10}$$

Where $_0$ denotes a certain reference distance. So that:

$$\left.\frac{\partial \beta}{\partial r}\right|_0 = -\frac{\beta_0 - \beta(r)}{r - r_0} \tag{6.11}$$

Note that those orbits have no applicative purpose while indeed shown once more that the network is faster as the orbit is closer to the body, at fixed β. Finally, it is also possible to use *hyperbolic* arcs for the identification, as shown in Figure 6.19.

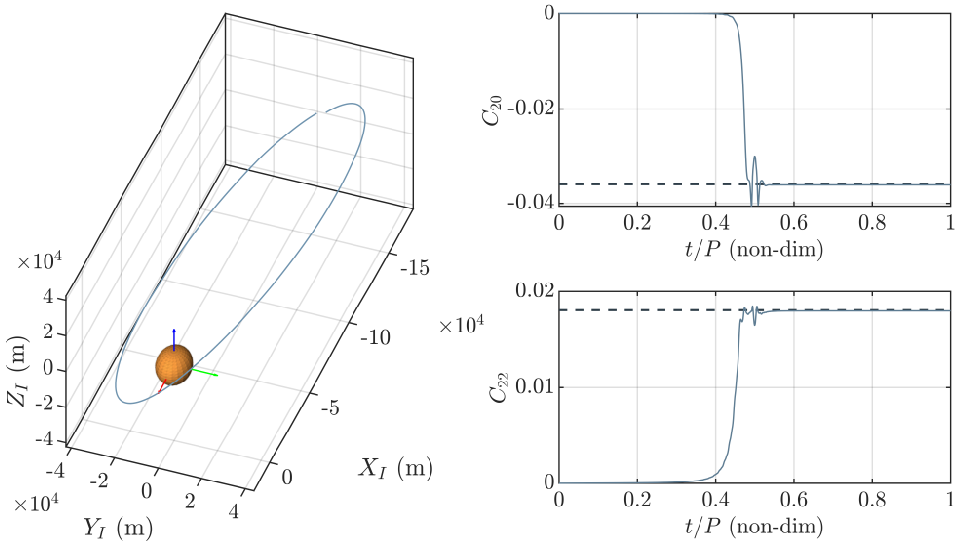

Figure 6.18: $\Gamma_{45}^{10R_0}$ orbit identification in the case of oblate Xc-class body with R_0 = 10 km, χ_α=1 and $\chi_\beta = \chi_\gamma = 0.8$. Network tuned with $\beta = 1e-5$. ν_0 = 180°.

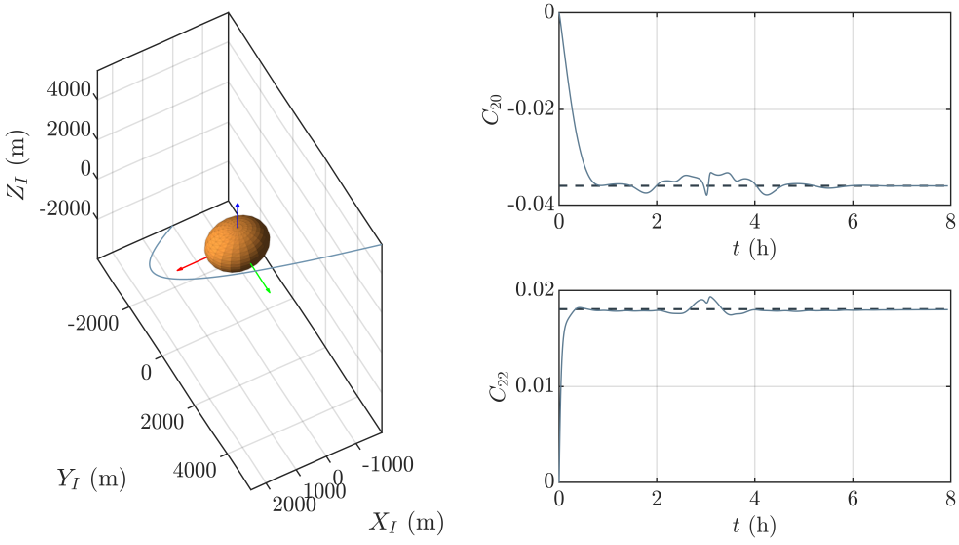

Figure 6.19: $\Gamma_{45}^{-4R_0}$ orbit identification in the case of oblate S-class body with R_0 = 1 km, χ_α=1 and $\chi_\beta = \chi_\gamma = 0.8$. Network tuned with $\beta = 1e-5$. ν_0 = -90° and $e_0 = 1.25$.

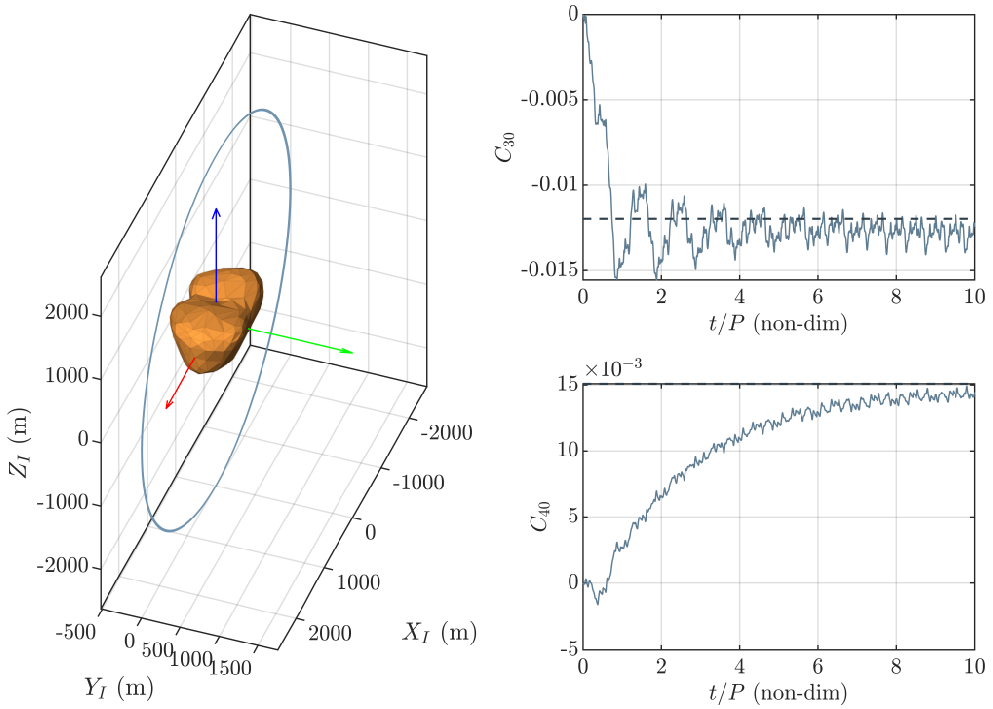

Figure 6.20: $\Gamma_{90}^{3\mathrm{R}_{\max}}$ about Castalia. ($\beta = 1e-8$).

6.3 Identification & Refinement Phases

Identification and refinement phases can be designed in several different ways, depending on the mission objectives too. In fact, scientific missions about asteroids have usually different objectives than the generation of a high fidelity gravitational model. A refined model is, instead, needed if a landing or an impact shall be designed.

In general, the identification & refinement phases can start from the results of the previous phase with the aim to built up other coefficients. As an example, consider the case in which the coefficients C_{20} and C_{22} are known from the previous phase. Then the LIP form to be used in the parametric identification may be corrected. In particular being C_{rs} the coefficients that have been estimated

$$\mathcal{U} = \sum_{r,s} \mathcal{U}_{rs} + \sum_{n,m} \mathcal{U}_{nm} \tag{6.12}$$

Then the LIP form becomes, in general:

$$\dot{\mathbf{v}} - \mathbf{a}_{\mathrm{CO}} - \mathbf{a}_{\mathrm{CF}} + \frac{\mu}{r^3}\mathbf{r} - \nabla \sum_{r,s} \mathcal{U}_{rs}(\mathbf{r}) = \mathbb{A}(\mathbf{r}) \cdot \mathbf{p} \tag{6.13}$$

Note that here the coefficients C_{rs} are considered to be constants and not varying in time, otherwise:

$$\dot{\mathbf{v}} - \mathbf{a}_{\mathrm{CO}} - \mathbf{a}_{\mathrm{CF}} + \frac{\mu}{r^3}\mathbf{r} - \nabla \sum_{r,s} \mathcal{U}_{rs}(\mathbf{r}, t) = \mathbb{A}(\mathbf{r}) \cdot \mathbf{p} \tag{6.14}$$

An example for the identification of the coefficients C_{30} and C_{40} using the modified LIP model for the MHNN, in the case of asteroid Castalia is presented in Figure 6.20.

CHAPTER 7

MHNN GRAVITY FIELD IDENTIFICATION

In this part the HNN is extensively tested on several case studies. Here a case-dependent expanded gravity field is developed and then identified to understand how the network behaves in the real applications. The major difference which respect to the performance evaluation performed in Chapter 5 on page 67 is the fact that the true dynamical environment of the body is considered so that the models presented in Chapter 1 on page 21 for the P2BP in the $\mathcal{T}_b$ reference and the MCR3BP have to be used, depending on the application. Moreover, in the real cases it is of interest also the influence of other perturbations such as the SRP or the other gravitational perturbations.

7.1 The Case of Asteroid 101955 Bennu

The first case study is on the parametric identification of the gravitational field of the asteroid 101955 Bennu. Since the aim of this work is to evaluate the performances of the network and not reproduce an high-fidelity environment of the dynamical environment about the selected body, instead of the P2BP, the ROP2BP is model selected for representing it. For clarity, the model is here recalled:

$$\ddot{\mathbf{r}} + 2\boldsymbol{\Omega} \times \dot{\mathbf{r}} + \boldsymbol{\Omega} \times (\boldsymbol{\Omega} \times \mathbf{r}) = \mathbf{a}_{\mathrm{T}} \tag{7.1}$$

where here $\boldsymbol{\Omega} = \Omega \hat{b}_3$. In this first part, only the main body gravitational attraction is retained, as a polyhedron-based one:

$$\mathbf{a}_{\mathrm{T}}(\mathbf{r}) = \frac{\partial \mathcal{U}(\mathbf{r})}{\partial \mathbf{r}} = -G\varrho \sum_{\text{edges}} \mathbb{E}_e \cdot \mathbf{r}_e L_e + G\varrho \sum_{\text{faces}} \mathbb{F}_f \cdot \mathbf{r}_e \omega_f \tag{7.2}$$

Here $\mathcal{U}(\mathbf{r})$ is the gravitational potential of the body. As discussed in Chapter 2 on page 39, if the polyhedron model is used to built up this potential then a high-fidelity model is obtained under the hypothesis of constant density. Instead, if the potential is represented through a spherical harmonics expansion then the fidelity of the model depends on the number of harmonics that are considered.

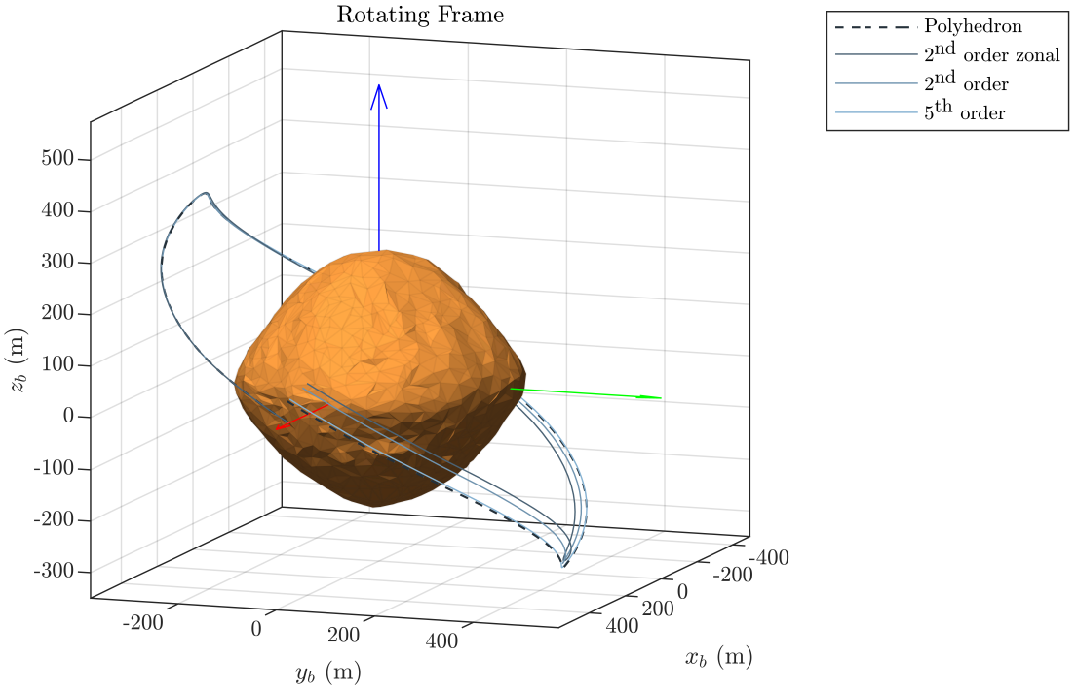

Figure 7.1: Model differences on two orbits about Bennu. Mid-quality polyhedron model of approx 2500 faces used.

In this work the interest is to reconstruct the gravity field of the body in question up to a certain degree N then some informations about this order are needed to initialize the network. Assuming that a model of the body is available from previous observations than a reference orbit Γ_{45} can be built. This orbit is characterized by a period $P = 2T_{\mathrm{r}}$, where T_{r} is the rotation period of Bennu ($\sim$4.2880 hours), and an inclination of 45°. Recall that for a Keplerian orbit, period and semimajor axis are related through the Kepler's third law:

$$P = 2\pi\sqrt{\frac{a^3}{GM}} \tag{7.3}$$

Defining non-dimensional semimajor axis as $\bar{a} = a/R_{\max}$ is this case it results $\bar{a} = 1.75$. So, if Γ_{45} would be a Keplerian orbit then it would be in 2:1 resonance with the asteroid rotation but since in this case a P2BP is considered then the resonance is not preserved. Since in the case of the P2BP the so called Keplerian parameters[1] can be used to characterize any point of the curve Γ_{45} (instead of the $\mathbf{r}, \mathbf{v}$ states) [5], then the variations on the orbital period as well as to the other parameters can be computed.

[1]Being nominally the semi-major axis (a), the eccentricity (e), the inclination (i), the longitude of the ascending node (Ω), the argument of the perigee (ω) and the true anomaly (ν)

Recall that in this case the integration of the equation of motion is performed in the $\mathcal{T}_b$ frame while, instead, the Keplerian parameters must be computed in the $\mathcal{T}_n$ frame so a proper conversion of the position vector $\mathbf{r}$ and the velocity vector $\dot{\mathbf{r}}$ to $\mathbf{R}, \mathbf{V}$ must be applied. Having defined $\mathbb{T}_\Omega(t)$ in Chapter 1 on page 21 then:

$$\mathbf{R}(t) = \mathbb{T}_\Omega^T(t)\mathbf{r}(t) \tag{7.4}$$

$$\mathbf{V}(t) = \mathbb{T}_\Omega^T(t)\left([\Omega]\mathbf{r}(t) + \dot{\mathbf{r}}(t)\right) \quad \text{where} \quad [\Omega] = \begin{bmatrix} 0 & -\Omega & 0 \\ \Omega & 0 & 0 \\ 0 & 0 & 0 \end{bmatrix} \tag{7.5}$$

Once $\mathbf{R}, \mathbf{V}$ are computed than the procedure described in [5] can be applied to convert the in the $a, e, i, \Omega, \omega, \nu$ Keplerian Parameters (KEPs). Note that here neither Ω neither ω are intended to be the angular velocity of the asteroid.

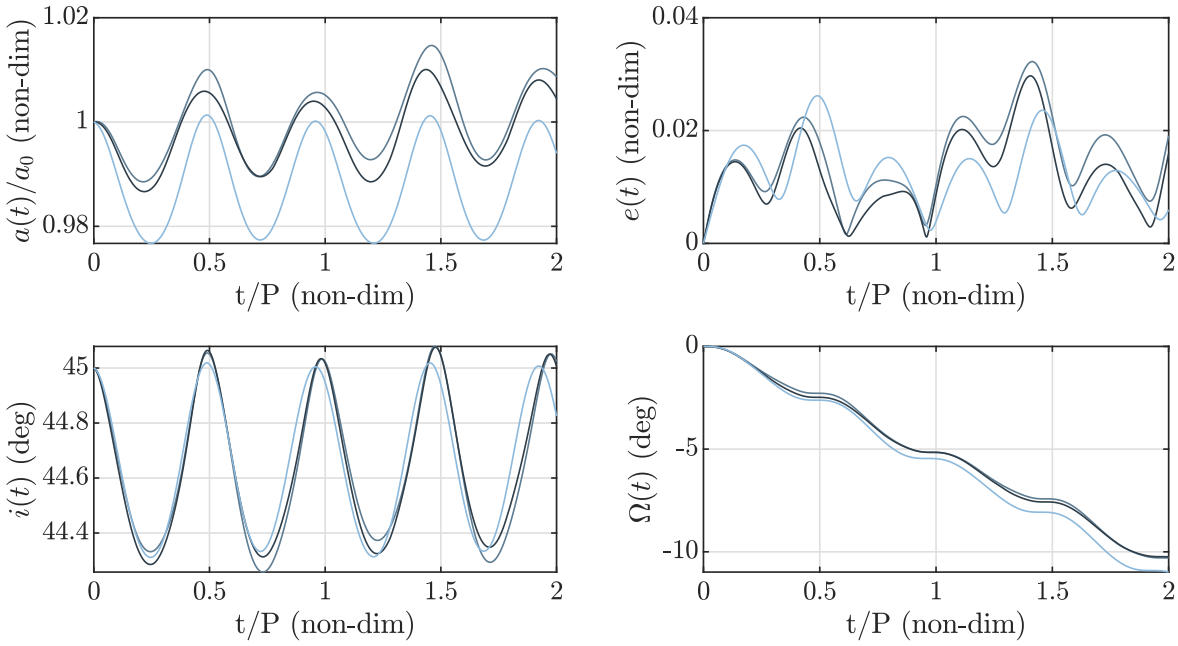

Figure 7.2: KEPs variations on 2 orbits about Bennu. Mid-quality polyhedron model of approx 5000 faces used.

In Figure 7.2 the results in terms of the KEPs variations for a polyhedron model based orbit, for the orbit resulting from a 10th degree spherical harmonics expansion (darker curve) and from the one resulting from a 10th degree spherical harmonics expansion with only zonal terms (lighter curve).

In Table 7.1 some of the coefficients of the spherical harmonics expansion for the asteroid Bennu are reported. Those are un-normalized coefficients. Note that the magnitude of the coefficients C_{20}, C_{22}, C_{30}, C_{31} and C_{40} are much larger than the one of the others. Note also that some of the coefficient are in brackets: this is because they should be zero since the equation of motion are written in the $\mathcal{T}_b$ frame, that is the principal inertia frame, but they're not zero because are computed from the polyhedron model that has a certain discretization.

Table 7.1: *Bennu spherical harmonics expansion coefficients up to degree 4.*

C_{20}	-0.040804		
C_{21}	0 (0.00055237)	S_{21}	0 (-0.00012594)
C_{22}	0.0018883	S_{22}	0 (-0.00058876)
C_{30}	0.0049144		
C_{31}	0.0011623	S_{31}	-0.00032144
C_{32}	-0.00024379	S_{32}	-0.00019989
C_{33}	0.00017464	S_{33}	-2.7456e-05
C_{40}	0.019919		
C_{41}	-0.00082558	S_{41}	-0.00061812
C_{42}	-0.00017304	S_{42}	-2.3051e-05
C_{43}	-8.2511e-06	S_{43}	-2.8951e-05
C_{44}	2.1742e-05	S_{44}	4.5268e-05

Assume now that the main objective is to reconstruct those five coefficients in order to built up the potential function $\mathcal{U}(\mathbf{r})$. In particular, this function can be expanded as:

$$\mathcal{U}(\mathbf{r}) = \frac{GM}{r} + \mathcal{U}_{g,2}(\mathbf{r}) + \mathcal{U}_{g,3}(\mathbf{r}) + \mathcal{U}_{g,4}(\mathbf{r}) \tag{7.6}$$

where here:

$$\mathcal{U}_{g,2}(\mathbf{r}) = \frac{GM}{r}\left(\frac{R_0}{r}\right)^2\left[C_{20}\left(\frac{3}{2}\cos^2\theta - 1\right) + 3C_{22}\sin^2\theta\cos 2\lambda\right]$$

$$\mathcal{U}_{g,3}(\mathbf{r}) = \frac{GM}{r}\left(\frac{R_0}{r}\right)^3\left[C_{30}\cos\theta\left(\cos^2\theta - \frac{3}{2}\sin^2\theta\right) + C_{31}\sin\theta\left(\frac{15}{2}\cos^2\theta - \frac{3}{2}\right)\cos\lambda\right]$$

$$\mathcal{U}_{g,4}(\mathbf{r}) = \frac{GM}{r}\left(\frac{R_0}{r}\right)^4 C_{40}\left(\frac{5}{8}\cos^4\theta - 3\cos^2\theta\sin^2\theta + \frac{3}{8}\right)$$

To fully understand the dynamics about this specific body as well as to validate the dynamical model adopted, before proceeding to the identification, long term behaviours on the orbit should be analysed. In Figure 7.3 the results of the propagation of a polar orbit Γ_{90} are presented in terms of KEPs. In this case Γ_{90} is taken as a 3:2 resonant orbit. It can be noticed that the behaviour of the KEPs is quite similar to the case in which a zonal harmonics expansion is considered, in fact both $i(t)$ and $\Omega(t)$ exhibit small variations, while the most important variations can be seen in the eccentricity. This can be related to the fact that the body have a pronounced bulged equatorial region so that strong zonal perturbations among the others are expected. This is further confirmed if another Γ_{90} is considered with a 5:1 resonance (Figure 7.4, the darker line comes from a polyhedron-based model while the lighter one form the integration of a spherical harmonics expansion with *only* the C_{20} term included). This result is important since it shows that even at a distance $\sim 3.2R_{\max}$ the major perturbation contribution is associated to the first zonal harmonics only. It can be shown that sectorial harmonics, in this particular case, have low influence on the overall perturbation. Finally, important conclusion that comes from the analysis is that orbits about this kind of bodies seems to be quite "stable" in this case, at least if the other non-gravitational perturbations are not considered.

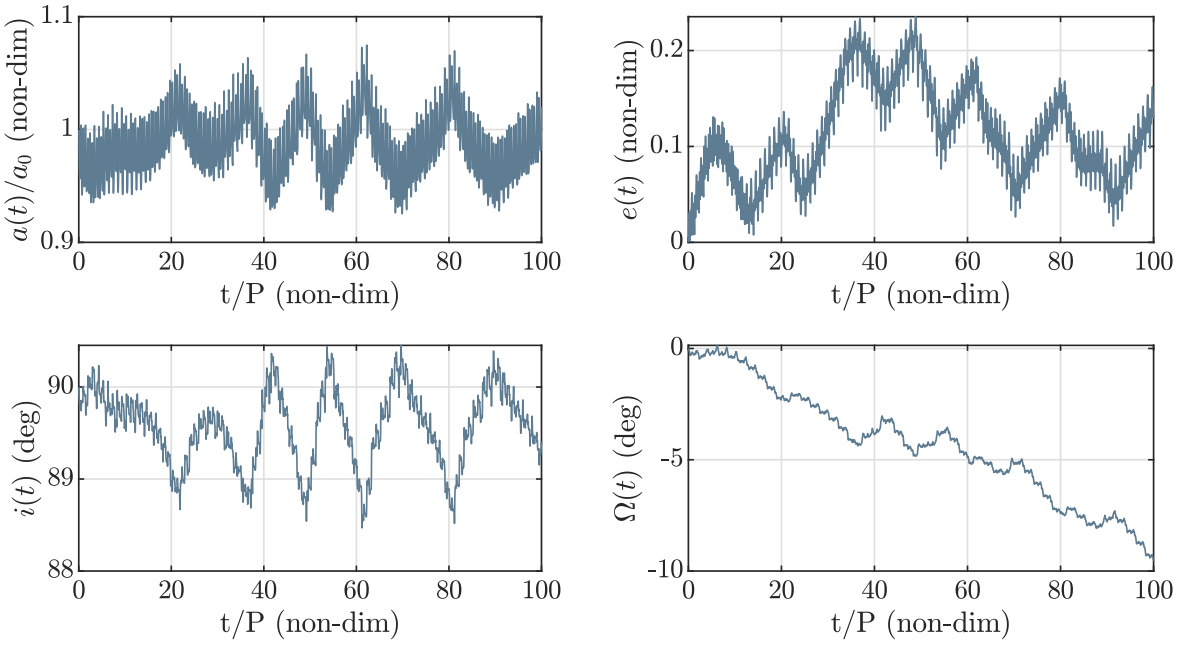

Figure 7.3: KEPs variations on 100 orbits about Bennu: Γ_{90}, 3:2 resonance case.

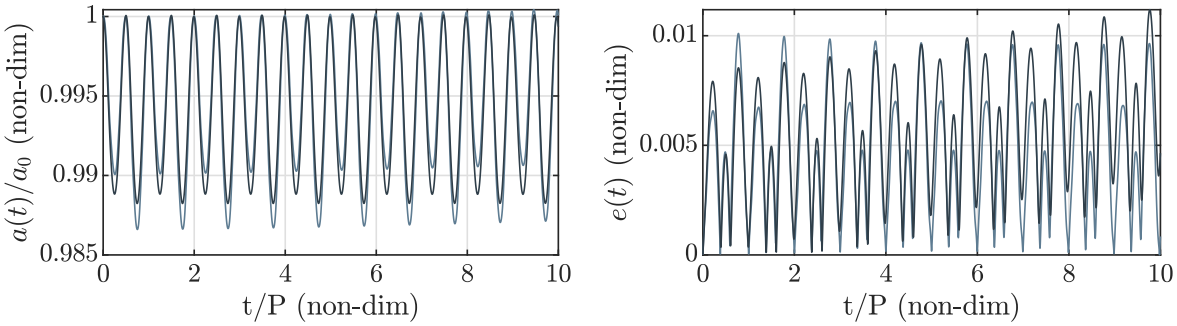

Figure 7.4: KEPs variations on 10 orbits about Bennu: Γ_{90}, 5:1 resonance case.

7.1.1 MHNN performances

In order to apply the parametric identification method based on the MHNN presented in Chapter 4 on page 59 the gravitational potential have to be written as:

$$\mathcal{U}(\mathbf{r}) = \mathbb{P}(\mathbf{r}) \cdot \mathbf{p} \tag{7.7}$$

where $\mathbf{p}$ is the vector of parameters to be estimated, that in this case contains C_{20}, C_{22}, C_{30}, C_{31} and C_{40}. In this manner, being $\mathbf{a}_{\mathrm{T}} = \nabla\mathcal{U}(\mathbf{r})$ the problem can be written in the usual LIP form.

Test 1. This test is performed on a $\Gamma_{90}^{2:1}$ orbit. All the parameters of the vector $\mathbf{p}$ defined before are estimated. The network is initialized with $\mathbf{p}_0 = \mathbf{0}$ and its convergence is presented in Figure 7.5. The estimated values of the parameters, expressed in terms of MLE are, instead, presented in Table 7.2. Note that the MLE is computed on the last orbits and not on all the time-series. Note also that the capability of reconstructing the coefficient is quite good in all cases except for C_{31}: in this case the variance is higher in magnitude that the mean value so the coefficient is considered *not*

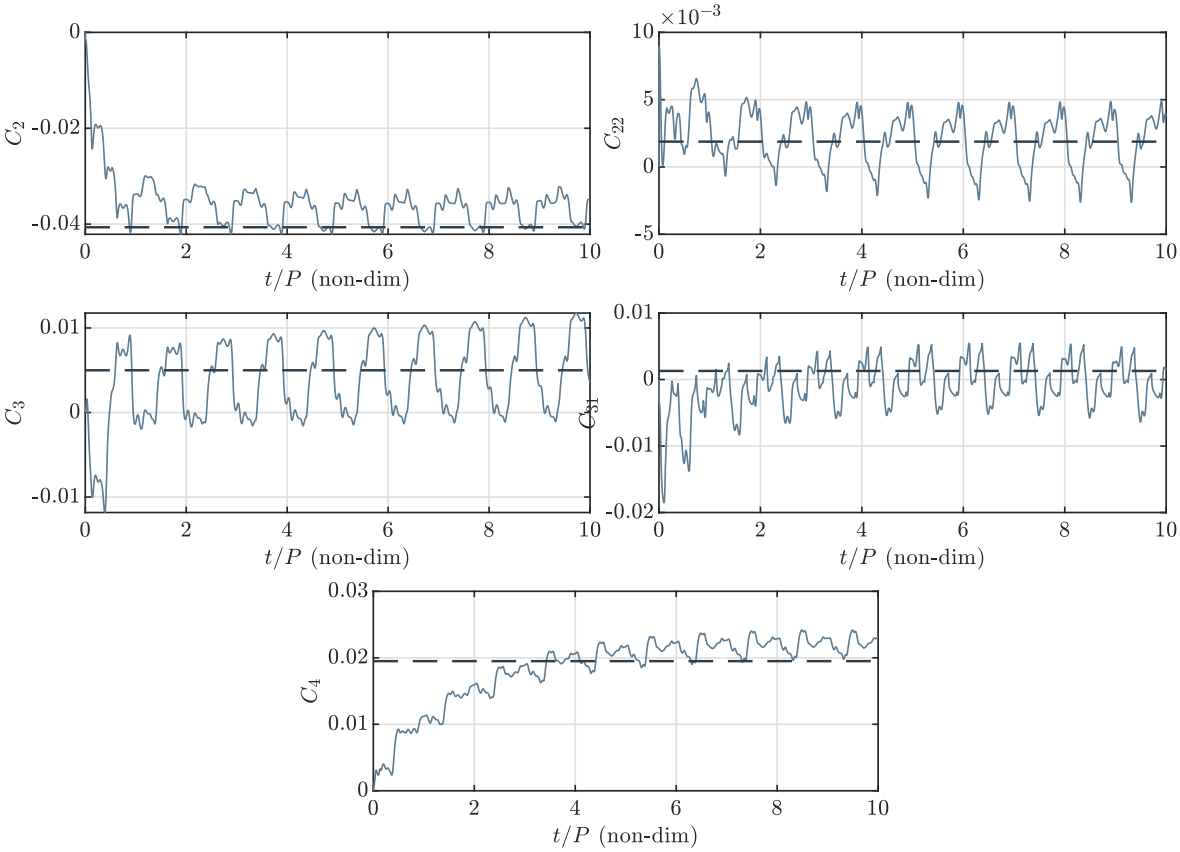

Figure 7.5: *Test 1* · SHs coefficients identification.

reconstructed correctly. Note also that the long term propagation ($20P = 20$ orbital periods) converges, as expected, with a smaller error with respect to the short term one.

Test 2. This test is performed on a Γ_{90}, in the case the orbit has a period of 1 day ($\sim 5.6P$). According to Chapter 3 on page 49 as far as the distance increases as far as the order of magnitude of the n-th degree perturbation is of order 10^{-n}. At this distance, in fact, can be shown that the network is capable to identify only C_{20} and C_{22}. In Figure 7.6 the results of the identification of C_{20}. Using a moving mean it can be found that the estimate converges to -0.039 in both the cases presented.

Table 7.2: Test 1 · *MLE with 95% confidence interval.*

	True	MHNN: $10P$				MHNN: $20P$	
		$\beta = 1e-6$		$\beta = 1e-7$		$\beta = 1e-6$	
		MLE	σ	MLE	σ	MLE	σ
C_{20}	-0.0406	-0.0390	0.00149	-0.0366	0.00283	-0.0400	0.0012
C_{22}	0.00188	0.00203	0.00170	0.00173	0.00190	0.00182	0.00125
C_{30}	0.00499	0.00621	0.00058	0.00443	0.00443	0.00552	0.00121
C_{31}	0.00129	-0.0005	0.0018	-0.0008	0.00326	-0.00043	0.00126
C_{40}	0.01949	0.0157	0.00103	0.0219	0.00126	0.01744	0.00124

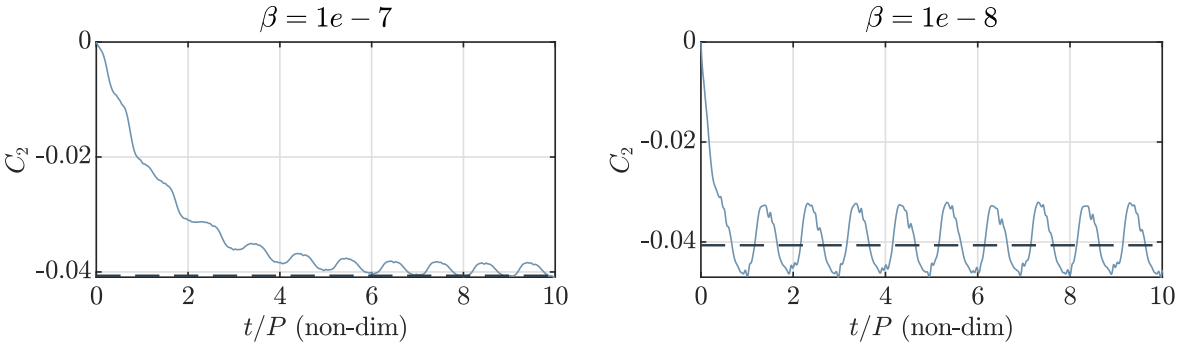

Figure 7.6: *Test 2* · SHs coefficients identification for the case of a $\Gamma_{90}^{5.6:1}$ orbit.

Test 3. Here a $\Gamma_{45}^{2:1}$ orbit is considered. The aim of this test it to verify the convergence of the method in case of a lower inclination orbit. The results for this case are shown

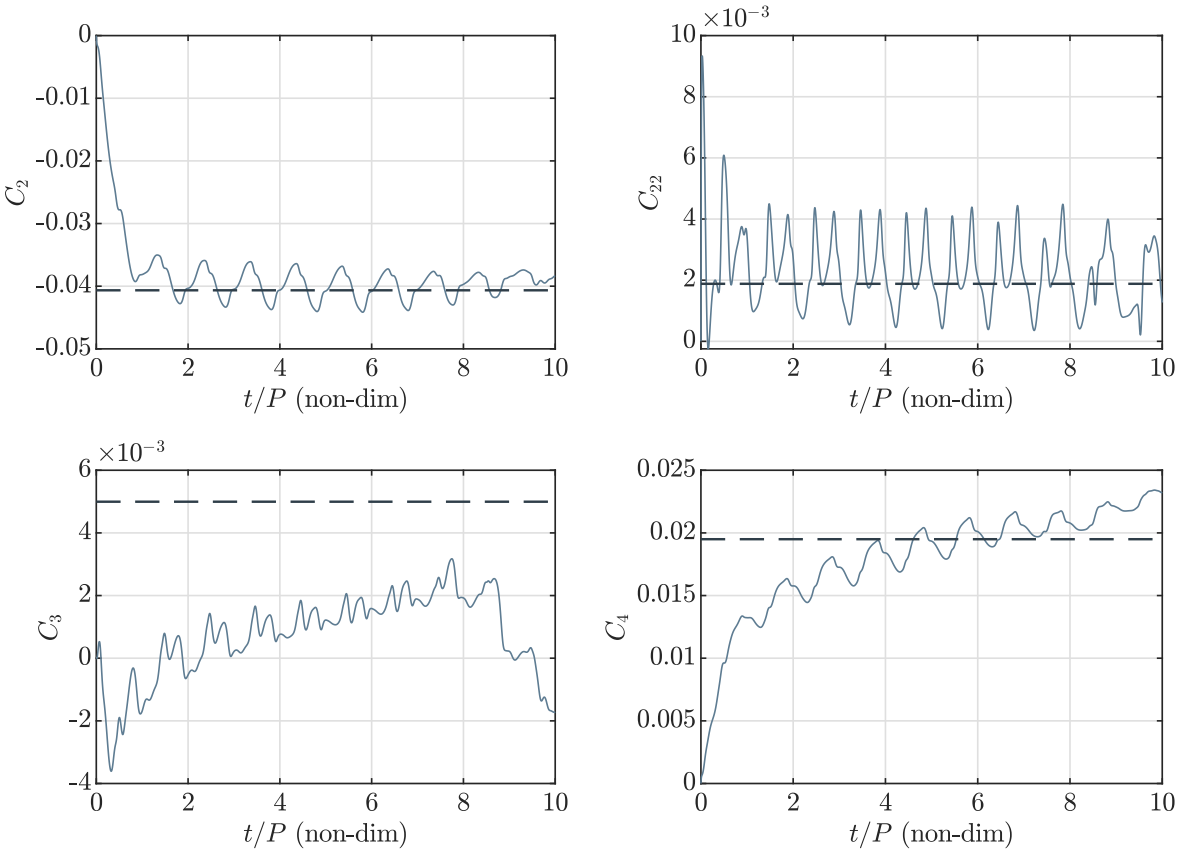

Figure 7.7: SHs coefficients identification for the case of $\Gamma_{45}^{2:1}$.

in Figure 7.7. It can be seen that the use of a low-inclination orbit does not influence the convergence of the 2nd degree terms but instead do influence (in a negative way) the one of higher-degree terms, at least if those coefficients are estimated all together.

Test 4. Here a set of orbits with $i_0 \in [0°, 90°]$ and $a_0 \in [2, 6]\, R_{\max}$ is built and propagated for a period $P = 10 \cdot P(a_0) = 10P_0$. The coefficients C_{20}, C_{22}, C_{30} and C_{40} are estimated. In order to evaluate the overall performance of the network a mean

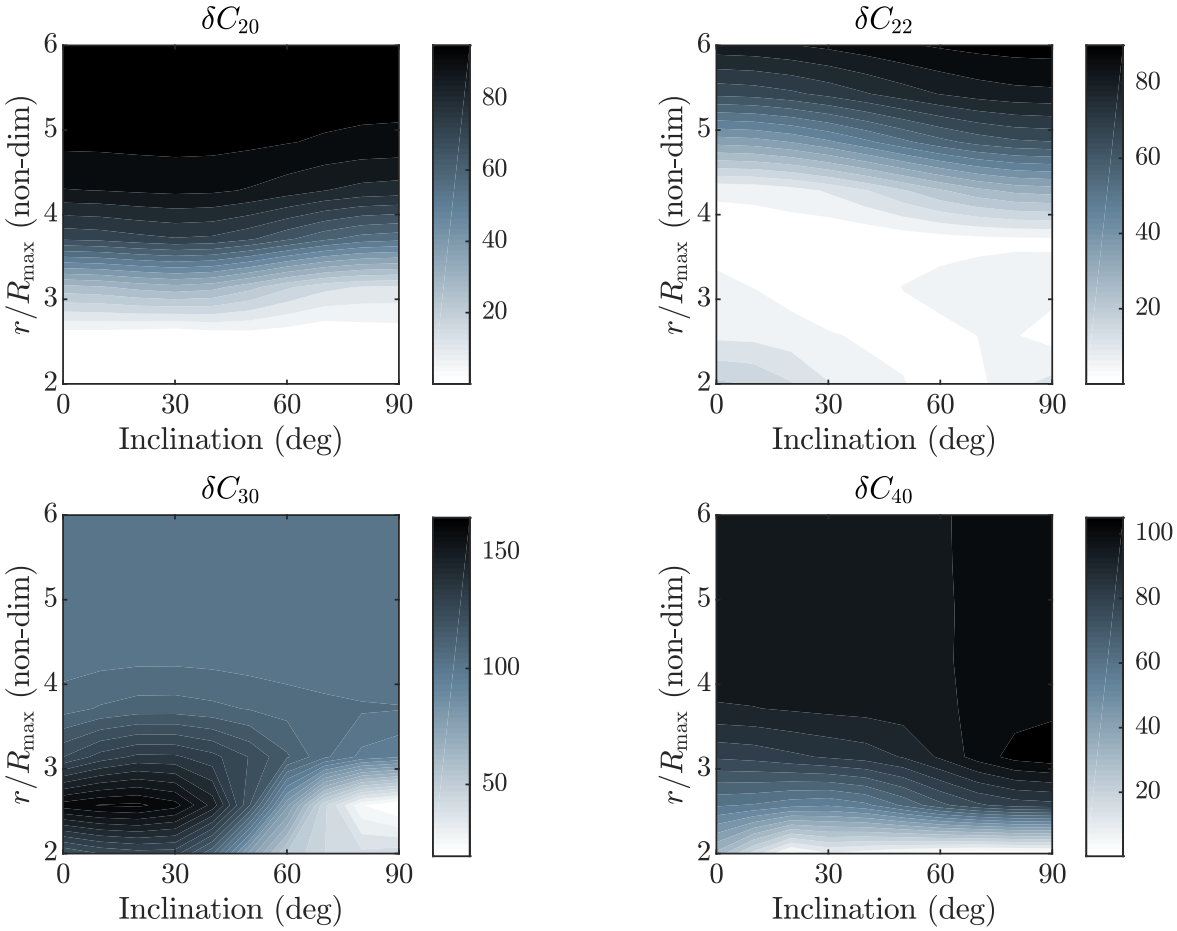

Figure 7.8: δC_{nm} analysis results for the case of Bennu.

operator is applied in such a way, for the n, m term:

$$\delta^* C_{nm}(a_0, i_0) = \frac{1}{5P_0} \int_{5P_0}^{10P_0} \frac{\hat{C}_{nm}(a_0, i_0, \tau) - C_{nm}}{C_{nm}} \, d\tau \tag{7.8}$$

where $\hat{C}_{nm}$ denotes the time dependant coefficients estimated from the MHNN while C_{nm} the true coefficients. Here the previous operator is nothing than mean in time over $5P_0$. Now define $\delta C_{nm}(a_0, i_0) = \delta^* C_{nm}(a_0, i_0) \cdot 100$ as the parameter of merit needed for the analysis of the global behaviour of the network.

The results in Figure 7.8. As it can be seen, the estimation coefficients C_{20} and C_{40} is independent from the inclination but do depend on the distance. In particular, C_{40} if estimated with the other coefficients, have a stronger dependence on the distance than C_{20}. The other coefficients, namely C_{22} and C_{30}, instead exhibit large variations in terms of δC_{nm} also in function of the inclination. In particular, the zonal term C_{30} seems to need an high inclination orbit to be estimated.

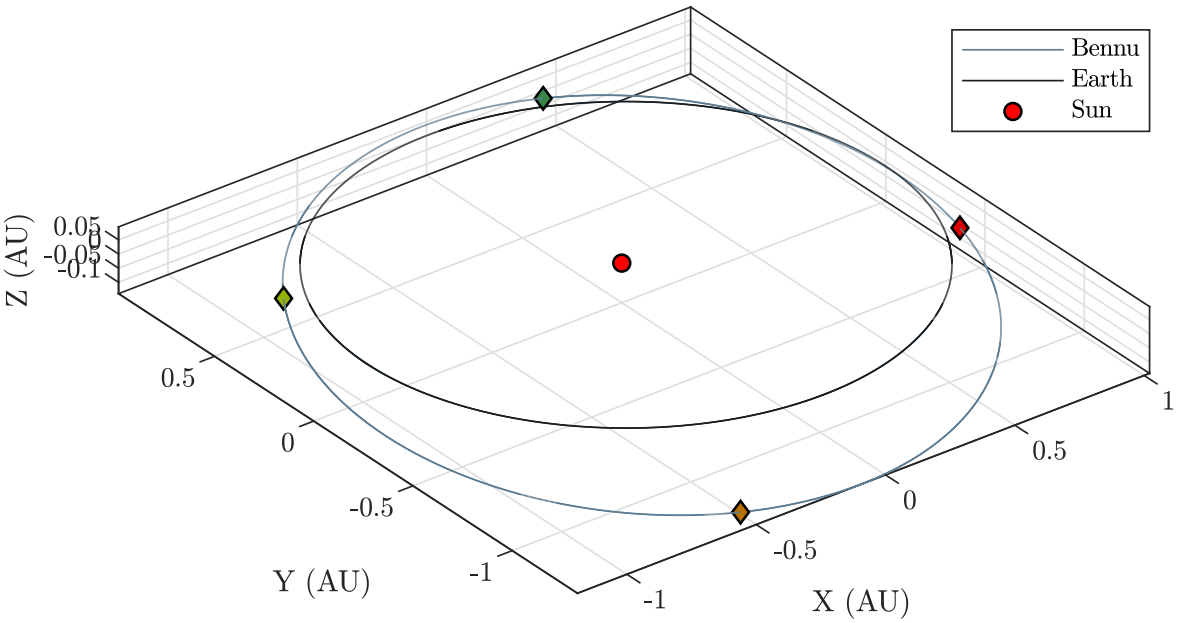

Figure 7.9: Bennu heliocentric orbit. Earth orbit for comparison.

7.1.2 MHNN sensitivity to force pertubations

In order to analyse the behaviour of the network in a dynamical environment that is more similar to the real one, the SRP and the Sun 3-rd Body Perturbation (3BP) are introduced. In Figure 7.10 the sensitivity of the identification for the $\Gamma_{90}^{2:1}$ orbit

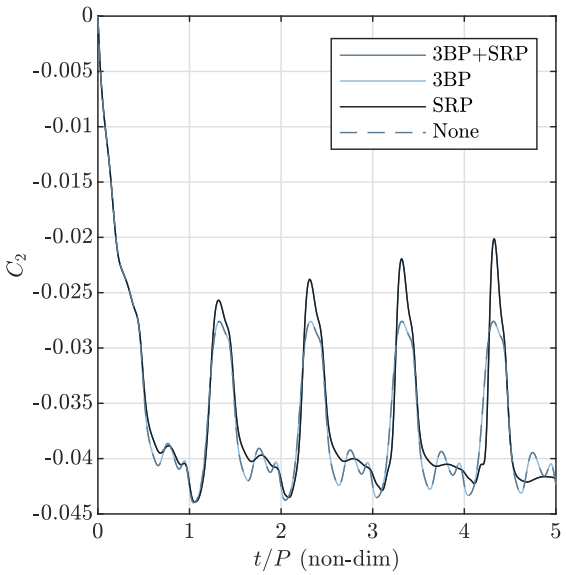

Figure 7.10: Sun and SRP effects on C_{20}.

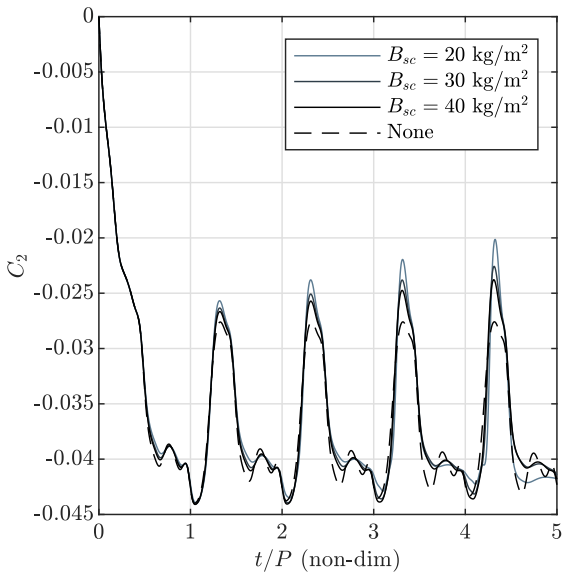

Figure 7.11: SRP effects on C_{20}.

considering the single perturbations. It can be seen that the predominant is the SRP while the Sun 3BP is negligible. The force model used is the one presented in Eq. (1.65)

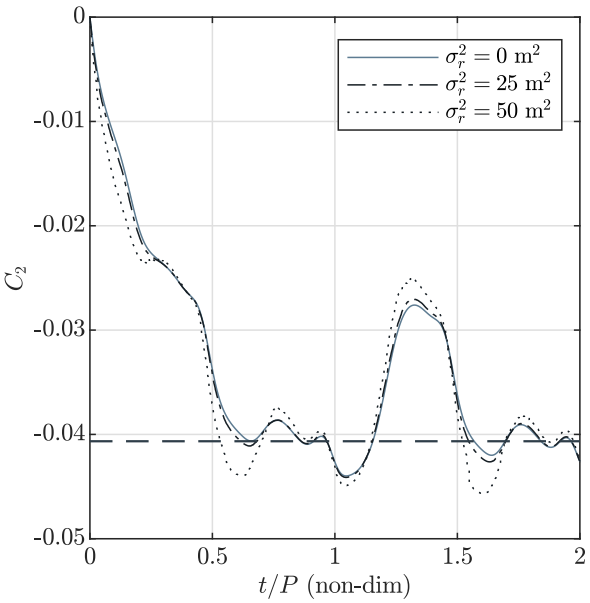

Figure 7.12: Effect of instrument noise on the reconstruction of C_{20}.

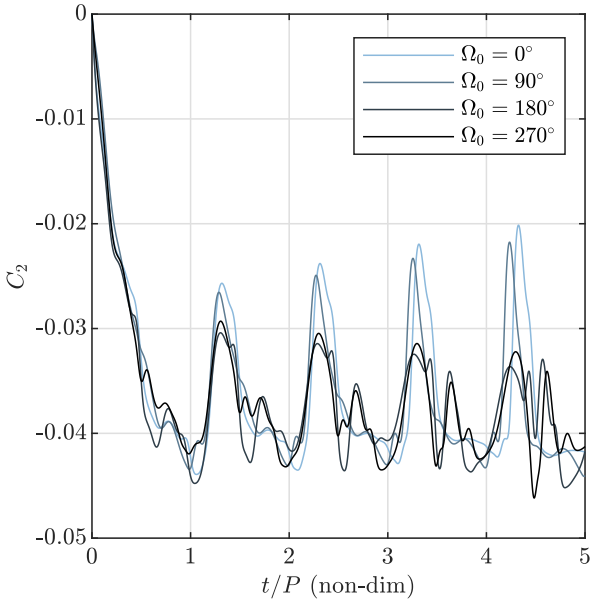

Figure 7.13: Effect of the ascending node Ω_0 on the reconstruction of C_{20}.

and recalled here for completeness:

$$\mathbf{a}_{\mathrm{T}}(\mathbf{r},\mathbf{s},\mathbf{d}_{\mathrm{k-a}}) = \mathbf{a}_{\mathrm{Poly}}(\mathbf{r}) - \overbrace{\frac{(1+\rho)P_0}{B_{\mathrm{sc}}s^3}\mathbf{s}}^{SRP} - \overbrace{\frac{GM_\odot}{s^3}\left[\mathbf{r} - 3\frac{\mathbf{r}\cdot\mathbf{s}}{s^2}\mathbf{s}\right]}^{Sun} \tag{7.9}$$

In Figure 7.9 the complete Bennu heliocentric orbit. On it, 4 points have been highlighted: they correspond to $\nu = 0, \pi/2, \pi$ and $3\pi/2$. These are the orbital points in which the sensitivity analysis is performed. A reference orbit $\Gamma_{90}^{2:1}$ is considered. The MHNN is initialized from zero, with $\beta = 1e-6$ and it is applied to reconstruct C_{20} only. For the SRP model is B_{sc} is taken as 20 kg/m^2 and ρ as 0.1.

Figure 7.14 the results for the analysis for those ν. It can be seen that the performances of the network have a strict dependence to the orbital position of Bennu with respect to the Sun. The performances, moreover, depends also on the ascending node position so on the orientation of the orbit with respect to the Sun: these effects can be seen in Figure 7.13.

7.1.3 MHNN sensitivity to instrument noise

In the previous part the perturbations effect on the parameters identification has been analysed. There may be, however, another source of deviation for the parameters: it may arise from the the noise of the instruments used on board. In fact, in order to be work properly, the network needs position and velocity measurements. In this work a standard Gaussian noise is added to the true state in order to emulate for this noise. To do so, the MATLAB function `randn` is used to generate a random noise with a certain variance. In this work we assume that the reconstructed position is given by the true one $\mathbf{r}$ plus a random one that has zero mean and standard deviation σ_r^2 assigned. In Figure 7.12 the results for this analysis: there is a variation of the reconstructed state just in case σ_r^2 is quite high.

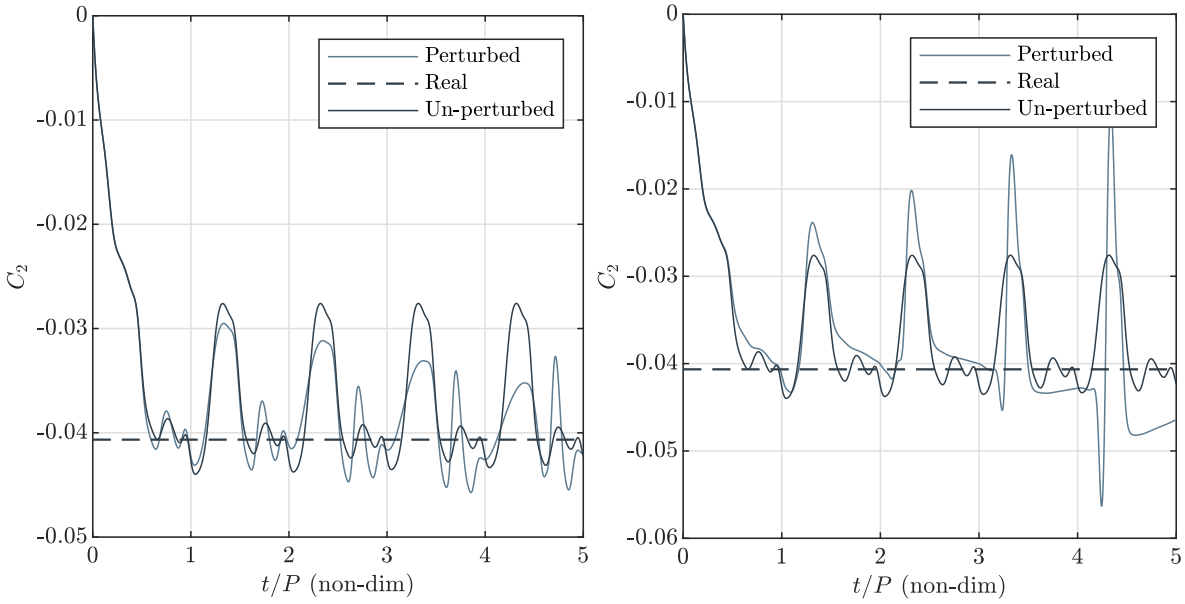

(a) $\nu = 0$ (b) $\nu = \pi/2$

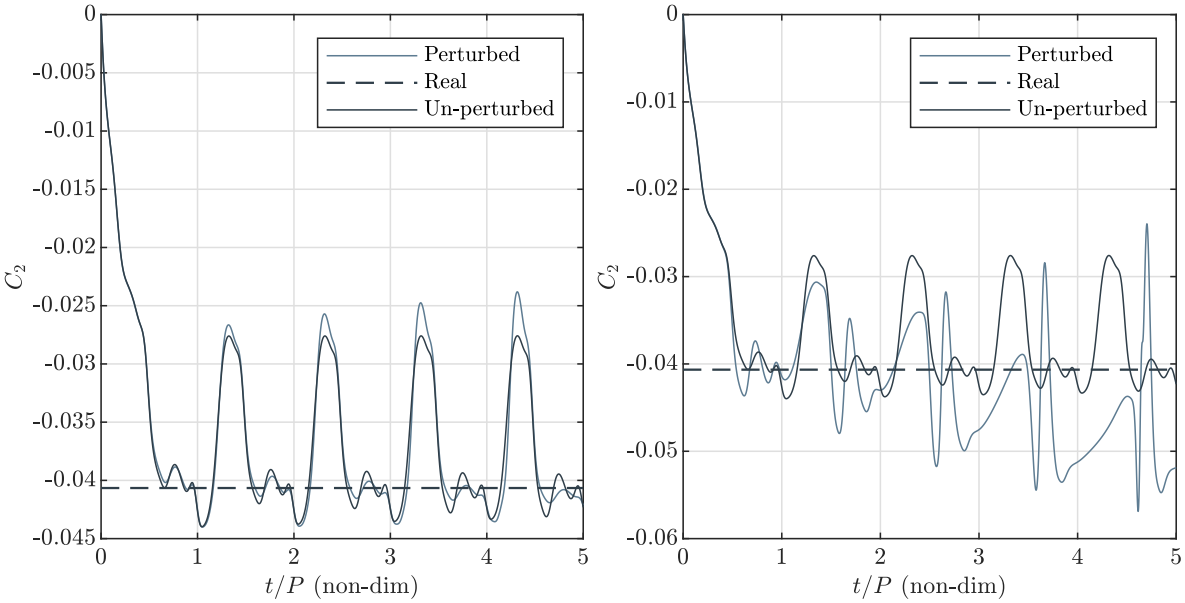

(c) $\nu = \pi/2$ (d) $\nu = 3\pi/2$

Figure 7.14: C_{20} MHNN identification results for some selected position on the Bennu heliocentric orbit.

Table 7.3: *Castalia spherical harmonics expansion coefficients up to degree 4.*

C_{20}	-0.08899		
C_{21}	0	S_{21}	0
C_{22}	0.03623	S_{22}	0
C_{30}	-0.01235		
C_{31}	0.008330	S_{31}	-1.879e-4
C_{32}	0.000933	S_{32}	1.797e-4
C_{33}	-0.0005785	S_{33}	3.878e-4
C_{40}	0.01520		
C_{41}	-0.000358	S_{41}	-2.238e-4
C_{42}	-0.001559	S_{42}	1.001e-4
C_{43}	-0.00006	S_{43}	3.206e-5
C_{44}	0.0001364	S_{44}	-3.714e-5

7.2 The Case of Asteroid 4769 Castalia

In this case, the parametric identification of the gravitational field of Castalia is presented. This case is far more complicated that the previous one since the shape of the body is highly irregular. This results in a far complicated gravitational field and yields to highly perturbed orbits. In Table 7.3 some of the coefficients of the spherical harmonics expansion are reported. Note that those are normalized coefficients. Note also that, in this case, the magnitudes of the coefficients C_{20}, C_{22}, C_{30} and C_{40} are much larger than the one of the others.

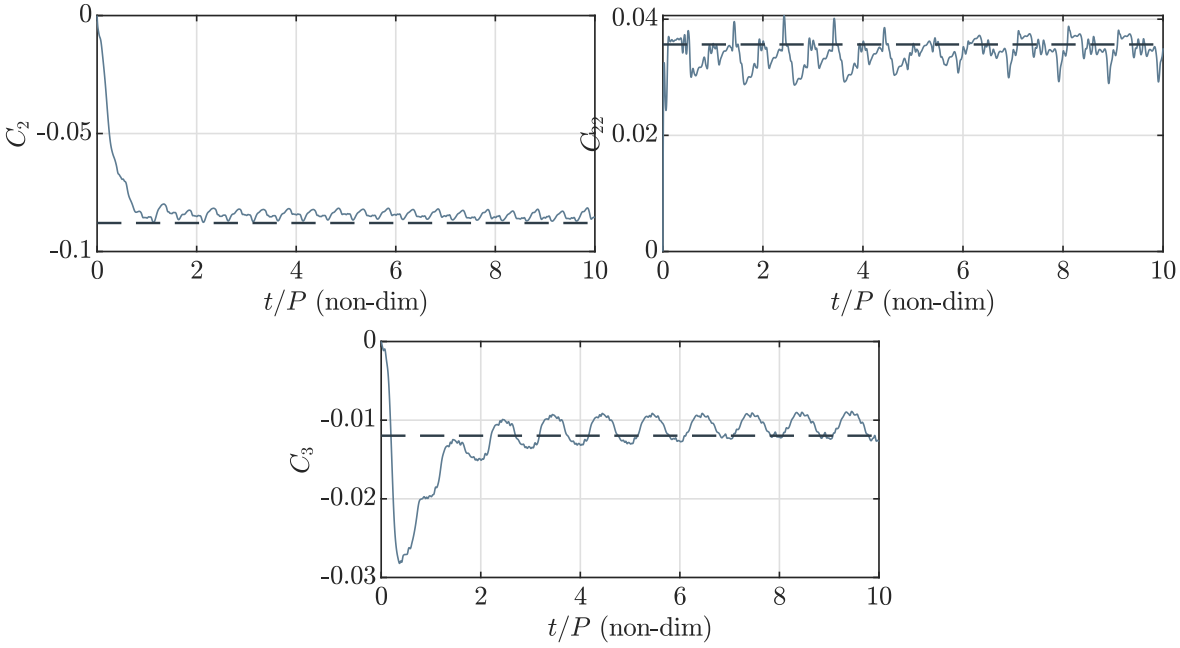

Figure 7.15: SHs coefficients identification, $\Gamma_{90}^{2:1}$.

In Figure 7.15 the results of the identification of the coefficients C_{20}, C_{22} and C_{30} in the case of a $\Gamma_{90}^{2:1}$ about Castalia are presented. The network is initialized with $\mathbf{p}_0 = 0$

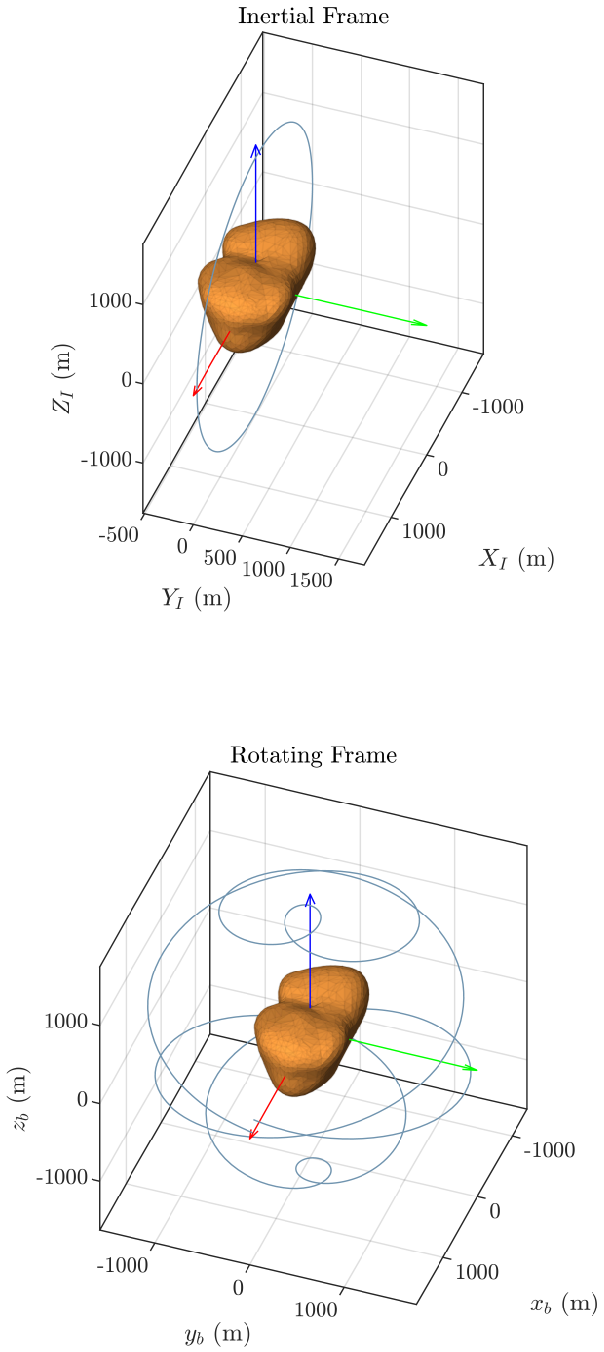

Figure 7.16: $\Gamma_{90}^{2:1}$ orbit about Castalia.

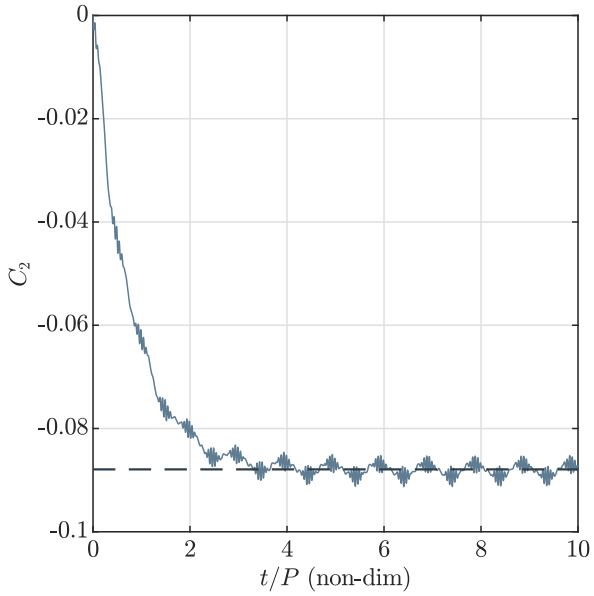

Figure 7.17: SHs coefficients identification, $\Gamma_{60}^{10:1}$

and $\beta = 1e-6$. The resulting orbit is presented in Figure 7.16.

As in the case of Bennu, the network is capable of identifying correctly the three coefficients to be estimated. Of course, the performances of the estimation depends on the initial conditions so on the resulting orbital path: this can be seen comparing the previous results with Figure 7.18 where the results of the estimation for a $\Gamma_{45}^{5:1}$ orbit are presented. Finally, the network is capable to identify the coefficients (in particular

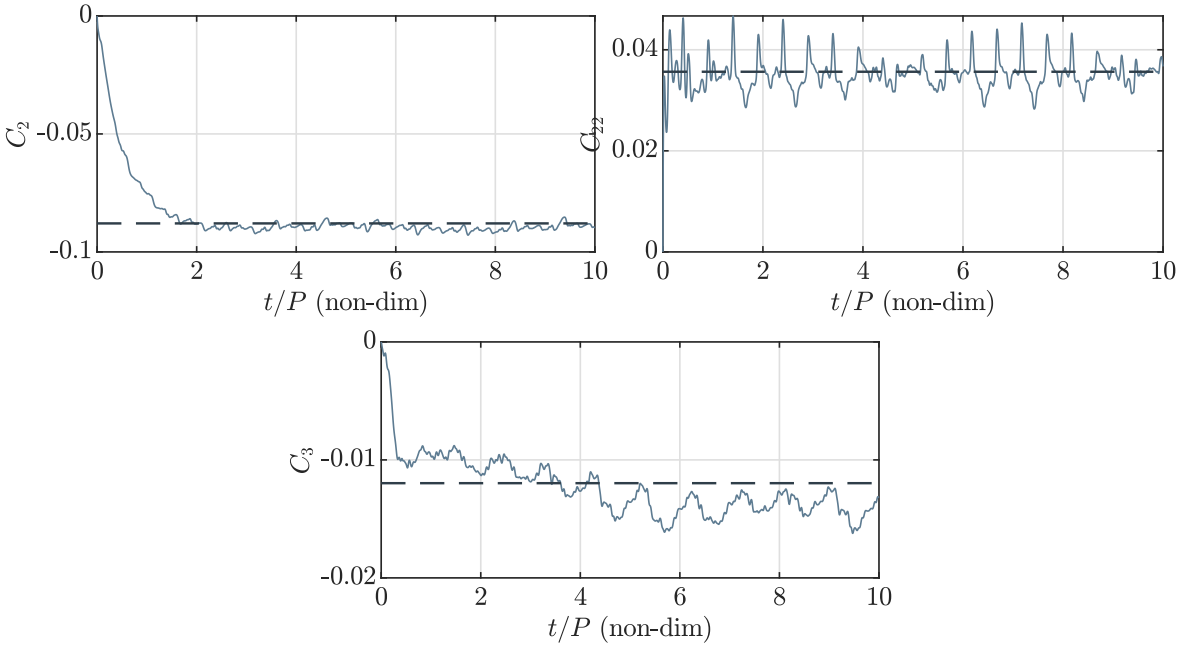

Figure 7.18: SHs coefficients identification, $\Gamma_{60}^{10:1}$

the low-degree ones) also in case the the reference orbit is quite far from the body: in Figure 7.17, as an example, the estimation of C_{20} based on a $\Gamma_{60}^{10:1}$ orbit. In this case $\beta = 1e-7$.

However, also in this case, perturbations can act to degrade the performance of the network. As for the case of Bennu, those perturbations can be divided in force perturbations and instruments noise. The results of the sensitivity of the network to those kind of perturbations are shown, for a $\Gamma_{90}^{5:1}$ orbit in Figure 7.19, where $\rho = 0.1$, $B_{\text{sc}} = 20$ kg/m^2 and the orbital position is the one of the asteroid on the 25$^{\text{th}}$ of July 2019 at noon and Figure 7.20, where $\sigma_r^2 = 50$ m^2.

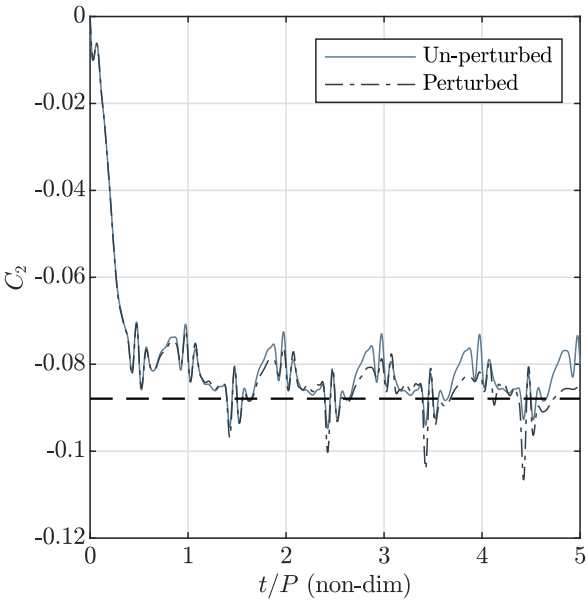

Figure 7.19: Effect of Sun 3BP and SRP on the reconstruction of C_{20}.

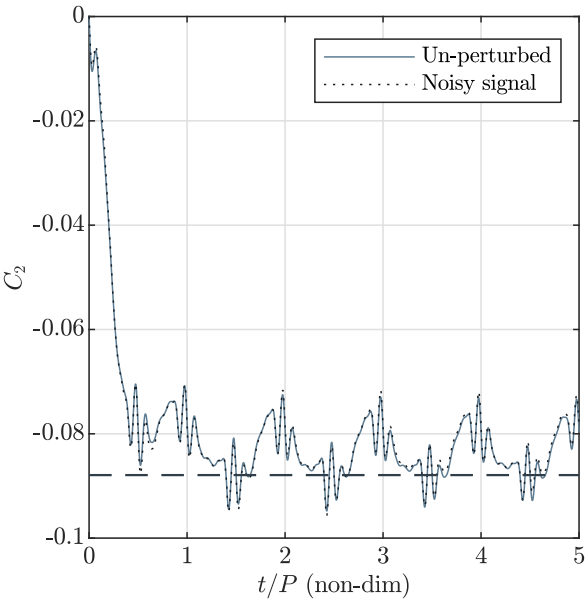

Figure 7.20: Effect of instrument noise on the reconstruction of C_{20}.

In this case a major difficulty comes from the fact that, orbits closer to the body feels a highly irregular field and results to highly unstable orbits. This obviously influence negatively the convergence of the MHNN as well as can lead to divergence.

7.2.1 MHNN sensitivity to asteroid rotation perturbations

In Chapter 1 on page 21 the equation of motion for the rotational dynamics of the central body where presented. Since the aim of this section is to analyse the effect of a *perturbation* on the rotational dynamics of the body, that in previous analysis was assumed to be uniform about the principal inertia axis $\mathbf{b}_3$, it convenient to reason with only the free dynamics associated to the body e. g., $\mathbf{m} = 0$. This is a strong assumption since the rotational dynamics of such kind of bodies is usually highly perturbed but for this analysis it would introduce a complexity that can be avoided considering perturbations to the ideal rotational axis $\boldsymbol{\omega} = \omega \mathbf{b}_3$. In fact expressing the rotational axis unit vector in spherical coordinates as

$$\hat{e}_\omega = \begin{Bmatrix} \cos(\delta\lambda)\sin(\delta\theta) \\ \sin(\delta\lambda)\sin(\delta\theta) \\ \cos(\delta\theta) \end{Bmatrix} \tag{7.10}$$

Then the reference state is the one where $\delta\theta = 0$. So, assuming every other conditions would lead to a perturbation to the rotational axis of the body. In order be a considered

a perturbation then $\delta\theta$ must be small, so that:

$$\hat{e}_\omega \approx \begin{Bmatrix} \delta\theta \cdot \cos(\delta\lambda) \\ \delta\theta \cdot \sin(\delta\lambda) \\ 1 \end{Bmatrix} \tag{7.11}$$

Note that $\delta\lambda$ can assumed to be any value between 0 and 360° since if $\delta\theta$ is small. Using this model the rotational axis would remain on the cone built from the revolution of $\hat{e}_\omega$ about the $\hat{b}_3$ axis e. g., precession motion is experienced.

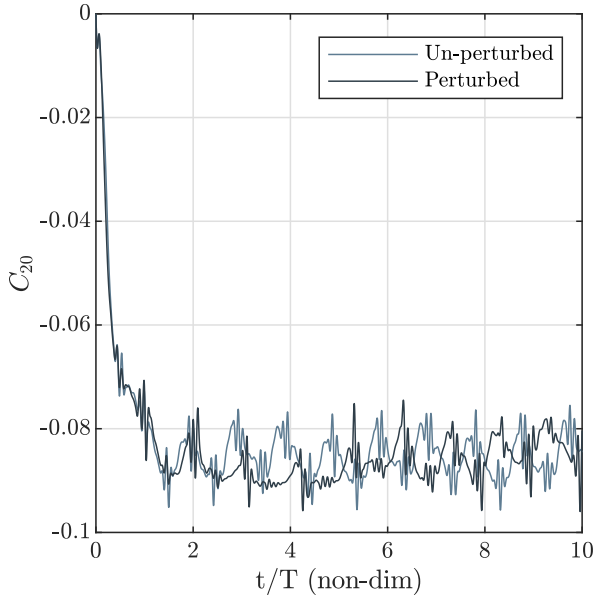

Figure 7.21: Identification of C_{20} in the case of the perturbed rotation of Castalia.

The sensitivity analysis results for the case of a $\Gamma_{90}^{4:1}$ orbit about the asteroid Castalia are presented in Figure 7.21. Here the perturbations to the rotational axis direction are assumed to be $\delta\theta = \delta\lambda = 5°$ and the MHNN is initialized with $\beta = 1e-5$. As it can be seen, the perturbations enters the identification. Of course, as far as the perturbations increase in magnitude as the rotation of the asteroid becomes less uniform resulting in a more perturbed identification.

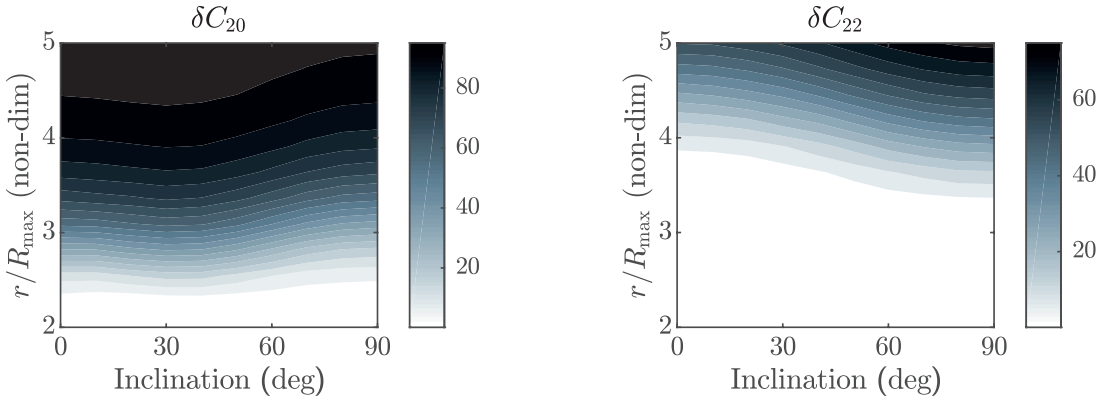

Figure 7.22: $\delta C_{nm}(i_0, a_0)$ analysis results for the case of Castalia.

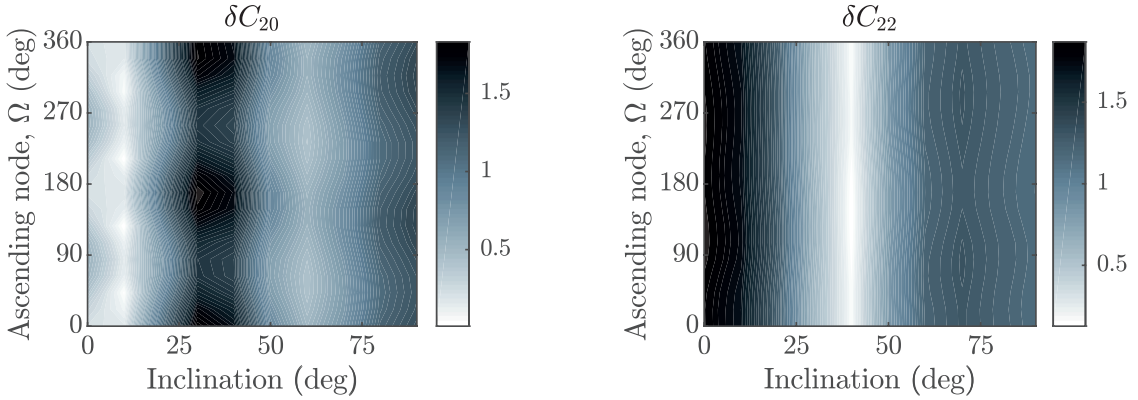

Figure 7.23: $\delta C_{nm}(i_0, \Omega_0)$ analysis results for the case of Castalia.

7.3 MHNN Performances Compared

In the previous sections of this Chapter the behaviour of the MHNN is being studied for some specific cases. The intention of this section is, indeed to sum-up those results in order to extract global behaviours of the identification. In this case the identification of the coefficients C_{20} and C_{22} is analysed.

7.3.1 Sensitivity to orbital initial conditions

First of all, also in the case of the asteroid Castalia it is possible to perform a parametric analysis on the initial conditions in terms of a_0 and i_0, as it has been done for the case of Bennu: referring to Figure 7.8 for it, the results for the case of Castalia are presented in Figure 7.22. Note that in this last case only the coefficients C_{20} and C_{22} have been computed. The network is initialized with the same β of the case of Bennu. It can be seen in both Figure 7.22 and Figure 7.8 that the behaviour of the parameter of merit δC_{nm} is really similar despite the fact that the asteroids are really different.

In the same way a parametric analysis can be done on the initial inclination i_0 and the longitude of the ascending node Ω_0. The results are presented in Figure 7.23 and Figure 7.24 for the case of Castalia and Bennu respectively. In this case a $\Gamma_{\alpha}^{3\mathrm{R}_{\max}}$ is considered and the network is initialized with $\beta = 1e-7$.

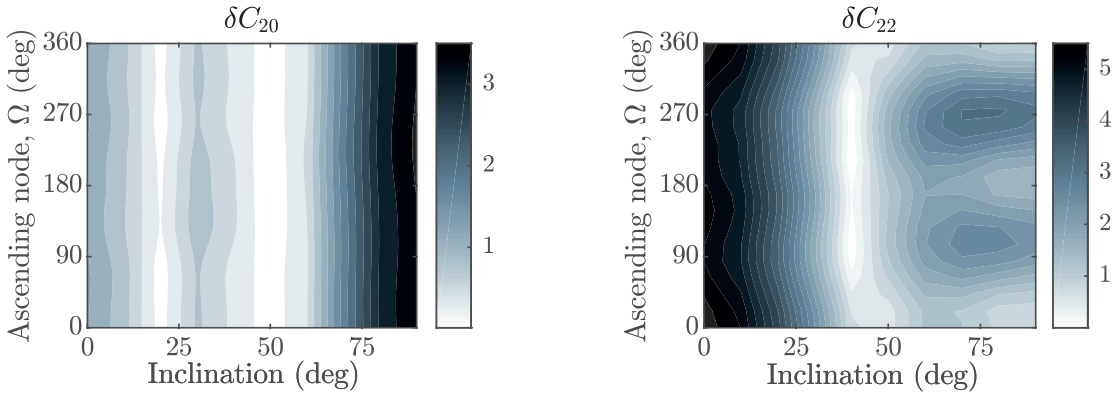

Figure 7.24: $\delta C_{nm}(i_0, \Omega_0)$ analysis results for the case of Bennu.

7.3.2 Results analysis

From all the previous results the previous results we can extract some general global behaviours:

(R1) The *estimation velocity* has a strong dependence on the distance and on β/α. This can be clearly noticed, for example, from Figure 7.22 where the error become large as far as the normalized distance increases and it is due to the fact that a fine tuning of the network is needed as far as the reference orbit changes.

(R2) The *estimation accuracy* is good whenever the network is well-trained e. g., β or α are correctly selected. This can be seen from both Figure 7.23 and Figure 7.24 where β is selected to be $1e-7$ as the result of a optimization. Moreover, the accuracy seems to be weakly dependant on combinations of i_0, Ω_0, at a fixed β.

(R3) The fact that the choice of beta β is fundamental for the overall performances of the network is underlined again. In Figure 7.25, the results associated to the evaluation of δC_{nm} for a $\Gamma_{45}^{3\mathrm{R}_{\max}}$ are presented: a wrong choice of beta can lead to completely wrong results. Recall also that a β too small lead to instability of the network as well as large oscillations.

(R4) Convergence as well as instability phenomena are non-linearly and probably stochastically coupled with the reference orbit and, in the case of rounded objects, strongly coupled with a_0, i_0 and β e. g., a *fine* tuning is needed.

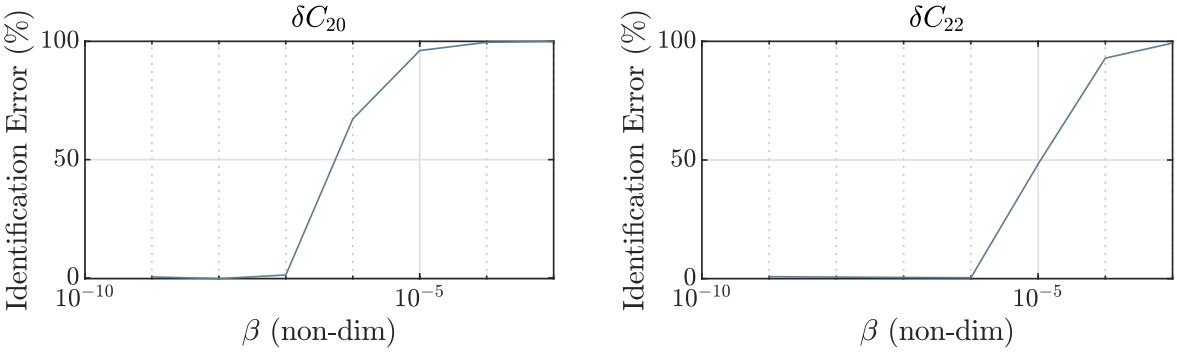

Figure 7.25: $\delta C_{nm}(\beta)$ analysis results for the case of Castalia.

In Figure 7.26, moreover the results for the case of a $\Gamma_{\alpha}^{3\mathrm{R}_{\max}}$ orbit are presented: it

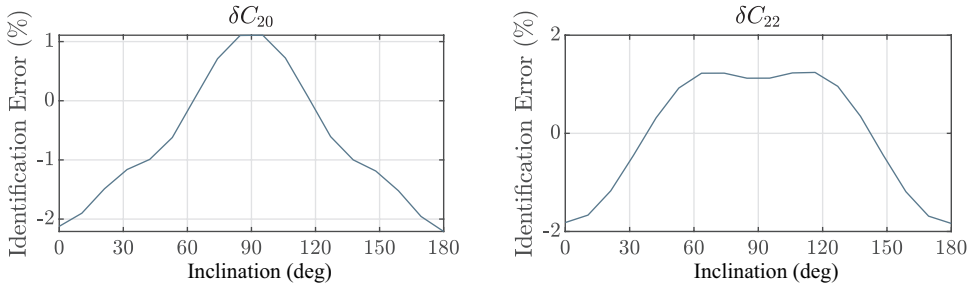

Figure 7.26: $\delta C_{nm}(i_0)$ analysis results for the case of Castalia.

can be seen that the behaviour as a function of the initial i_0 is symmetric with respect to $i_0 = 90°$ and symmetric for the two cases. In fact, for $i_0 = 90°$, δC_{20} exhibit a maximum of the parameter of merit as also δC_{22}. These maximum are, however, not a maximum of magnitude. Moreover, the errors in the estimation of C_{20} are comparable with respect to the ones associated with C_{22} in this case. Finally it is interesting the fact that retrograde orbits' estimation performances are specular to direct ones. Note that the optimal condition for C_{20} is near 60° while for C_{22} near 40° in this case.

7.3.3 Sample-based convergence analysis

(S1) In Figure 7.27 and Figure 7.28 the results for a $\Gamma_{90}^{3\mathrm{R}_{\max}}$ based identification in the case of Bennu and Castalia respectively. In those cases $\beta = 1e-7$. In both cases a good convergence for both the coefficients is evident.

(S2) The identification capabilities of the network are further confirmed by the analysis of the reconstructed accelerations. An example of the performances in the approximation of the acceleration is presented in Figure 7.30 for the case of a $\Gamma_{45}^{3\mathrm{R}_{\max}}$ about Bennu. In this case $\beta = 1e-7$. Here the normalized accelerations are defined as $\tilde{a} = \frac{a}{\mu} R_{\max}^2$.

So, in general we can conclude that the capability of the network to reconstruct low-degree harmonics is good, fast and accurate for both the case of rounded as well as of irregular bodies. Of course, there is a dependence on the body and on the initialization of β, that seems again to be a *critical* parameter.

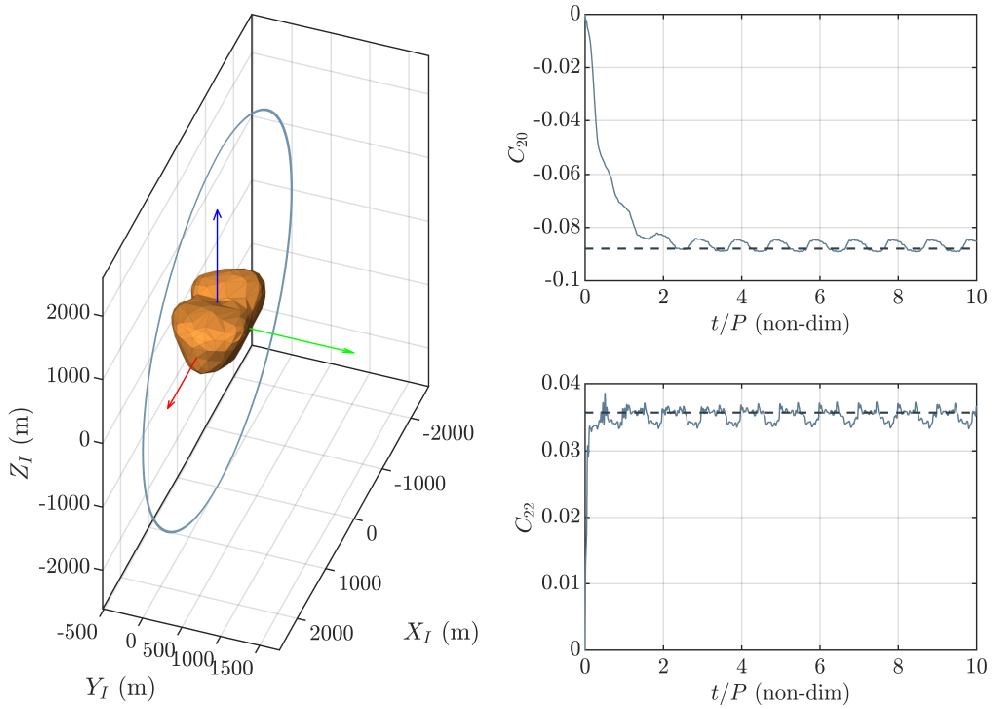

Figure 7.27: MHNN identification: a $\Gamma_{90}^{3R_{max}}$ orbit about Castalia.

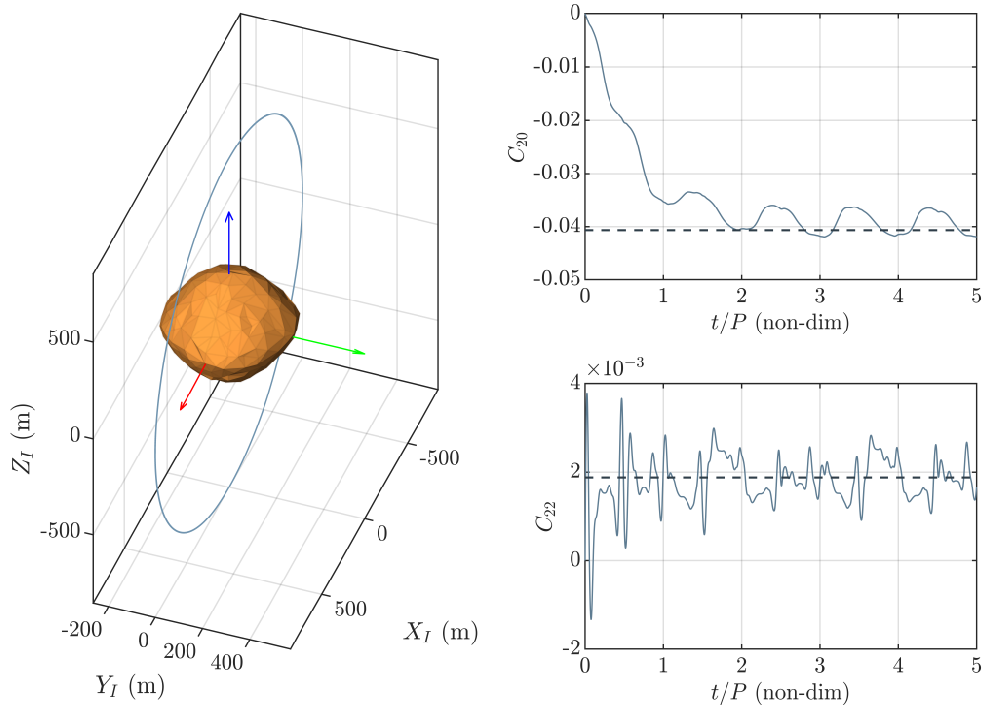

Figure 7.28: MHNN identification: a $\Gamma_{90}^{3R_{max}}$ orbit about Bennu.

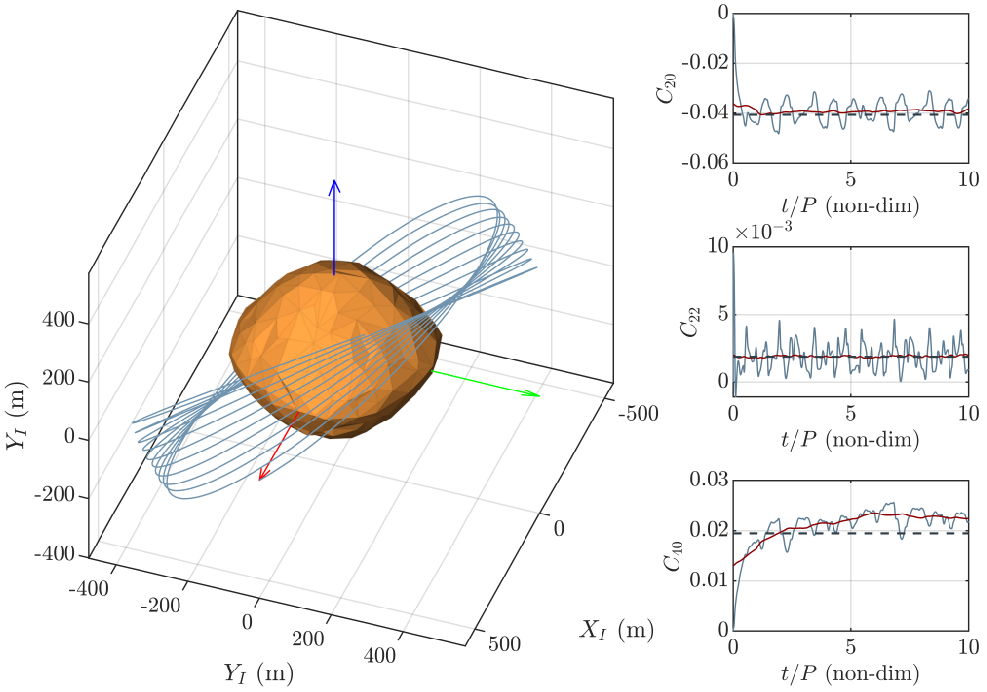

Figure 7.29: MHNN identification: a $\Gamma_{45}^{3R_{max}}$ orbit about Bennu. Red curve represents a moving mean performed over a single period.

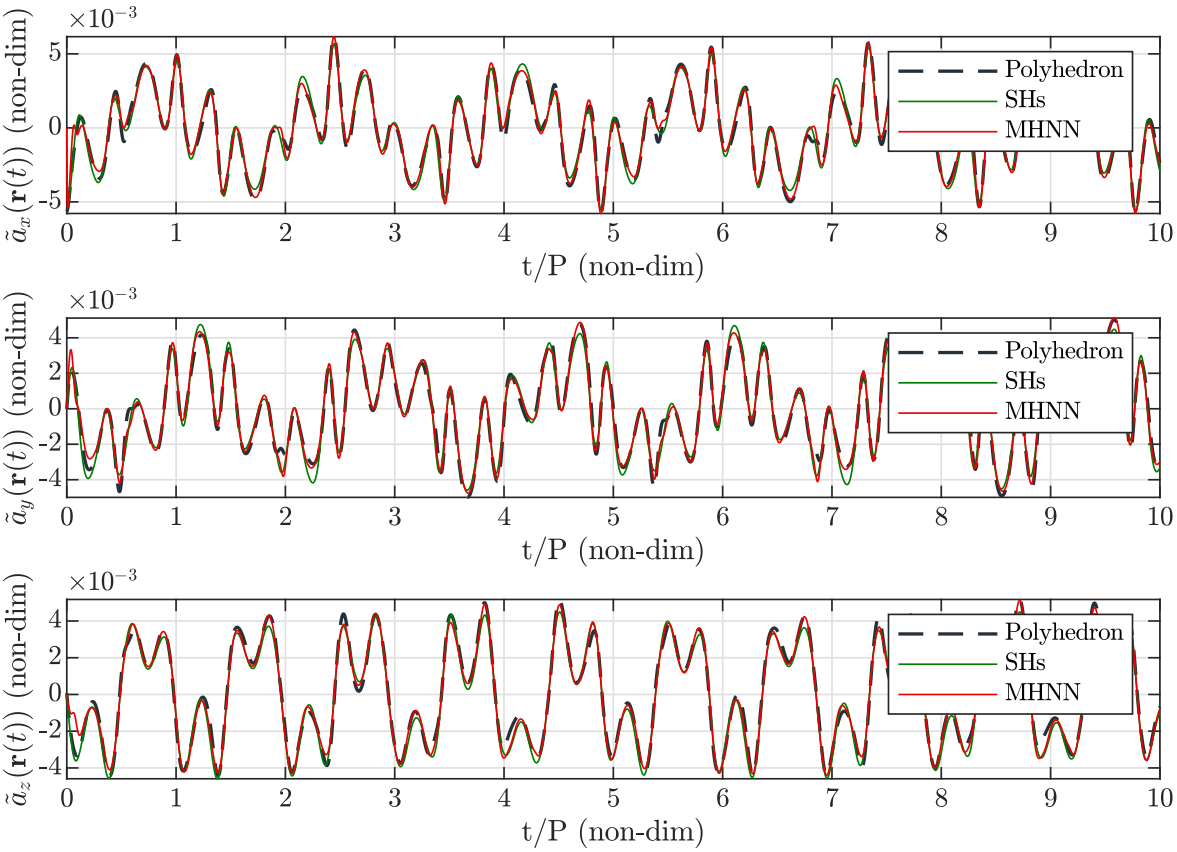

Figure 7.30: Main body normalized acceleration perturbations reconstruction associated to the orbit presented in Figure 7.29.

7.4 The Case of the Binary 66391 (1999 KW4)

In previous sections, the analysis of the convergence of the MHNN has been studied on the basis of the P2BP. The aim of this part is to show how to extend the methodology to a three-body case. In particular, the case of the binary system 66391 (1999 KW4) is considered under the MCR3BP hypothesis.

Table 7.4: *KW4 binary main parameters*

μ (non-dim)	Ω_S (rad/s)	d_{12} (m)
0.05430	1.0019e-4	2548

In Table 7.4, the main parameter associated to the corresponding CR3BP. Note that in this case the triangular points results to be unstable.

7.4.1 Force model

In this case two force models are used as the basis of the identification. In particular, a spherical harmonic expansion in which the terms associated to the coefficients C_{20} ad C_{22} are retained for both bodies is considered as a baseline in this case.

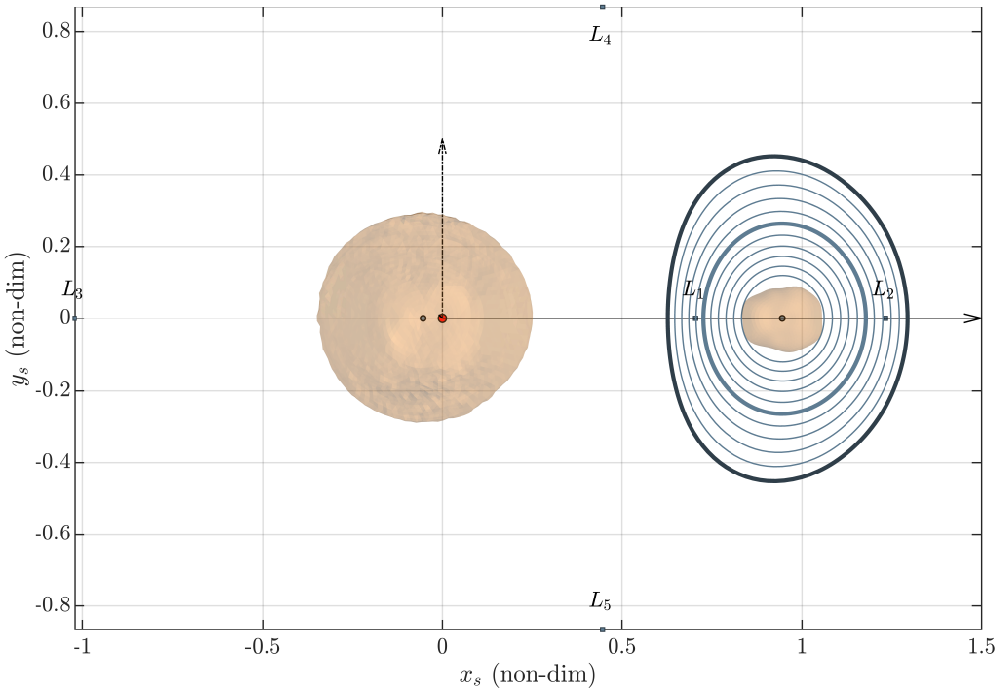

Figure 7.31: DRO family.

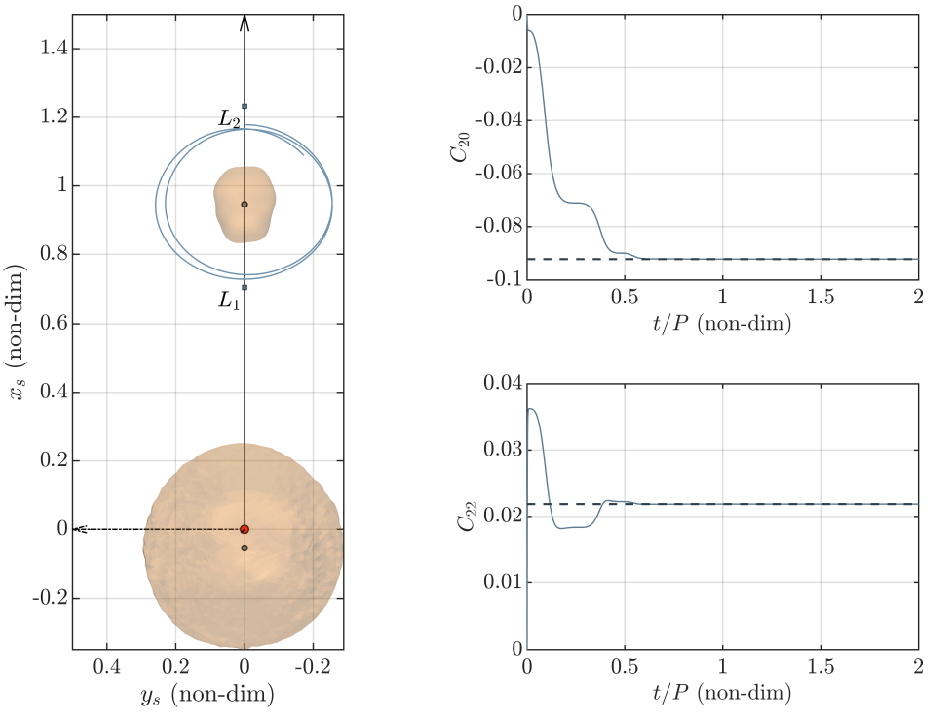

Figure 7.32: Results for the binary system in the case of a DRO close to KW4-β. For the network, $\beta = 1e-7$.

7.4.2 Identification

It is of interest to see if the method based on the MHNN works also in the case the orbit is a non-Keplerian orbit that lives in the three-body problem. For this purpose, a simulation is setted up with the aim to reconstruct the coefficient associated with KW4-β. In this case the LIP form of the equations is tricky since both the asteroids are rotating with different angular velocities. Then defining $\mathbb{T}_k = \mathbb{T}_{\Omega_1}\mathbb{T}_{\Omega_S}^T$, then:

$$\mathbb{T}_2^T\left(\dot{\mathbf{v}} - \mathbf{a}_{\text{CO}} - \mathbf{a}_{\text{CF}} - \mathbb{T}_1\mathbf{a}_1\right) + \frac{\mu_2}{r_2^3}\mathbf{r}_2 = \mathbb{A}(\mathbf{r}_2)\cdot\mathbf{p} \tag{7.12}$$

DROs are preferred for the identification due to their stability. Refer to 1.4.2 on page 31 for their generation in the CR3BP/MCR3BP. In Figure 7.31 some orbits of the family are presented. Then, for the identification the dark thick orbit is used as the example of the identification on distant orbit while the gray-blue one as the case of a much closer orbit (referred to KW4-β). In this case, since the interest of the thesis is only to address the possibility to apply the method for the case of a binary systems, the generation of the DRO is performed on the basis of the CR3BP using the single shooting method. From the results presented in Figure 7.32, Figure 7.33 it can be seen that the capability of the network to reconstruct the dynamics is good also in that case.

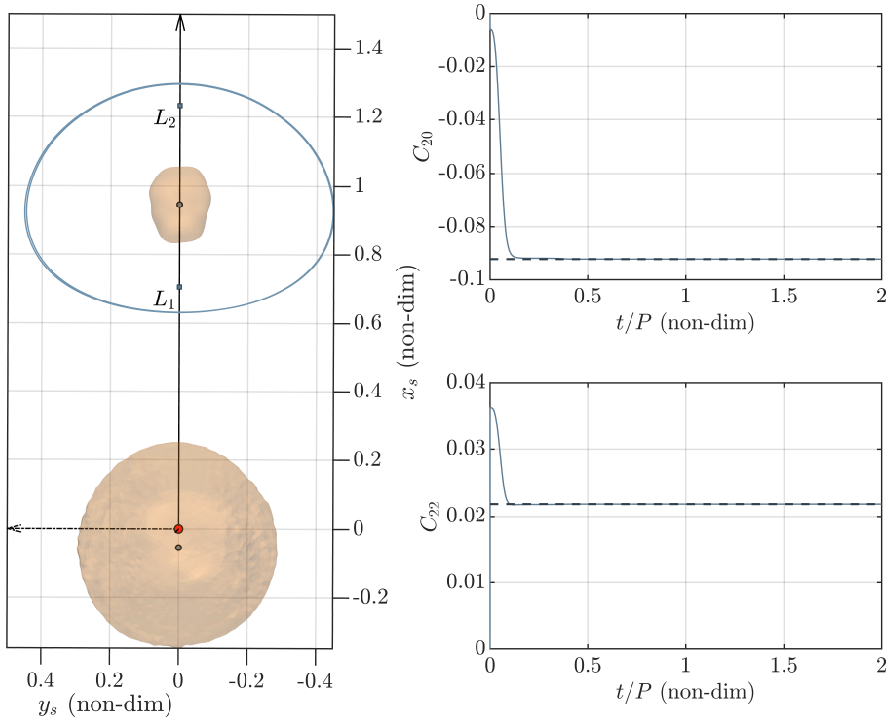

Figure 7.33: Results for the binary system in the case of a DRO at a mid-distance from KW4-β. For the network, $\beta = 1e - 9$.

Part IV

MHNN-Based Small Bodies Navigation Filter

CHAPTER 8

THE EXTENDED KALMAN FILTER

The use of the EKF for navigation has a long history of flight-proven success [65]. Since the filter needs a model of the dynamical environment, the implementation in parallel to the MHNN identification seems to be promising. First, it has to be said that the use of a EKF is preferred over the one of a Unscented Kalman Filter (UKF) since one of the aims of this thesis is to enhance the autonomy degree of small satellites with limited computational capabilities, then being the EKF much lighter from this point of view, it is selected.

The Kalman Filter (KF) was firstly developed by Rudolf E. Kalman in 1960's [66]: it can statistically minimize the error of the state combining the actual available measurements and the prior knowledge of the system. However, this approach involves some basic assumptions. The classical KF, in fact, is used only with linear system. Moreover, the noise is assumed to be white. This means that the noise value is not correlated in time and that its power is equal for each frequency. This would imply that the noise has infinite power and this is not applicable to any real case. Finally, the noise has to be a Gaussian distribution [67].

However, many real-world applications use non-linear models for describing the system or the measurements. Then, in the early 1980's, Maybeck [68] introduces the EKF that tries to overcome the limitations of the linearity of the models used in the KF. The idea is to use a non-linear description of the system model and linearise this model about the state estimation for each time step. So, as soon as a new estimate is predicted, a linearised trajectory is available in the estimation process. Remembering that the linearisation process involves the assumption of small deviations from the reference trajectory, this can be ensured by incorporating the update of the reference trajectory in the estimation process.

Algorithm 2 EKF procedure

Require: $\hat{\mathbf{x}}(0|0), \mathbb{P}(0|0)$
1: **for** $k = 1, \ldots, n$ **do**
2: **procedure** PREDICTION
3: $\hat{\mathbf{x}}(k|k-1) = \hat{\mathbf{x}}(k-1|k-1) + \int_{k-1}^{k} \mathbf{f}(\mathbf{x}(t))\, dt$ *(state prediction)*
4: $\mathbb{F} = \left.\frac{\partial \mathbf{f}(\mathbf{x})}{\partial \mathbf{x}}\right|_{\mathbf{x}=\hat{\mathbf{x}}(k|k-1)}$ *(process Jacobian)*
5: $\mathbf{\Phi}_k = \mathbb{I} + \mathbb{F}\Delta t$ *(state transition matrix)*
6: $\mathbb{P}(k|k-1) = \mathbf{\Phi}_k \mathbb{P}(k-1|k-1)\mathbf{\Phi}_k^T + \mathbb{Q}$ *(covariance prediction)*
7: $\mathbf{h}(\hat{\mathbf{x}}(k|k-1))$ *(measurement prediction)*
8: **end procedure**
9: $\mathbf{z}(k) = \mathbf{y}(k) - \mathbf{h}(\hat{\mathbf{x}}(k|k-1))$ *(innovation evaluation)*
10: $\mathbb{H} = \left.\frac{\partial \mathbf{h}(\mathbf{x})}{\partial \mathbf{x}}\right|_{\mathbf{x}=\hat{\mathbf{x}}(k|k-1)}$ *(measurements Jacobian)*
11: $\mathbb{S}(k) = \mathbb{H}\mathbb{P}(k|k-1)\mathbb{H}^T + \mathbb{R}(k)$ *(covariance innovation)*
12: $\mathbb{K}(k) = \mathbb{P}(k|k-1)\mathbb{H}^T[\mathbb{S}(k)]^{-1}$ *(Kalman gain)*
13: **procedure** UPDATE
14: $\hat{\mathbf{x}}(k|k) = \hat{\mathbf{x}}(k|k-1) + \mathbb{K}(k)\mathbf{z}(k)$ *(update state)*
15: $\mathbb{P}(k|k) = [\mathbb{I} - \mathbb{K}(k)\mathbb{H}]\mathbb{P}(k|k-1)$ *(update covariance)*
16: **end procedure**
17: **end for**

8.1 Dynamical Model

Now, for the development of the filter, assume to ave a stochastic differential equation given by [65]:

$$d\mathbf{x}(t) = \mathbf{f}(\mathbf{x}(t), t) + \mathbb{B}(t)\, d\mathbf{w}_x(t) \tag{8.1}$$

where $\mathbf{x}(t) \in \mathbb{R}^n$ is a random process whose distribution is known at t_0 and $d\mathbf{w}_x(t)$ is the *process noise* that reflect the uncertainty to in the dynamical model. Suppose also that the initial distribution $\mathbf{x}(t)$ is Gaussian with mean and covariance given by

$$E[\mathbf{x}(t_0)] = \bar{\mathbf{x}}_0 \quad \text{and} \quad E[(\mathbf{x}(t_0) - \bar{\mathbf{x}}_0)(\mathbf{x}(t_0) - \bar{\mathbf{x}}_0)^T] = \mathbb{P}_0 \tag{8.2}$$

and suppose that the infinitesimal increments of $\mathbf{w}(t)$ are Gaussian, with:

$$E[\mathbf{w}_x(t)] = \mathbf{0} \quad \text{and} \quad E[\mathbf{w}_x(t)\mathbf{w}_x^T(\tau)] = \mathbb{Q}(t)\, \delta(t - \tau) \tag{8.3}$$

Assume also that:

$$E[\mathbf{w}_x(t)(\mathbf{x}(t_0) - \bar{\mathbf{x}}_0)^T] = 0, \forall t \tag{8.4}$$

Note that even though we have assumed that $\mathbf{x}(t_0)$ and $\mathbf{w}_x(t)$ are Gaussian, we cannot assume that $\mathbf{x}(t)$ remains Gaussian for $t > t_0$, because $\mathbf{f}(\mathbf{x}(t), t)$ is non-linear.

8.2 Measurement Model

In an ideal world, we might have devices for measuring all of the state vector components directly. Unfortunately, this is almost never the case. Instead measures of other

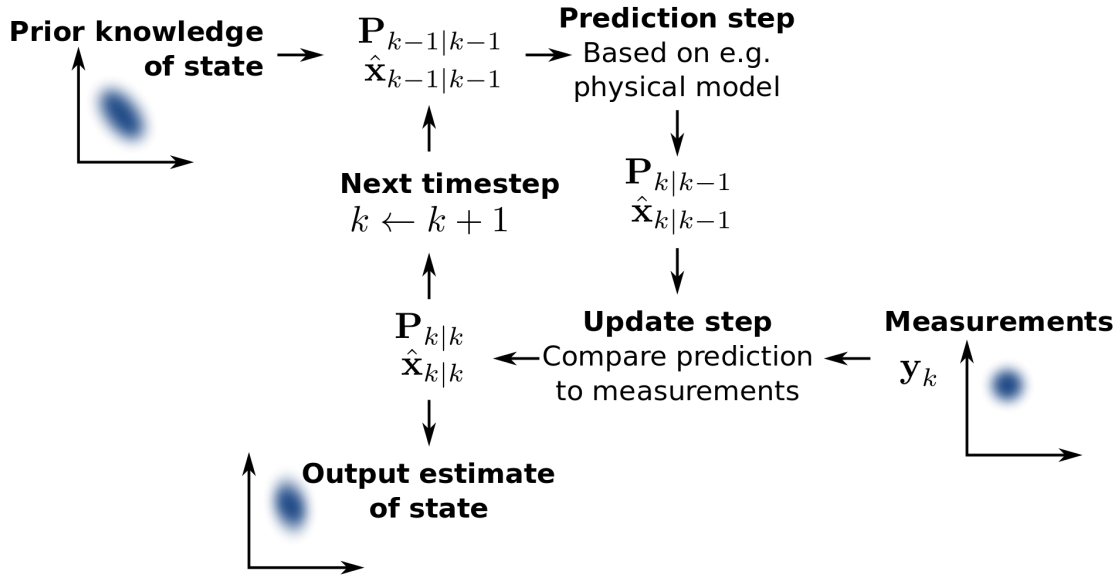

Figure 8.1: EKF algorithm scheme. Credits [31].

quantities related to the state are usually available, at discrete times t_i as:

$$\mathbf{y}(t_i) = \mathbf{h}(\mathbf{x}(t_i), t_i) + \mathbf{w}_y(t_i) \tag{8.5}$$

where here $\mathbf{h} : \mathbb{R}^n \to \mathbb{R}^m$ is the *measurement function* and $\mathbf{w}_y(t_i)$ a Gaussian *measurement noise* with mean and covariance given by

$$E[\mathbf{w}_y(t)] = \mathbf{0} \quad \text{and} \quad E[\mathbf{w}_y(t_i)\mathbf{w}_y^T(t_j)] = \mathbb{R}(t_i)\,\delta(t_{ij}) \tag{8.6}$$

Assume also that:

$$E[\mathbf{w}_y(t_i)(\mathbf{x}(t_0) - \bar{\mathbf{x}}_0)^T] = 0 \quad \text{and} \quad E[\mathbf{w}_x(t)\mathbf{w}_y^T(t_i)] = 0 \quad \forall t, i \tag{8.7}$$

8.3 Numerical Implementation

As already said, the system and the measurement equations are non-linear. This implies that a first-order approximation has to be used in the continuous Riccati equations for the systems dynamics matrix $\mathbb{F}$ and the measurement matrix $\mathbb{H}$ respectively. These are defined as:

$$\mathbb{F} = \left.\frac{\partial \mathbf{f}(\mathbf{x})}{\partial \mathbf{x}}\right|_{x=\hat{x}} \quad \text{and} \quad \mathbb{H} = \left.\frac{\partial \mathbf{h}(\mathbf{x})}{\partial \mathbf{x}}\right|_{x=\hat{x}} \tag{8.8}$$

The fundamental matrix for the discrete Riccati equations is approximated by the Taylor-series expansion of $e^{\mathbb{F}\Delta t}$, and can be expressed as:

$$\mathbf{\Phi}_k = \mathbb{I} + \mathbb{F}\Delta t + \dots \tag{8.9}$$

where Δt is the sampling time. In general, the Taylor-series expansion is approximated with only the first two terms [67],[65]. Then the EKF procedure is briefly summarized in pseudo-code in Algorithm 2 on the preceding page.

8.3.1 System Dynamics

The dynamical model associated to the stochastic differential equation under the hypothesis of the P2BP have state vector $\mathbf{X}$ defined as

$$\mathbf{X} = \{\mathbf{r}; \mathbf{v}\} = \{x \quad y \quad z \quad u \quad v \quad w\}^T \tag{8.10}$$

So that the dynamics function results:

$$\mathbf{f}(\mathbf{X}(t), t) = \begin{cases} u \\ v \\ w \\ 2\Omega v + \Omega^2 x + \frac{\partial \mathcal{U}_{\text{NET}}}{\partial x} \\ -2\Omega u + \Omega^2 y + \frac{\partial \mathcal{U}_{\text{NET}}}{\partial y} \\ \frac{\partial \mathcal{U}_{\text{NET}}}{\partial z} \end{cases} = \begin{cases} u \\ v \\ w \\ 2\Omega v + \frac{\partial \mathcal{V}_{\text{NET}}}{\partial x} \\ -2\Omega u + \frac{\partial \mathcal{V}_{\text{NET}}}{\partial y} \\ \frac{\partial \mathcal{V}_{\text{NET}}}{\partial z} \end{cases} \tag{8.11}$$

Where the *modified potential function* is defined as:

$$\mathcal{V}_{\text{NET}}(\mathbf{r}, t) = \mathcal{U}_{\text{NET}}(\mathbf{r}, t) + \frac{1}{2}\Omega^2(x^2 + y^2) \tag{8.12}$$

Note that here the underscore NET means that the potential function $\mathcal{U}$ is the one reconstructed by the MHNN. Moreover, the Jacobian associated to the dynamics is $\mathbb{F}$ and can be computed as:

$$\mathbb{F}(\mathbf{r}, t) = \frac{\partial \mathbf{f}}{\partial \mathbf{X}} = \begin{bmatrix} \frac{\partial f_1}{\partial x} & \frac{\partial f_1}{\partial y} & \cdots & \frac{\partial f_1}{\partial w} \\ \frac{\partial f_2}{\partial x} & \ddots & \vdots & \vdots \\ \vdots & \cdots & \ddots & \vdots \\ \frac{\partial f_6}{\partial x} & \cdots & \cdots & \frac{\partial f_6}{\partial w} \end{bmatrix} = \begin{bmatrix} \mathbf{O}_{3\times 3} & \mathbb{I}_{3\times 3} \\ \nabla\nabla\mathcal{V}_{\text{NET}}(\mathbf{r}, t) & -2\Omega[\mathbf{I}] \end{bmatrix} \tag{8.13}$$

where here $\nabla\nabla\mathcal{V}_{\text{NET}}(\mathbf{r}, t)$ represent the gravity gradient and $[\mathbf{I}]$ the skew-symmetric cross product matrix.

8.3.1.1 System Dynamics with SRP

The inclusion of the SRP in the dynamical model of the filter is important since it can be of the same order of magnitude of the body's gravity. So, even, a simple SRP model can help the filter to converge and give more accurate results. In this case the dynamic function can be written as: So that the dynamics function results:

$$\mathbf{f}(\mathbf{X}(t), t) = \begin{cases} u \\ v \\ w \\ 2\Omega v + \frac{\partial \mathcal{V}_{\text{NET}}}{\partial x} + a_{x,\text{SRP}} \\ -2\Omega u + \frac{\partial \mathcal{V}_{\text{NET}}}{\partial y} + a_{y,\text{SRP}} \\ \frac{\partial \mathcal{V}_{\text{NET}}}{\partial z} + a_{z,\text{SRP}} \end{cases} \tag{8.14}$$

Where here, according to Chapter 1, the SRP model can be written as:

$$\mathbf{a}_{\text{SRP}} = -C\frac{\mathbf{s}-\mathbf{r}}{|\mathbf{s}-\mathbf{r}|^3} \tag{8.15}$$

Then defining $\tilde{r} = |\mathbf{s}-\mathbf{r}|$ and $\mathcal{SX}_i = s_i - r_i$, the SRP model can be rewritten as, per components:

$$a_{i,\text{SRP}} = -C\frac{\mathcal{SX}_i(\mathbf{r},\mathbf{s})}{\tilde{r}^3(\mathbf{r},\mathbf{s})} \tag{8.16}$$

So, in general, at each time step k, the EKF needs an information of the spacecraft state relative to the body ($\mathbf{r}$) as well as an information of the state of the body about the Sun ($\mathbf{s}$). Moreover, the coefficient C can depend on the attitude of the spacecraft so that can be time dependant. Finally, the orbit of small solar system bodies are usually uncertain and this introduce a further complexity on the problem. There are a number of approaches possible. Among the others, the most accurate are:

1. Introduce the body state inside the EKF estimation;
2. Use a Schmidt-Kalman filter ([69],[70]): this method allows to propagate the uncertainty associated to the orbit of the body without the introduction of its orbital states in the estimation process.

However, in this work, since the preliminary performances of the filter are assessed, none of those methods is used: since the orbital period of a spacecraft about any small body is much smaller than the orbital period of the body about the Sun, the Sun position vector is assumed to be well known and time fixed e. g., $\mathbf{s}(t) = \bar{\mathbf{s}}$, such that.

$$a_{i,\text{SRP}} = -\bar{C}\frac{\mathcal{SX}_i(\mathbf{r})}{\tilde{r}^3(\mathbf{r})} \tag{8.17}$$

Then the Jacobian associated to the SRP part of the model can be written as:

$$\mathbb{F}^*_{\text{SRP}}(\mathbf{r},t) = \frac{\partial \mathbf{a}_{\text{SRP}}}{\partial \mathbf{X}} = \begin{bmatrix} \dfrac{\partial \mathbf{a}_{\text{SRP}}}{\partial \mathbf{r}} & \mathbf{O}_{3\times 3} \end{bmatrix} \tag{8.18}$$

where here, being δ_{ij} the Kronecker delta:

$$\frac{\partial a_{i,\text{SRP}}}{\partial r_j} = \frac{\bar{C}}{\tilde{r}^3}\left[\delta_{ij} - 3\frac{\mathcal{SX}_i\mathcal{SX}_j}{\tilde{r}^2}\right] \tag{8.19}$$

So that the model Jacobian results:

$$\mathbb{F}(\mathbf{r},t) = \frac{\partial \mathbf{f}}{\partial \mathbf{X}} = \begin{bmatrix} \mathbf{O}_{3\times 3} & \mathbb{I}_{3\times 3} \\ \nabla\nabla\mathcal{V}_{\text{NET}}(\mathbf{r},t) + \dfrac{\partial \mathbf{a}_{\text{SRP}}}{\partial \mathbf{r}} & -2\Omega[\mathbf{I}] \end{bmatrix} \tag{8.20}$$

CHAPTER 9

MHNN-BASED EKF FILTER

In this chapter a basic EKF navigation filter is implemented and integrated with the results obtained by the MHNN. The aim of the discussion is to improve the performances of the filter through the use of a reconstructed spherical harmonics expansion as system dynamical model. Since the aim is not to implement a real-world test case for the filter, a simplified measurement model is implemented. In particular, recalling that the discrete time measurement model can be written as

$$\mathbf{y}(t_i) = \mathbf{h}(\mathbf{x}(t_i), t_i) + \mathbf{w}_y(t_i) \tag{9.1}$$

In this case, since the real dynamics $\mathbf{x}_{\mathrm{R}}(t)$ is assumed to be available, then the measures can be assumed to be a Gaussian distribution about it with a variance $\boldsymbol{\sigma}_y$, such that

$$\boldsymbol{\sigma}_y = \{(\sigma_{y,r})_{1\times 3} \ ; \ (\sigma_{y,v})_{1\times 3}\} \tag{9.2}$$

Then the measurement dynamics can be written as

$$\mathbf{y}(t_i) = \mathcal{N}(\mathbf{x}_{\mathrm{R}}(t_i), \boldsymbol{\sigma}_y) \tag{9.3}$$

This constraint, from the mathematical point of view, the form of the covariance matrix associated to the measures, that is:

$$\mathbb{R} = \mathbb{R}(t_i) = \mathrm{diag}\{\boldsymbol{\sigma}_y^2\} \tag{9.4}$$

The last assumptions are associated to the model covariance and the process covariance. In particular for what regards the model, its covariance matrix is assumed to be a diagonal time-independent matrix of the form:

$$\mathbb{Q} = \mathrm{diag}\{(\sigma_{q,r}^2)_{3\times 1} \ , \ (\sigma_{q,v}^2)_{3\times 1}\} \tag{9.5}$$

while the process covariance is initialized as:

$$\mathbb{P}(0) = \text{diag}\{(\mathbf{x}_{\text{R}}(t_p) - \mathbf{x}_{\text{M}}(t_p))^2\} \tag{9.6}$$

where here $\mathbf{x}_{\text{M}}(t)$ represents the propagation of the filter model dynamics and $t_p \in (0, T_{\max})$. In this case, if the time step of the propagation is defined t_s then $t_p = t_s$, so that the process covariance is initialized by the models difference after a step.

Finally, a note on the system dynamics must be said: the MHNN identification, has it has been extensively analysed in the previous chapters, is a time dependant process. Indeed, if a dynamical model is built on it, it would be time dependant too. This is a complicating effect since in this case the filter need a fine time-dependant tuning. This task goes beyond the aim of this work but is deeply investigated by other authors [**67**].

9.1 Numerical Investigation on Simple Bodies

In order to assess the performance of the navigation filter, some test cases are analysed in this section on ellipsoidal bodies. First, the notation that used is presented: the body physical and geometrical properties are organized in a row vector $\{\chi_\alpha, \chi_\beta, \chi_\gamma; \varrho, R_0\}$, with dimensions $\{\text{n.d.}, \text{n.d.}, \text{n.d.}; \text{kg/m}^3, \text{km}\}$; the orbit selected is, instead, denoted as $\Gamma^{a_0}_{i(^\circ)}$ while the filter parameters as $\{T_s; \sigma_{y,r}, \sigma_{y,v}, \sigma_{q,r}, \sigma_{q,v}\}$. The filter dynamics model is assumed to be time-fixed, as the result of the convergence of the MHNN.

Finally, the results are compared in terms of normalized Root Mean Square Error (nRMSE) as:

$$\text{nRMSE}(t_i) = \frac{||x_{\text{R}}(t_i) - \hat{x}(t_i)||}{||x_{\text{R}}(t_i)||} \tag{9.7}$$

where here the quantity of interest is x and x_{R} is its real value while $\hat{x}$ the EKF reconstructed value. Please note that, substuting $\hat{x}$ with the measures y, the normalized precision of the measures is obtained.

Case 1. In this case, the performance of the filter are assessed on a simple case. An oblate spheroid with $\{1, 1, 0.7; 2700, 1\}$ is considered and a $\Gamma^{2R_0}_{45}$ orbit is assumed. In Figure 9.1 the results for a case in which the EKF is tuned according to $\{30 \cdot 60; 1, 1e-2, 1e-3, 1e-3\}$, with T the orbital period. Note that in this case the measurements are assumed to be extremely precise and the performances of the 2-body dynamical model are similar to the one of the 2nd-degree SHE model: small differences can be seen and the last appears to be more precise than the former. However, a deeper statistical analysis is needed to asses the real performances of the filter but it goes beyond the scope of this test.

Case 2. In this case, a parametric analysis is performed on the object of *case 1.* To do so, consider two non-dimensional coefficients ξ_Q and ξ_R such that the filter parameters becomes: $\{t_s; \sqrt{\xi_R}\sigma_{y,r}, \sqrt{\xi_R}\sigma_{y,v}, \xi_Q\sigma_{q,r}, \xi_Q\sigma_{q,v}\}$. Note that the coefficient ξ_R enters both the measure covariance matrix as well as the measures equation. In Figure 9.2 the results of a parametric analysis are presented. From that it can be seen that the choice of both the ξ coefficient is crucial since it can bring the filter to diverge.

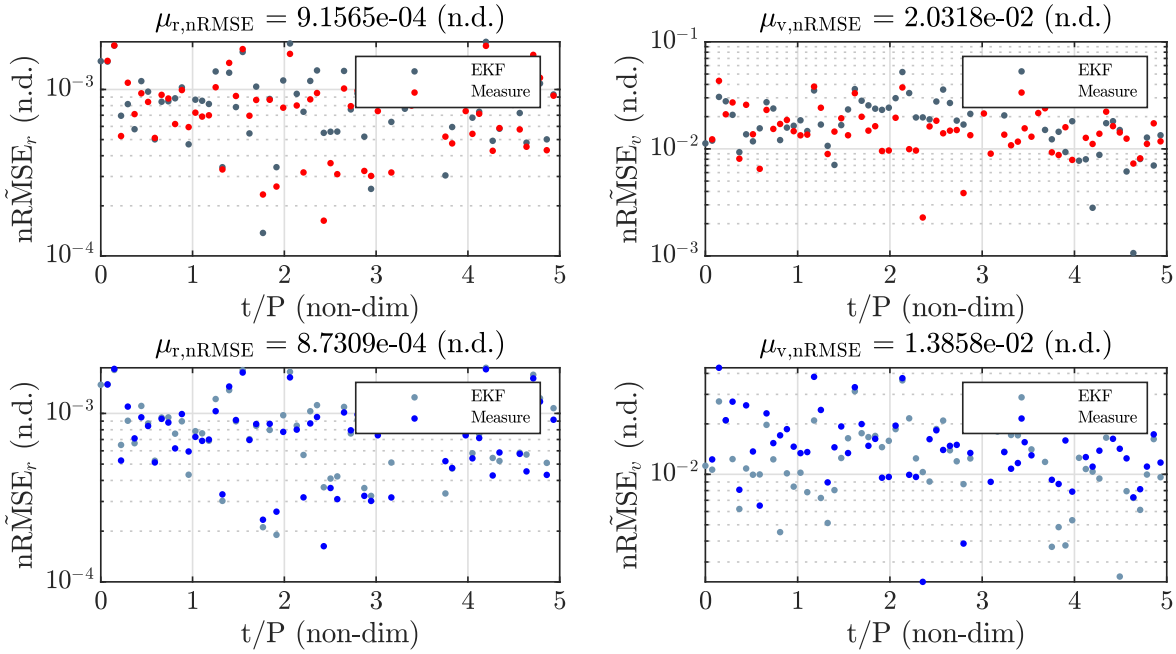

Figure 9.1: *Case 1* · EKF's *vs* measures' nRMSE. First row: 2B dynamical model. Second row: 2nd-degree SHE dynamical model.

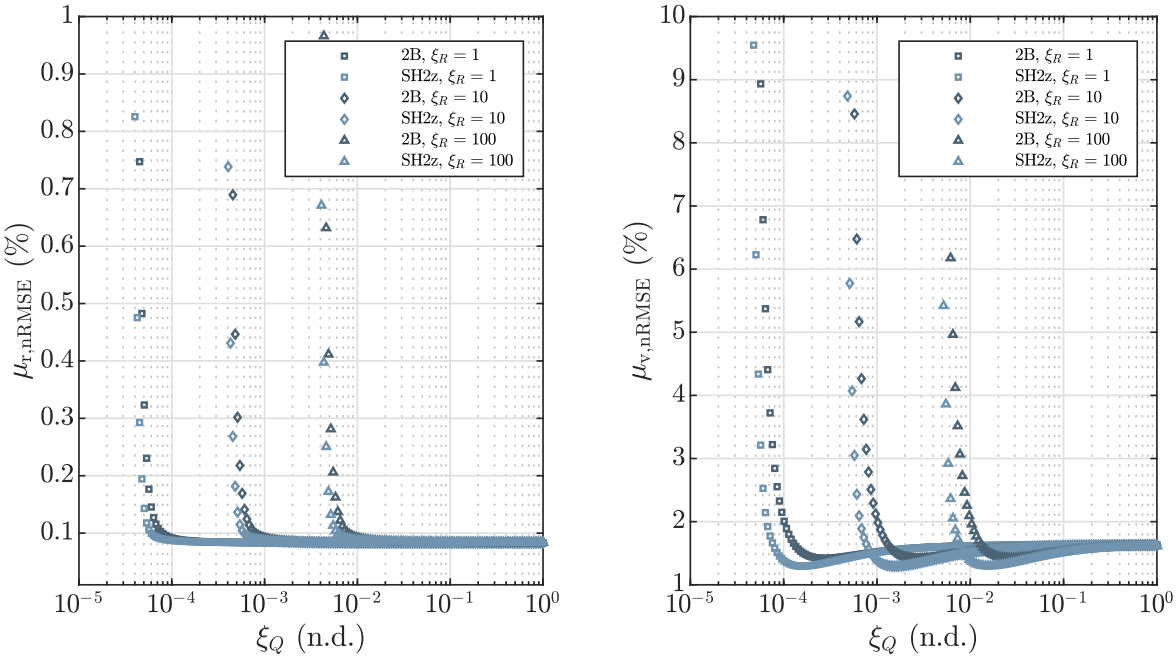

Figure 9.2: *Case 1/2* · EKF results: parametric analysis.

Moreover, the choice of ξ_Q seems to be driven by the $\mu_{v,\text{nRMSE}}$. However the results appears to be quite similar if the dynamical models are considered to be the R2BP and a 2^{nd} degree SHE model, but there is a difference: the last diverges for ξ_Q that are smaller than the ones that bring the first to diverge: the last is of higher fidelity with respect to the first.

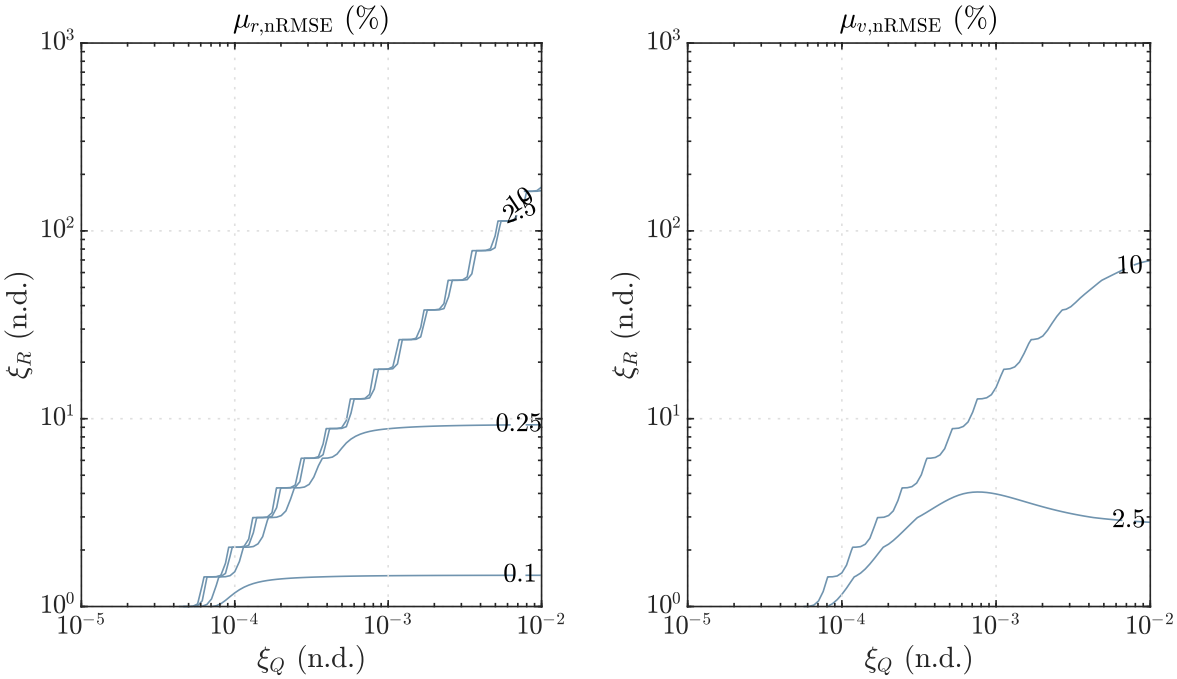

Figure 9.3: *Case 1/2* · EKF results: parametric analysis on $\xi_{Q,R}$.

In Figure 9.3, instead, the results for a parametric analysis on both ξ_Q and ξ_R are shown for the R2BP case. The results for higher order models are similar so to avoid confusion they are not represented. In both cases (r and v), assuming the 10% limit a good approximation, the bi-logarithmic plots are divided in two parts by a quasilinear line between $(1e-4, 1)$ and $(1e-2, 100)$. At the right of the line the filter converge, with a precision that depends from ξ_R (in fact there are horizontal curves where nRMSE increases with ξ_R). At the left, instead, the filter diverges. Along the horizontal lines, recalling the results Figure 9.2, the filter follows the measures while along the quasilinear line the behaviour is associated at the dynamical model. Note that the slope of the line can be written as:

$$m = \frac{\Delta \log y}{\Delta \log x} \simeq 1 \tag{9.8}$$

It can be seen also that the divergence region of the filter is really sharp and coincide with the quasilinear line. So for this specific case there exists a sort of linear correlation between ξ_R and ξ_Q that can be seen as a convergence threshold. To conclude this analysis one expect that for a model of increased fidelity, this line shifts to the left, as confirmed by Figure 9.2.

Case 3. In this case, a parametric analysis is performed on the object of *case 1*. The DoFs, in this case, are $\xi_{Q,R}$ and the discretization, T_s.

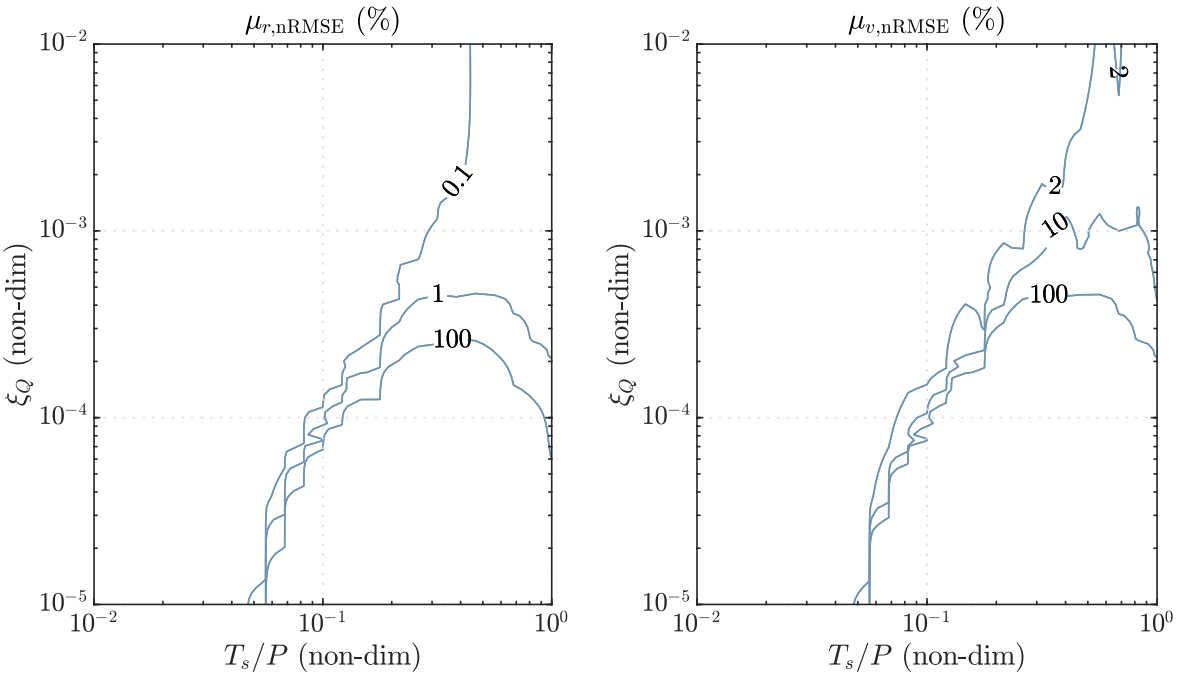

Figure 9.4: *Case 3* · EKF results: parametric analysis on ξ_Q and T_s.

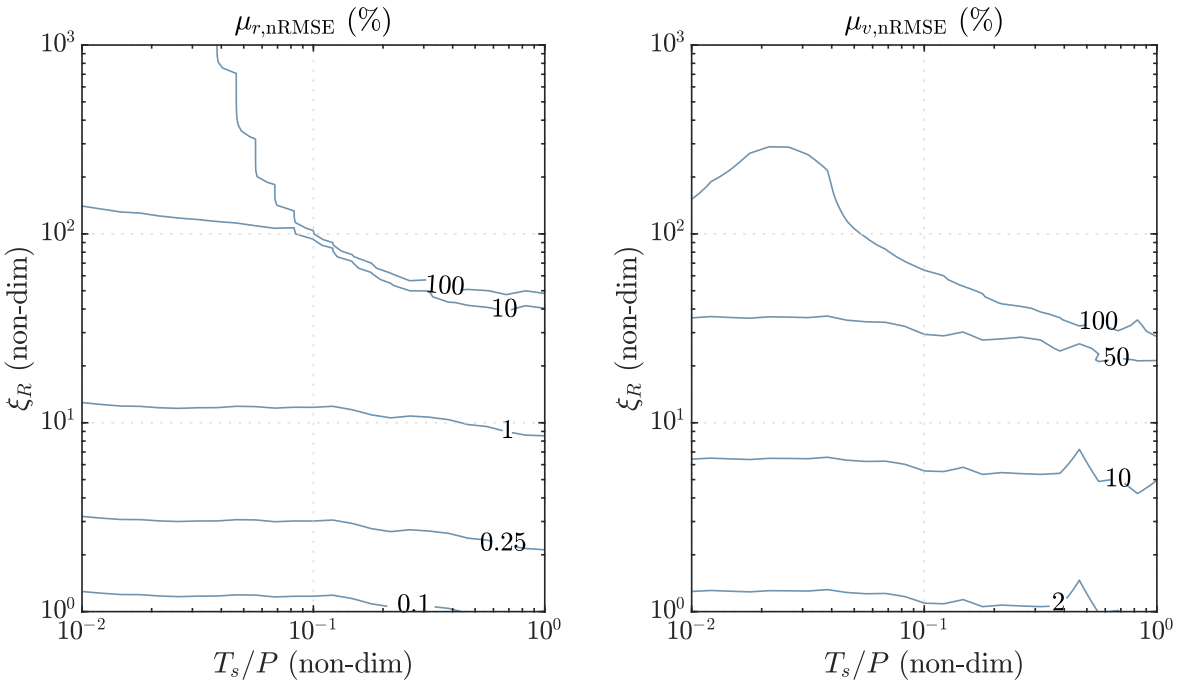

Figure 9.5: *Case 3* · EKF results: parametric analysis on ξ_R and T_s.

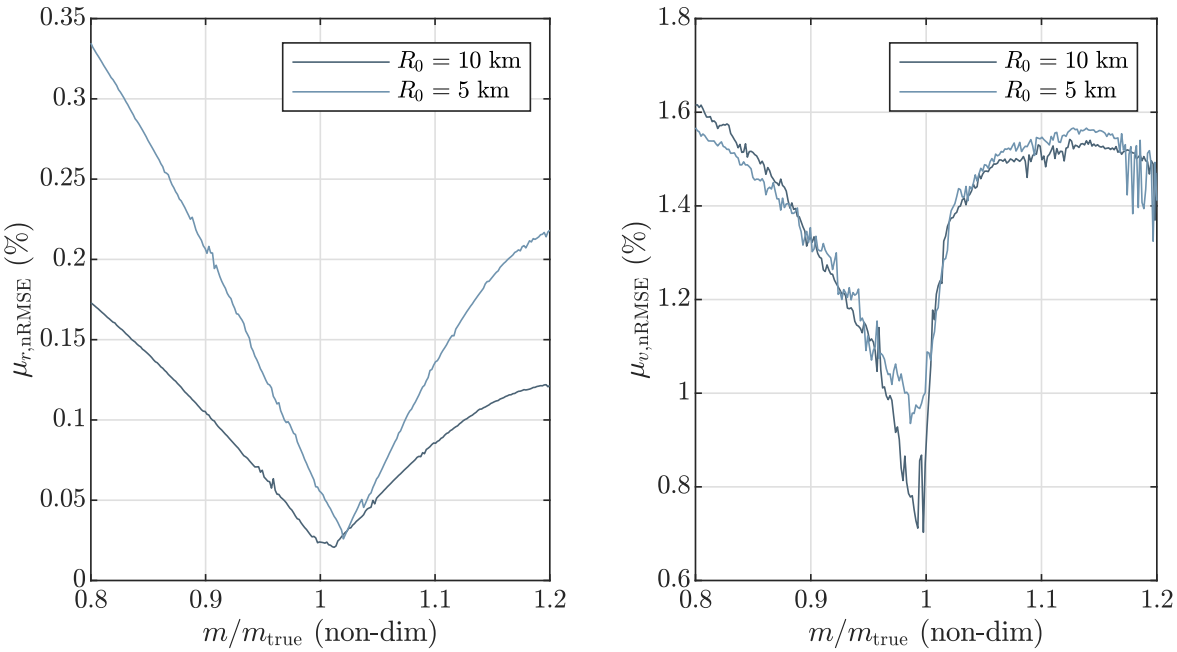

Figure 9.6: EKF results: parametric analysis on m.

The results for this case are presented in Figure 9.4 for the nRMSE(ξ_Q, T_s) case and the behaviour is much more complicated that in the previous case but can be summarized as follows:

1. The EKF exhibit good convergence properties for small values of T_s (upper-left).
2. As far as the T_s increases, as the divergence is more pronounced for smaller ξ_Q values (bottom-right).
3. For larger ξ_Q values the filter follows the measures more than the model: the nRMSE, in fact appears to be mostly independent from T_s in the upper part of the plots.

For what regards the results for the nRMSE(ξ_R, T_s) case, instead, they are shown in Figure 9.5 and appears to be, independent from T_s up to $\xi_R \sim 100$ and appears to diverge quickly in the upper-right part of the plot, where both ξ_R and T_s assume the biggest values.

9.2 Parametric Analysis

Up to now the analysis of the convergence of the EKF is assessed for a particular case and two dynamical models have been compared. However, to further assess the convergence of the filter a parametric analysis is performed on the physical/orbital DoFs of the problem.

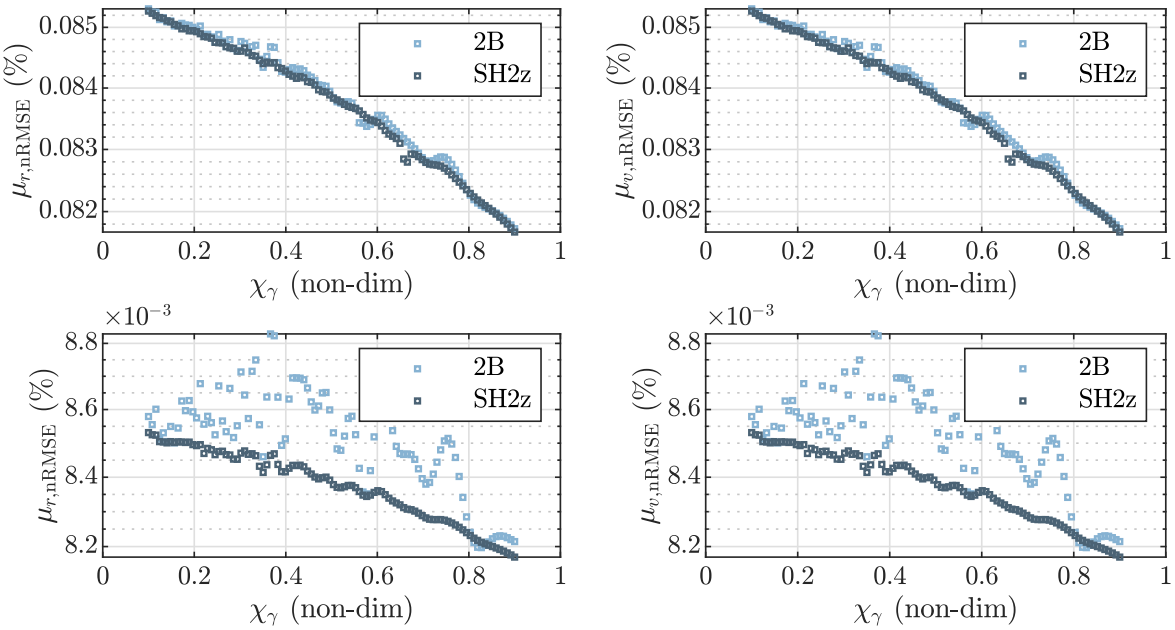

Figure 9.7: EKF results: parametric analysis on χ_γ.
$R_0 = 1$ km for the first row and $R_0 = 10$ km for the last.

9.2.1 Mass uncertainty

Usually to the mass of an object is associated an uncertainty, at least in the initial phases of the mission. However, as studied in the previous chapters, the network is capable to reconstruct it correctly so that even the R2BP is refined. In this section a brief parametric analysis is performed assuming a spherical body $\{1, 1, 1; 2700, 10-5\}$ with the mass m that is uncertain with a variance of $20\%m$. The results of the analysis on a $\Gamma_0^{10R_0}$ orbit with the EKF tuned as $\{0.5 \cdot T, \sqrt{10}, 1e-2\sqrt{10}, 1, 1e-2\}$ are presented in Figure 9.6 where it can be noticed that:

1. As expected, the filter has a lower nRMSE for $\chi_m = m/m_{\text{true}} \to 1$.
2. As far as m_{true} increases as far as the minimum for the nRMSE is located at $\chi_m = 1$.
3. The position estimation is more precise than the velocity one.
4. There is a dependence of the performances on the dimensions i. e., on the mass of the body. The higher the mass the better the performances.

9.2.2 Shape parametric analysis

In this section a parametric analysis that involves the shape of the body is considered. First, in Figure 9.7 the results for a *oblate spheroid* are assessed for varying χ_γ. A $\Gamma_0^{2R_0}$ orbit is considered and the EKF is tuned according to $\{0.1 \cdot T, 1, 1e-4, 1e-1, 1e-1\}$ while the body properties are $\{1, 1, \chi_\gamma; 2700, 1-10\}$. The results that, show that, as far as R_0 increases, as the nRMSE decreases in magnitude but increases in variance for both the position (r) and the velocity (v). In Figure 9.8, instead, the results for the parametric analysis of an *triaxial ellipsoid* are presented. For clarity, the results

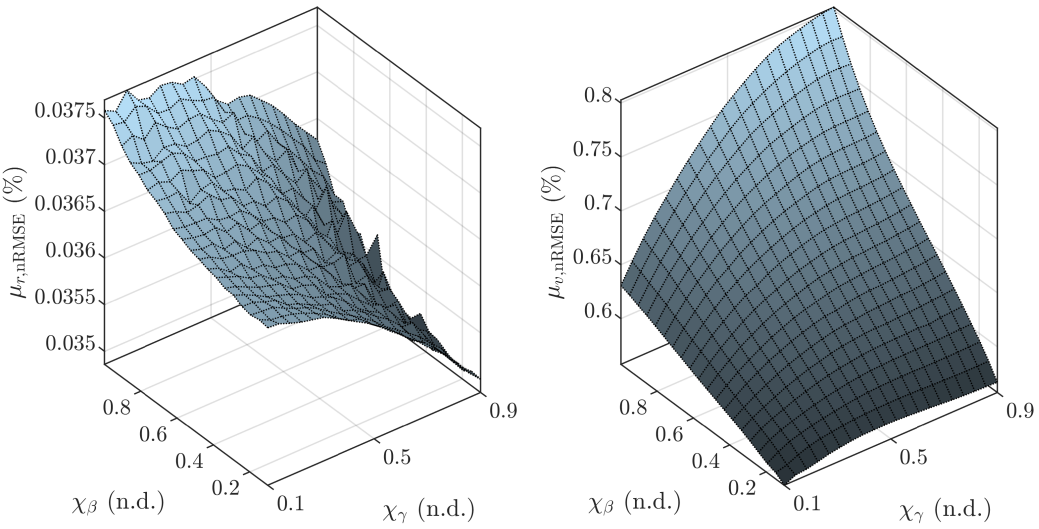

Figure 9.8: EKF results: parametric analysis on $(\chi_\gamma, \chi_\beta)$. $R_0 = 2.5$ km.

presented are only the one obtained with a 2nd-degree SHE model. The analysis pointed out that the sensitivity of the nRMSE to the shape of the body is low, since the variations are small.

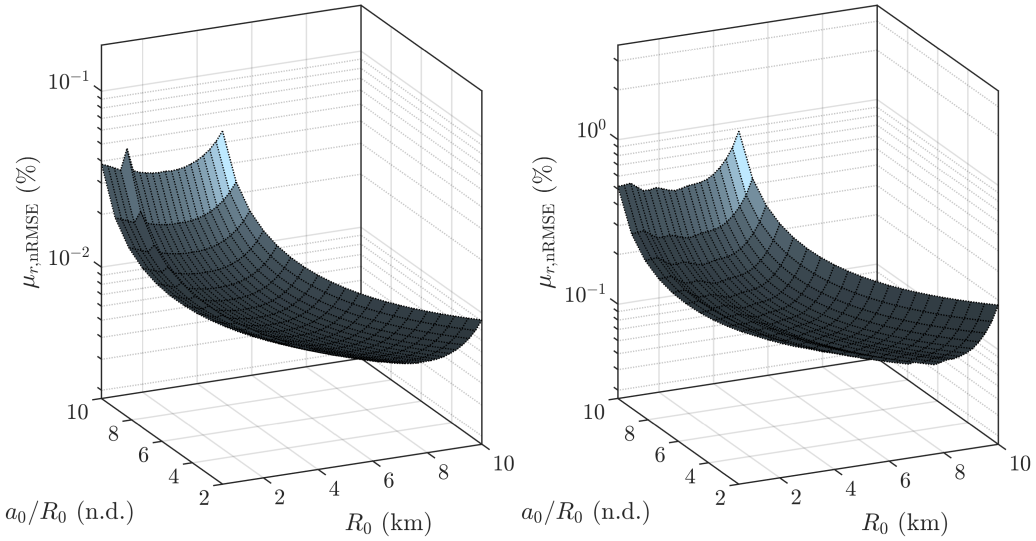

Figure 9.9: EKF results: parametric analysis on (R_0, a_0).

In Figure 9.9, instead, the results of a parametric analysis on the dimensions and the orbit semi-major axis are presented. In this case a soft dependence on both the parameters can be noticed. In particular, as R_0 and a_0 increases the filter becomes more precise. This can be probably explained by the fact that for high a_0 the influence of the higher-order harmonics can be neglected and the asteroid can be seen as a point mass. This analysis is performed on an oblate spheroid, so probably the network would behave *differently* in case the body is more irregular.

9.3 MHNN-Based Filter in High Fidelity Models

The aim of the previous section was only to asses the performance of the filter and to understand when a fine tuning is needed as well as how to do it. The major results can be summed-up in:

(R1) The filter tuning depends, in this formulation, on 8 constants, namely $t_s, \xi_R, \xi_Q, \sigma_{y,r}, \sigma_{y,v}, \sigma_{q,r}$ and $\sigma_{q,v}$. They influence the overall performances as well as the convergence of the filter. In particular $\xi_R, \sigma_{y,r}$ and $\sigma_{y,v}$ are associated to the *measurements* model and the filter performances degrades if they increases while $\xi_Q, \sigma_{q,r}$ and $\sigma_{q,v}$ are associated to the *dynamics* model and the performances of the filter increases if the model order increase. Finally, the *discretization* t_s plays and important role in the performances too: the higher, the lower the performances of the filter. In particular as t_s increases it can be seen that the filter follows more the measures than the model.

(R2) The filter performances have a dependence on the dimension/mass of the body. In general, the higher the mass, the better the performances.

(R3) The $\sigma_{i,j}$'s can drive the filter to diverge. In general if the model is not accurate a low ξ_R together with an high ξ_Q lead to divergence.

(R4) Higher-order models (than the R2BP one) can improve the overall performances of the filter.

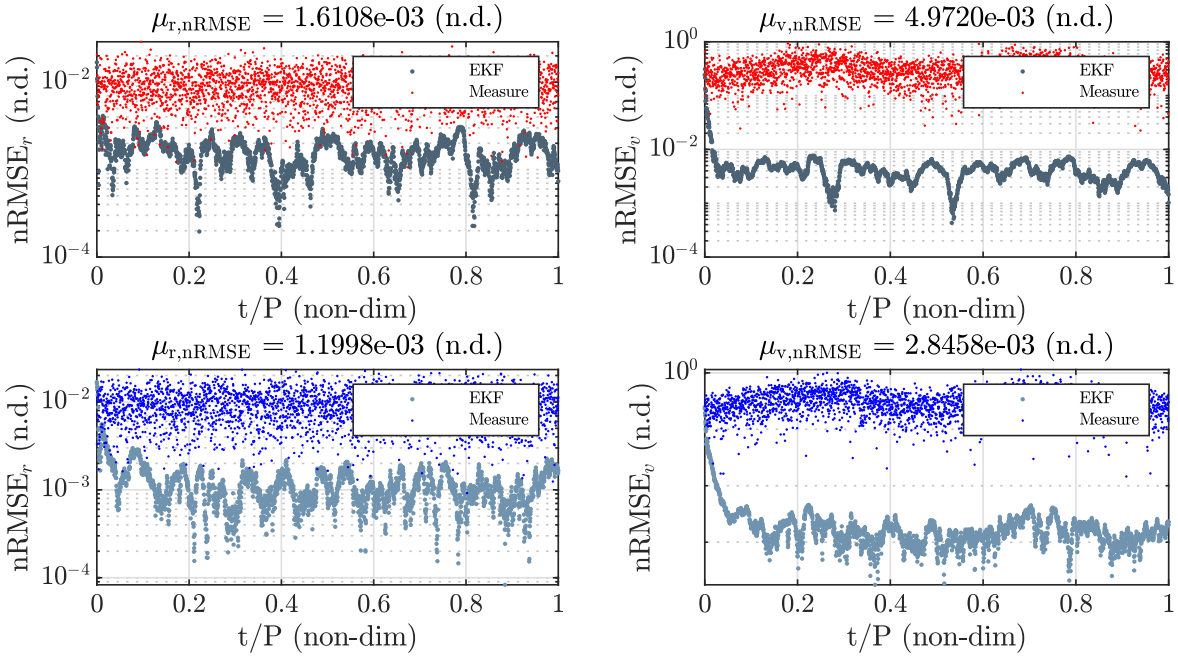

Figure 9.10: EKF results. First row R2BP, second 2nd-degree SHE.

9.3.1 The case of Castalia

In this section the analysis of the performances of an EKF are analysed for the case of asteroid 4769 Castalia. Since the higher degree gravitational perturbations tends to

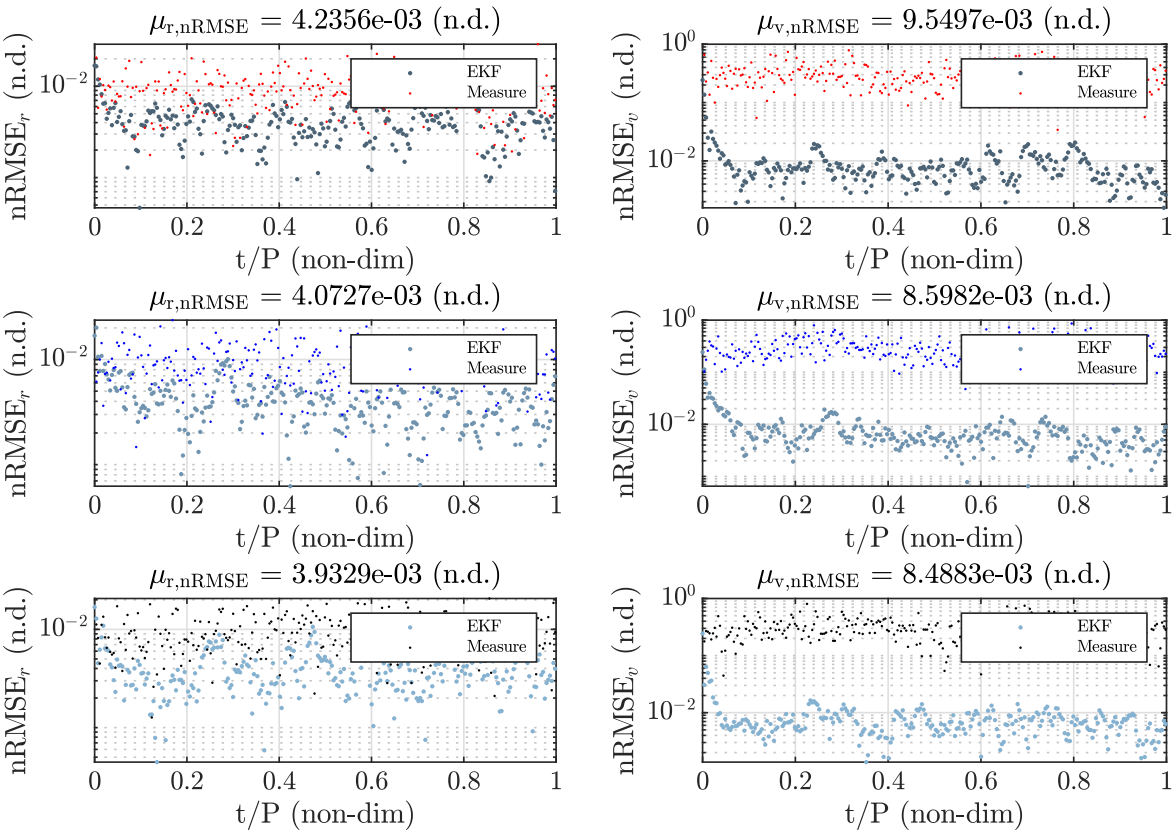

Figure 9.11: EKF results. First row R2BP, second 2nd-degree SHE, third 4nd-degree SHE with only zonal terms.

disappear as far as a_0 increases and the perturbed model tend to be equal to the R2BP, then the filter is tested for a close-proximity orbit e. g., a $\Gamma_{45^\circ}^{2R_{\max}}$.

In Figure 9.10 the results for a case which the sampling is 30 seconds. It can be seen that the performances of the filter gets better with the higher order model, especially for the velocities, where the error is halved. In this case the filter is tuned with:

(C1.1) $\sigma_{y,r} = 10$;

(C1.2) $\sigma_{y,v} = 0.1$;

(C1.3) $\sigma_{q,r}^2 = \sigma_{q,v}^2 =$ 1e-8.

In Figure 9.11, instead, the results for a case in which the sampling is 300 seconds. Also in this case, it can be seen that higher order models gives better results. However, in terms of magnitude, the fact that t_s has increased increases the nRMSE. In that case the filter is tuned with:

(C2.1) $\sigma_{y,r} = 10$;

(C2.2) $\sigma_{y,v} = 0.1$;

(C2.3) $\sigma_{q,r}^2 = \sigma_{q,v}^2 =$ 1e-6.

Indeed, the *measurements* model is not changed while the σ_q terms are increased to prevent the filter to diverge. To further asses the previous results, a statistical analysis on the performances can be assessed. The results in terms of mean (μ) and standard

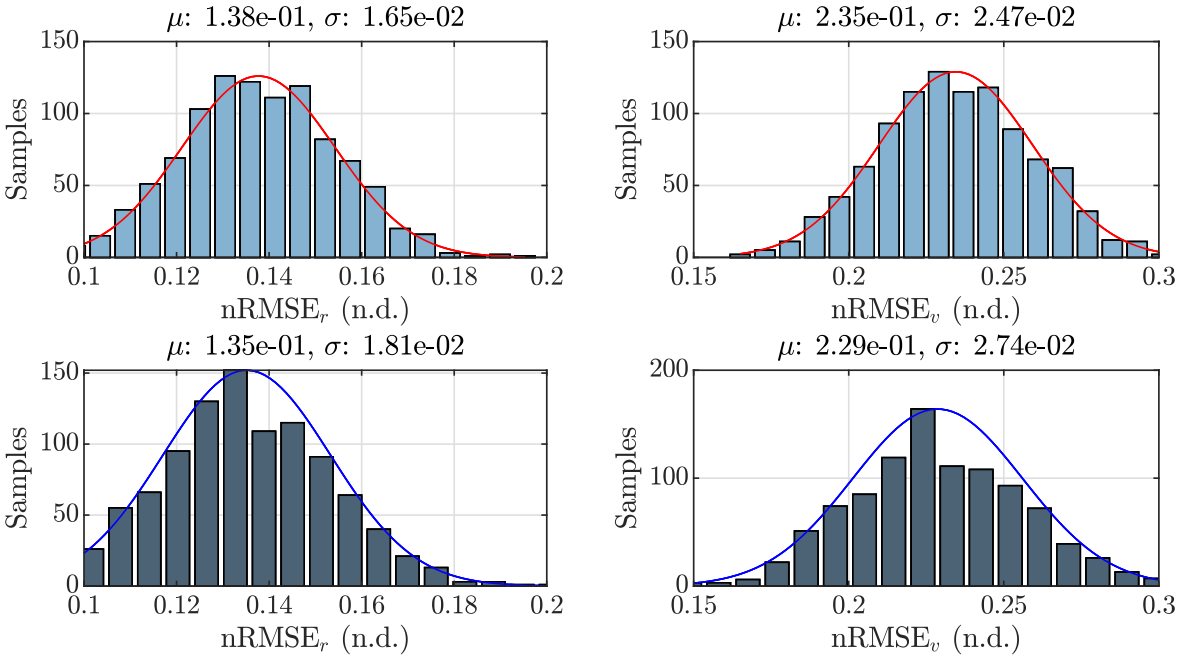

Figure 9.12: EKF statistical results. First row associated to R2BP, second to a 2$^{\text{nd}}$-degree SHE model.

deviation (σ) computed on the mean nRMSE of a batch of 1000 of simulations are presented in Figure 9.12. In this case the filter is tuned as in (C2.1,2,3). The results show that the μ of the higher-order model is lower than the one of the R2BP meaning that the performances are enhanced. However, the 2$^{\text{nd}}$-degree model exhibit an higher standard deviation.

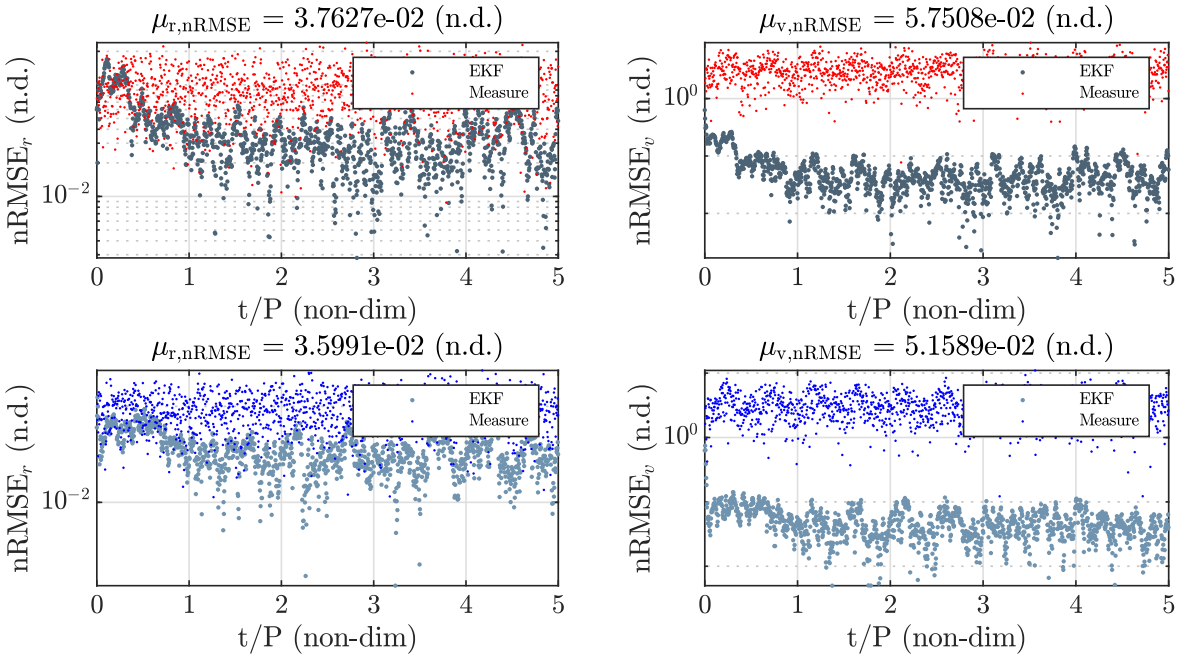

Figure 9.13: EKF results. First row R2BP, second 4$^{\text{nd}}$-degree SHE.

In Figure 9.13, instead, the results for a lower-precision measurement model are presented showing lower but still good performances of the filter. In this case, in fact, the

filter is tuned according to:

(C3.1) $\sigma_{y,r} = 100$;

(C3.2) $\sigma_{y,v} = 1$;

(C3.3) $\sigma^2_{q,r} = \sigma^2_{q,v} = 1\text{e-}6$.

In that case the filter is exhibit still good performances but it results slower and less precise than in the previous cases.

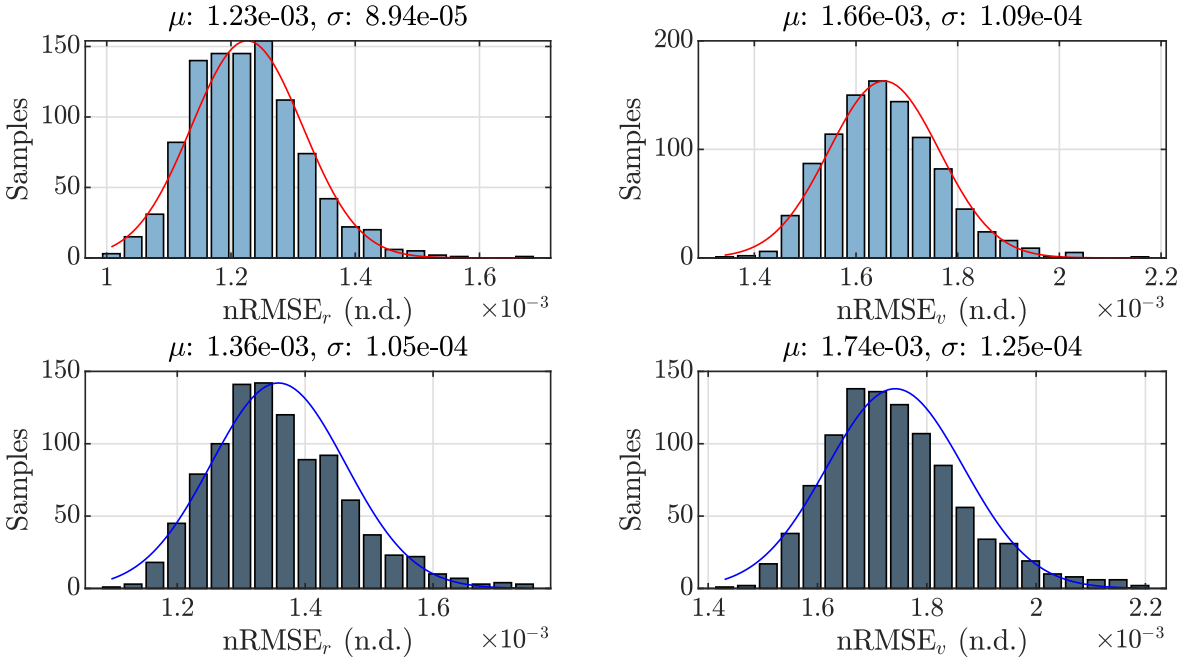

Figure 9.14: EKF results. First row R2BP, second 4$^{\text{nd}}$-degree SHE.

Finally the case of a larger orbit is tested: a $\Gamma^{5R_{\max}}_{45^\circ}$ is considered. The results of a statistical analysis of a batch of 1000 samples is shown in Figure 9.14. Also in that case the two models are quite similar and the convergence does not change that much. However, for this specific test the R2BP model seems to be more accurate than the 4$^{\text{nd}}$-degree model.

9.3.2 The case of Eros

The previous section deals with the analysis of the performances of a EKF navigation of asteroid Castalia. In this part, instead a much larger asteroid is considered: Eros. In the introduction of this work it was pointed out that Eros has a mass ~ 1000 times the one of Castalia. So one expect different performances of the filter.

In Figure 9.15 and Figure 9.16 are presented two analysis performed on a $\Gamma^{5R_{\max}}_{45^\circ}$ orbit. In particular in the first case the filter is tuned according to:

(E1.1) $\sigma_{y,r} = 100$;

(E1.2) $\sigma_{y,v} = 1$;

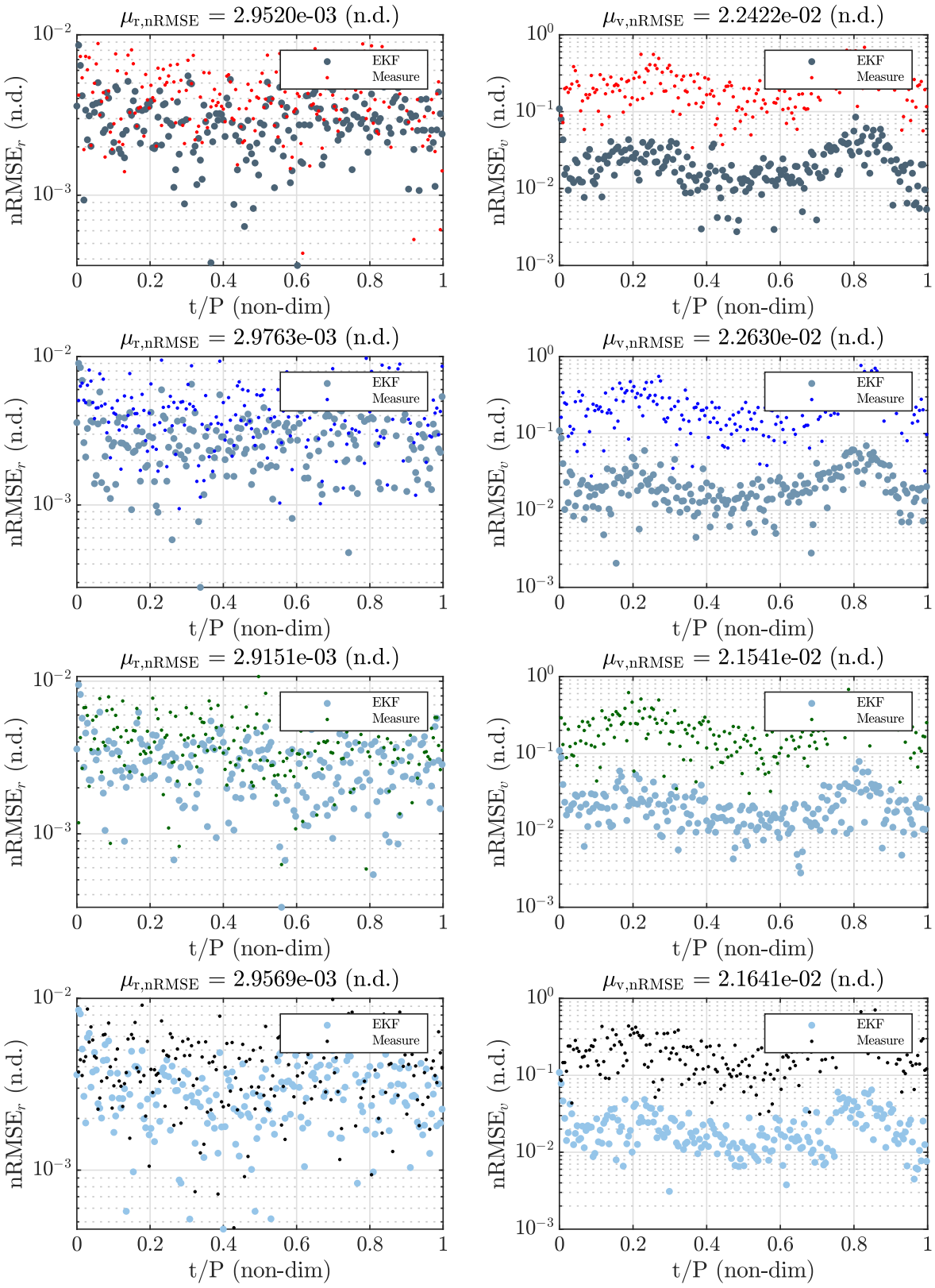

Figure 9.15: EKF results. First row R2BP, second 2nd-degree SHE, third 4nd-degree SHE and forth 8nd-degree SHE.

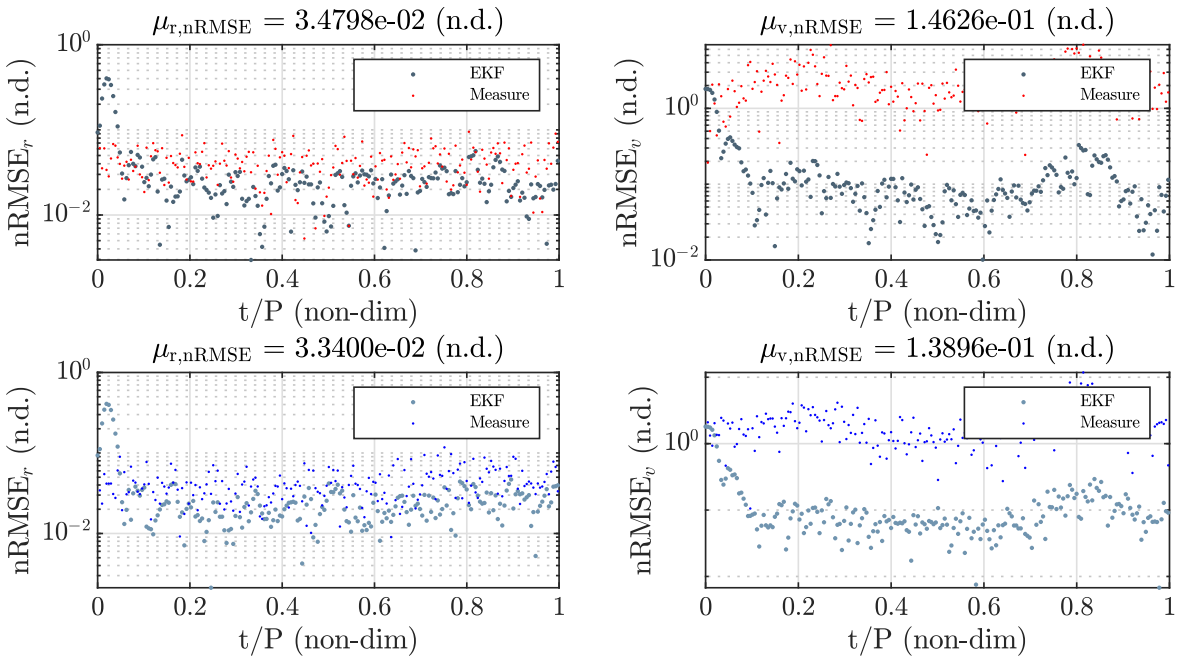

Figure 9.16: EKF results. First row R2BP, second 8$^{\text{nd}}$-degree SHE.

(E1.3) $\sigma_{q,r}^2 = \sigma_{q,v}^2 = 0.01$.

While in the second case according to:

(E2.1) $\sigma_{y,r} = 1000$;

(E2.2) $\sigma_{y,v} = 10$;

(E2.3) $\sigma_{q,r}^2 = \sigma_{q,v}^2 = 0.1$.

Note this is not an optimal tuning but a trial/error tuning performed to mimic the optimality. However both the cases show an increased precision in the filtering process if higher-order models are used. However, with respect to the case of Castalia, the tuning phase of the filter is much different (the σ_q are much different in that case with respect to the previous).

A final note is needed regarding the SRP. All the results of the previous analysis consider a case in which no SRP model neither disturbance is present. However, in real applications the SRP plays an important role and even a rough model of it should be implemented in the filter. It can be shown, in fact, that in case the SRP model is not added and the σ_q's are chosen to be small (say, for example $1e-6$) then the filter diverges while if the model is added then, for the same σ_q the filter does not diverge. So, one can conclude that a simple SRP model would increase the stability of the filter to its tuning.

9.4 MHNN identification coupled EKF navigation

In the previous sections of this chapter the numerical assessment of the EKF performances where addressed in case the dynamical model is updated to a spherical harmonics expansion one by the MHNN. From the operative point of view, in fact, a strong

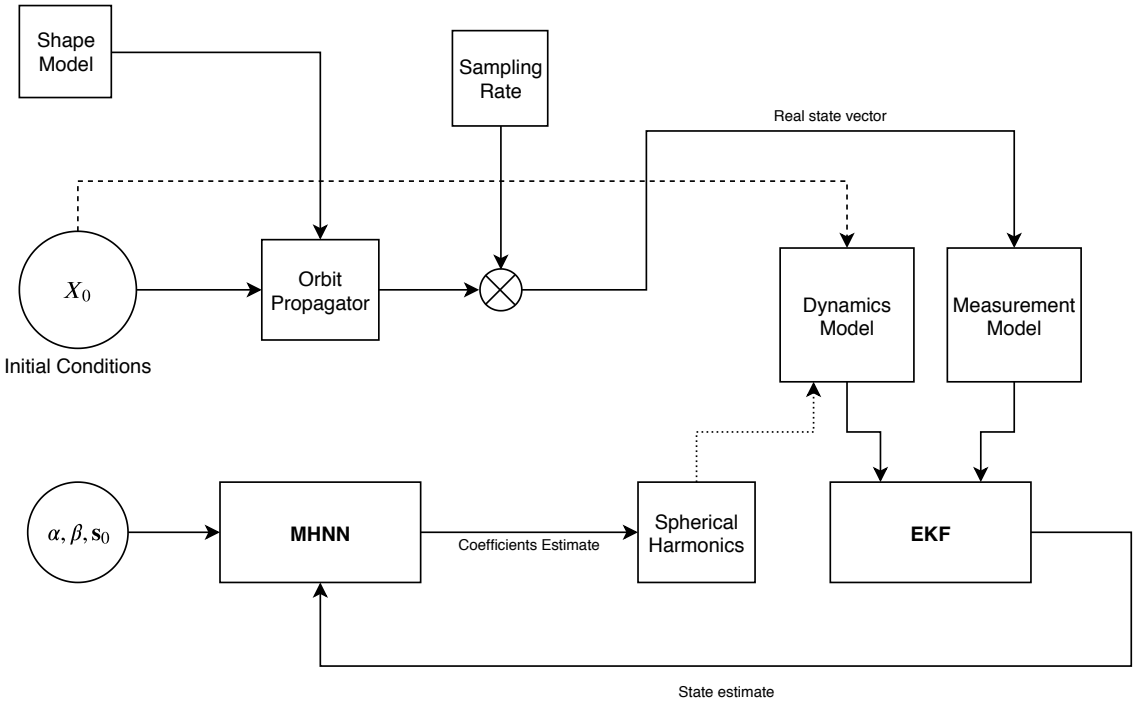

Figure 9.17: Coupled MHNN-EKF workflow.

coupling is expected between the MHNN and the EKF, as presented in Figure 9.17. In particular one can identify two ways of coupling:

1. MHNN to EKF: the MHNN reconstruct time dependant coefficients that updated the dynamical model inside the filter. However, in this case the filter tuning becomes more challenging [71]. In fact this work uses a time fixed model since there is no need to tune perfectly the filter, being the measurement model not well defined. So, this coupling is *not* analysed here.
2. EKF to MHNN: the MHNN reconstruct the coefficient taking as input the state reconstructed from the filter. The performances, in this case, are addressed here.

MHNN performances in flying asteroid Castalia. As an example, in this paragraph the integration EKF to MHNN is performed in the case of asteroid Castalia. In particular a EKF model with C_2, C_3 and C_4 is considered and C_{22} is reconstructed. First consider the case of a $\Gamma_{45}^{2R_m}$. Consider the network tuned with $\beta = 1e-6$ and the EKF tuned with:

(EKMH1.1) $\sigma_{y,r} = 100$;

(EKMH1.2) $\sigma_{y,v} = 1$;

(EKMH1.3) $\sigma_{q,r}^2 = \sigma_{q,v}^2 = 0.01$.

The results in terms of state estimation are presented in Figure 9.18 while the network behaves as in Figure 9.19. Indeed in this case the performances of the identification are changed but neither the 2BP nor the higher order one associated to the filter gives important differences in the identification. This is further confirmed if the case of a $\Gamma_{45}^{5R_m}$ orbit is considered: in that case the higher order harmonics are only barely sensed

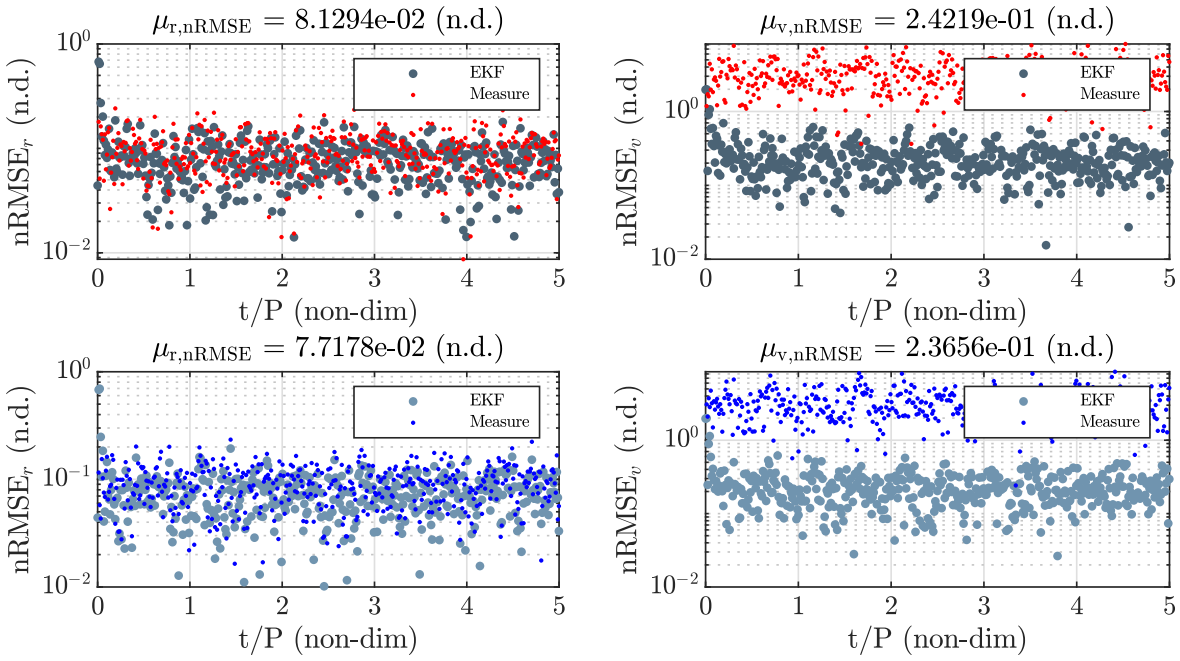

Figure 9.18: EKF to MHNN results: state estimation.
First row, 2BP model, second row, 4^{th} degree zonal SHE.

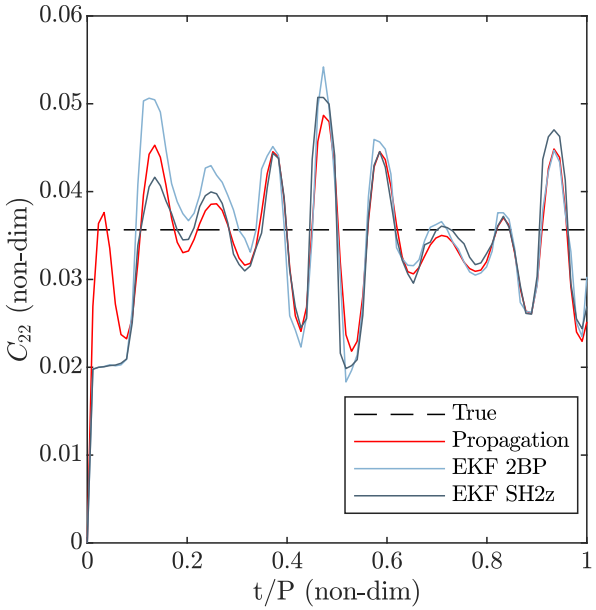

Figure 9.19: EKF to MHNN results: coefficient identification.

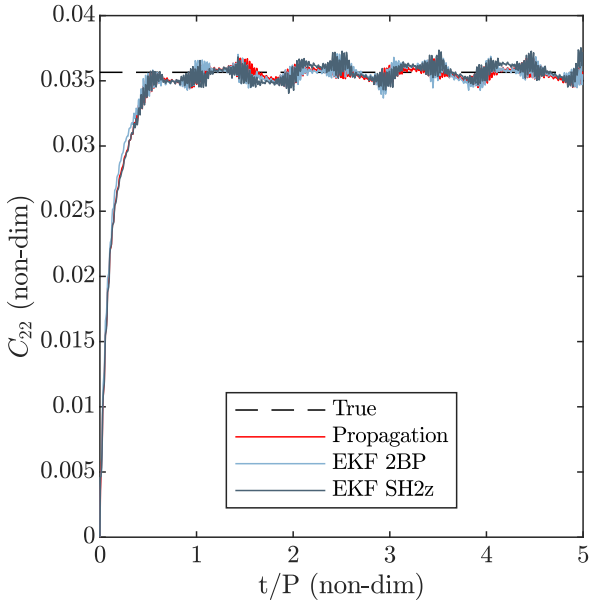

Figure 9.20: EKF to MHNN results: coefficient identification.

by the flying object so that, from the identification point of view the use of a higher order navigation filter gives basically the same results that the ones of a 2BP-based filter, as it can be seen in Figure 9.19.

However, in case the measurement model is really inaccurate, i. e., tuning the EKF with:

(EKMH1.1) $\sigma_{y,r} = 1000$;

(EKMH1.2) $\sigma_{y,v} = 10$;

(EKMH1.3) $\sigma_{q,r}^2 = \sigma_{q,v}^2 = 10$.

the network basically *diverges*. This is related to the fact that the state estimate gives about a 90% error so that subsequent state becomes basically uncorrelated and this bring to divergence the identification. Note that assuming a $\sigma_{y,r} = 1000$ means that we admit errors in the position reconstructions that are bigger than the dimension of the body ($R_{\text{mean}} \sim 500$ m).

CHAPTER 10

CONCLUSIONS

Most of the future space mission are planned to explore and study asteroids and, in general, small solar system bodies. During those missions, as pointed out in previous chapters, the study of the dynamical environment of the body is a one of the most important phases of every mission: either a landing, a deflection or a scientific mission *need* to have a refined dynamical model in order to safely and successfully address its objectives.

The present work developed a methodology, based on a feedback ANN called MHNN, capable of reconstructing the gravitational field of a body. In particular, the coefficient of the analytical SHE are identified by using the specific tailored MHNN. This approach results to be really powerful since the SHE approximate the global gravitational field of the body so that the results of the identification can be used also to extract the shape and/or the density distribution of the body.

Small body environment modelling

The first part of the work is dedicated in the dynamical modelling of the environment that one could expect flying about an asteroid, a comet or a moon. In particular two main models have been presented, one associated with a single rotating body (P2BP) and the second associated to a binary system of rotating bodies (MCR3BP). The influence of higher order gravitational and non-gravitational perturbations is included (such as SRP and Sun 3BP). Then, the state of the full coupled equations have been reduced according to some assumption, such as, for example, a P2BP with uniform asteroid rotation leads to the ROP2BP and some basic trajectory design tools for the MCR3BP have been introduced.

Finally, a series of gravitational models have been critically presented. First, the differences between them have been highlighted then the SHE model is studied more in detail, especially for simplified bodies.

MHNN Gravity Field Identification

This is the core of the work. In that part the performances of the MHNN has been extensively studies through a series of specific tests. In general, the convergence and the stability of the network was proved by other authors [55], [56] analytically. So, the aim of this work was to understand how to use this network in the gravitational field identification. To do so, first a series of tests have been performed on simplified axis-symmetric bodies, varying the orbital elements. Then a *conceptual mission* has been presented as a parametrized methodology to use the MHNN basically with any kind of bodies. Finally, some test cases have been presented on real environments to underline perturbation effects on the identification. Those real environments comprise also a binary system. All those analysis have been used to understand how the network have to be tuned as well as how it performs in different dynamical environments.

MHNN-Based EKF Navigation

The last part of the work presents the performances of a EKF navigation filter whose dynamics is based on the MHNN results. Since it wanted to be only a preliminary analysis, the EKF formulation is simplified as well as the MHNN results are considered to be stationary. However, the results of this analysis are significant since the filter shows increasing performances as the model order increases.

Future Work

The present work is a pioneering study about the use of machine learning techniques in the aerospace world. Being pioneering, there is a lot of research to be done, on different fields.

- From the *gravitational model* view point, the Internal Spherical Bessel Functions Expansion can be implemented instead of the SHE: this can be useful in case the a landing or close proximity operations are planned, in particular in case the target body is highly irregular. Moreover, the case of a binary system needs further investigations.
- From the *network* point of view, a trial-error tuning was analysed in this work: this is clearly not the best for an autonomous mission. In particular, this work underline that the tuning of the activation function parameters α, β is crucial to the network convergence and performances: an adaptive network is needed also from the point of view of its parameters. Some ideas have been analysed, but their development goes beyond the scope of this work. Moreover, the choice of the model order to stop the identification in such a way the identified SHE model represents a sufficiently accurate model of the reality can be automatized also.

- Finally, the EKF implemented in this work needs to be refined: first of all the measurement models are needed depending on a real-case application. Moreover, in this work the filter dynamical models are assumed to be dependent only on the state and not on time. In this application, however, since the network gives time dependant results, an adaptive version of the filter has to be implemented, as in [71].

ACRONYMS

DoF	Degree of Freedom
nRMSE	normalized Root Mean Square Error
SHE	Spherical Harmonics Expansion
R2BP	Restricted Two-Body Problem
P2BP	Perturbed Two-Body Problem
MCR3BP	Modified Circular Restricted Three-Body Problem
SRP	Solar Radiation Pressure
ROP2BP	Reduced-Order P2BP
F2BP	Full Two-Body Problem
FR3BP	Full Restricted Three-Body Problem
SOI	Sphere of Influence
SOE	Surface of Equivalence
KEPs	Keplerian Parameters
SHs	Spherical Harmonics
CR3BP	Circular Restricted Three-Body Problem
3BP	3-rd Body Perturbation
STM	State Transition Matrix
DRO	Distant Retrograde Orbits
AIDA	Asteroid Impact and Deflection Assessment
R2BP	Restricted Two-Body Problem
GOCE	Gravity field and steady-state Ocean Circulation Explorer
GRACE	Gravity Recovery And Climate Experiment

ALF	Associated Legendre Functions
MATLAB	Matrix Laboratory
GD	Gradient Descent
2B-IP	2B-Identification Phase
NEA	Near-Earth Asteroid
LSM	Least-Square Method
ODE	Ordinary Differential Equation
LIP	linear in the parameters
ANN	Artificial Neural Network
HNN	Hopfield Neural Network
MHNN	Modified Hopfield Neural Network
DAE	Differential Algebraic Equation
GPS	Global Positioning System
TAGG	Tidal Acceleration Gravity Gradiometry
DSN	Deep Space Network
ELM	Extreme Learning Machine
SLFN	Single-Layer Forward Networks
MDP	Markov Decision Process
DPS	Direct Policy Search
FFNN	Feed Forward Neural Networks
BPANN	Back Propagation Artificial Neural Network
RBF	Radial Basis Functions
MLP	Multi-Layer Perceptors
MSO	Modified State Observer
MLE	Maximum Likelihood Estimation
ESA	European Space Agency
NASA	National Aeronautics and Space Administration
EKF	Extended Kalman Filter
KF	Kalman Filter
UKF	Unscented Kalman Filter

BIBLIOGRAPHY

[1] G. et al Benedetti. "Interplanetary CubeSats for Asteroid Exploration: Mission Analysis and Design". In: *Acta Astronautica* (2018) (cit. on p. 3).

[2] T. et al Kohout. "Feasibility of asteroid exploration using CubeSats â ASPECT case study". In: *Advances in Space Research* (2017) (cit. on p. 3).

[3] A.S. Konopliv, S.W. Asmar, and B.G. et al Bills. "The Dawn Gravity Investigation at Vesta and Ceres". In: *Springer Science* (2011) (cit. on pp. 4, 5).

[4] I. Netwon. *Philosopiae Naturalis Principia Mathematica*. 1687 (cit. on p. 4).

[5] Vallado. *Fundamentals of astrodynamics and applications*. The McGraw-Hill Companies, 1997 (cit. on pp. 4, 21, 33, 102, 103).

[6] D.G. King-Hele. "The Effect of the Earth's Oblateness on the Orbit of a Near Satellite". In: *Proceedings of the Royal Society of London. Series A, Mathematical and Physical Sciences* 247 (1958), pp. 42–72 (cit. on p. 4).

[7] P.N.A.M. Visser. "Gravity field determination with GOCE and GRACE". In: *Advances in Space Research* 23 (1999), pp. 771–776 (cit. on p. 4).

[8] Hayabusa2 Project Team. "Hayabusa2 Information Fact Sheet". In: (1918) (cit. on p. 4).

[9] Study on Quasi-periodic Orbits around an Asteroid Using an Impulsive Delta-V. In: *24th Workshop on JAXA, Astrodynamics and Flight Mechanics* () (cit. on p. 4).

[10] Haibin Shang, Xiaoyu Wu, Yuan Ren, and Jinjun Shan. "An efficient algorithm for global periodic orbits generation near irregular-shaped asteroids". In: *Communications in Nonlinear Science and Numerical Simulation* 48 (2017), pp. 550 –568. DOI: https://doi.org/10.1016/j.cnsns.2017.01.021 (cit. on p. 4).

[11] Demyan Lantukh, Ryan Russell, and Stephen B Broschart. "Heliotropic Orbits at Asteroids: Zonal Gravity Perturbations and Application at Bennu". In: Jan. 2015 (cit. on p. 4).

[12] Scheeres-D.J. et al. Miller J.K. "Determination of Shape, Gravity, and Rotational State of Asteroid 433 Eros". In: *Icarus* 155 (2002), pp. 3–17 (cit. on p. 5).

[13] Romain Garmier, Jean-Pierre Barriot, Alexander S. Konopliv, and Donald K. Yeomans. "Modeling of the Eros gravity field as an ellipsoidal harmonic expansion from the NEAR Doppler tracking data". In: *Geophysical Research Letters* 29.8 (2002), pp. 72–1–72–3. DOI: 10.1029/2001GL013768. eprint: https://agupubs.onlinelibrary.wiley.com/doi/pdf/10.1029/2001GL013768 (cit. on p. 5).

[14] Patrick Wittick and Ryan Russell. "Hybrid Gravity Models for Kleopatra, Itokawa, and Comet 67P/C-G". In: Sept. 2018 (cit. on p. 5).

[15] Gonzalo Tancredi, Santiago Roland, and Sebastian Bruzzone. "Distribution of boulders and the gravity potential on asteroid Itokawa". In: *Icarus* 247 (2015), pp. 279 –290. DOI: https://doi.org/10.1016/j.icarus.2014.10.011 (cit. on p. 5).

[16] Abe et al. In: *Science* 312 (2006), pp. 1344–1347 (cit. on p. 5).

[17] J. Atchison, R. Mitch., and A. Rivkin. "Swarm Flyby Gravimetry, NIAC Phase I Final Report". In: (2015) (cit. on p. 5).

[18] J.W. et al. McMahon. "The Gravity and Global Geophysical Environment of Bennu". In: *50th Lunar and Planetary Science Conference 2019* (2019) (cit. on p. 5).

[19] Zuber et al. In: *Space Sci. Rev.* 178 (2013), pp. 3–24 (cit. on p. 5).

[20] Kieran Carroll and Daniel Faber. "Tidal Acceleration Gravity Gradiometry for Measuring Asteroid Gravity Field From Orbit". In: Oct. 2018 (cit. on p. 5).

[21] Roberto Furfaro, Richard Linares, Vishnu Reddy, Jules Simo, and Lucille Le Corre. "Modelling Irregular Small Bodies Gravity Field via Extreme Learning Machines". In: Feb. 2017 (cit. on p. 6).

[22] S. Willis, D. Izzo, and D. Hennes. "Reinforcement Learning for Spacecraft Maneuvering Near Small Bodies". In: *AAS/AIAA Space Flight Mechanics Meeting* (2016) (cit. on p. 6).

[23] B. Turgut. "Application of back propagation artificial neural networks for gravity field modelling". In: *Acta Montanistica Slovaca* 21 (2016), pp. 200–207 (cit. on p. 6).

[24] A.A. Gret, E.E. Klingele, and H.-G. Kahle. "Application of artificial neural networks for gravity interpretation in two dimensions: a test study". In: *Bollettino di Geofisica Teorica ed Applicata* 41 (2000), pp. 1–20 (cit. on p. 6).

[25] Yue Wu, Hui Wang, Biaobiao Zhang, and K.-L Du. "Using Radial Basis Function Networks for Function Approximation and Classification". In: *ISRN Applied Mathematics* 2012 (Mar. 2012). DOI: 10.5402/2012/324194 (cit. on p. 6).

[26] Mohammad Reza Jafari, Tohid Alziadeh, Gholami Mehdi, Abdollah Alizadeh, and K Salahshoor. "On-line Identification of Non-Linear Systems Using an Adaptive RBF-Based Neural Network". In: *Lecture Notes in Engineering and Computer Science* 2167 (Oct. 2007) (cit. on p. 6).

[27] Nathan Harl, Karthikeyan Rajagopal, and S. N. Balakrishnan. "Neural Network Based Modified State Observer for Orbit Uncertainty Estimation". In: *Journal of Guidance, Control, and Dynamics* 36.4 (2013), pp. 1194–1209. DOI: 10.2514/1.55711. eprint: https://doi.org/10.2514/1.55711 (cit. on p. 6).

[28] IAU. *Minor Planet Center*. URL: http://minorplanetcenter.net// (cit. on pp. 9, 10).

[29] A. Kokorev and O. Golubov. "Modeling of asteroids shapes". In: () (cit. on p. 9).

[30] J. Torppa. "Ligthcurve inversion for asteroid spins and shapes". PhD thesis (cit. on p. 9).

[31] *Wikipedia*. URL: https://en.wikipedia.org/ (cit. on pp. 12, 129).

[32] S. Lien and J.T. Kajiya. "A Symbolic Method for Calculating the Integral Properties of Arbitrary Nonconvex Polyhedra". In: (1984) (cit. on pp. 12, 44, 45).

[33] D.J. Scheeres, D. Britt, B. Carry, and K.A. Holsapple. "Asteroid Interiors and Morphology". In: *Asteroids IV* (), 745â766 (cit. on pp. 13, 86, 87).

[34] *Asteroid Data*. URL: https://nssdc.gsfc.nasa.gov/planetary/factsheet/asteroidfact.html (cit. on p. 14).

[35] S.J. et al Ostro. "Radar Imaging of Binary Near-Earth Asteroid (66391) 1999 KW4". In: *Science* (2006) (cit. on p. 16).

[36] J.R. Wertz. *Spacecraft attitude determination and control*. Springer, Space Technology Library, 1978 (cit. on p. 23).

[37] A. Colagrossi. "Coupled Dynamics around Irregularly-Shaped Bodies with Enhanced Gravity Field Modelling". PhD thesis (cit. on pp. 23, 45).

[38] J. Bellerose. "The Restricted Full Three-Body Problem: Application to Binary Asteroid Exploration". PhD thesis (cit. on p. 26).

[39] V. Szebehely. *Theory of Orbits: The Restricted Problem of Three Bodies*. Academic Press, 1967 (cit. on pp. 28, 29).

[40] D. Guzzetti. *Coupled Orbit-Attutude Mission Design in the Circular Restricted Three-Body Problem*. West Lafayette, Indiana, 2016 (cit. on p. 29).

[41] L. Chappaz. *The Dynamical Environment in The Vicinity of Small Irregularly-Shaped Bodies with Application to Asteroids*. West Lafayette, Indiana, 2011 (cit. on pp. 30, 31).

[42] V. Szebehly. *The Theory of Orbits: The Restricted Problem of Three Bodies*. Academic Press Inc., 1967 (cit. on p. 30).

[43] F. Ferrari. "Non-Keplerian Models for Mission Analysis Scenarios About Small Solar System Bodies". PhD thesis (cit. on pp. 31, 36).

[44] D.J. Scheeres. *Orbital motion in strongly perturbed environments: application to asteroid comet and planeraty satellite orbiters*. Springer, 2012 (cit. on pp. 32–34, 43, 47).

[45] *NASA HORIZONS System*. URL: `https://ssd.jpl.nasa.gov/?horizons` (cit. on p. 35).

[46] S.J. et al Osto. "Radar Imaging of Binary Near-Earth Asteroid (66391) 1999 KW4". In: *SCIENCE* (2006) (cit. on p. 36).

[47] E.W. Hobson. *The theory of spherical and ellipsoidal harmonics*. Cambridge University Press, 1981 (cit. on p. 41).

[48] W.M. Kaula. *Theory of satellite geodesy*. Blaisdell Publishing Company, 1966 (cit. on p. 43).

[49] Robert A. Werner. "Spherical Harmonic Coefficients for the Potential of a Constant-Density Polyhedron". In: (1997) (cit. on p. 44).

[50] In: () (cit. on p. 44).

[51] W.D. MacMillan. *The Theory of Potential*. Dover Publications, 1958 (cit. on p. 45).

[52] D.J. Scheeres. "Dynamics About Uniformly Rotating Triaxial Ellipsoids". In: (1994) (cit. on p. 47).

[53] A. Capannolo. "Nanosatellites Formation Flying in Binary Asteroids Systems". PhD thesis (cit. on p. 47).

[54] Z. et al Zhenjiang. "Modeling and Analysis of Gravity Field of 433 Eros using Polyhedron Model Method". In: (2010) (cit. on p. 49).

[55] H. Alonso, T. Mendonca, and P. Rocha. "Hopfield neural networks for on-line parameter estimation". In: () (cit. on pp. 60, 63, 65, 152).

[56] M. Atencia, G. Joya, and F. Sandoval. "Hopfield Neural Networks for Parametric Identification of Dynamical Systems". In: () (cit. on pp. 61, 65, 152).

[57] Saratha Sathasivam, Nawaf Hamadneh, and Hong Choon Ong. "Comparing Neural Networks: Hopfield Network and RBF Network". In: *Applied Mathematical Sciences* 5 (Jan. 2011) (cit. on p. 62).

[58] J. J. Hopfield. "Neurons with graded response have collective computational properties like those of two-state neurons". In: (1984) (cit. on p. 63).

[59] M. Atencia and G. Joya. "Hopfield networks: from optimization to adaptive control". In: *IEEE* () (cit. on p. 63).

[60] S. Kamaleddin and Y. Nikraves. *Nonlinear Systems Stability Analysis*. CRC Press, 2013 (cit. on p. 63).

[61] S. Abe. "Theories on the Hopfield Neural Network". In: () (cit. on p. 63).

[62] M. Atencia, G. Joya, and F. Sandoval. "Parametric identification of robotic systems with stable time-varying Hopfield networks". In: () (cit. on p. 65).

[63] J. Solano, M. Atencia, G. Joya, and F. Sadoval. "A discrete gradient method to enhance the numerical behaviour of Hopfield networks". In: () (cit. on pp. 65, 66).

[64] J. Solano, M. Atencia, G. Joya, and F. Sadoval. "Numerical implementation of gradient algorithms". In: () (cit. on p. 65).

[65] J.R. Carpenter and D'Souza C.N. *Navigation Filter Best Practices*. NASA, 2018 (cit. on pp. 127–129).

[66] R.E. Kalman. "A new approach to linear filtering and prediction problems". In: *Journal of Fluids Engineering* (1960) (cit. on p. 127).

[67] V. Pesce. *Stereovision-Based Pose and Inertia Estimation for Unknown and Uncooperative Space Objects*. 2013 (cit. on pp. 127, 129).

[68] P.S. Maybeck. "Stochastic models, estimation, and control". In: *Academic press* (1982) (cit. on p. 127).

[69] Tai-shan Lou, Huimin Fu, Zhihua Wang, and Zhang Yongbo. "Schmidt-Kalman Filter for Navigation Biases Mitigation during Mars Entry". In: *Journal of Aerospace Engineering* 28 (Oct. 2014), p. 04014101. DOI: 10.1061/(ASCE)AS.1943-5525.0000423 (cit. on p. 131).

[70] S.F. Schmidt. "Application of State-Space Methods to Navigation Problems". In: ed. by C.T. LEONDES. Vol. 3. Advances in Control Systems. Elsevier, 1966, pp. 293 –340. DOI: https://doi.org/10.1016/B978-1-4831-6716-9.50011-4 (cit. on p. 131).

[71] V. Pesce, S. Silvestrini, and M. Lavagna. "Radial Basis Function Neural Network aided Adaptive Extended Kalman Filter for Spacecraft Relative Navigation". In: (2019) (cit. on pp. 147, 153).

[72] D.J. Scheeres and P. Sancherz. "The Strength of Rubble Pile Asteroids". In: *American Geophysical Union, Fall Meeting 2012, abstract id.P34A-05* (2012).

[73] K.A. Carrol, D.R. Faber, and Gedex Systems Inc. "Asteroid Orbital Gravity Graviometry". In: *49th Lunar and Planetary Science Conference* (2018).

[74] Y. Takahashi and D.J. Scheeres. "Small Body Surface Gravity Fields via Spherical Harmonic Expansions". In: *AIAA/AAS* (2014).

[75] E. Herrera, P.L. Palmer, and R.M. Roberts. "Modelling the gravitational potential of a non-spherical asteroid". In: ().

[76] Brandon A. Jones. "Efficient Models for the evaluation and the estimation of the gravity field". PhD thesis.

[77] *3D Asteroid Catalogue*. URL: http://space.frieger.com/asteroids/asteroids/4179-Toutatis.

[78] NASA. *JPL Small-Body Database*. URL: http://ssd.jpl.nasa.gov/sbdb.cgi?sstr=4179.

[79] *Space.com*. URL: https://www.space.com/51-asteroids-formation-discovery-and-exploration.html.

[80] NASA. *NASA Solar System Exploration*. URL: https://solarsystem.nasa.gov.

[81] Y. Shi, Y. Wang, and S. Xu. "Mutual gravitational potential, force, and torque of a homogeneous polyhedron and an extended body: an application to binary asteroids". In: *Celestial Mechanics and Dynamical Astronomy* (2017).

[82] Y. Takahashi and D.J. Scheeres. “Small body surface gravity field via Spherical Harmonic Expansion”. In: *AIAA* (2014).

[83] J. Kennedy and R. Eberhart. “Particle Swarm Optimization”. In: (1995).

Colophon

This document was typeset using the typographical look-and-feel `PhD_Dis` developed by Diogene Alessandro Dei Tos. The style is inspired by J. Stevens and L. Fossati *phdthesis Style*.

`PhD_Dis` is available for both LaTeX and LyX:

`https://gitlab.com/diogene/PhD_Dis.git`